SEARCH FOR DOUBLE ALPHA DECAY

By

Joseph Dopfer

A DISSERTATION

Submitted to
Michigan State University
in partial fulfillment of the requirements
for the degree of

Physics—Doctor of Philosophy

2026

ABSTRACT

There are two scientifically disparate projects presented in this thesis, linked by their use of shared experimental hardware. One being the development, characterization, and simulation of the Lifetimes and Branching Ratios Apparatus (LIBRA) setup, designed to measure lifetimes and branching ratios by applying and expanding upon the particle X-ray coincidence technique (PXCT). The other is a rare event search for simultaneous, back-to-back double alpha decay in ^{220}Rn using the GADGET II Time Projection Chamber (TPC).

LIBRA was designed to measure all photons and charged particles emitted in decays used to constrain astrophysically-relevant reaction rates. Using this information, through the PXCT technique, the lifetimes of particular resonances populated in electron capture or β^+ decay can be measured to the sub-femtosecond level. This, along with the branching ratios of these resonances, can be used to constrain reaction rates that would require multiple experiments to measure using a variety of other techniques. The results of the performance tests performed after building the apparatus are reported.

In the past few years there has been an increased effort theoretically to investigate the simultaneous emission of two alpha particles from heavy nuclei, motivating experimental searches to discover this novel mode of radioactive decay. Measured double alpha decay branching ratios would provide valuable information on the dynamics of alpha- and cluster-decay of heavy nuclei. Depending on the model used to predict double alpha decay half-lives, the results can vary widely. For the case of ^{220}Rn, the half-life predictions range over 17 orders of magnitude. Pursuant to the goal of constraining this theoretical discrepancy, the GADGET II Time Projection Chamber was modified to operate at higher pressures, up to 2,000 torr, and used to carry out a search for double alpha decay in ^{220}Rn. By imaging alpha decay events in 3D in the TPC and performing 3D fitting to determine the properties, double alpha candidate events have been investigated in detail. The TPC system was also coupled to LIBRA's two high purity germanium detectors to search for alpha decay to excited states of daughters in the decay chain of ^{220}Rn. Results from this experiment find no signal of $\alpha\alpha-$decay, and rule out two of the three theoretical models investigated.

ACKNOWLEDGEMENTS

TABLE OF CONTENTS

LIST OF TABLES vi

LIST OF FIGURES viii

CHAPTER 1: INTRODUCTION 1
- 1.1: Nuclear Physics Fundamentals 1
- 1.2: Astrophysics Background for LIBRA 3
- 1.3: Nuclear Structure Background for GADGET II 19

CHAPTER 2: LIBRA DESIGN AND TESTING 31
- 2.1: Rutherford's Measurement of the Half-life of 220Rn 31
- 2.2: The Theory of PXCT 35
- 2.3: LIBRA Design and Actualization 39
- 2.4: Performance Data and Simulations 54
- 2.5: Lifetime Measurement 63
- 2.6: 60Ga Decay Measurement 66

CHAPTER 3: MOTIVATION FOR DOUBLE ALPHA DECAY SEARCH 70
- 3.1: Double Decays 70
- 3.2: Previous Work on Double Alpha Decays 71

CHAPTER 4: PREPARING TO SEARCH FOR RARE EVENTS 79
- 4.1: LIBRA Germanium Setup 79
- 4.2: TPC 81
- 4.3: Calibration 88

CHAPTER 5: EXPERIMENTAL DATA AND ANALYSIS 93
- 5.1: Data Processing 93
- 5.2: Energy Spectrum 101
- 5.3: Gamma Data 114
- 5.4: Fitting GADGET II Data 122

CHAPTER 6: SUMMARY & DISCUSSION 144
- 6.1: LIBRA and the Particle X-ray Coincidence Technique 144
- 6.2: Alpha Decay to Excited States 144
- 6.3: Double Alpha Decay Branching Ratio 146

CHAPTER 7: OUTLOOK 148
- 7.1: Future Improvements to Data Analysis 148
- 7.2: Future Tests of Double Alpha Decay 149

BIBLIOGRAPHY 151

LIST OF TABLES

Table 2.1 The decrease in the rate of discharge between two parallel plates, with one plate covered in either a thin or thick layer of thorium. The rates were taken for successive layers of foolscap-paper placed on the thorium. The rate of discharge with uncovered thorium is taken to be unity [63]. 32

Table 2.2 Summary of the properties of all nuclei investigated using PXCT. Columns 1–7 list the EC/β^+ decay, the half-life ($T_{1/2}$) of the precursor, the β-decay energy (Q_{EC}), the proton-separation energy (S_p) of the EC/β^+-decay daughter nucleus, the total intensity of EC/β^+-delayed proton emission (I_p), the primary X-ray energies ($E_{K\alpha}$) that must be resolved for the $(Z-2)$ and $(Z-1)$ nuclei, the known lifetime of the K-shell vacancy, and the range of lifetimes of proton-emitting states in the EC/β^+-decay daughter nucleus obtained in each study. The last two rows list the properties of ^{60}Ga and ^{64}As for comparison. Table adopted from Sun, et al. [5]. 40

Table 3.1 All published predictions of $\alpha\alpha-$decay half-life and branching ratios for ^{220}Rn. . 77

Table 4.1 DDAS trapezoidal filter and timing parameter settings for each input in the double alpha search experiment. Note that the GADGET trigger is a TTL logic signal, and thus uses leading edge timing rather than CFD timing. 80

Table 4.2 Operating Parameters for the GADGET II TPC during the double alpha search [110]. Note the gating grid was always set to a transparent voltage. 86

Table 4.3 The range of volatges tested on the Micromegas as the pressure of the gas was increased in the TPC. The flow rate was adjusted throughout the tests, as well as values in the GET software. The gas pressure shown here is what was read out by the MKS flow controller, but the DATAQ pressure transducer, which is believed to be more accurate in this range of pressures, read about 150 torr grater than the MKS throughout the experiment and test runs. 89

Table 5.1 Total Number of Alpha Particles in each Peak 112

Table 5.2 Alpha gated gammas compared to background. Alpha gate uses mesh spectrum above 5,000 ADC counts. Resolution of the peaks must be within 5% of each other and mean must be within 2 keV of the previously measured value. . . 120

Table 5.3 Branching ratios for α decays of ^{220}Rn and ^{216}Po populating excited states in the daughter nuclei, inferred from the observation of α–γ coincidence peaks at the listed γ-ray energies. Energies without an uncertainty were not measured in this experiment and taken from literature. Quantities with a < symbol represent 90% confidence interval upper limits, because there is no statistically significant excess in counts in the alpha-gated gamma spectrum above background. The excitation energy and J^π of the state comes from NNDC data. . 121

Table 5.4 Standard deviations (uncertainties) for reconstructed parameters. 128

Table 5.5 Quality of the fits of the backgrounds for different models. One approach fits the background in the dxy > 5.0 mm dz projection, and scales that model to the statistics of the dxy < 5.0 mm dz projection ('fit on Accidental Coin. Band'). The values in the table for this approach represent how well the model fit the accidental coincidence band, prior to being scaled and applied to the RnPo data. The second approach fits the RnPo data (sans the first dz bin) directly as background ('direct'). 141

Table 5.6 Results from Fitting Background to Signal Peak in Two Alpha Data. The excess uncertainties combine the Poisson uncertainty from statistics with the model uncertainty from the covariance matrices of the fit. 142

Table .1 Valve Status Summary (V – open, X - closed) 171

Table .2 Total number of alpha particles in each peak, assuming Bismuth decays on the cathode. 181

LIST OF FIGURES

Figure 1.1 The Chart of Nuclides colored by decay modes. β^+/EC decay is colored in blue, β^- decay in pink, α decay in yellow, and spontaneous fission in green. Stable nuclei that do not decay by any of these modes are colored black. Figure taken from the National Nuclear Database Center (NNDC), *https://www.nndc.bnl.gov/*. 2

Figure 1.2 Experimental binding energy per nucleon (BE/A) versus mass number, taken from from the AME2012. Each point is the most tightly bound (highest binding energy) nucleus for a given mass number [1]. 4

Figure 1.3 A small portion of the chart of nuclides that illustrates which process created which isotopes. Each stable element in yellow is labeled with the processes that contribute to its abundance [3]. 8

Figure 1.4 'The breakdown of solar system (meteoritic) n-capture isotopic abundances into r- and s-process components [3].' 8

Figure 1.5 X-ray burst light curves found by varying reaction rates of proton capture on ^{59}Cu in a multi-zone model simulation of a type I X-ray burst. Figure taken from Cyburt, et al. [4]. 10

Figure 1.6 Experimental cross section of the $^{16}\mathrm{O}(p,\gamma)^{17}\mathrm{F}$ reaction. Note the logarithmic scale. Taken from Iliadis [1]. 12

Figure 1.7 Multiplying the Maxwell-Boltzmann distribution (dashed line) with the Gamow factor (dashed-dotted) gives the Gamow Peak (solid line), for an example reaction at a temperature of 0.2 GK. Taken from Iliadis, page 167 [1]. 13

Figure 1.8 rp-process path in the Ni-Cu and Zn-Ga cycle region on the proton rich side of the chart of nuclides. Dark gray boxes are stable isotopes. Taken from Sun et al. [5]. 18

Figure 1.9 Evaluated decay scheme of ^{60}Ga. Information on sources for evaluated data can be found in Figure 2 of Sun et al. [5]. 18

Figure 1.10 Visualization of the five terms of the liquid-drop model described in Equation 1.14. Figure from Obertelli [24]. 20

Figure 1.11 Binding energy per nucleon as calculated with the liquid-drop model, for stable nuclei. The contributions to the BE/A for each term is shown. The parameters used to calculate the corrections are: $a_V = 15.85$ MeV, $a_S = 18.34$ MeV, $a_C = 23.21$ MeV, $\delta = +12, 0, -12$ MeV for even-even, even-odd, and odd-odd nuclei, respectively. Figure from Obertelli [24]. 21

Figure 1.12 Potential barrier that a charged particle must overcome for decay to occur as a function of radius, r. The total potential is built from the nuclear, Coulomb, and centrifugal potentials. Figure taken from [26]. 23

Figure 1.13 DFT Workflow for fission. A similar approach is taken for cluster decay calculations with Microscopic theories [30]. 24

Figure 1.14 Taken from Royer and Remaud [58], this shows the evelution of a deformed nucleus parameterized by the equation $R(\theta) = a^2 \sin^2\theta + c^2 \cos^2\theta$, as a/c goes from 0 (one sphere) to 1 (two spherical fragments). They call it an elliptic lemniscatoid shape. 27

Figure 2.1 Drawing of Rutherford's experimental setup to measure this radioactive 'emanation', as he called it at the time. It later was found to be ^{220}Rn, which decays with a half-life of 55.6 seconds. Rutherford's result was 60 seconds [63]. 33

Figure 2.2 Results of the first ever half-life measurement by Rutherford. Curve B shows the increase in activity via bellows transporting ^{220}Rn to the measurement vessel. Curve A shows decay of activity of ^{220}Rn after the bellows had been stopped [63]. 34

Figure 2.3 The time range over which a few lifetime measurement techniques are effective. Taken from Nolan et al. [72]. 36

Figure 2.4 Schematic illustrating electron capture to a proton-unbound excited state and the Particle X-ray Coincidence Technique [5]. 37

Figure 2.5 CAD Drawing (top) and photograph (bottom) of LIBRA. The insets show the target in two configurations, tuning and collection. Tuning the beam requires a Faraday cup and a simpler to produce beam that ensures the beam of interest will be on target. Collection uses a foil to stop the slow beam in the center of the chamber for greatest detection efficiency by our Si and Ge detectors for decay measurements. 41

Figure 2.6 Top panel shows entirety of FRIB, from experimental areas to beam line to facilities that manufacture and repair accelerator parts. The bottom panel shows a zoomed in section of the beam line where the beam is stopped and brought to the experimental area for measurement. Figures courtesy of Jill Berryman and Craig Snow. 43

Figure 2.7 Cross section of gamma ray interactions with NaI detectors. Rayleigh scattering is coherent, elastic scattering off of electrons. Taken from Knoll [107]. . . 46

Figure 2.8 Schematic of a Mesytec MPR-1 preamplifier, configured in a charge sensitive mode. In this mode the voltage signal produced by the preamp will be directly proportional to the incoming charge from the detector (assuming the time pulse of the signal is short compared to the time constant of the preamp and that the input capacitance is typical of a radiation detector). Figure from Mesytec data sheet for MPR-1 [112]. 51

Figure 2.9 Parallel-encoded ("flash") ADC. Taken from Horowitz and Hill [113]. 53

Figure 2.10 Caption for Dead Time of LIBRA Figure 55

Figure 2.11 X-ray and γ-ray spectra measured by the LEGe detector using the ^{55}Fe (top), ^{152}Eu (middle), and ^{241}Am (bottom) sources. Taken from Sun, et al. [5]. 56

Figure 2.12 Photopeak efficiency of the LEGe X-ray detector using the characteristic X-rays of Samarium and Neptunium from ^{152}Eu and ^{241}Am, respectively. X-ray tests were taken with the LEGe attached to the LIBRA chamber, with the sources placed in the center of the chamber at a 45° angle to mimic the position of the target during an experiment. Dashed and solid lines represent simulated data from GEANT4. Taken from Sun, et al. [5]. 57

Figure 2.13 γ-ray spectra measured with XtRa1 (red) and XtRa2 (blue) using a ^{152}Eu source. Top panel: the ^{152}Eu source is placed midway between the two XtRa detectors facing each other. Bottom panel: the ^{152}Eu source is placed at the center of the vacuum chamber, with the two XtRa detectors positioned as shown in Figure 2.5. All γ-ray energies are adopted from Ref. [117] and rounded to the nearest 0.01 keV. The insets demonstrate the detector responses at 122 and 1408 keV. Taken from Sun et al. [5]. 58

Figure 2.14 Absolute γ-ray photopeak detection efficiency of the two XtRa detectors were determined using the ^{152}Eu, ^{137}Cs, and ^{60}Co sources placed at the center of the chamber. For energies above 1500 keV, efficiency values were obtained from GEANT4 simulations and scaled to align with the experimentally measured low-energy data. The efficiency curves along with the 1σ uncertainty bands are generated by fitting all data points. Taken from Sun et al. [5]. 59

Figure 2.15 α spectrum measured by MSD26 using the ^{241}Am source. The energy resolution of the MSD026 at 5485 keV is 031% (FWHM is 17.0 keV). Taken from Sun et al. [5]. 60

Figure 2.16 Upper: α-energy spectra measured by MSD12 (red), MSD26 (blue), and MSD12+MSD26 (black) using the ^{241}Am source. Lower: ΔE-E 2D plot of the same data. Taken from Sun et al. [5]. 61

Figure 2.17 Coincidence timing between detectors in LIBRA. Taken from Sun et al. [5]. . . 62

Figure 2.18 Coincidence spectrum between the MSD detector telescope and LEGe obtained using an ^{241}Am source placed at the center of the chamber. A simplified ^{241}Am decay scheme illustrating the dominant α-γ sequence is also shown as an inset. Taken from Sun et al. [5]. 62

Figure 2.19 Black line represents the ungated γ spectrum of ^{152}Eu measured by the XtRa 1 detector. This spectrum has been scaled down by a factor of 5. The red spectrum is the same data as the black, but gated on coincident, characteristic X-rays from Samarium measured by the LEGe detector. The blue spectrum represents the data from the black spectrum, gated on β-particles measured by MSD026. Taken from Sun et al. [5]. 64

Figure 2.20 ^{241}Am X-ray and γ-ray energy spectra measured by LEGe. X-ray energy values are adopted from Ref. [118] rounded to the nearest 0.01 keV. γ-ray energy values are adopted from Ref. [119] rounded to the nearest 0.01 keV. . . . 65

Figure 2.21 Time differences between the 59.5 keV γ-ray signals in LEGe and the 5486-keV α signals in MSD. For Run 1 and Run 3, an α gate of 5417 ± 60 keV is set on the MSD sum energy. For Run 2, an α gate of 5479 ± 20 keV is set on the energy measured by MSD026 alone. 66

Figure 2.22 Time differences between the 59.5 keV γ-ray signals in LEGe and the 5486 keV α signals in MSD. The fit curves in red, blue, and green represent Run1, Run2, and Run3, respectively. 67

Figure 2.23 Top panel: Charged-particle ΔE–E spectrum simulated using the theoretical decay properties of ^{60}Ga together with the measured detectors' responses. Middle panel: X-ray spectrum gated on all protons in the ΔE–E spectrum, yielding a total X-ray ratio of $R_{\mathrm{Cu/Zn}} = 3.2(3)$. A double-Gaussian function with a linear background is fit on the Cu and Zn K_α peaks. Bottom panel: Cu/Zn K_α X-ray count ratio and the inferred lifetime as a function of the coincident proton energy. The error bars show statistical uncertainties, with the leftmost and rightmost points representing upper and lower limits, respectively. Taken from Sun et al. [5]. 69

Figure 3.1 Deformation energy surface of ^{224}Ra calculated with the relativistic Hartree-Bogoliubov model based on the DD-PC1 functional and separable pairing interaction. The β_{20} and β_{40} axes represent the quadrupole and hexadecapole deformations, respectively. The black and white line follows the least-action path of $\alpha\alpha$−decay from equilibrium deformation to the scission point. Figures taken from Mericer et al. [128]. 72

Figure 3.2 Nuclei with Z and N greater than 50, whose $Q_{\alpha\alpha} > 0$, computed from experimentally measured masses in AME 2003 [140]. The red dots represent nuclei whose second alpha decay in the sequential decay is energetically forbidden, and the blue dots represent nuclei whose first alpha decay is energetically forbidden. Figure from Mercier et al. [128]. 73

Figure 3.3 Santhosh and Jose's calculations showing the half-life vs the mass number of the parent nuclei for Radon and Francium [62]. 74

Figure 3.4 The reflection-symmetric deformation energy surface is plotted in the quadrupole-hexadecapole plane, calculated with RHB with a DD-PC1 functional. The gray curve shows the least-action path, with insets displaying the nuclear densities from equilibrium deformation to scission [141]. Figure from Zhao et al. [141]. 76

Figure 3.5 Results from Zhao et al.'s calculations of the different decay mode half-lives (and equivalent branching ratios in blue diamonds, labeled on the right y-axis) for ^{212}Po, $^{216-220}$Rn, and $^{220-224}$Ra, compared to available experimental values in black. Figure from Zhao et al. [141] 77

Figure 4.1 Schematic of the top-down view of the TPC, with the LIBRA germanium detectors flanking the chamber. The red lines indicate the distance from the lip of the chamber to the edge of the germaniums, which was 11.4 cm for the south detector and 4.2 cm for the north. 79

Figure 4.2 Cartoon schematic of the GADGET II TPC with a $\alpha\alpha-$decay event. 82

Figure 4.3 ^{228}Th Source location in the GADGET II gas handling system. 84

Figure 4.4 ^{228}Th decay chain to the stable isotope ^{208}Pb. Numbers in red are the alpha particle energies in keV. Only ^{220}Rn can make it into the chamber in theory, so the TPC only observes decays below radon. 85

Figure 4.5 ATTPCROOT simulation of a double alpha track in gas at 800 torr and 2000 torr, respectively. 85

Figure 4.6 Metal plate reinforcement of the micromegas board for safe operation at higher pressures. 87

Figure 4.7 Replacing the kapton window with an aluminum window to be used during the $\alpha\alpha-$decay search. This entrance window is where a beam would enter the detector during a beamline decay experiment. For future experiments, the new metal window can be left on, or replaced with kapton again, depending on the experiment's needs. Notice that the kapton shows signs of minor wear and flexing due to pumping the detector to vacuum and back to atmosphere many times over years. That being said, it remains durable and may be reused if necessary. 87

Figure 5.1 Trace data from an event in GADGET, operating at 2,000 torr. Dashed lines represent veto pad data. The ADC in the AsAds is 12-bit. 95

Figure 5.2 Processed trace data of the same event shown in Figure 5.1. The top image shows the background subtraction used in the double alpha search. The bottom image shows the example of a different approach to finding the peaks to keep in the background subtraction, rather than using a fixed window around the time bins nearest to the maximum value in each pad trace. 96

Figure 5.3 Drift Velocity of Electrons in P10 gas. Data from English and Hanna 1953 [162] 97

Figure 5.4 Plots of calculated ranges versus angles for three different z-scale parameter inputs. First the z-scale is set to a too low 0.1, then it is set to 0.65, and finally set to 1.45. Since this data comes from run 342 during the double alpha search, the chamber was operating at 2000 torr, and a z-scale of 0.65 looks to be about right, where the range of the event is not dependent on the angle of the track. 98

Figure 5.5 Result of measuring gain via minimization method described in the text. Each pixel represents a pad in the pad plane. The color indicates the conversion from ADC counts to energy in MeV. This uses 100,000 events from the ^{212}Po peak. 99

Figure 5.6 Effect of pad gain match correction on a single run in the double alpha search data. Because of the large size of the full dataset, this pad-by-pad gain matching procedure was not applied to the entire dataset due to time and computing resource constraints. 101

Figure 5.7 Range versus energy plot for all runs in the double alpha search. In panel (a) there was no attempt to center peak means run-by-run on a common value. In panel (b), the runs were aligned in range and counts by gating on and fitting the 8.78 MeV alpha peak, and adjusting the centroid to match a constant value before combining the runs. Since the gain drifts slightly on the pads throughout the experiment, the horizontal widths of the clusters in (a) are wider than in the matched version, (b). 103

Figure 5.8 The top figures show the changes in the range and energy run-over-run, respectively. These runs occurred over the course of 6 months, from May to November 2024. The bottom figures correct for gain and range drift over that time. The red lines show the Po-212 reference peak used for gain matching. Panel (a) shows shifts in gain at run numbers that line up with P10 bottle changes, e.g. around run 300. 104

Figure 5.9 Energy histogram combined using the same procedure as was used for Figure 5.7. In blue there is no veto condition applied to the data. In orange, the data is only plotted if the hits on each veto pad do not exceed 300 ADC counts. . 106

Figure 5.10 Centroid detection on events with angle no more than 10° off of the z-axis. This is done for dozens of events in each of the $>$ 550 runs in the data, and compiled and used as our radiation distribution. Left gives a centroid of (5.4,21.0), the right gives a centroid of (22.1,18.1). 107

Figure 5.11 The 2D distribution derived from real data as described in the text. The figure on the left is gated on the lower energy peak, which encompasses alphas from ^{212}Bi, ^{220}Rn, and ^{216}Po. The figure on the right is gated on the higher energy peak, alphas from the decay of ^{212}Po. This view shows the distribution of radiation on the pad plane from the view inside the chamber, in other words, from the radiation's perspective of the pad plane. 108

Figure 5.12 Two-dimensional cuts on the range versus energy plot, to select events whose widths were analyzed. 109

Figure 5.13 Distribution of track widths for the four cuts made. If all the decay products of ^{220}Rn decay at the cathode, one should expect their width distributions to be alike. All events' track widths are shown in blue. 110

Figure 5.14 Fitted simulated (left) and real (right) alpha energy spectra. The data is gain matched run-by-run. The dashed magenta peak is ^{212}Po, green is ^{216}Po, blue is ^{220}Rn, red is ^{212}Bi. The solid black line is the sum. 112

Figure 5.15 Alpha energy spectrum with the total fit, including all four peaks. In the lower half of the plot are the residuals from the fit, which are used as errors in the estimates of the total number of observed alpha particles from each nucleus, as described in the text. 113

Figure 5.16 Efficiencies from both ATTPCROOT simulations (red) and geometric efficiency (blue) simulationsas a function of opening angle for two-alpha events. Both datasets are shifted to recover the efficiency to detect a ^{216}Po single alpha at an opening angle of 0°. The error shown in the plot is statistical. 115

Figure 5.17 Simulated gamma efficiency of the two detectors used in the double alpha experiment. Red points are the north detector, blue points are the south detector, and black points are the combined efficiency of the two. Gammas were emitted isotropically at 550 keV. Uncertainty of ±3 mm are placed on the data based on limitations in the measurements of the absolute positions of the detectors relative to the chamber. 116

Figure 5.18 Simulated efficiency of the south (blue), north (red), and combined (black) gamma detectors versus energy of the emitted gamma ray. The distribution of the radiation in this simulation comes from the method described in Section 5.2.2. 117

Figure 5.19 Comparing the counts found in the 550 keV peak in the north germanium detector (left) to the south germanium detector (right). Notice that the south peak is wider due to gain drift that the north detector does not experience. . . . 118

Figure 5.20 Mesh data recorded by the XIA DAQ. Events below 5,000 ADC counts are removed. 118

Figure 5.21 Gamma spectrum in coincidence with alphas (black). Background gamma data taken before the experiment was run, scaled to the ^{40}K gamma ray peak (blue). 119

Figure 5.22 Time difference histogram between the north Germanium detector and the mesh signal from the GADGET TPC. The solid red line shows the entire summed fit with residuals. The dashed lines show each component of the fit, three gaussians and a second order polynomial. The gaussian components are shifted up by 1200 counts so they can be seen in the plot. This plot can act as an indicator of the steady-state distribution of radiation in the detector. A 4 μs delay was added to the Germanium signal in the DAQ to ensure that the alpha signals on the mesh would fall within the coincidence window. 122

Figure 5.23 Gating on mesh spectrum events in the ^{212}Po peak and plotting those events' timestamp difference with the gammas in the same event window. 123

Figure 5.24 Histogram of the background-subtracted peak height of each pad that fired in random events across all runs taken for the $\alpha\alpha$-decay search. 126

Figure 5.25 Output of the clustering algorithm written for the purpose of distinguishing between two alpha particle tracks, and using the values pulled from the algorithm as starting values for the fitter. Note that the ADC threshold used for this algorithm was set to 1300 in order to remove as much noise as possible. . . 127

Figure 5.26 Example of Noisy Events that show up above the energy cut. On the left is an event where the trace is entirely noise. On the right is an event where there was likely a real alpha particle, but the noise at the beginning of the trace comes from the electronics. 129

Figure 5.27 A noisy event that lights up the entire pad plane and is not caught by the flagging algorithm. 129

Figure 5.28 Four examples of events classified as disintegration events. 131

Figure 5.29 Total energy of the two alpha events from fits. The fit requires a ADC counts to MeV parameter which was set using single alpha data, and ended up systematically underestimating the energy of the particles. The data in this plot is corrected for that effect. 132

Figure 5.30 Energy sharing between the two alphas in the fitted data. 132

Figure 5.31 Two alpha events' energies. The larger energy is plotted on the y-axis, and the smaller energy is plotted on the x-axis. This plot incorporates the residual and location constraints described in the text. The diagonal dashed lines represent the energy cut used when extracting fit data for further double alpha analysis described later on in this chapter. 134

Figure 5.32 GADGET TPC alpha geometric efficiency map created from simulation. 136

Figure 5.33 Radial distribution of radiation in the detector, generated from the centroid method shown in Figure 5.10. 137

Figure 5.34 Best model fit of the dxy-dz distribution. Left panel shows the data from the fit values. Middle panel shows the scaled simulation with both the AC and RnPo background. Right panel show the residuals. 138

Figure 5.35 Left: Y-projection (dz) of the data and model for dxy > 5.0 mm. Right: Y-projection (dz) of the data and model for dxy < 5.0 mm. 138

Figure 5.36 Left: Projection of data and models for dxy > 5.0 mm. Right: Projection of the data and normalized models for dxy < 5.0 mm. 139

Figure 5.37 All of the models applied to the d_{xy} < 5.0 mm data. The solid lines represent the fits to the AC background region, which is then scaled to the statistics in the RnPo region. The dashed lines represent direct fits to the RnPo region. . . . 141

Figure 5.38 Opening angle distribution of all fitted two alpha events (blue), two alpha events with origins near (dxy < 5 mm and dz < 10 mm), and a theoretical isotropic opening angle distribution weighted by the geometric efficiency. The geometric efficiency was simulated in ten degree increments from ten degrees to 180 degrees (back-to-back). Because there is low statistics in the similar origin events data, the 68% Garwood confidence intervals were used for error bars. [168] 143

Figure 6.1 ^{220}Rn $\alpha\alpha-$decay branch. Results from different fits to the data compared to the theoretical estimates. The nominal model is the direct linear fit, and the error takes into account model and statistical uncertainties. The hatched region on the right uses the excess in counts in the last bin of Figure 5.38, and assumes back-to-back alpha particles. It shows the 90% confidence interval. . . . 146

Figure A.1 Zhao et al.'s version of Figure 3.2. The chart shows nuclei whose Z and N are > 50, and whose $Q_{2\alpha}$ values are > 0. Zhao et al. states the higher the Q-value, the more favorable that nuclei is as a candidate [141]. 172

Figure A.2 Schematic of GADGET Gas Handling System (GHS). Components highlighted in a dashed red line are outside of the GHS rack-mounted enclosure. . . . 177

Figure A.3 Range versus Energy plots with no veto condition for runs throughout the experiment 179

Figure A.4 Efficiency corrected radial distribution of the radiation, fit with a quadratic and extended to the edge of the radius of the active surface of the TPC. 180

Figure A.5 Results of fitting the data with the simulation using the extended quadratic radial distribution. 180

Figure A.6 The same simulated data is plotted on the left. However, when the parameters of that fit are used to fit the real data on the right, the ^{212}Bi peak (lowest energy) is assumed to have half the counts in it in an attempt to compensate for a scenario in which the Bismuth is decaying after getting stuck to the surface of the cathode. 181

Figure A.7 Event displays for selected runs. 182

CHAPTER 1

INTRODUCTION

This thesis covers two different projects, each with their own distinct physics goals. The first of these projects that will be discussed is the planning, design, assembly, and testing of the LIfetimes and Branching Ratios Apparatus (LIBRA), using and expanding upon the **P**article **X**-ray **C**oincidence **T**echnique (PXCT). LIBRA allows for measurements of lifetimes in the sub-femtosecond range, which is useful for many aspects of nuclear physics, as lifetimes are among the most basic properties of nuclei and used in wide-spread applications in nuclear physics. At the same time, LIBRA is able to measure the branching ratios of many decay channels of astrophysically relevant nuclei. LIBRA was initially designed to measure lifetimes and branching ratios of resonances populated by electron capture and β^- decay. Finally, the **GA**seous **D**etector with **GE**rmanium **T**agging II (GADGET II) pressure upgrade and subsequent experiment will be discussed. This experiment was proposed to probe for a new decay mode, simultaneous double alpha decay, which has been discussed theoretically and gained renewed interest in recent years due to new work predicting half-lives that are feasible to measure experimentally.

1.1 Nuclear Physics Fundamentals

Before approaching the topics discussed in this thesis, this chapter will be useful for uninitiated readers, which begins with a brief introduction to the field of nuclear physics, then dives deeper into the particular areas of interest. The two projects using LIBRA then GADGET aim to answer questions in the fields of nuclear astrophysics and nuclear structure & dynamics, respectively. As such, this chapter covers how astrophysical reaction rates are measured in the lab, and how physicists use experimental observables to discover the structure of nuclei across the chart of nuclides.

Just as in chemistry the map by which the elements are categorized is the periodic table, so too in nuclear physics is there a map that describes the areas of interest. In the case of the study of the nucleus, the number of neutrons within the nucleus are equally important to the number of protons. Continuing with the chemistry parallel, if one wants to understand the properties of an atom, the number of electrons typically governs how that element interacts. And under normal circumstances,

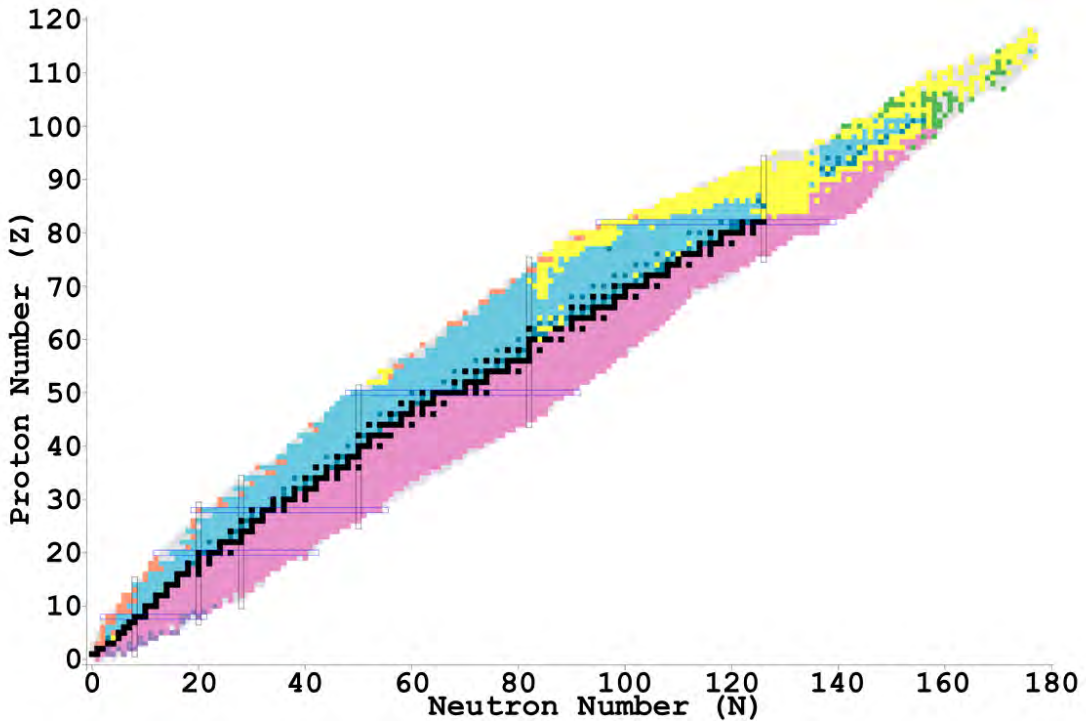

Figure 1.1 The Chart of Nuclides colored by decay modes. β^+/EC decay is colored in blue, β^- decay in pink, α decay in yellow, and spontaneous fission in green. Stable nuclei that do not decay by any of these modes are colored black. Figure taken from the National Nuclear Database Center (NNDC), *https://www.nndc.bnl.gov/*.

the number of electrons of an atom is equal to the number of protons. From the point of view of a physicist, chemistry is primarily described by the electromagnetic force. If this force is well understood in theory scientists can make accurate predictions about how atoms and molecules will interact and behave, before even testing it ourselves. In nuclear physics, the fundamental forces that govern how nuclei behave and interact with each other are the strong and weak forces, with only part of the behavior emerging from the electromagnetic force. Because of this, the nuclear physicist's map looks different from the periodic table, but it still retains similar features. In Figure 1.1, we see that it is most convenient to map the Chart of Nuclides, as it is called, in two dimensions; increasing proton number on the y-axis and increasing neutron number along the x-axis. In chemistry, we are concerned mainly with those nuclei in black, the stable nuclei. Whereas to get the full picture of the nuclear forces, we as nuclear physicists must broaden our map to include the unstable isotopes, shown in color in Figure 1.1. Additionally, we can see shell closures - analogous to electron shell

closures on the periodic table - highlighted by vertical and horizontal lines on Figure 1.1. Just as noble gases represent shell closures at electron shells that contain electrons in numbers of 2, 8, 18, 32, etc., so too does nuclear physics have these 'magic numbers' as they are called, at proton **or** neutron numbers 2, 8, 20, 28, 50, 82, and 126. Those nuclei whose proton and neutron number are both magic are referred to as 'doubly magic', such as ^{16}O, and as a result are more tightly bound as compared to their surrounding neighbors. This can be seen in the structure of the chart of nuclides, notice how along the border of measured isotopes, especially at higher masses, it bulges out near magic numbers - it is easier to produce these nuclei than very unstable nuclei far from the magic numbers. The nuclei with magic numbers can be considered an analog to the noble gases of the periodic table.

Instead of the ~100 elements on the periodic table, there have been 3,000 nuclides discovered, each with their own nuclear structures and properties. Almost all nuclides have something about them that is not described in sufficient detail by our current theories. By providing some of the most exotic isotopes, the Facility for Rare Isotope Beams (FRIB) enables us to learn about these properties, and in doing so reach its goals of better understanding nuclear structure/dynamics, nuclear astrophysics, fundamental interactions, and applications in industries such as medicine and national defense. Experimental nuclear physics' ultimate goal is to measure the properties of enough of these nuclei, especially in the exotic regions FRIB allows us to reach, to understand the forces that hold all nuclei together.

1.2 Astrophysics Background for LIBRA

One of our main goals in nuclear astrophysics is to study the origin of the elements. For this, we need to understand the mechanisms by which stellar environments produce the elements, and the rates at which these reactions and decays take place. Nuclear physics not only governs the abundances of the elements produced, but also provides an explanation of: the energy generation in stars required during this production, the stellar events we observe such as X-ray bursts (XRBs), and highly dense matter in neutron stars.

Starting at the beginning, just minutes after the Big Bang, the universe had cooled down enough

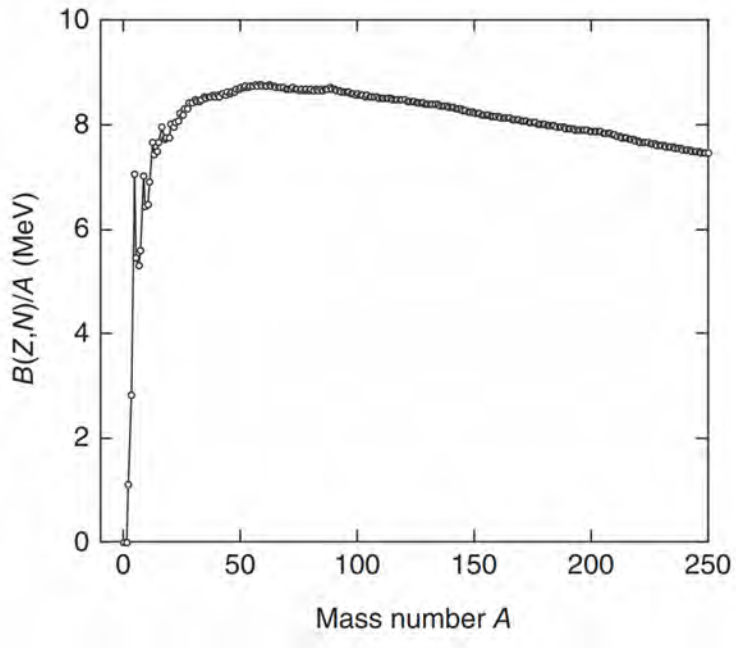

Figure 1.2 Experimental binding energy per nucleon (BE/A) versus mass number, taken from from the AME2012. Each point is the most tightly bound (highest binding energy) nucleus for a given mass number [1].

that free protons and neutrons could exist at a ratio of 7-to-1 [1]. The elements of hydrogen and helium had precipitated out of the soup of energy in a ratio that we still see today in metal-poor clouds of hydrogen, about 4-to-1 mass abundance ratio of hydrogen to helium[1] We can verify this with a counting argument. If we have a proton to neutron ratio of 7, and we create one ^{4}He nuclei, we use 2 neutrons and 2 protons, with 12 protons left over. As the universe expanded and matured, eventually the first stars formed as gravity grouped large quantities of these hydrogen and helium atoms together. Once this mass becomes large enough, the temperature and density due to gravity can become so great in the cores of the protostars formed that the electric repulsion between nuclei can be overcome and fuse elements together, creating heavier and heavier elements. Luckily, this burning (or fusion) produces a surplus of energy, and as such provides an opposite thermal pressure to the gravitational force compacting the matter towards the core of the star.

How do we know fusion produces a surplus of energy? Keeping in mind one of the many

[1]Regression to zero metallicity helium abundance: $Y_p = 0.2465 \pm 0.0097$ compared to the result obtained for BBN based on Planck determination of baryon density: $Y_p = 0.2485 \pm 0.0002$ [2].

applications of Einstein's mass-energy equivalence, $E = mc^2$, we write the equation for the mass of a given nucleus in the following way

$$M(Z, A) = Zm(^1\mathrm{H}) + Nm_n - B(Z, A)/c^2, \tag{1.1}$$

where M is the mass of the nucleus, Z is the number of protons in the nucleus, N is the number of neutrons in the nucleus, A is $Z + N$, $m(^1\mathrm{H})$ is the rest mass of hydrogen, m_n is the rest mass of a free neutron, c is the speed of light, and B is the binding energy of the nucleus. Measuring accurately the mass of a given nucleus will tell us the difference in mass between that nucleus and its constituent pieces. Natural systems prefer lower energy configurations, so if we think about each term in Equation 1.1 as energy, the system of individual hydrogen nuclei (protons) and free neutrons is in a higher energy state than the combined nucleus. The larger the binding energy per nucleon, the harder it becomes for any given nucleon in the nucleus to escape the system, resulting in a more stable nucleus. In the case of fusion, we have the following equation:

$$M(Z, A) = M(z_1, a_1) + M(z_2, a_2) + B(z_1, a_1)/c^2 + B(z_2, a_2)/c^2 - B(Z, A)/c^2. \tag{1.2}$$

Note that in the previous equation 1.2, $z_1 + z_2 = Z$ and $a_1 + a_2 = A$, so the total number of nucleons is conserved in this process; this means that we can think of the binding energy requirements in terms of binding energy per nucleon without any loss in generality in the case of fusion. If we rearrange this equation to group mass terms on one side, we see that if the *BE/A* increases after fusion, the mass difference will be negative, meaning the resulting nucleus after fusion takes place is more stable and releases energy.

As we can see from Figure 1.2, at low mass numbers like hydrogen and carbon, a fusion of nuclei will produce a nucleus with a higher binding energy per nucleon. Once you reach a mass number of about 20, the binding energy remains remarkably stable at around 8 MeV/nucleon. However, we can see from the figure that it peaks at ^{56}Fe. This means that for elements lighter than iron, fusion into heavier elements will produce energy, and for elements heavier than iron, they may break apart to produce energy in a process called fission. In both cases, nuclei release energy by moving towards that iron peak. The mechanism for stars to combat gravity and prevent collapse is

generating thermal energy from fusion. Once a star has burned all of the hydrogen in its core, it does not have enough energy (or temperature, if you want to think of it that way) to fuse helium together to keep gravity from pressing the star inward. This leads to a contraction of the star, rapidly increasing its temperature until helium is able to ignite, and fusion of this heavier element can begin to equalize gravity.

If the star has low mass, this continues until the helium runs out. Then the star contracts again, but it does not have enough total mass for gravity to ignite the next heaviest element, and the star becomes a white dwarf, slowly dimming for the rest of time. If the star is large enough, it can keep up this process of fusing heavier and heavier elements until it gets to ^{56}Fe. At that point, no matter how large the star is, fusing ^{56}Fe and the heavier elements removes energy from the star, and it will be impossible for fusion to sustain the star.

If this is the case, why do we see non-zero chemical abundances of elements heavier than iron in the universe; how did they end up on Earth? If not in stars, where are these elements produced, can we see the stellar events that cause this production?

Much of the abundances of heavy elements are thought to be made in massive stars during core helium burning and in AGB (Asymptotic Giant Branch) stars. However, as we already discussed, it is not possible for elements heavier than iron to be used as fuel by the star, so these elements are created in a different way. These elements are created through a path known as the 'slow neutron capture', or 's-process'. This s-process occurs when a seed nuclei such as ^{56}Fe captures free neutrons, creating an unstable, heavier nucleus. This heavier nucleus then has an excess of neutrons, and β^--decays back to stability. Nature's trick here to bypass the need for fusion is clever because in the case of neutron capture, the nucleus does not have to worry about like charges repelling (protons against protons), making the probability of neutron capture much higher. Using the case of ^{56}Fe to demonstrate this process, the nucleus is allowed to capture neutrons to ^{57}Fe and then to ^{58}Fe, both of which are stable. However, when a third neutron capture occurs, we end up with an unstable ^{59}Fe. At this point, the path can branch. ^{56}Fe can continue to capture neutrons, but if that takes too long (the timescale to neutron capture depends on the availability of free neutrons), then ^{56}Fe can

also undergo β^--decay, turning one of its neutrons into a proton, an electron, and antineutrino, thus becoming ^{56}Co.

This process can continue up the chart of nuclides (Figure 1.1) until reaching ^{208}Bi. At this point, another branch in the path opens up as we move to higher mass nuclei - alpha decay. Unlike our neutron captures and β decays, α-decays cause the nucleus to lose two protons and two neutrons. Nuclei can no longer proceed up the chart of nuclides via the s-process at this point, any attempt to do so will be reversed by an eventual α-decay.

So it seems the main goal of nuclear astrophysics has been solved. Light elements are produced by fission in stars like our Sun, and the elements heavier than iron are produced in massive and asymptotic giant branch (AGB) stars through a series of neutron captures and β-decays known as the s-process. However, there are still a few troubling pieces of data that suggest we do not have the full picture. First, we have found on Earth naturally occurring, primordial elements heavier than Bismuth. For example, Thorium (Z=90) and Uranium (Z=92) can be found on Earth naturally. How did these come to be if we cannot synthesize them in the stars?

There are also other, stable elements that cannot be reached through the s-process pathway. If these isotopes with mysterious origins appear on the neutron-rich side of the valley of stability, we call them 'r-process' nuclei, which stands for 'rapid neutron capture'. If they instead appear on the proton-rich side, we call them 'p-process' nuclei, which stands for 'proton capture process'. As we can see in Figure 1.3, there are some nuclei that can only be created by a single astrophysical process, either because the s-process is incapable of reaching that far away from stability (^{136}Xe), or there exist stable nuclei that block the r- or p-processes from contributing to its abundance — ^{136}Ba is only produced by the s-process because the r-process contribution goes to ^{136}Xe instead.

Physicists determine the contributions of each of these processes by comparing the solar system abundances in meteoric data to what we predict the s-process can synthesize. The s-process contributions are 'readily estimated, because in this regime the abundances of individual isotopes are inversely proportional to their n-capture cross sections [3].' This means that because the s-process path is more well known, and the nuclei involved are much easier to obtain and measure in labs

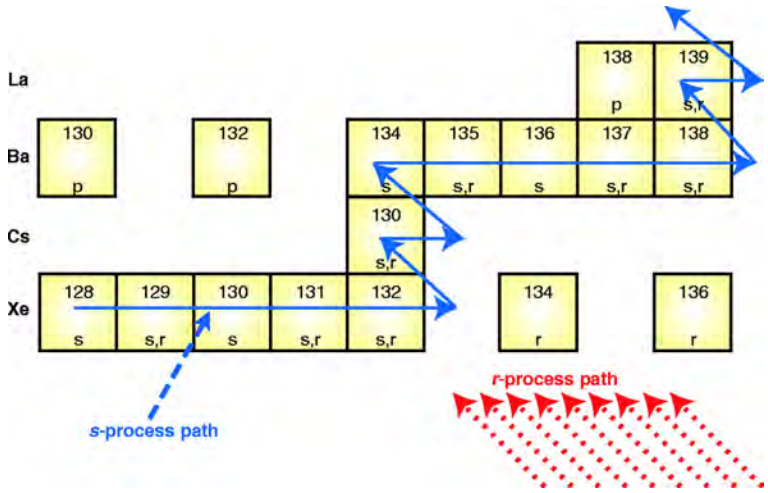

Figure 1.3 A small portion of the chart of nuclides that illustrates which process created which isotopes. Each stable element in yellow is labeled with the processes that contribute to its abundance [3].

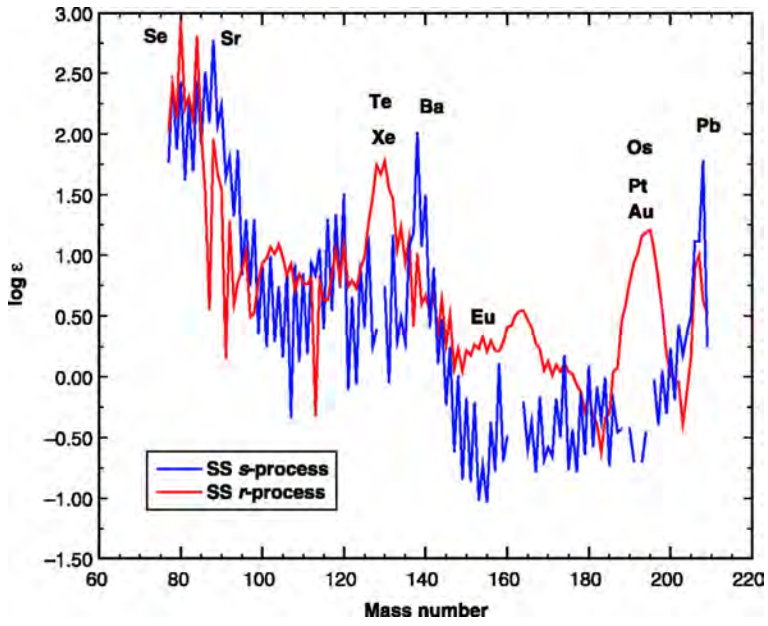

Figure 1.4 'The breakdown of solar system (meteoritic) n-capture isotopic abundances into r- and s-process components [3].'

on Earth, we first fit the s-process to solar system abundances, then include a component from the r-process that explains the abundances of isotopes under-produced by the s-process — an example of this would be Europium or Platinum in Figure 1.4.

The sites (and sightings!) of these processes is of great interest to nuclear astrophysics, and

so we turn to observational astronomy for answers. Since ordinary stars cannot alone produce all of the elements in their proper abundances, other objects and events must be the source. The r-process is must occur in sites with a high density of neutrons. Stellar events such as neutron star-neutron star mergers and types Ib/Ic and II[2] core collapse supernovae are the leading candidates for the astrophysical sites of the r-process.In particular, supernova 1987A and GW170817 are two observations that provided important evidence of this. P-nuclei are thought to be made in core-collapse supernovae, where heavy seed nuclei are broken apart by photons produced in the collapse. This photodisintegration of the seed nuclei allows for a production of the stable p-nuclei which the r-process cannot reach.

One of the most frequently observed thermonuclear events in nature are type I X-ray bursts [4]. These events occur in a binary system where a neutron star accretes (by which we mean 'obtains more') mass from its companion over time, and as that mass creates a thin layer of hydrogen and helium on the surface of the star, eventually the some of the material becomes electron-degenerate. The pressure of electron degenerate matter no longer depends on temperature, but mostly density. So the temperature on the surface of the neutron star increases, and it does not expand to cool it, creating a flash of nuclear burning that ends when the fuel is used up, or when the temperature reaches a point where its pressure is comparable to the degeneracy pressure. Expansion and cooling lifts the electron-degeneracy, shutting down the runaway. These reactions are fueled by alpha particles and protons, and thus the chain, along with beta decays, proceeds up the proton rich side of the chart of nuclides. Reaction rate information involving many proton rich nuclei is necessary to compare models with the observable light curves of type I X-ray bursts, see Figure 1.5. Notice that uncertainties in a single reaction rate could have large effects on the resulting light curve. This is important because an accurate understanding of the inputs to the light curve would provide us with the knowledge required to convert those observations to isotopic production in these events. LIBRA is positioned to measure nuclear information that will provide insight into understanding the light curves and composition of the ashes of type I X-ray bursts.

[2]Type II supernovae spectra contain hydrogen lines, while Type I do not. Type Ib/Ic supernovae spectra do not contain silicon lines.

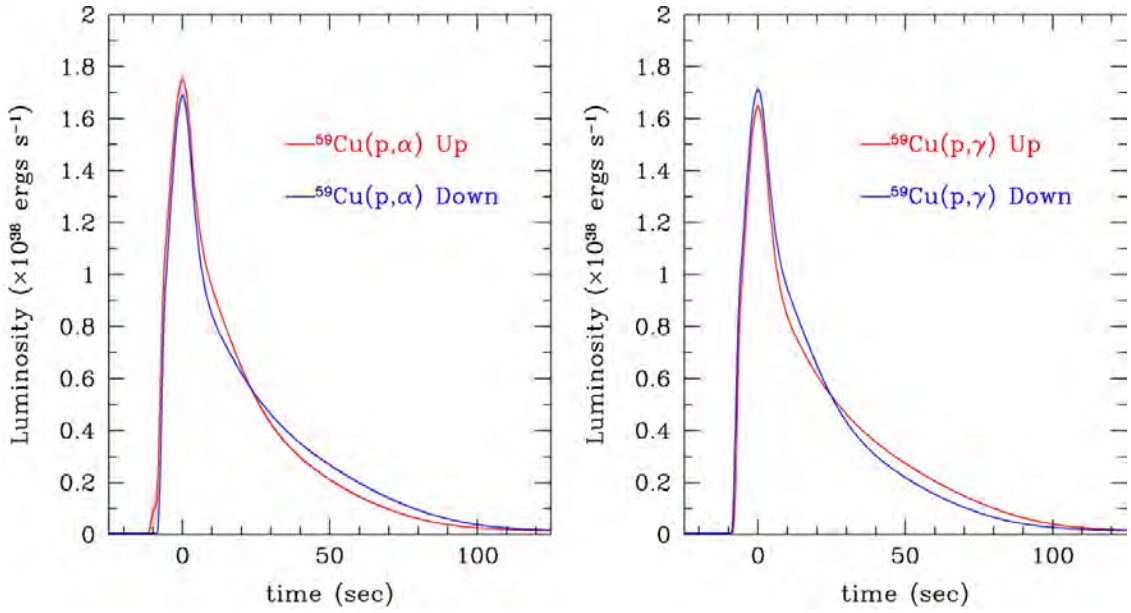

Figure 1.5 X-ray burst light curves found by varying reaction rates of proton capture on ^{59}Cu in a multi-zone model simulation of a type I X-ray burst. Figure taken from Cyburt, et al. [4].

Although not entirely complete, this propaedeutic should give an adequate idea of the complexity of understanding the processes by which nucleosynthesis occurs. Not only is a vast amount of nuclear data necessary to determine the paths of these processes and ultimately their contribution to the overall composition of the universe, but calculations of these reaction networks are required to simulate how these reaction rates affect overall abundances. Not only this, but physicists also have to hypothesize about and model the stellar environments these processes can take place in, and verify with observational astronomy that these environments exist and do indeed produce the isotopes we predict from our data collected here on Earth. The LIBRA setup was built with the ultimate goal of measuring resonant nuclear reaction lifetimes and branching ratios, which would allow one to constrain the reaction rates of important nuclear reactions that occur astrophysically, but would be difficult to measure directly, even in the most state-of-the-art laboratories today.

1.2.1 Reaction Rates

Typically, a reaction rate measurement would be set up in the following way. There exists some reaction one wishes to probe that occurs in stellar environments, take as a simple example proton capture on ^{16}O. In this case, one would place a chamber filled with oxygen (target) at the end of a

beam line, shoot protons at it, and measure how many protons are captured by the ^{16}O, and how many are scattered or pass through. Based on the total probability that ^{16}O is able to capture the proton (known as the reaction cross section), one can determine the reaction rate in the following way. The experimental cross section is given by this equation:

$$\sigma = \frac{\text{(number of interactions)}}{\text{(number of incident particles)(number of target nuclei)}} \tag{1.3}$$

With a good understanding of the target composition and the beam, and a reasonably efficient detection setup, the cross section can be measured in the lab. To relate this to the thermonuclear reaction rate, the following equation is used:

$$N_A \langle \sigma \nu \rangle_{01} = \frac{3.7318 * 10^{10}}{T_9^{3/2}} \sqrt{\frac{M_0 + M_1}{M_0 M_1}} \int_0^\infty E\sigma(E) e^{-11.605 * E/T_9} \, dE \tag{1.4}$$

where N_A is the Avogadro constant, $\langle \sigma \nu \rangle_{01}$ is the reaction rate per particle pair, T_9 is the temperature of the environment in gigakelvin, M_0 and M_1 are the masses of the particles, E is the energy in MeV, and $\sigma(E)$ is the cross section of the reaction [1]. Notice that our cross section is dependent on the incident energy of the particles, as seen in Figure 1.6. To understand how this energy dependence translates to a stellar environment, such as in a type I X-ray burst, we need to consider two factors.

First, what energies of particles are available to undergo these reactions? To determine this to first order, we consider this environment to contain ideal gases, which means we can use the Maxwell-Boltzmann distribution to estimate the distribution of energies of the particles. And indeed, we can see included in Equation 1.4 (and any other form of equation modelling stellar reaction rates), a term in the integrand that reflects this $e^{-E/kT}$ dependence. What this means is that the majority of our particles in an XRB will be at lower energies, with a higher energy tail.

Secondly, we must consider directly the effect of the energy dependence of the cross section on the reaction rate. We have already stated that the distribution of energies of charged particles follows a Maxwell-Boltzmann distribution. Even at the extreme temperatures of an XRB, the vast majority of charged particles will not have enough energy to crest the Coulomb barrier, and thus will be required to quantum tunnel through the barrier for a reaction to occur. Begin with the result

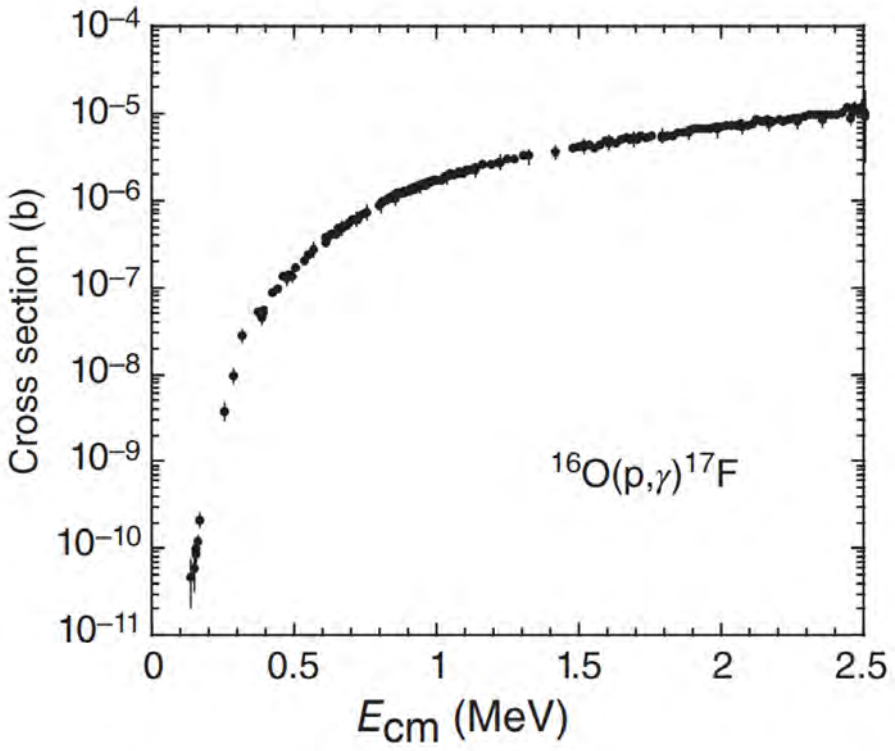

Figure 1.6 Experimental cross section of the $^{16}\mathrm{O}(p,\gamma)^{17}\mathrm{F}$ reaction. Note the logarithmic scale. Taken from Iliadis [1].

for the transmission coefficient of the s-wave scattering of a neutral particle through a square well:

$$\hat{T} \approx \exp\left(-\frac{2}{\hbar}\sqrt{2m(V_1 - E)}(R_1 - R_0)\right) \tag{1.5}$$

where $R_1 - R_0$ and V_1 define the width and height of your square barrier, respectively. The transmission coefficient can be thought of as the probability of a particle to pass through a potential barrier. Using this result, we can construct the transmission coefficient we expect for a Coulomb potential by summing thin slices of square barrier potentials, reminiscent of a Riemann sum in calculus. Taking the resulting product of the transmission coefficients, plugging in the Coulomb potential, expanding for low energy (with respect to the Coulomb barrier height) and taking the first, dominating term gives:

$$\hat{T} \approx \exp\left(-\frac{2\pi}{\hbar}\sqrt{\frac{m}{2E}}Z_0 Z_1 e^2\right) \equiv e^{-2\pi\eta}. \tag{1.6}$$

This is called the **Gamow Factor**, and explains the rough energy dependence of the non-resonant cross sections relevant to thermonuclear environments: $\sigma(E) \propto e^{-2\pi\eta} \propto e^{\sqrt{E}}$, as shown with

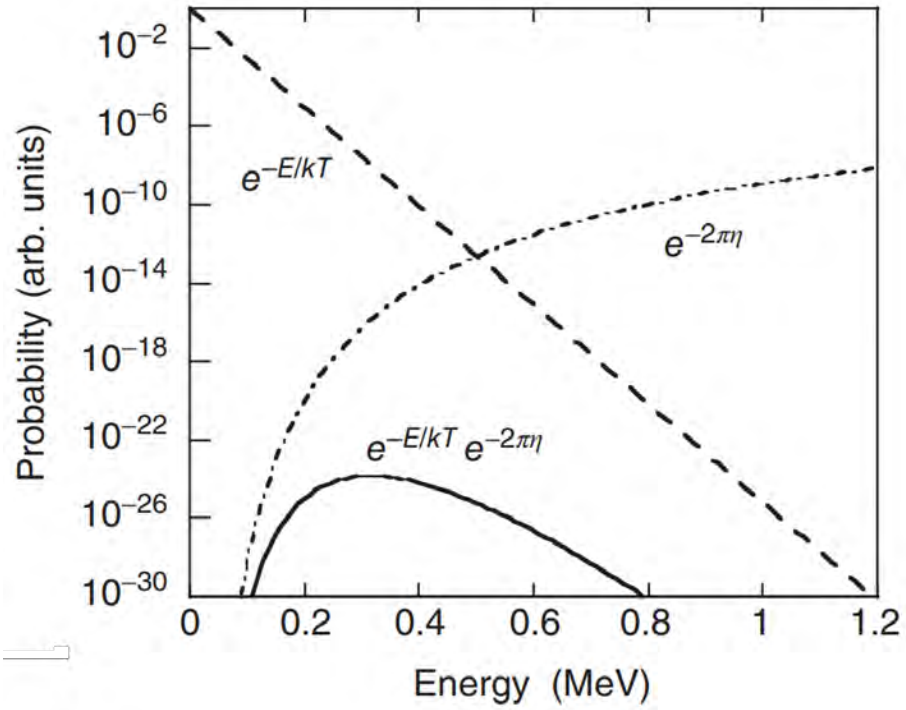

Figure 1.7 Multiplying the Maxwell-Boltzmann distribution (dashed line) with the Gamow factor (dashed-dotted) gives the Gamow Peak (solid line), for an example reaction at a temperature of 0.2 GK. Taken from Iliadis, page 167 [1].

experimental data in Figure 1.6. Consider the Gamow factor as a correction to take into account Coulomb barrier which, when multiplied by an S-factor, gives you back the total cross section.

The result of multiplying these two factors together gives an idea of the relevant energies over which a reaction in a stellar environment is likely to occur. Notice in Figure 1.7, that the vast majority of particles are at a lower energy than those at the Gamow peak, but those at higher energy are much more likely to penetrate the Coulomb barrier.

1.2.2 Narrow Resonances

It is not uncommon that reaction rates in stellar environments are dominated by single, isolated resonances with narrow energy widths. Consider an incoming and outgoing wave function at the boundary of a square potential well. This will represent some neutral particle interacting with the nuclear potential of another particle. The wave functions will have the form:

$$\psi_i = A \sin Kr, \psi_o = C \sin kr + \delta_0 \tag{1.7}$$

where k and K describe the depth and width of the nuclear potential. Imposing continuity conditions on the wave functions as they interact with the potential well, we can solve for the following quantity:

$$\frac{|A|^2}{|C|^2} = \frac{k^2}{k^2 + [K^2 - k^2]\cos^2(KR_0)}. \tag{1.8}$$

The quantities A and C are related to the amplitude of the incoming particle inside and outside of the potential well, respectively. From this result, we can see, from the cosine in the denominator of Equation 1.8 an oscillatory behavior of the likelihood of the particle to be located within the nucleus. This emergent phenomenon is called resonance, and can play a large role in the otherwise nicely behaved cross sections of thermonuclear reactions. The resonance reaction rate has a well-known equation that looks slightly different from the non-resonant rate, and is shown below as:

$$N_A \langle \sigma v \rangle_r = 1.5394 \times 10^1 1 (\mu T_9)^{-3/2} \times \omega\gamma \times \exp \frac{11.605 E_r}{T_9} (\mathrm{cm^3 s^{-1} mol^{-1}}) \tag{1.9}$$

where μ is the reduced mass number ($\frac{M_0 M_1}{M_0 + M_1}$) of the two reactants in amu, T_9 is the temperature at which the reaction takes place in gigakelvin, $\omega\gamma$ is the resonance strength (proportional to the area under the resonance cross section) in units of MeV, and E_r is the resonance energy (center of mass frame) also in MeV. If there are multiple resonances that affect a single reaction rate, and for each resonance the strength and energy are known, you can use the same equation above and sum the rates together to get the total reaction rate. The energy is straightforward enough to measure: it can be found experimentally by measuring the cross section of a particular reaction, say (p, γ), where for a broad range of energies the number of γ-rays detected is related to the cross section, and the energy where the peak occurs can be directly related to resonance energy, assuming appropriate knowledge of the nuclear masses involved in the reaction. The resonance energy can also be obtained by measuring excitation energies and masses, or from proton-emission energy if applicable to the reaction of interest. The resonance strength can be determined if the quantities in the following equation are measured:

$$\omega\gamma = \frac{2J_r + 1}{(2J_p + 1)(2J_T + 1)} \frac{\Gamma_p \Gamma_\gamma}{\Gamma_{\mathrm{tot}}} \tag{1.10}$$

where J_r is the spin of the resonance level, J_p is the spin of the incoming particle, J_T is the spin of the ground state of the target nucleus, and each of the Γ's represent the widths of each channel, with

Γ_{tot} being the sum of all open decay channels. In the case of our $^{16}\text{O}(p,\gamma)^{17}\text{F}$ example, $J_p = 1/2$, $J_T = 0$.

An alternative but equivalent way to write out the equation for the resonance strength is:

$$\omega\gamma = \frac{2J_r + 1}{(2J_p + 1)(2J_T + 1)} B_p B_\gamma \frac{\hbar}{\tau} \tag{1.11}$$

where we have changed out the widths for branching ratios: $B_x = \Gamma_x/\Gamma_{\text{tot}}$, and included the lifetime, τ. This means that the important quantities to measure experimentally are the resonance energies, the spins of the states involved, the branching ratios, and the lifetimes of the resonances. Especially at lower energies the cross section becomes exceedingly small (Figure 1.6), so low statistics and high background to signal ratios has driven the nuclear physics field to build facilities providing very high intensity beams, and underground labs to keep measuring these reaction cross sections. In the cases where your target or projectile (or both!) are unstable, direct measurements of the reaction cross section can be impossible with the technology currently available. Indirect approaches are therefore used, but these often have to piece together the branching ratios and lifetimes from multiple independent measurements using different methods. The LIBRA set up is able to measure both the average branching ratio and lifetimes of decays **and** the decay lifetimes and branching ratios of individual resonances populated by EC/β^+ decay. This can be useful to measure those rates whose cross sections cannot be measured by any other direct method employed today.

1.2.3 Hauser-Feshbach

In cases of nuclear reactions in stellar environments that have many, unresolved resonances, theorists employ the Hauser-Feshbach model. In these reactions, the compound nucleus that is formed can have excitation energies high enough that many broad resonances live very close together, and thus are difficult to account for in the method described in the previous section. Instead, a statistical approach is taken to model the cross section of these types of reactions.

The equation used in the Hauser-Feshbach model is derived entirely from the principles of reciprocity, momentum and parity conservation, and requiring probabilities must always sum to one. Reciprocity is the conceptually simple idea that treats the entrance and exit channels of a

reaction as equal with respect to time reversal symmetry. In essence, the reaction occurs with some given total momentum, and proceeds through specific initial and final states. If the final states and initial states were swapped in our equations for calculating the reaction cross section, the new cross section would be proportional to the energy of the new final states. As long as we know the total energy involved in the reaction, we can connect the forward (Aa) and reverse (Bb) cross sections via the following equation:

$$\sigma_{Bb\to Aa} = \frac{(2j_A+1)(2j_a+1)}{(2j_B+1)(2j_b+1)}\frac{k_{Aa}^2(1+\delta_{Bb})}{k_{Bb}^2(1+\delta_{Aa})}\sigma_{Aa\to Bb}, \tag{1.12}$$

where the j's are the spins of the states, k is the wave number (proportional to the total momentum) of the entrance and exit channels, and σ is the cross section of the reaction.

The steps required to derive the Hauser-Feshbach formula are given in Iliadis, Section 2.7 [1]. The result is that the averaged cross section of a reaction can be given as:

$$\langle\sigma_{\rm re}(\alpha,\alpha')\rangle = \frac{\pi\hbar^2}{2\mu E_\alpha}\sum_{J\pi}\frac{2J+1}{(2J_1+1)(2J_2+1)}\frac{\left[\sum_{s\ell}\hat{T}_\ell(\alpha)\right]\left[\sum_{s'\ell'}\hat{T}'_\ell(\alpha')\right]}{\sum_{\alpha''}\sum_{s''\ell''}\hat{T}_{\ell''}(\alpha'')}, \tag{1.13}$$

where μ is the reduced mass, E_α is the energy available in the entrance channel (initial energy), J and π are the spins and parities of the resonances in the compound nucleus, J_1 and J_2 are the spins of the projectile and target involved in the forward reaction, and the $\hat{T}$'s are the transmission coefficients for the projectile and target. The sum over double primed variables in the denominator represents the sum over the transmission coefficients in the outgoing channels of the resonance. The transmission coefficients for particle channels are calculated numerically using an optical model potential, while the $\gamma-$ray transmission coefficient is found from the $\gamma-$ray strength function. In Section 2.2.1, we will discuss the impact of this on our estimation of stellar reaction rates, and describe the method by which LIBRA will work to reduce these uncertainties hindering our capability to make these predictions.

1.2.4 NiCu Cycle in X-ray Bursts

As mentioned earlier in Chapter 1, Type I XRBs are the most frequent thermonuclear stellar explosions in the Galaxy, occurring on neutron stars in low-mass X-ray binaries. These explosions involve nuclear reactions and β^+ decays along the rapid proton (rp) capture process path near the

proton drip line. Modeling this process in order to better understand how elements are produced requires not only direct observations, but also nuclear data inputs, such as: β decay rates, nuclear masses, and reaction rates of proton-rich isotopes.

One feature of the rp-process path that affects the production of heavy elements and changes the observed light curve of XRBs is the existence of waiting points, or cycles, shown for NiCu and ZnGa in Figure 1.8. Our cycle of focus for an initial experiment with LIBRA is the NiCu (Nickel-Copper) cycle. This waiting point at ^{56}Ni may or may not prevent an XRB environment from producing heavier elements depending on the reaction rates of ^{59}Cu(p,α)^{56}Ni and ^{59}Cu(p,γ)^{60}Zn. If the (p,α) rate is much higher than the (p,γ) rate, then the flow primarily returns to that ^{56}Ni waiting point. However, if reverse is true, and the (p,γ) rate dominates, then the flow continues to heavier regions of the chart. The balance of these two reaction rates also impacts the νp process in core-collapse supernovae.

Direct measurement of these two reaction rates is difficult, especially at the relevant energies for the astrophysical environments, because of very low cross sections and difficulties producing an intense beam of these radioactive isotopes. We propose using a ^{60}Ga beam, which EC decays to ^{60}Zn, populating states in the Gamow window for both reactions. In Figure 1.9, the known information on the nuclei involved are compiled.

Currently, both rates of the reactions in the Ni-Cu cycle recommended by REACLIB are calculated with the Hauser-Feshbach statistical model [6]. Previous work aimed at measuring these reactions include a study done with a ^{59}Cu beam on a cryogenic ^{2}H target, which found that ^{59}Cu(p,α) proceeds mostly to the ground state of ^{56}Ni, and statistical model calculations overestimate the cross section by a factor of $1.6-4$ [7]. Additionally, a ^{58}Ni(^{3}He,n)^{60}Zn reaction measurement found that the nuclear level density in ^{60}Zn could be too low to accurately apply the Hauser-Feshbach statistical model [8]. Kim et al. [9] evaluated available experimental results on ^{60}Zn resonances in 2022, and found a lower ^{59}Cu(p,α)^{56}Ni reaction rate than the recommended REACLIB rate at XRB temperatures.

There are many recent and ongoing efforts to measure these reactions with both direct and indi-

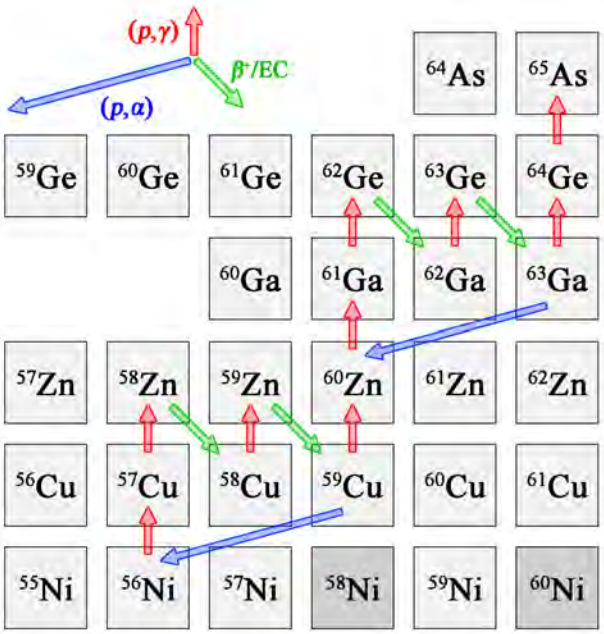

Figure 1.8 rp-process path in the Ni-Cu and Zn-Ga cycle region on the proton rich side of the chart of nuclides. Dark gray boxes are stable isotopes. Taken from Sun et al. [5].

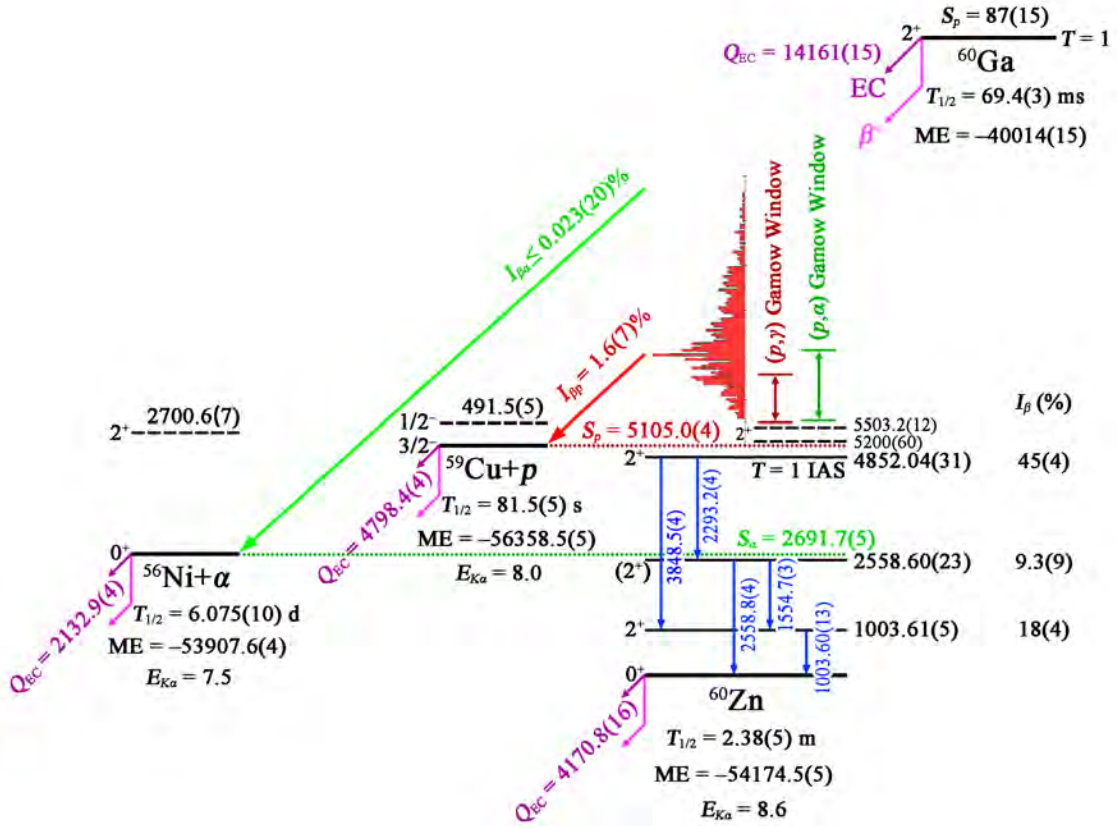

Figure 1.9 Evaluated decay scheme of ^{60}Ga. Information on sources for evaluated data can be found in Figure 2 of Sun et al. [5].

rect approaches [10–18]. Current gaps in our knowledge of the ^{59}Cu(p,α)^{56}Ni and ^{59}Cu(p,γ)^{60}Zn reactions limit our ability to determine their influence on XRB light curves.

The Gamow windows for these two reactions range from $\sim 0.5 - 1.5$ MeV for XRB temperatures. Due to the large Q-value of electron capture of ^{60}Ga, $Q_{EC}(^{60}\text{Ga}) = 14.161(15)$ MeV [19–21], and the proton and alpha separation energies of ^{60}Zn, $S_p(^{60}\text{Zn}) = 5.1050(4)$ MeV [22] and $S_\alpha(^{60}\text{Zn}) = 2.6917(60$ meV [22], the ^{60}Zn resonances of interest astrophysically are accessible via decay of ^{60}Ga. The first ^{60}Ga decay study by Mazzocchi et al. found a total ^{60}Gaβp intensity of $I_p = 1.6(7)\%$ and an upper limit of $\beta\alpha$ intensity of $I_\alpha \leq 0.023(20)\%$, as well as 5 ^{60}Ga($\beta\gamma$) transitions through 3 ^{60}Zn states [23]. A more recent study by Orrigo et al. confirmed the known $\beta\gamma$ transitions, and discovered 24 previously unknown $\beta\gamma$ transitions correlated with ^{60}Ga implants [19]. However, the β-feeding intensities are not known, and individual proton peaks were not resolved in either work. Using the information of the $\beta\gamma$ intensities in both studies, unplaced $\beta\gamma$ transitions constitute $> 20\%$ of β-feeding intensities [5]. Further measurements of β-feeding at high-lying states of ^{60}Zn are needed, as indicated by a recent total absorption spectroscopy experiment which observed β-feeding above the ^{60}Zn proton separation energy. A LIBRA experiment at FRIB would allow for high-statistics data of ^{60}Ga decay, measuring the charged particles and γ-rays. This would allow us to gather information of states involved in the ^{59}Cu(p,α)^{56}Ni and ^{59}Cu(p,γ)^{60}Zn reactions at thermonuclear energies, as well as collect lifetimes of the excited states of ^{60}Zn, providing all ingredients to constrain the reaction rates. More information on the details of this planned experiment can be found in Chapter 2.6.

1.3 Nuclear Structure Background for GADGET II

Nuclear structure is another pillar of nuclear physics whose ultimate goal is to develop a model that accurately and completely describes the properties and behaviors of nuclei, regardless of their position on the chart of nuclides. In practice, this means that physicists collect nuclear data via experiments on all types of isotopes, and then try to explain the findings with models that have predictive and interpretive power.

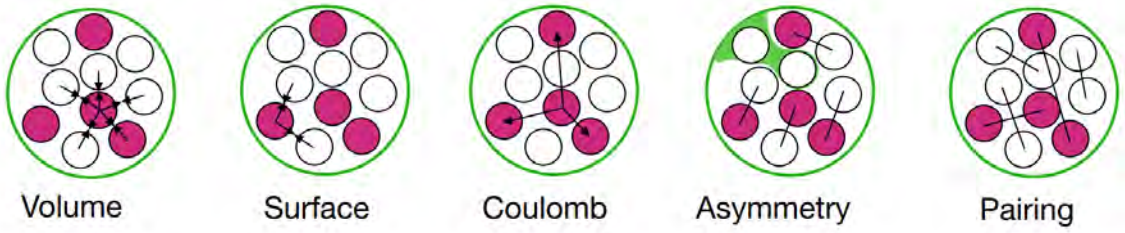

Figure 1.10 Visualization of the five terms of the liquid-drop model described in Equation 1.14. Figure from Obertelli [24].

1.3.1 Liquid-Drop Model

One of the earliest models that demonstrates this idea is the 'Liquid-Drop Model' (LDM). If we consider Figure 1.2, we notice that for medium to heavy mass nuclei, the binding energy per nucleon is saturated, meaning unlike gravity, nucleons do not attract all others within the nucleus, if they did, the trend of the binding energy would increase like A^2, as it does in gravity: $F = G\frac{m_1 m_2}{r^2}$. Since it clearly does not, this can be explained by recalling that the strong force is a very short range force, so once a given nucleon is fully surrounded, additional nucleons added will not contribute to the force on that given nucleus. The LDM theory models the binding energy of a given nucleon (Z, N, and A being the number of protons, neutrons, and total nucleons respectively) with different well-defined terms fit to the data in Figure 1.2 in the following way

$$B_{\mathrm{LDM}} = a_V A - a_S A^{2/3} - a_C \frac{Z(Z-1)}{A^{1/3}} - a_A \frac{(N-Z)^2}{A} + \delta \tag{1.14}$$

where the coefficients a_x are chosen to most accurately fit the data. Each term in Equation 1.14 is meant to account for a different effect, illustrated in Figure 1.10. And these cumulative effects are illustrated in Figure 1.11. By combining all the terms, we recover the trend of the BE/A shown via experimental data in Figure 1.2.

The first term (a_V) gives a constant binding energy per nucleon, which serves as the base onto which all further corrections are made. If we leave our model just at this first term, we have included in it the fact that the strong force is short range and saturated — no matter how many nucleons we add, the force applied to any nucleon does not change.

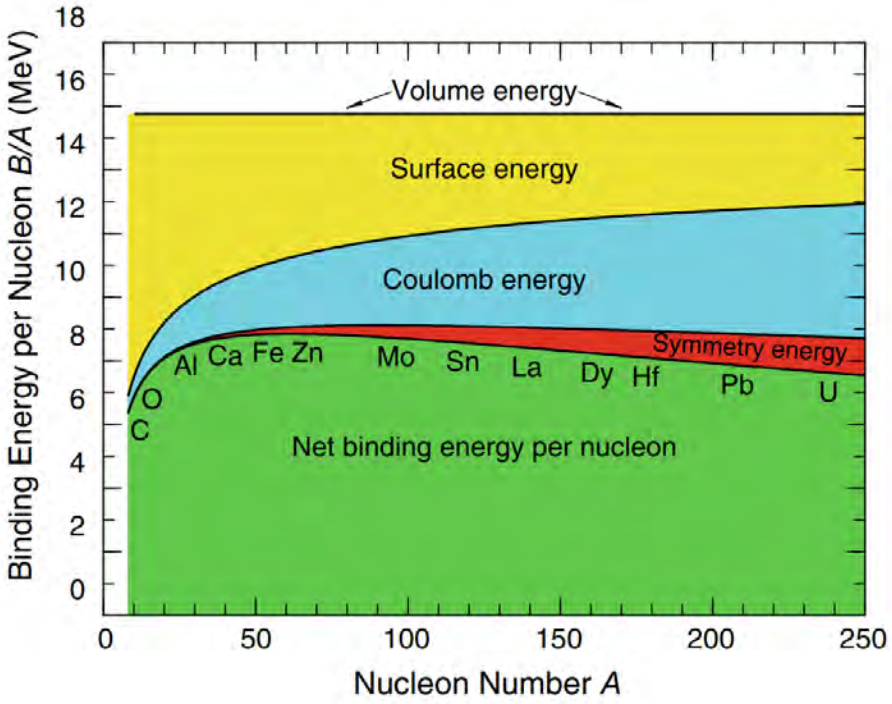

Figure 1.11 Binding energy per nucleon as calculated with the liquid-drop model, for stable nuclei. The contributions to the BE/A for each term is shown. The parameters used to calculate the corrections are: $a_V = 15.85$ MeV, $a_S = 18.34$ MeV, $a_C = 23.21$ MeV, $\delta = +12, 0, -12$ MeV for even-even, even-odd, and odd-odd nuclei, respectively. Figure from Obertelli [24].

The second term is the surface term, which corrects for the fact that nucleons on the surface of a nucleus are not fully saturated; they are not totally surrounded by other nucleons and thus do not feel the full possible magnitude of the nuclear force.

The third term is the Coulomb term, which corrects for the repulsion between protons at these close distances.

Notice that the volume term scales with A, or number of nucleons; doubling the number of nucleons doubles the total volume of the nucleus. The surface term is proportional to $A^{2/3}$, raising volume to one third gives length, and squaring that gives area. The Coulomb term takes the form of the Coulomb force among all proton pairs $\propto Z(Z-1)/A^{1/3}$ which, when the exact calculation is done to find the energy of this repulsion from a uniformly charged sphere, takes the form: $-\frac{3}{5}\left(e^2/4\pi\epsilon_0 R_0\right)\frac{Z(Z-1)}{A^{1/3}}$ [25].

The final two terms in the liquid-drop model compensate for quantum mechanical effects. The

Pauli Exclusion Principle states that no two Fermions (particles with spin $1/2$, so nucleons and electrons), can occupy the same state in a given system. This principle, which gave rise to the electron degeneracy pressure that supports some stars against gravitational collapse, is also the culprit causing these last two corrections. Protons and neutrons are distinguishable, and so sit in their own nuclear potential wells. When a system has many more of one type than the other (say the nucleus is very neutron-rich), that well fills up very high, to high energies, causing the total system to be less bound and therefore have a lower binding energy per nucleon. The last pairing term comes about from this same Pauli Exclusion Principle, but in a pair interaction way. Towards the lighter end of Figure 1.2, there is a zig-zag pattern between adjacent nuclei. This comes from the fact that these spin $1/2$ nucleons like to pair up, one spin up proton and one spin down proton cancel each other out, and increase the overall binding energy compared to a neighbor nucleus who has a lone, unpaired nucleon in its system. With all else equal, an even-even system is the most bound, and odd-even is less bound, and odd-odd systems — nuclei who have an unpaired proton and neutron — are the least bound.

The values assigned to the 'a_x' parameters are not calculated based on any strict theory, but fit to some data and extrapolated to the nuclei or region one is interested in.

This model is one of the first examples of a theory that attempts to explain these nuclear properties over the range of nuclear data available. As shown, it nicely describes the trend in binding energy, and it can also be useful in describing fission properties as well. However, it struggles to describe more in-depth quantum mechanical effects, such as the magic numbers described in Section 1.1.

1.3.2 Fission, Alpha, and Cluster Decay

The liquid-drop model is a beautiful example of a phenomenological theory that is classically intuitive and works well to describe many of the trends we see in nuclear data. In the context of this thesis, however, we need a theory that can accurately predict the properties of fission or alpha decay and extend it to double alpha decay. Similarly to our discussion of charged particle capture in XRBs, fission and alpha decay must tunnel through a potential barrier to explain these decay

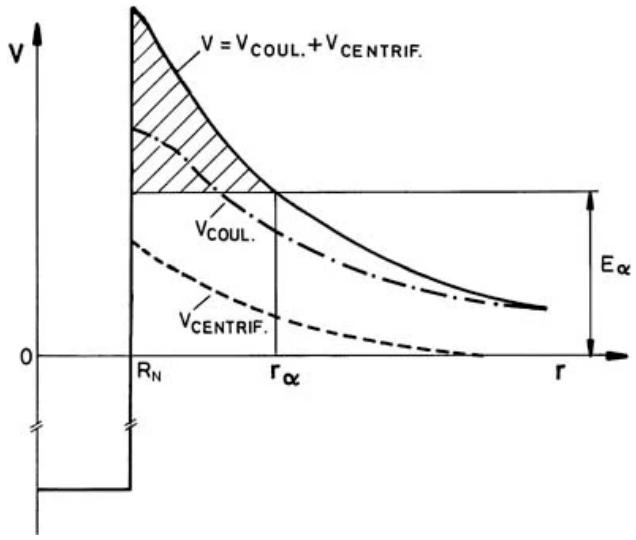

Figure 1.12 Potential barrier that a charged particle must overcome for decay to occur as a function of radius, r. The total potential is built from the nuclear, Coulomb, and centrifugal potentials. Figure taken from [26].

modes. The likelihood to tunnel through a potential barrier depends on the width and depth of the potential well created by the nuclear strong force and Coulomb potential, shown in Figure 1.12. The goal of theory in this case is to develop a description of the effective potential energy that the decay products feel and must tunnel through.

1.3.2.1 Density Functional Theory (DFT) and Energy Density Functionals (EDF)

To obtain the characteristics of the potential well our charged particles are stuck in, we turn to Density Functional Theory (DFT).

$$\hat{H} = \underbrace{\sum_{ij} t_{ij} a_i^\dagger a_j}_{\text{one-body term}} + \underbrace{\frac{1}{2!} \sum_{ijkl} \bar{v}_{ijkl} a_i^\dagger a_j^\dagger a_l a_k}_{\text{two-body term}} + \cdots \tag{1.15}$$

We can write out the general Hamiltonian for our nuclear system as a collection of increasingly higher order terms, where the first term describes the kinetic energy of the system, and the following terms describe the 2-, 3-, $\cdots$, A-body interactions.

Once we obtain a Hamiltonian which describes our system, we can use the variational principle to find the energy of the ground state:

$$E_\phi \equiv \frac{\langle \phi | \hat{H} | \phi \rangle}{\langle \phi | \phi \rangle} \geq E_{\text{gs}}. \tag{1.16}$$

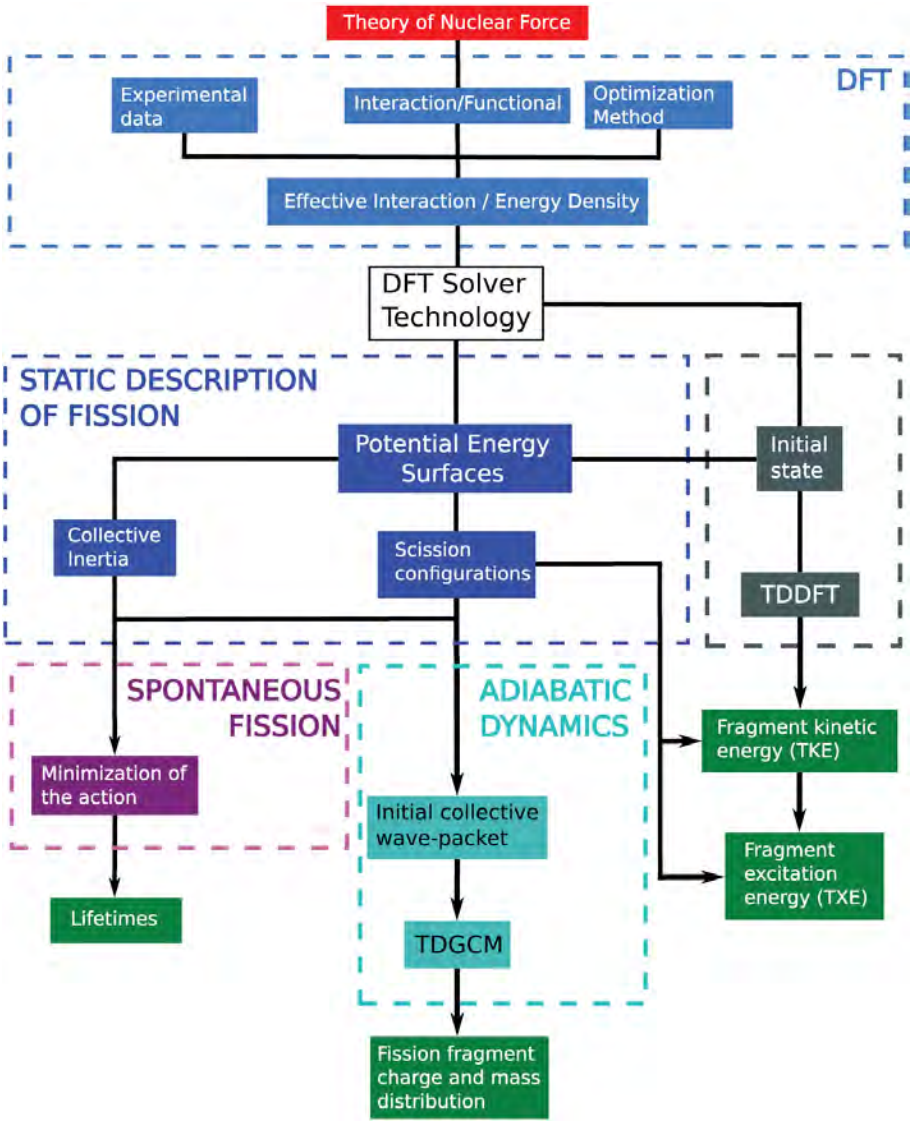

Figure 1.13 DFT Workflow for fission. A similar approach is taken for cluster decay calculations with Microscopic theories [30].

This is proven to work via the Hohenberg-Kohn theorems, which find that 'for every many-body interaction, there exists an EDF whose lowest energy configuration has the same energy as the ground state of the many-body Hamiltonian [27] [28, 29].' The type of EDF chosen for a given system can take many forms, whether it be the Skyrme interaction, Gogny interaction, relativistic mean-field, or universal nuclear energy density functional (UNEDF).

After choosing an interaction, the parameters of the functional are constrained by our knowledge of the nuclear forces and further adjusted to agree with experimental data. Schunck and Robledo

state, "allowing for spontaneous breaking of the symmetries of the nuclear force at the level of the quasiparticle vacuum is reminiscent of the historical picture of fission: if the one body density matrix is not rotationally invariant, its spatial distribution represents a deformed nuclear shape. Fission can then be viewed as a process during which the deformation becomes so large that two separate fragments appear. This viewpoint can be formalized by introducing a set of collective variables that represent the motion of the nucleus as a whole and control the fission process. The characteristics of the resulting potential energy surface (PES), i.e. the energy as a function of the chosen collective variables, determines fission properties [30]." Examples of the application of this approach to cluster decay will be shown in later chapters, see Figure 3.1. For a more comprehensive explanation of the process for calculating properties of fission, see either Schunck and Robledo [30], Daniel Lay's thesis [27], or reference [31] which gives an overview of the successes of DFT in describing nuclear phenomena at the microscopic level, such as: mass and charge radii, excited states and decay rates, collisions, and fission.

Cluster decays were first successfully described theoretically by Sandulescu et al. in 1980 [32], and shortly after, in 1984, Rose and Jones [33] found the first experimental evidence of this type of decay — ^{12} C cluster emitted from ^{223}Ra. Since then, cluster decay has been found in twelve even-even isotopes [34–53] and seven odd-even isotopes (see references in Refs. [54, 55]). How to handle this new decay mode then becomes a subject of debate. Since it exists between fission and alpha decay, which theories would be best suited to describe the properties of this new decay? Theorists from both camps work to apply their theories to accurately predict properties of this new decay. The theories used to model both cluster decay and double alpha decay are outlined in the following sections, where we see that the results of each approach vary wildly.

1.3.3 Analytical Super Asymmetric Fission Model

The Analytical Super Asymmetric Fission Model (ASAFM) was first derived in 1980 [56]. Its strength was its ability to calculate half-life in a short time. This theory was then used to run a systematic search for new decay modes, utilizing the model for a large number of parent and emitted ion combinations. ASAFM was extended to include angular momentum and small excitation energy

effects [56]. The results from this initial effort found that ^{8}Be, ^{12}C, and ^{16}O are the preferred candidates for new decay modes, whereas all nuclides of known masses (at the time) were stable relative to emission of ^{2,3}H, $^{3,6-9}$He, ^{4}Li, ^{7}B, and ^{9}C. This lead to Rose and Jones experimentally discovering the most favorable case of ^{14}C decay (via ^{223}Rn) in 1984 [33].

To obtain better agreement with experimental data on α-decay half lives, Poenaru et al. [57] introduced shell effects in the zero point vibration energy, E_{v}:

$$E_{\mathrm{v}} = Q\left[0.056 + 0.039\exp\left(\frac{4 - A_2}{2.5}\right)\right]; Q > 0, A_2 \geq 4, \tag{1.17}$$

where A_2 is the mass number of the lighter fragment. This equation is then used to estimate the half lives for new decay modes by emission of more than one heavy ion simultaneously. Poenaru goes on to state that for double alpha decay, 'competition with ^{8}Be and even ^{12}C is to be envisioned. The best chance of seeing these processes seems to be from the decay of excited levels such as in beta-delayed heavy-ion emission [57].' The GADGET Collaboration has an accepted proposal to measure beta-delayed fission decay at FRIB, which will serve as a proof of concept for these kinds of experiments in the future.

1.3.4 Extension to the Liquid-Drop Model

In Section 1.3.1, we use the liquid-drop Model to calculate binding energies by assuming nuclei are held together by some short range, strong interaction, and corrections are made to adjust for geometry and other properties of the nucleus. Royer and Remaud [58, 59] used this same principle to extend the concept of the liquid-drop model to calculate nuclear deformation energies, with the goal of estimating properties of fission. Briefly, fission can be thought of as a competition between the Coulomb force and the attractive surface tension of the strong nuclear force that shows up in the liquid-drop model. At the surface of the nucleus, nucleons do not feel the full attraction of the strong force, and thus, if conditions are right, can be ejected as a cluster of nuclei. As this process occurs, the nucleus becomes more and more deformed until it breaks apart in either a fission decay (by which I mean a decay of a nucleus in roughly equal parts) or a cluster decay[3], where the ejected

[3]Cluster decays are the focus of study in this work, but the theoretical physics remain similar in both cases.

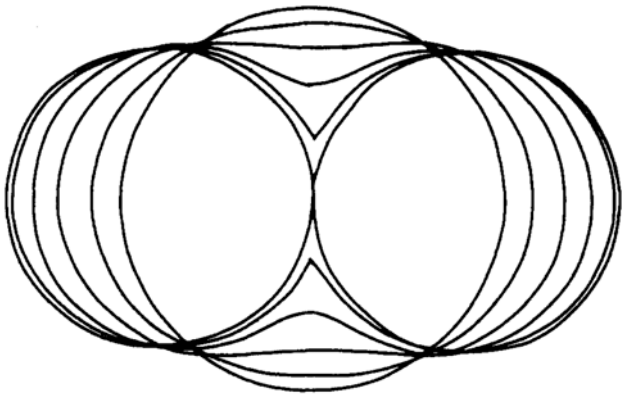

Figure 1.14 Taken from Royer and Remaud [58], this shows the evelution of a deformed nucleus parameterized by the equation $R(\theta) = a^2 \sin^2\theta + c^2 \cos^2\theta$, as a/c goes from 0 (one sphere) to 1 (two spherical fragments). They call it an elliptic lemniscatoid shape.

particle is larger than an alpha particle, but smaller than the products of fission. How one determines the conditions under which a fission decay occurs can be derived from minimising the sum of the Coulomb (repulsive) and surface (attractive) forces at the end of a deformed nuclei as it proceeds from some initial surface shape [60]. The competition between the Coulomb force and weakening nuclear force at the surface of a nucleus is the basic property that drives this model to explain decay properties. The only changes to the terms used to calculate decay properties are due to the unique conditions of the nucleus, namely the deformation throughout the process of nuclear decay.

In Royer and Remaud's 1984 paper, they use a combination of rotational liquid-drop model (RLDM) and a nuclear proximity term, which attempts to 'takes into account the finite-range effects of the nucleon-nucleon force inside the crevice separating the fragments' (i.e. the sharp points in Figure 1.14). The calculated energy then is something like:

$$E(r) = E_S + E_C + E_{\text{rot}} + E_N(r). \tag{1.18}$$

We can clearly see the two base terms, surface and Coulomb (E_S and E_C), although in this case they are parameterized by shape dependent functions that adjust their strengths based on the nuclear deformation. They also absorb the asymmetry correction into the surface term. Additionally, they include a few new terms to resolve discrepancies in the predicted and measured fission barrier,

namely the rotational energy term:

$$E_{\text{rot}} = \hbar^2 \ell(\ell+1)/2J_{\perp} \tag{1.19}$$

and the nuclear proximity energy:

$$E_N(r) = 2\gamma \int_a^{h_m} \varphi(D(r)/b) 2\pi h \, \mathrm{d}h. \tag{1.20}$$

The parametrization is defined in the text of the paper [58], but the idea is that these terms better account for the total energy of a deformed nuclear system.

This is the basis for the underlying theory of the Modified Generalized Liquid-Drop Model (MGLDM). In this case, we play the same game as above for fission, but implemented for our decay of choice. Chandran and Santhosh [61] go through this in detail in their paper, and the total energy is calculated in the same way as above, using parameters from Royer and Remaud. They also separate their energy calculation into a pre- and post-scission region. Scission can be thought of as the 'point of no return' for a cluster decay. Prior to scission, we think of the system as an extremely deformed nucleus, and after scission, we consider the system to be more like two, separated fragments. Thinking of it this way, it may make sense to treat the before and after as distinct for the purposes of calculating decay properties.

With the energy of the system calculated using MGLDM, the next step is using it to calculate the barrier penetrability. The barrier penetrability is calculated using the WKB approximation, shown the following integral as [62],

$$P = \exp\left[-\frac{2}{\hbar}\int_{R_{\text{in}}}^{R_{\text{out}}} \sqrt{2B(r)[E(r) - E(\text{sphere})]}\, dr\right] \tag{1.21}$$

where $R_{\text{in}} = R_1 + R_2$, $B(r) = \mu$, and $R_{\text{out}} = \frac{e^2 Z_1 Z_2}{Q}$. R_1 and R_2 are the radii of the daughter nuclei and the emitted cluster, respectively, μ is the reduced mass, and Q is the released energy. This equation for barrier penetrability is rather intuitive. If the energy you calculate from the MGLDM is a lot different than the energy you would get from a regular, spherical nucleus, the barrier penetrability is larger. In other words, it is easier for a nucleus like that to fission or cluster decay. Finally, we

can calculate the partial half-life of a given decay mode via the following equation,

$$T_{1/2} = \left(\frac{\ln 2}{\lambda}\right) = \left(\frac{\ln 2}{\nu P_C P}\right), \tag{1.22}$$

where ν is the frequency of the cluster attempting to overcome the barrier and is taken as $10^{20} s^{-1}$ and P_C is the preformation factor.

The preformation factor was introduced to the generalized liquid-drop model to better predict the half-lives of cluster decays. Without this term, there were deviations of about three orders of magnitude from the experimentally measured half-lives. The basic idea of the preformation factor is to account for the formation of the cluster within the nucleus prior to the decay. In principle, this makes intuitive sense: if the nucleus is already in a configuration similar to the two products at the beginning of the decay process, it should have an easier time decaying via that channel. A common procedure when using this method is to create a preformation factor term that takes into account as much known information about the decay as possible, and fit the parameters to data.

Although Santhosh and Jose explore a wide range of variables that the preformation factor for double alpha decay can depend on, it is difficult to know if this model accurately takes into account all of the system's properties. The preformation factors used to generate these results can be described as follows:

1. $P_c(Q)$ is the preformation factor that depends on Q value (Q), and is defined phenomenologically as:

$$P_c(Q) = 10^{aQ+bQ^2+c}, \tag{1.23}$$

with a = -0.25736, b = 6.37291×10^{-4}, and c = 3.35106.

2. $P_c(A_c)$ is the preformation factor that depends on the size of the cluster (A_c), and is defined as:

$$P_c(A_c) = 10^{aA_c+b} \tag{1.24}$$

with $a = -0.51325$ and $b = 2.80787$.

3. $P_c(Z_cZ_d)$ is the preformation factor that depends on the proton numbers of the cluster (Z_c) and daughter nuclei (Z_d):

$$P_c(Z_cZ_d) = 10^{aZ_cZ_d+b}, \tag{1.25}$$

with $a = -0.01555$ and $b = 3.22940$.

4. $P_c(C)$ is a preformation factor that depends on all of the above effects:

$$P_c(C) = 10^{aA_c+bZ_cZ_d+cQ+dQ^2+e}, \tag{1.26}$$

with $a = -0.5559$, $b = 0.028716$, $c = -0.4233358$, $d = 0.001143$, and $e = 1.490754$.

5. $P_c(I)$ is the final preformation factor considered by Santhosh et. al., and depends on the isospin of the parent nuclei (I):

$$P_c(I) = 10^{a\sqrt{\mu Z_cZ_d}+bI+c}, \tag{1.27}$$

for odd-A parent nuclei, $a = -0.11539$, $b = 89.1166$, and $c = -14.1128$. For even-A parent nuclei, $a = -0.1085$, $b = 29.3158$, and $c = -1.25385$

In the above equation, μ is the reduced mass and can be found via the equation: $\mu = A_cA_d/(A_c+A_d)$. All of the constants written above are obtained by fitting to data with the least-squares method.

"It is worth noting that the factors on which preformation depends are crucial in determining [the 2α particle decay] half-life [62]." Herein lies the difficulty with readily extending this approach to predict the half-life of double alpha decay, or any decay which has not already been experimentally measured.

CHAPTER 2

LIBRA DESIGN AND TESTING

2.1 Rutherford's Measurement of the Half-life of ^{220}Rn

A typical and straight forward way to measure lifetimes is to measure the amount of radiation given off by a sample of the material over a long period of time. The time it takes the intensity of the radiation to reduce to half its initial value is the half-life of the nucleus. The first ever half-life measurement was conducted by Ernest Rutherford and published in 1900 [63]. Because this is a nice example of a half-life measurement for nuclei with moderate lifetimes, and is also connected to the work done for this thesis using GADGET, I will briefly describe Rutherford's experiment to measure the half-life of ^{220}Rn.

In the late 1800's, the field of nuclear physics had yet to take shape. The work on what would eventually be called radioactive nuclei had just begun, with Henri Becquerel's study of uranium salts' effect on photographic plates [64]. He found that these photographic plates were being exposed, even in the absence of light, while being stored in a drawer that also contained these salts. This unexpected phenomenon marked the birth of nuclear physics and opened the door to the study of radioactivity.

Shortly after this time, the first nuclear physicists were busy learning all they could about this emerging field. In 1900, Rutherford conducted an experiment as a professor at McGill University in Montreal, Canada. It was set up in the following way: First, Rutherford noticed that the activity of a thorium source varied in a way unlike other radioactive sources at the time — he found the cause to be slow air currents in the room at the time of measurement, "[w]hen the apparatus is placed in a closed vessel, to do away with air-currents, the intensity is found to be practically constant." [63] If radioactivity is an inherent property of a given nucleus, why would air currents be affecting its radiation intensity, especially when this same change is not observed in uranium?

Next, Rutherford continues by testing the penetrating power of thorium's radiation through paper. He spreads a layer of thorium between two parallel plates, and adds a potential difference to the plates. Any charged particles that can flow between the plates will create a measurable current,

Thick Layer of Thorium		Thin Layer of Thorium	
Layers of Paper	Rate of Discharge	Layers of Paper	Rate of Discharge
0	1	0	1
1	0.74	1	0.37
2	0.74	2	0.16
5	0.72	3	0.08
10	0.67		
20	0.55		

Table 2.1 The decrease in the rate of discharge between two parallel plates, with one plate covered in either a thin or thick layer of thorium. The rates were taken for successive layers of foolscap-paper placed on the thorium. The rate of discharge with uncovered thorium is taken to be unity [63].

which Rutherford calls the 'rate of discharge'. He then adds successive pieces of paper, covering the thorium, and measures the change in the rate of discharge.

He does this for both a thick[1] layer of thorium and a thin layer of thorium. The results can be seen in Table 2.1. Notice that with a thin layer of thorium, the rate of discharge falls off in 'geometric progression', which means that each layer of paper roughly halves the amount of observed radiation. In the case of the thick layer of thorium, this pattern does not hold. We begin to see a decrease in rate of discharge initially, but instead of tending to 0 with successive pieces of paper, it flattens to a constant rate. Rutherford states this can be explained by thorium giving off two different kinds of radiation. One is the same kind of radiation that uranium gives off, which explains the results from the thin layer experiment, and the other kind of radiation is 'given out from the mass of the active substance [of thorium]', and diffuses through the paper to be ionized by the plates and detected as an increased rate of discharge. He calls this radiation, 'emanation', and studies its properties to confirm his findings.

In the final part of this experiment, Rutherford measures the 'duration of the radio-activity of the emanation' emitted from thorium.

The experimental setup can be seen in Figure 2.1. The thorium source, 'A' in Figure 2.1, was encased in foolscap-paper (which was thick enough to stop the regular 'uranium-like' radiation), and placed in the long metal tube 'B' on the figure. On the other end of the apparatus, the detection

[1]Rutherford states: 'To produce a thin layer on a plate, the oxide, in the form of a fine powder, was sprinkled by means of a fine gauze, so as to cover the plate to a very small depth. By a thick layer is meant a layer of oxide over a millimetre in thickness' [63]

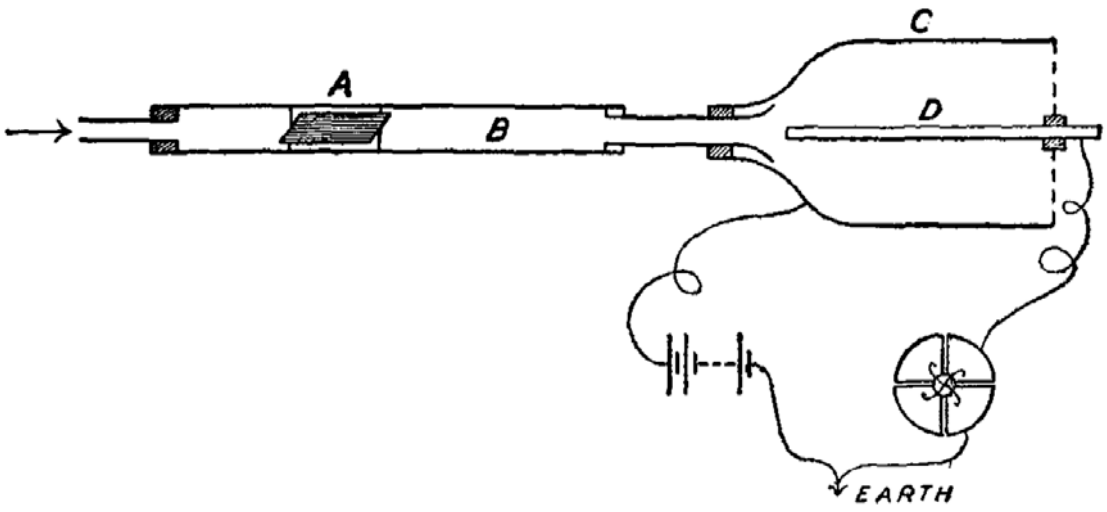

Figure 2.1 Drawing of Rutherford's experimental setup to measure this radioactive 'emanation', as he called it at the time. It later was found to be ^{220}Rn, which decays with a half-life of 55.6 seconds. Rutherford's result was 60 seconds [63].

of the 'emanation' takes place. The insulated cylinder 'C', is connected to a battery at 100 V, and the electrode 'D' is connected to ground. This detector acts just like the plates in the previous tests that discovered the 'emanation' in thorium, and allows measurement of the rate of discharge over time. On the left side of the figure, a bellows creates a wind that drifts the 'emanation' to the detection side of the apparatus[2]. Until this wind carried the radiation to the right, there was no rate of discharge, so it is assumed that the only radiation being measured is this new 'emanation' that we want to measure. After the bellows had been moving air for a few minutes, the rate of discharge reached a constant value. Once this steady-state was formed, the bellows were stopped and the rate of discharge was recorded for several minutes. The results of this half-life measurement of ^{220}Rn is shown in Figure 2.2

He found that the half-life of the ^{220}Rn 'emanation' was 60 seconds, remarkably close to the modern value of 55.6 seconds found in the National Nuclear Data Center database [65].

Rutherford is most famous for his supervision of the Geiger-Marsden gold foil experiment, which found that nuclei have a net positive charge and concentrate nearly all of an atom's mass. It is worth noting that the gold foil experiment was conducted over a decade after the first half-life

[2]This procedure will seem oddly familiar when reading Chapter 4.2.1

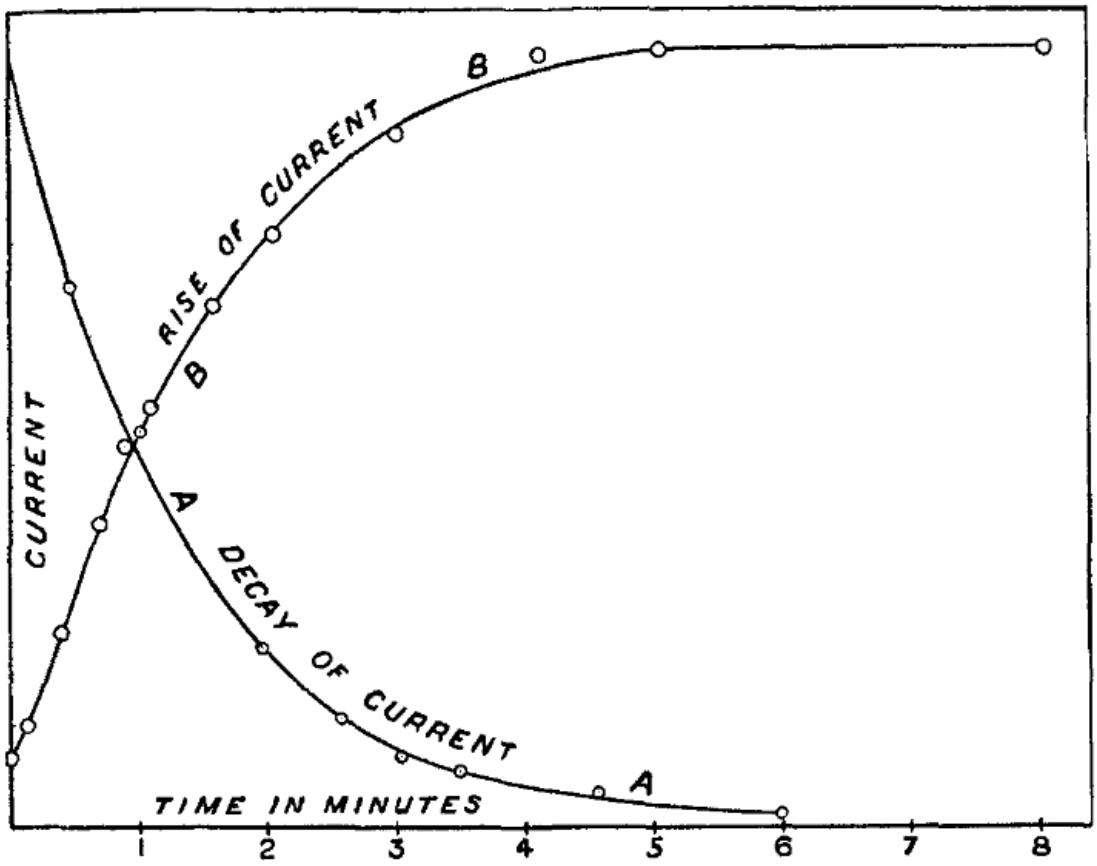

Figure 2.2 Results of the first ever half-life measurement by Rutherford. Curve B shows the increase in activity via bellows transporting ^{220}Rn to the measurement vessel. Curve A shows decay of activity of ^{220}Rn after the bellows had been stopped [63].

measurement was performed by Rutherford! Not only did Rutherford not know what the nucleus was, it would take him eight more years to discover that the alpha particles emitted by thorium and the like were helium nuclei [66]. One can only imagine the puzzle of interpreting one's experimental results during this era of nuclear physics. [3]

[3]It is worth noting here that helping to solve this puzzle was Rutherford's graduate students at McGill (his first being Harriet Brooks, followed by Robert K. McClung, A. G. Grier, then S. J. Allen). I especially want to highlight the work of Harriet Brooks from 1901-1905, who worked closely with Rutherford to help unravel the mystery of the Thorium decay chain [67–69]. Rutherford published the same work in *Nature* under his name alone, with the acknowledgment "In these experiments I have been assisted by Miss H. T. Brooks [70]." I also highly recommend the book on Harriet Brooks' life by Geoff and Marelene Rayner-Canham, which described Brooks' contribution to the early field of nuclear science. [71] She is one of the only people to have worked with Rutherford, Thomson, and the Curies all in her career.

2.2 The Theory of PXCT

The following section is based off of work abridged in 'Lifetimes and Branching Ratios Apparatus (LIBRA)' by Sun, et al. [5]. For much of the analysis of LIBRA data, and its construction, I am indebted to Lijie Sun.

The Particle X-ray Coincidence Technique (PXCT) was first developed to measure nuclear lifetimes for nuclei whose half-lives are too short to be measured in other ways. Unlike the technique used by Rutherford, which is only sensitive to a narrow range of lifetimes — else he would have been able to measure not only the half-life of ^{220}Rn but also the half-life of the naturally occurring precursor nucleus, ^{232}Th ($t_{1/2}$ = 1.4 * 10^{10} y, see Figure A.6) — many newer methods have been developed for increasingly more difficult to measure lifetimes. [4] For short-lived nuclei whose half-lives are in the range 10^{-15} – 10^{-18} seconds, there are only two methods currently available to experimentalists: Blocking and PXCT.

The PXCT method was introduced in the 1970s, measuring the average lifetimes of proton unbound states in ^{69}As, which are populated by the electron capture decay (EC) of ^{69}Se [73]. A diagram illustrating the operating principle of PXCT is shown in Figure 2.4.

Once the precursor (Z) nucleus decays via electron capture, the resulting system is left in a kind of 'two-fold excited state', i.e. an excited atomic and nuclear structure. An electron capture decay is defined as a decay of a nucleus that converts a proton and an inner-shell atomic electron into a neutron and electron neutrino — $p + e^- \rightarrow n + \nu_e$. For our purposes, we ignore the neutrino emitted in this stage, our setup has a virtually 0 cross section to measure it anyway. This EC is crucial to set up the atom in a state that allows us to measure the lifetime of the resulting excited nuclear state. After the EC decay of the precursor nucleus, a proton unbound nuclear state and an atomic electron shell vacancy may be created simultaneously. From this proton emitter (Z-1) stage, the system will decay from this dual excited state. The electron shell vacancy is typically created in the K-shell. An electron from an outer shell drops to fill in this lower energy K-shell, emitting a characteristic

[4] For a discussion on half-lives, see Section A.1 in the Appendix

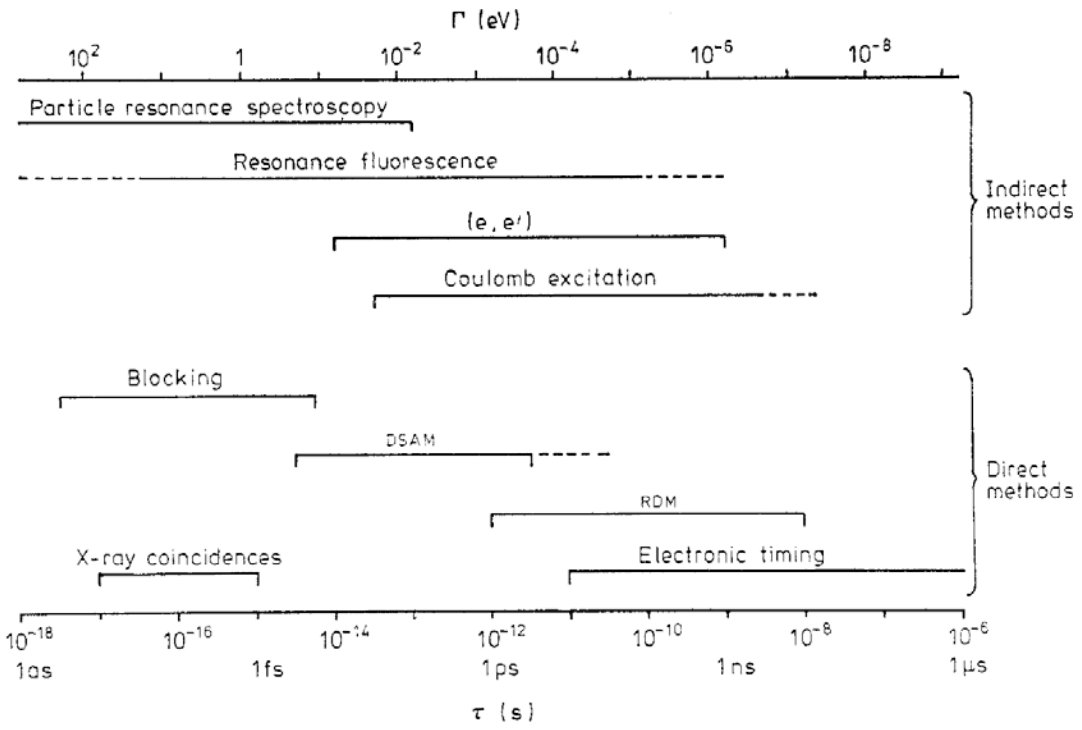

Figure 2.3 The time range over which a few lifetime measurement techniques are effective. Taken from Nolan et al. [72].

X-ray in the process. On a similar timescale, the proton unbound state of the nucleus can emit a proton — decaying to a state in the daughter (Z-2) nucleus.

If the proton is emitted first (left branch of Figure 2.4), the energy of the subsequent X-ray will correspond to a $(Z-2)$ nucleus. If instead the proton is emitted last (right branch of Figure 2.4), the X-ray energy will be that of a nucleus with $(Z-1)$. By measuring the energy spectrum of the X-rays coming from a nucleus that electron captures to a proton unbound state, we can measure the very short lifetimes of that state by comparing the relative intensities of two X-ray peaks we observe — with the condition that we also observe a proton at the same time — shown at the bottom of Figure 2.4. The relative intensities, $I_{K_\alpha(Z-1)}/I_{K_\alpha(Z-2)}$ can be related to the lifetimes in the following way:

$$\frac{\tau_{p-\text{emit}}}{\tau_{K\text{shell}(Z-1)}} = \frac{\Gamma_{K\text{shell}(Z-1)}}{\Gamma_{p-\text{emit}}} = \frac{I_{K_\alpha(Z-1)}}{I_{K_\alpha(Z-2)}}, \tag{2.1}$$

where $\tau_{p-\text{emit}}$ and $\Gamma_{p-\text{emit}}$ are the lifetime and resonance width of the proton-emitting state, respectively, and $\tau_{K\text{shell}(Z-1)}$ and $\Gamma_{K\text{shell}(Z-1)}$ are the lifetime and resonance width of the excited atomic

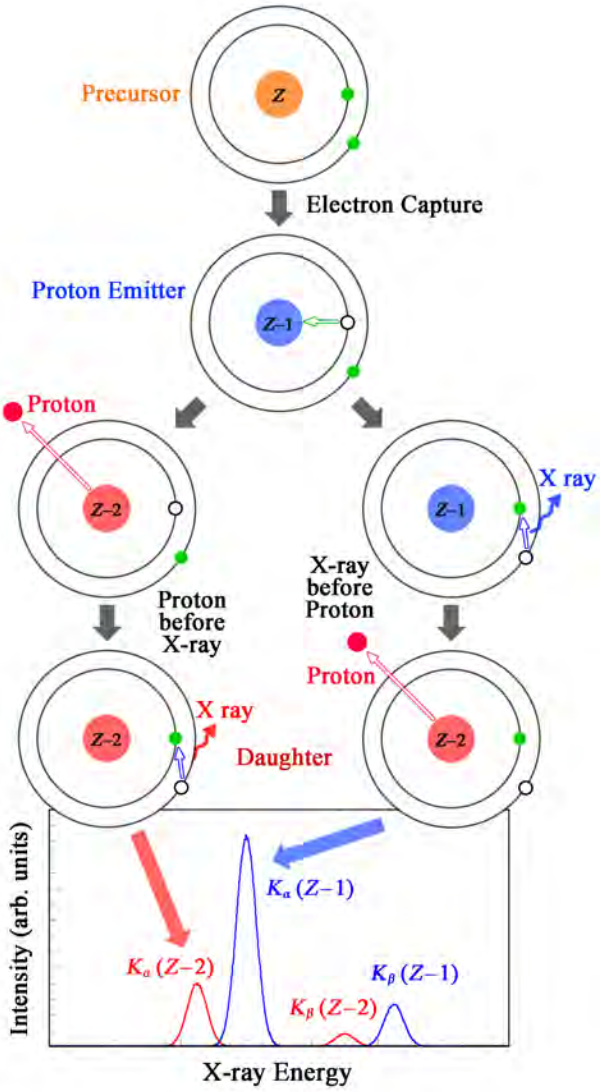

Figure 2.4 Schematic illustrating electron capture to a proton-unbound excited state and the Particle X-ray Coincidence Technique [5].

state. Because the K-shell vacancy lifetimes are well-known [74], and we measure the X-ray intensity ratios, the unknown lifetime of the proton-emitting state can be calculated.

The K-shell vacancy can be filled in the range of 1.1×10^{-14}s for Carbon (Z=6) down to 5×10^{-18}s for Fermium (Z=100) [74–78]. Because we rely on the comparison between the nuclear lifetime and atomic lifetime, the range of lifetimes that are possible to measure with PXCT is limited to values within a few orders of magnitude of the K-shell vacancy lifetime. For example, if the K-shell lifetime and nuclear lifetime are the same, then the integrals of the $K_\alpha(Z-2)$ and $K_\alpha(Z-1)$ peaks should be the same. However, if the nuclear lifetime is very different from the K-shell lifetime, then

only one peak will be observed. In the case of a very long nuclear lifetime, the K-shell will always fill first, meaning only the $K_\alpha(Z-1)$ peak will appear — the opposite occurs in the case where the proton unbound state has an extremely short lifetime, only the $K_\alpha(Z-2)$ peak is produced. In these cases it is only possible to constrain an upper or lower limit to the lifetimes.

Additionally, PXCT can be used in the same way as described above, but with electron captures to alpha unbound states. In this case, the (Z-2) proton decay daughter nucleus is replaced by a (Z-3) alpha decay daughter, providing a greater separation of the two X-ray peaks of interest compared to proton emission. The final open decay channel after the precursor nucleus decays via electron capture is gamma (γ) decay. In this case, the schematic remains largely the same as that in Figure 2.4, with the protons exchanged for γ-rays, but PXCT cannot work to determine lifetimes, because γ-rays do not change the atomic number of the nucleus, and the X-rays that are emitted will always have energy associated with a (Z-1) nucleus.

2.2.1 PXCT: Astrophysics Applications

At the time of writing this, PXCT has been used in decay studies involving six nuclei, the results of which are summarized in Table 2.2. In these studies, the X-ray ratios are taken from gating on the proton energy distribution. From the X-ray ratios and proton energy spectrum, observables such as the average proton partial widths ($\langle\Gamma_p\rangle$), average γ-ray partial widths ($\langle\Gamma_\gamma\rangle$), and the level densities (ρ) can be constrained. They are found by tuning statistical model parameters to match the measured observables [79–82].

The initial γ-ray partial widths are calculated using γ-ray strength functions, based on experimental giant resonance cross-section data, fit with a Lorentzian [83]. To fit the level densities, the back-shifted Fermi gas model can be used [84]. The proton partial width is calculated using the following equation

$$\langle\Gamma_p\rangle = \frac{\Sigma_\ell T_\ell(E_p)}{2\pi\rho(E_x, J, \pi)} \tag{2.2}$$

where $T_\ell(E_p)$ is the transmission coefficient (see 1.2.1) for protons with angular momentum ℓ and energy E_p, and $\rho(E_x, J, \pi)$ is the level density with spin and parity J, π at excitation energy E_x. Because the transmission coefficient is calculated with the optical model, PXCT measurements

done in a particular region of the chart of nuclides can benchmark the local optical model potentials in that region.

As mentioned in Section 1.2, there exist reactions that occur in nature that are exceedingly difficult, and currently impossible, to measure in the laboratory. These include reactions with radioactive reactants with short half-lives, and reactions on nuclei in thermally populated excited states. We plan to use PXCT in an astrophysical context for the first time in order to measure data on these out-of-reach reactions. As described in Section 1.2.3, if the reaction is given enough initial energy, it is possible to populate a high-lying state in the compound nucleus. States at high enough energy are typically surrounded by states close in energy to their own. If this level density is high enough, a statistical treatment is appropriate to theoretically calculate the reaction rate. The Hauser-Feshbach model requires many inputs of nuclear data such as mass, radius, level density, and transmission coefficients. LIBRA has been designed, built, and tested to examine individual resonances, providing spins and parities, resonance energies, lifetimes, and branching ratios for calculating narrow resonance reaction rates using Equations 1.9 and 1.10. LIBRA also has the capabilities to extend PXCT to measure the essential ingredients of the Hauser-Feshbach model, as seen in Equation 1.13.

2.3 LIBRA Design and Actualization

The strength of LIBRA is that we are able to measure many properties of a particular nucleus in a single experiment. Our initial designs of the LIBRA setup required a moving target that would collect radioisotopes for a period of time, and then move to be measured. We found that this would inhibit us from measuring nuclei whose β^+/EC decay half lives were so short that they mostly decayed away before the target was able to switch from the collection position to the measurement position. Additionally, while the target was moved out of the beam line, we would not be collecting nuclei to be measured, cutting our effective beam rate and limiting our overall statistics. This led us to design an apparatus with a fixed target position, where the collection of radioactive nuclei and the subsequent measurement of its decay would occur in the same place, see Figure 2.5.

All beams delivered at FRIB and used by the LIBRA set up are accelerated by the linac, fragmented by a rotating carbon target, separated by the Advanced Rare Isotope Separator (ARIS),

Table 2.2 Summary of the properties of all nuclei investigated using PXCT. Columns 1–7 list the EC/β^+ decay, the half-life ($T_{1/2}$) of the precursor, the β-decay energy (Q_{EC}), the proton-separation energy (S_p) of the EC/β^+-decay daughter nucleus, the total intensity of EC/β^+-delayed proton emission (I_p), the primary X-ray energies ($E_{K\alpha}$) that must be resolved for the $(Z-2)$ and $(Z-1)$ nuclei, the known lifetime of the K-shell vacancy, and the range of lifetimes of proton-emitting states in the EC/β^+-decay daughter nucleus obtained in each study. The last two rows list the properties of ^{60}Ga and ^{64}As for comparison. Table adopted from Sun, et al. [5].

EC/β^+-decay	$T_{1/2}$ (s)	Q_{EC} (keV) [22]	S_p (keV) [22]	I_p (%)	$E_{K\alpha}$ (keV) [85]	$\tau_{K\mathrm{shell}}$ (fs) [74]	$\tau_{p-\mathrm{emit}}$ (fs)
^{65}Ge→^{65}Ga	30.9(5) [86]	6179.3(23)	3942.4(6)	0.011(3) [80, 87, 88]	8.6, 9.2	0.374	~1.7 [81]
^{69}Se→^{69}As	27.4(2) [89]	6680(30)	3420(30)	0.052(10) [82, 90]	9.9, 10.5	0.315	0.3–3.3 [73, 80, 82]
^{73}Kr→^{73}Br	27.3(10) [91]	7094(9)	3067(7)	0.47(22) [92, 93]	11.2, 11.9	0.264	0.3–2.7 [79, 80, 94]
^{77}Sr→^{77}Rb	9.0(2) [95]	7027(8)	3106(4)	0.08(3) [80, 87]	12.6, 13.4	0.222	~1.5 [80]
^{113}Xe→^{113}I	2.74(8) [96]	8916(11)	841(12)	7(4) [97]	27.5, 28.6	0.062	0.3–2.9 [98]
^{117}Ba→^{117}Cs	1.75(7) [99]	9040(260)	740(60)	16(3) [98]	29.8, 31.0	0.054	>4.7 [97]
^{60}Ga→^{60}Zn	0.0694(3)[a]	14161(15)[b]	5105.0(4)	1.6(7) [23]	8.0, 8.6	0.406	
^{64}As→^{64}Ge	0.0690(14) [100]	14606(110)[c]	5057(4)	unreported [102]	9.2, 9.9	0.343	

[a] See Figure 2 of Sun et al. [5] for evaluation details.
[b] See Figure 2 of Sun et al. [5] for evaluation details.
[c] Deduced based on ^{64}As mass [101] and ^{64}Ge mass [22].

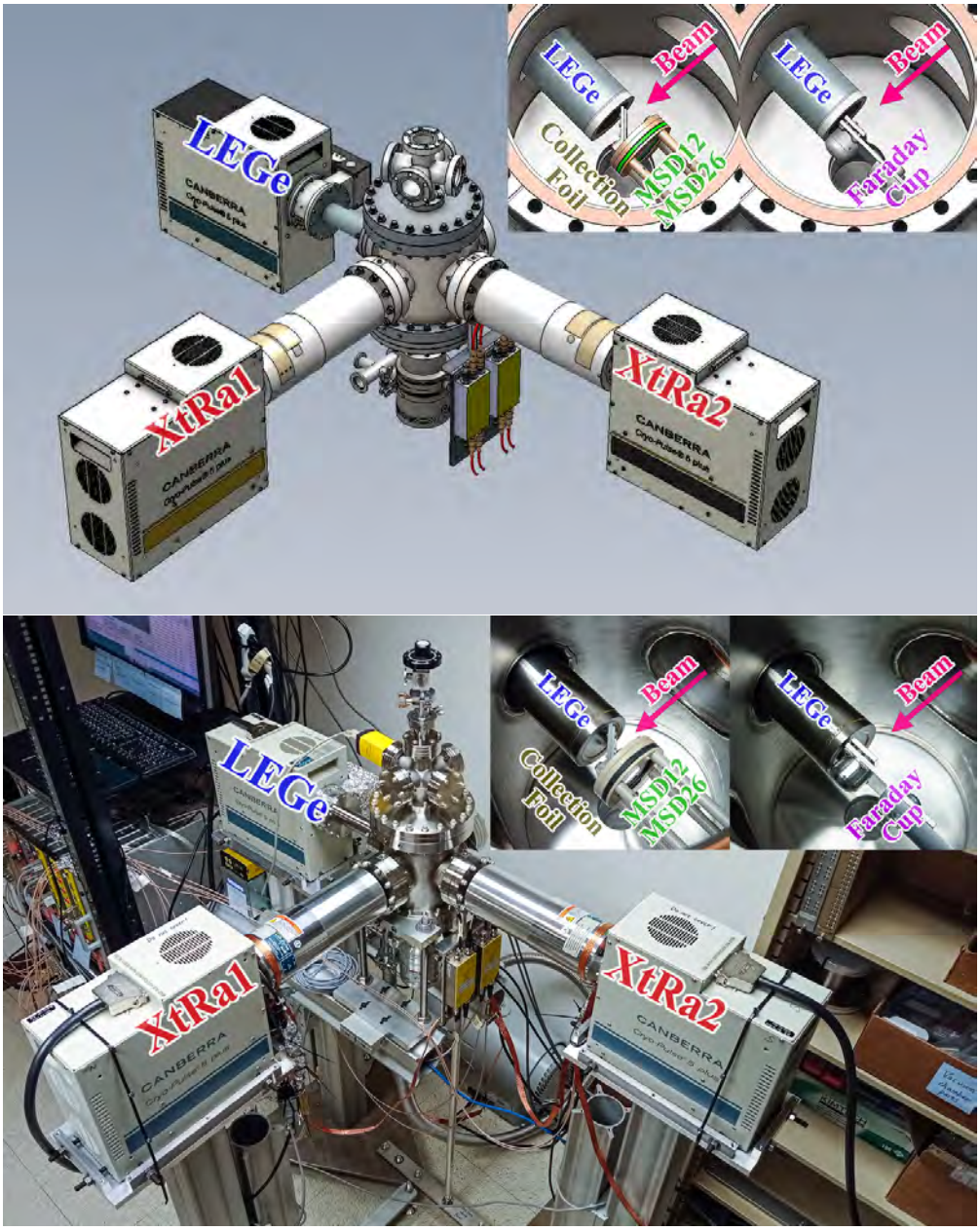

Figure 2.5 CAD Drawing (top) and photograph (bottom) of LIBRA. The insets show the target in two configurations, tuning and collection. Tuning the beam requires a Faraday cup and a simpler to produce beam that ensures the beam of interest will be on target. Collection uses a foil to stop the slow beam in the center of the chamber for greatest detection efficiency by our Si and Ge detectors for decay measurements.

stopped by metal degraders and thermalized in helium gas stoppers before a 30 keV beam of the nuclei of interest is delivered to our set up [103]. Xu, et al. [104] shows a detailed figure of the FRIB beam line, which can also be seen in Figure 2.6. Prior to a typical experiment, a stable beam of mass number near the desired beam will be tuned from an offline ion source into into the Faraday cup through a collimator in the center of our vacuum chamber. Once this is done, the Faraday cup is removed and a thin, aluminized Mylar foil is added in its place. This foil is oriented at an angle of 45° w.r.t. the beam. If the foil was instead perpendicular to the beam, the Si or X-ray detectors adjacent to it would have reduced efficiency to detect decay products. The beam of interest is then directed into the center of the Mylar foil. In practice, we want a beam whose energy and energy spread is as low as possible so that the foil can be made thin. If the foil is too thick, the particles emitted after EC decay will be more likely to be absorbed or scattered by the foil, and thus not reach our detectors.

2.3.1 LIBRA Detectors

As shown in Figure 2.5, LIBRA is comprised of a planar germanium detector used for X-ray detection, two large-volume coaxial germanium detectors for γ-ray detection, and a silicon telescope to detect charged particles.

2.3.1.1 Semiconductor Detectors

Before continuing, I hope it will be instructive to describe the process by which radiation is measured via semiconductor detectors. This way, it will be easier to understand the choices made in picking each detector, and why it excels in measuring a particular type of radiation.

Any type of radiation detector, including everyday cameras, work through an interaction of the incoming radiation with the matter of the detector's sensitive region. In the case of modern cameras, for example, incoming light enters the lens and is focused on a sensor that creates electrical signals proportional to the intensity of light coming from the photograph's subject. This charge is read off and processed into an image of what the sensor was exposed to during the time that the charges were being recorded to the camera's memory. [5] A similar principle is used in the detection of radiation

[5]Before electronic sensors, cameras were designed to expose film to the desired scene. This film had silver-halide

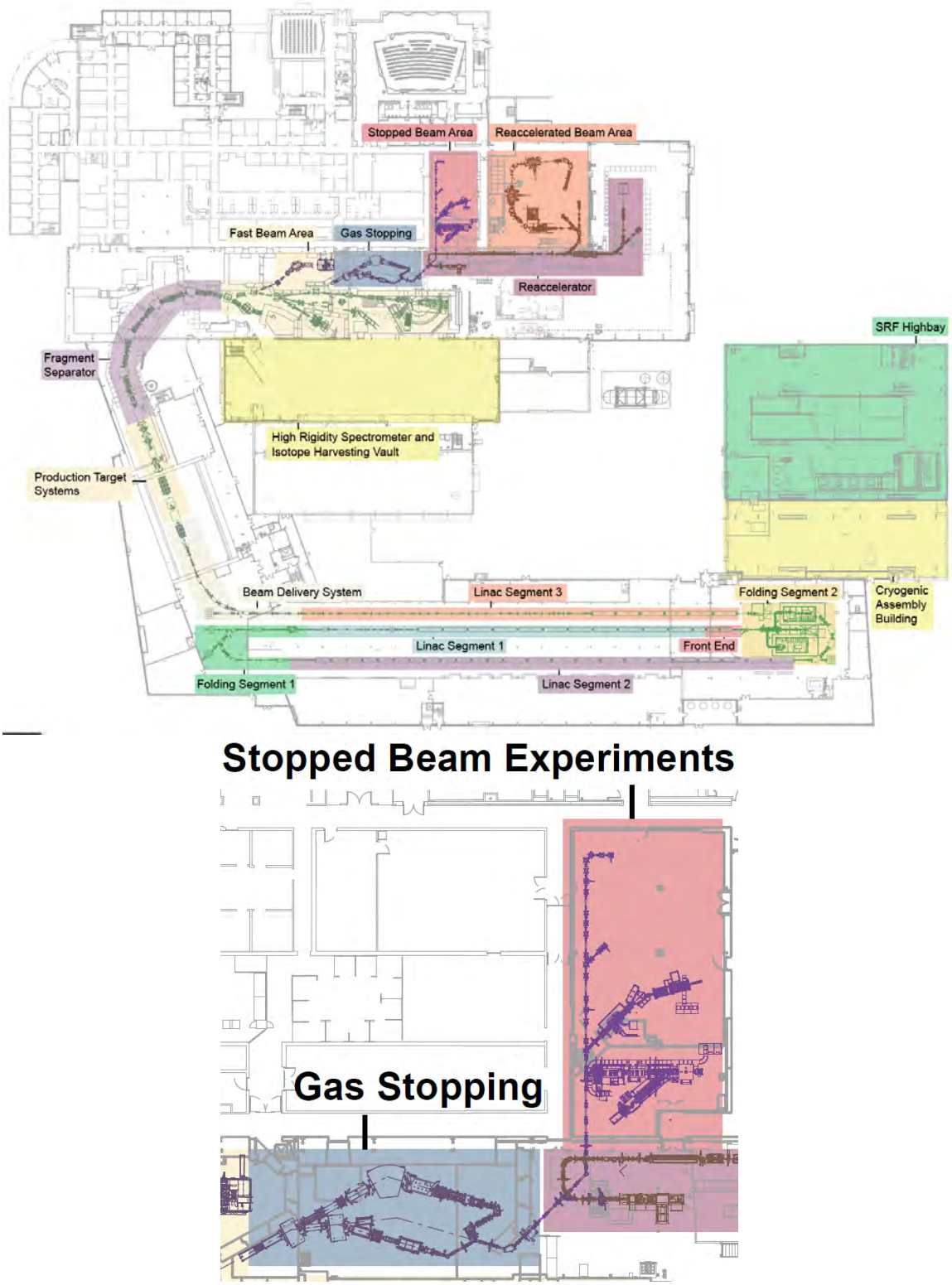

Figure 2.6 Top panel shows entirety of FRIB, from experimental areas to beam line to facilities that manufacture and repair accelerator parts. The bottom panel shows a zoomed in section of the beam line where the beam is stopped and brought to the experimental area for measurement. Figures courtesy of Jill Berryman and Craig Snow.

from the nucleus. Radiation passes through some sensitive volume of a detection medium that is instrumented to read out the charge produced by this radiation. This charge is proportional to the energy deposited by the radiation. Once this charge is produced in the sensitive region, it must be swept to a location where the electrons can be collected and their signal can be measured. Handling the signal after it is produced is discussed in an upcoming section.

To extract meaningful information from the signal generated by the radiation, we must understand how the radiation of interest interacts with our detectors' sensitive regions. Charged particles are most likely to interact with the electrons of a material as they pass through, and their energy loss to these inelastic collisions can be modeled by the Bethe-Bloch formula:

$$-\left\langle \frac{dE}{dx} \right\rangle = 2\pi N_A r_e^2 m_e c^2 \cdot \rho \frac{Z}{A} \frac{z^2}{\beta^2} \left[\ln\left(\frac{2m_e \gamma^2 v^2 W_{\max}}{I^2} \right) - \beta^2 \right] \tag{2.3}$$

where v, z, and E are the velocity, charge, and energy of the radiation, N_A is Avogadro's number, c is the speed of light, $\beta = \frac{v}{c}$, γ is the Lorentz factor [6], r_e and m_e are the electron's radius and rest mass, and Z, A, ρ, I and $W_{\max}$ are the absorbing material's atomic number, atomic weight, density, mean excitation energy, and maximum energy transfer in a single collision. For our purposes, the radiation we are interested in has a much higher energy than the mean excitation energy of the atoms it is transferring energy to. This means that we do not focus on an individual interaction between the radiation and the detector, but rather consider it a statistical process, where the path of the radiation is determined by the stopping power of the material and many random interactions between the material and the radiation.

From an experimentalist's perspective, we can only control the material of detection. To this end, the relevant variables for stopping power are Z, A, and ρ. The higher the proton number and

crystals which reacted to the incoming light and formed a latent image that could later be processed in a darkroom. There is a nuclear physics equivalent to this analogue process: nuclear emulsion. Ionizing radiation passes through a medium and creates visible defects in the crystal, leaving behind a latent image of the path that radiation traveled through the crystal. This was first seen to occur via natural radiation in mica by Price and Walker in 1962 [105]. There has been very interesting work proposed to search for very rare particle events in undisturbed mica, that have had many millions of years to be exposed to cosmic rays [106]. Additionally, nuclear emulsions are used as passive detectors to monitor ambient radiation exposure in a variety of settings. In fact, as I type this, I am wearing a radiation badge that uses nuclear emulsion to ensure that I remain below the annual limit of radiation exposure for a radiation worker!

[6] defined as $\gamma = \frac{1}{\sqrt{1-\beta^2}}$

density of the absorbing material, the greater the stopping power. The lower the atomic weight, the greater the stopping power. For charged particle detection, a standard detector in nuclear physics is silicon semiconductors.

Semiconductors have the unique property of a band gap energy in a range useful for our purposes. All crystalline materials have energy bands where electrons are allowed to be. In the 'ground state', or valence band, the outer-shell electrons of the material are bound to the lattice. In the 'excited state', or conduction band, the electrons are free to move around in the crystal. The size of the gap between these bands determines whether the material is classified as a semiconductor or insulator. The electrons in this lattice must be excited in order to move from the valence band to the conduction band. Once radiation passes through the semiconductor material, electrons jump across the band gap into the conduction band and are free to move around the lattice. This creates holes in the valence band, which act similarly as carriers with opposite charge. If we then apply a voltage across the region, we can collect these electrons and holes at the anode and cathode, respectively, and use that information to measure the energy deposited in our detector.[7]

In the case of gamma rays, we cannot treat their interaction with matter statistically. This is because they have lower cross sections for interaction, and when they do interact, via either photo absorption, Compton scattering, or pair production (see Figure 2.7), the gamma ray's energy and path will change substantially. Photo absorption is a process in which the photon is totally absorbed via the photon's interaction with an electron. The Compton effect is a process by which the photon is inelastically scattered off of an electron in the material. And pair production occurs at photon energies above 1.022 MeV, where the photon interacts with the *electric field* of the atom or nucleus and is converted into an electron-positron pair. Because of the nature of the photon's interaction with matter, we want detectors with large volumes and made out of materials with high Z and ρ, because increasing the total efficiency of gamma ray detectors is important due to the low intrinsic

[7]What I have described here is only accurate for so-called 'intrinsic' semiconductor detectors. In reality, silicon detectors are doped with impurities from groups III (p-doped) and V (n-doped) of the periodic table, creating regions of surplus holes and electrons, respectively. This means that applying a reverse bias has the dual outcome of allowing us to collect the charge produced by radiation, but also creates a large depletion region (so named because this region is depleted of charge carriers), where this doped silicon detector acts like the intrinsic detector I described. For a more in-depth explanation see Chapter 11 of Knoll [107].

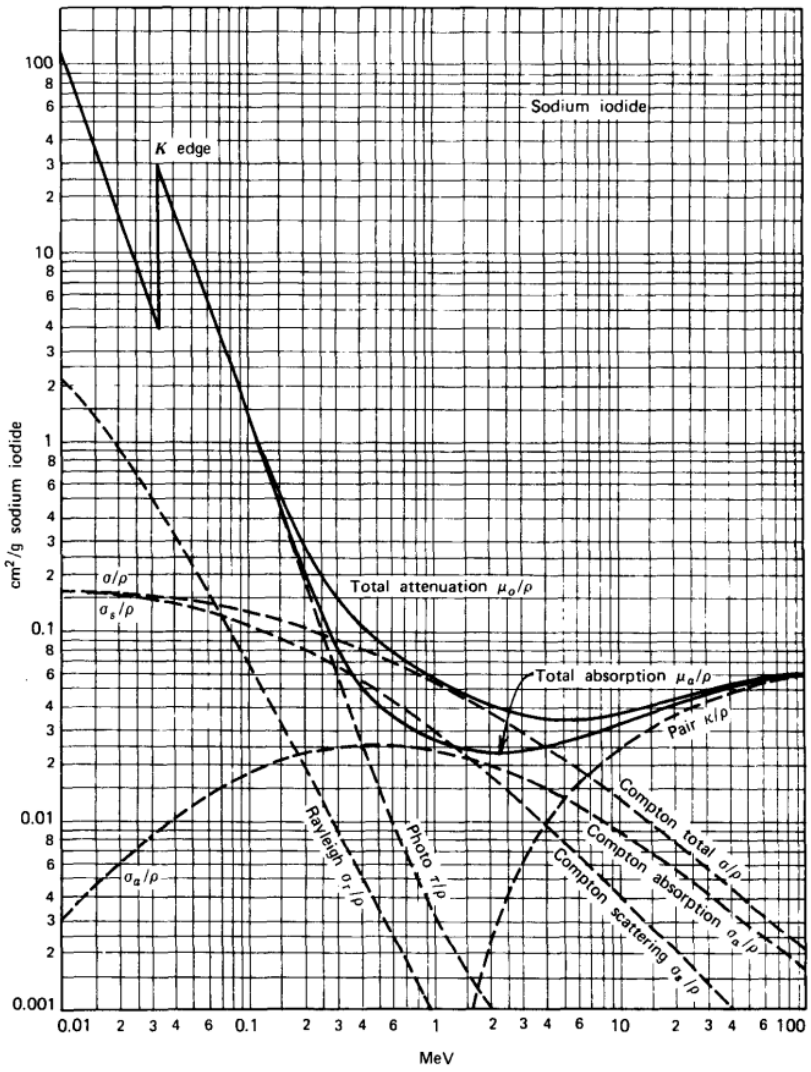

Figure 2.7 Cross section of gamma ray interactions with NaI detectors. Rayleigh scattering is coherent, elastic scattering off of electrons. Taken from Knoll [107].

efficiency (as compared to the efficiency of semiconductor detectors to observe charged particles). Germanium is a semiconductor material that best fits these requirements. It also has a smaller band gap than Silicon, meaning that the Ge crystals require cooling to avoid thermal noise in the signal. This means that germanium detectors are our choice for gamma and X-ray detection.

One additional note of importance to LIBRA is the discontinuity of the X-ray cross section near the lower energies, called the 'K-edge'. This is due to the electronic structure of the material used, in the case of Figure 2.7, that would be sodium iodide. If the photon is above that energy, any electron it interacts with can be fully excited into the conduction band and collected. However, if the incident

photon has energy below this K-edge, the most tightly bound electrons in the material, even when absorbing the full energy from the photon, do not have enough energy to excite the electron to the conduction band, and thus cannot contribute to our detection efficiency. Because we are interested in measuring X-rays at energies in this region, it is important to know our detection efficiency down to these energies, which is discussed in Section 2.4.

Finally, once our photon has excited the electron, the electron interacts with other electrons, exciting them across the band gap, enabling their collection and read out as an energy and timing signal. The size of the band gap determines the average number of electron-hole pairs created for a given energy deposition, which is directly responsible for the energy resolution of our detectors. The smaller the band gap, the more electrons created, and the better the energy resolution. This comes down simply to a matter of statistics. The larger the number of charge carriers, the smaller the fractional differences between number of charge carriers (and thus measured energy) from event to event. Silicon has a band gap energy of 1.11 eV, and germanium has a band gap energy of 0.7 eV [25].

For X-ray detection, we selected the Low Energy Germanium detector (LEGe) by Mirion, Model GL0510 [108]. This is a planar HPGe detector that is designed specifically to measure low energy photons, in the range of keV. The sensitive region is disc shaped, and has a 25.0 mm diameter and a thickness of 10.5 mm. Because it is a specialized detector to measure lower energy photons, it has a thin window made of low Z material (0.13 mm of Beryllium), in order to minimize the photons' interactions before reaching the sensitive region of the detector. This LEGe detector is designed to be fitted to a flange so it can be placed in a vacuum chamber. The entrance window of the detector is placed 11.0 mm from the center of the chamber, and the Ge crystal sits 5.6 mm behind the entrance window, giving us a 10.1% solid angle coverage of the radiation emanating from the center of the chamber (which is where the isotopes are to be implanted during beam experiments, see Figure 2.5). The LEGe detector has a thin, p^+-doped contact on the front side of the crystal, and a rear n^+-doped contact. The rear contact does not cover the entire active area, which generally does not hinder collection of charge, but does reduce the internal capacitance of

the detector. This results in a lower signal-to-noise ratio for X-ray spectroscopy (as low as 3 keV events), while allowing use of a larger area detector for maximum geometric efficiency.

The γ-ray detectors chosen for LIBRA are the Mirion GX10020, the Extended Range Coaxial Germanium Detectors (XtRa). For these higher energy photons, we prioritize a high volume of sensitive material. To that end, the crystal dimensions are 84.8 mm diameter and 65.2 mm thickness for the XtRa 1, and a 79.8 mm diameter and 80.0 mm thickness for the XtRa 2. Both detectors are equipped with 0.6 mm thick carbon composite entrance windows, and the Ge crystals are positioned 6.8 and 6.3 mm from their respective windows. Since these two detectors are designed to measure higher energy photons emitted from the nucleus, which have a relatively low interaction cross section with matter, we are not as worried about the photons stopping in the chamber material before reaching the detector's sensitive region. Because of this, we operate the XtRa detectors outside of the vacuum chamber, and can place them in any location around the set up. We have also used this modular design of LIBRA to couple the XtRa detectors to other experimental set ups. The two XtRa detectors have been coupled with a silicon cube array [109] and with our group's time projection chamber, the GADGET II TPC [110]. We also have the option to integrate LEGe and the central chamber with larger Germanium detector arrays, such as the DEcay Germanium Array initiator [111], to achieve a higher γ-ray detection efficiency.

All three HPGe detectors of LIBRA are cooled mechanically with a Canberra Cryo-Pulse 5 Plus cryostat. Because the band gap energy of Germanium is so low, if these HPGe detectors are not cooled, the ambient room temperature can cause electrons in the crystal to jump the band gap, creating a leakage current and drowning out the signal of the photons we are interested in measuring. To this end, each of the detectors' housing is connected to a compact cold-head containing a 5 Watt pulse tube cooler. The assembly is powered by a bench-top controller, which contains logic to ensure the safe and reliable operation of the cryostat in normal and adverse conditions. During standard operation, the cold tip is maintained at the preset -185°C. A control panel application allows for remote control, monitoring, and logging of cryostat status, all of which are useful during an experiment.

For charged particle detection, we designed the chamber flanged to hold a ΔE-E silicon telescope, consisting of two single-sided, single-area, circular silicon detectors made by Micron Semiconductor Ltd. The reason two silicon detectors are required for charged particle identification can be explained by recalling the discussion of the Bethe-Bloch formula earlier in this chapter, Figure 2.3. Let's assume two different charged particles enter a 1 mm thick silicon detector, one after the other, with the exact same energy — 10 MeV. The first, a proton, deposits 100% of its energy within 710 μm of entering the detector. Based on the band gap of silicon, this proton liberates about 10 million electron-hole pairs that are swept to the electrodes of the detector and read out, providing a signal proportional to the energy of the 10 MeV proton that entered the sensitive region.

After the charge from the proton is collected and recorded, a 10 MeV alpha particle now enters the detector. In this case, the band gap of silicon remains the same, so the number of electron-hole pairs created is still roughly 10 million, generating a signal whose amplitude is proportional to a charged particle depositing 10 MeV of energy in to our detector. However, the stopping power for an alpha particle is much different from a proton's in silicon, and the alpha particle deposits its 10 MeV over a shorter distance of 70 μm.

If we are only using this one silicon detector, then it is difficult to separate protons from alpha events. However, let's assume we use two silicon detectors, one behind another. The first is a very thin (ΔE) silicon detector that does not fully stop either of the particles in our example, let's say it is 14 μm thick. The second, rear silicon detector is the 1 mm thick detector from before, and fully stops any particle and records the remainder of its energy. Given these circumstances, the proton would deposit roughly one percent of its energy into the ΔE detector, with the remainder of the energy going into the E detector. On the other hand, the alpha particle would deposit 10% percent of its energy in the ΔE detector. In this way, we can use the stopping powers of different ions to categorize the particles event-by-event. In our example, we look at events that deposited energy in both the ΔE and E detectors at the same time, then plot their energies on a two-dimensional histogram, see Figure 2.23 for an example in simulation. Like particles will group into bands, allowing us to collect like particles together, and better understand the experimental data.

In the case of LIBRA, it is important to know which charged particles are being emitted from the decaying isotopes of interest, so we need this capability. To this end, our purchased silicon detectors consist of the MSD012 (12 μm thick and 12 mm in diameter) and the MSD026 (1000 μm thick and 26 mm in diameter). Because we are interested in measuring alpha particles at energies lower than 10 MeV, this requires our ΔE detector to be very thin, so it is able to deposit some energy into the E detector and be tagged as an alpha event. The junction side of both MSDs has a 50 nm thick, boron-doped silicon dead layer and a 30 μm wide peripheral metal band for wire bonding. These parts of the detector do not collect and record charge, but are thin enough to minimally interfere with the sensitive region, leaving the majority of the active area without metal coverage. The rear, ohmic side of the MSD012 also needs to be as thin as possible, because all charged particles must pass through this 'dead region' to continue to the active region of the MSD026. Because of this, we opted for an ohmic side with a dead layer of 300 nm and no metal coverage. The MSD026 has a standard ohmic side, with a 500 nm dead layer and 300 nm thick aluminum layer for wire connections. Because it is at the end of the telescope and we planned for the MSD026 to be thick enough to prevent punch-through in all cases we plan to operate, the dead region of the MSD026 will not affect the signals from charged particles we see with the set up. This silicon is assembled onto an FR4 PCB for both silicon detectors. The MSD026 is then placed in the holder, positioned 15.7 mm from the center of the chamber during data collection. This covers 11.5% of the 4π solid angle. The MSD012 is also placed on this holder and remains 11.2 mm from the center of the chamber, and defines the solid angle coverage of the ΔE-E telescope at 5.9% of 4π.

2.3.1.2 Electronics of LIBRA

Radiation enters our detectors, electron-hole pairs are created, charge is swept to the electrodes, but now it is our task to measure this charge and save it for analysis. This means that we produce ten million electron-hole pairs that we can read out at the cathode. A preamplifier is used to convert this tiny current into a reasonable voltage, and then this signal is sent through the rest of the chain for further processing. The preamplifier we use for both the detectors in the ΔE-E telescope is the Mesytec MPR-1, configured as a charge-sensitive preamp, pictured in Figure 2.8.

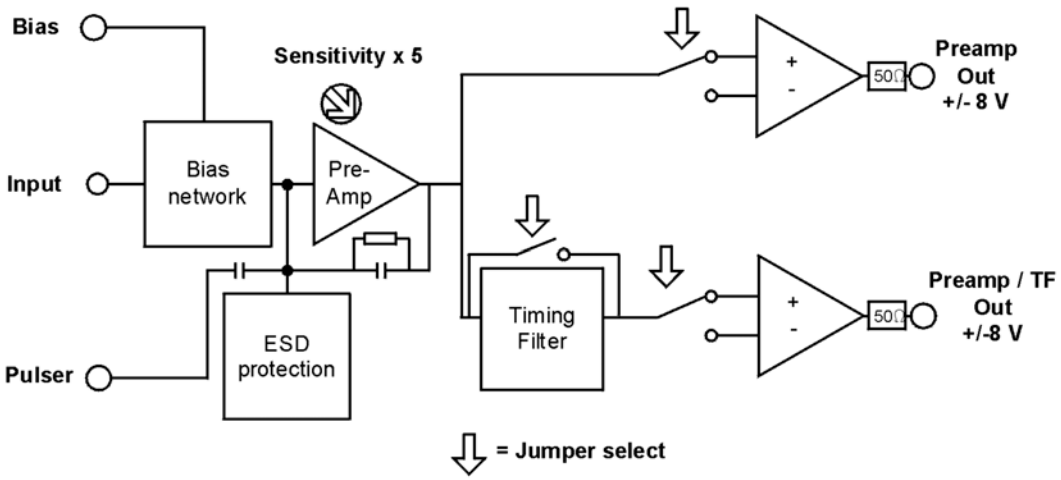

Figure 2.8 Schematic of a Mesytec MPR-1 preamplifier, configured in a charge sensitive mode. In this mode the voltage signal produced by the preamp will be directly proportional to the incoming charge from the detector (assuming the time pulse of the signal is short compared to the time constant of the preamp and that the input capacitance is typical of a radiation detector). Figure from Mesytec data sheet for MPR-1 [112].

The three Germanium detectors from Mirion are all using Intelligent Preamplifiers (iPA). These preamps are specifically designed to work well with their coupled Germanium crystals, by using a low-noise field-effect transistor (FET) input circuit that is optimized for the high impedance of the Germanium detectors. The iPA acts as a charge integrator and has four gain settings. Its output is split into two channels, with impedances of 93 Ω and 50 Ω. It is also bundled with instruments that monitor leakage currents, temperatures, and preamplifier operating voltages. These values can be remotely monitored and recorded via USB connection. The thermometer on each detector consists of two, platinum resistance thermometers, which are thermally connected to the crystal holder (PRTD1) and the cold tip (PRTD2). If either thermometer measures a temperature rise above the preset threshold, it can trigger the high-voltage inhibit via the iPA.

We use two ORTEC 660 Dual Bias Supply modules to bias the Germanium detectors. The ORTEC 660 bias shutdown mode is set to accept TTL to be compatible with the iPA high voltage inhibit logic. A negative bias is applied to the p^+ contacts of the LEGe detector and a positive bias to the n^+ contacts of the XtRa detectors. The data sheets for all three of our detectors can be found in the appendix, which provides information on the depletion and operating voltages of the detectors of LIBRA from the manufacturer. The typical leakage current we observe for the XtRa detectors

are below 20 pA and below 100 pA for the LEGe detector. The signals from the XtRa (LEGe) iPAs have a rise time of 250 ns ($\sim$ 150 ns) and a 50 μs decay constant.

We bias both the Silicon MSD detectors with a Mesytec MHV-4 bias supply. The p^+ contacts on the MSDs are supplied with a negative bias via MPR-1 charge-sensitive preamps [112] and the n^+ contacts are grounded. The MHV automatically ramps the voltage, and we set the speed to 5 V/s to protect the preamps. MSD012 has a leakage current of approximately 1 nA, whereas MSD026 maintains a leakage current of 60 nA. The output signals for both MSDs have a 50 Ω impedance. The signals from the Silicon detectors out of the MPR-1 preamps have a rise time of $\sim$ 400 ns for the MSD012 and $\sim$ 70 ns for the MSD026, with a 120 μs decay constant.

2.3.1.3 Data Acquisition

Now that all of the decay products we are interested in measuring produce signals in our detectors and are amplified to a measurable voltage, we now must process and store the resulting information to extract the results of the experiment. The way this is done in most modern nuclear physics experiments, including all of the ones carried out for this thesis, is via a digital data acquisition. In LIBRA, we digitize our signals with a 16-bit, 250 MHz Pixie-16 module manufactured by XIA LLC. What this means is the voltage signal is broken up into 65536 (2^{16}) ADC channels whose time bins are 4 ns apart. This can be done in the most basic implementation with a parallel-encoded, or "flash" ADC, shown in Figure 2.9.

Here, the input signal is compared with n different reference voltages via n comparators, the output of which forms a 'thermometer code' and is converted to a ($\log_2 n$)-bit binary output corresponding to the highest measured comparator signal [113]. Of course, in reality, the integrated circuits on the XIA have more elegantly implemented the 16-bit ADCs aboard the Pixie module. As for the sampling rate, as long as the ADC samples the signal at twice the rate of the highest frequency component of the signal, then the converted waveform loses no information. This is known as the 'Nyquist–Shannon theorem.' If we happen to undersample the incoming signal, we get an effect called aliasing, which we try to avoid in our applications. For us, a sampling frequency of 8 ns works perfectly fine, given that the rise time of the signal out of the preamp is at minimum an or-

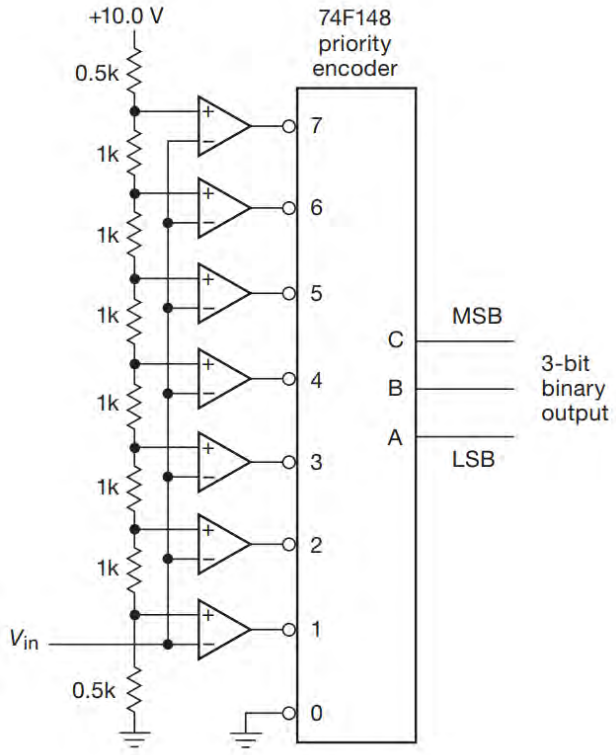

Figure 2.9 Parallel-encoded ("flash") ADC. Taken from Horowitz and Hill [113].

der of magnitude larger than this. The only information we would be losing then, is high frequency noise.

The signals then are processed using the Digital Data Acquisition (DDAS) [114, 115], which scans the digitized trace and uses trapezoidal filtering algorithms for timing and energy. The parameters of these filters can be optimized starting with the XIA User Manual. Each one of the 16 channels on our XIA Pixie module triggers independently, whenever a signal into that channel exceeds a user-set threshold. These events are timestamped using a constant fraction discrimination (CFD) method which handles events of different amplitudes better than a simpler leading edge technique. [8]

The energy is extracted from the amplitude of the signal. Our signals have been tuned to minimize rise times and have a comparably long decay tail. A trapezoidal filter is used to reliably extract the energy of the pulse, which is typical and effective in high precision spectroscopy [116]. The

[8]Leading edge timing produces an effect called 'walk' in events with high energies, causing them to be recorded with an earlier relative timestamp than the same pulse with a smaller amplitude.

filter's gap time is adjusted according to the rise time of the pulse for optimal performance. In the case of pile-up (one signal occurring so near in time to another that it sits on the exponential tail of the first), both events are flagged as such and can be rejected. In the following section on system performance, the pile-up rejection is turned off and the first trace's timestamp is recorded; the second's is thrown out. The energy of the first trace will be affected by the added amplitude of the following signal depending on its proximity in time to the first.

2.4 Performance Data and Simulations

We have carried out comprehensive tests on LIBRA using radioactive sources (^{55}Fe, ^{60}Co, ^{137}Cs, ^{148}Gd, ^{152}Eu, ^{241}Am) [9] and a pulser module to determine the performance of LIBRA under experimental conditions.

First, we connected a DB-2 Random Pulser to each detector input of LIBRA, and varied the signal rate. Recording this data in DDAS allowed us to determine what number of events are actually able to be recorded at each event rate, leading to the results in Figure 2.10.

For the rest of the source tests, an event-build window of ± 1 μs was used. The event rate in each detector was kept below 1,500 pps, except in the case of the ^{152}Eu source and the LEGe detector, which had a count rate of 3,000 pps.

2.4.1 X-ray Tests

The performance of the LEGe detector was evaluated using ^{55}Fe, ^{152}Eu, and ^{241}Am radioactive sources, which produce X rays through electron capture (EC) and internal conversion (IC) processes. The resulting X-ray and γ-ray spectra were used to assess energy resolution, modeled with exponentially modified Gaussian fits, which can be seen in Figure 2.11.

Detection efficiencies were experimentally measured using characteristic Sm and Np X rays and compared with GEANT4 simulations incorporating full detector geometry and response; see Figure 2.12.

Recall from Figure 2.7 that at X-ray energies, the primary way photons interact with our Germa-

[9] Comprehansive information on sources used can be found in Sun, et al. [5]

[10] On lower resolution monitors or print versions of this document, it may be difficult to tell that both XtRa detectors have nearly identical live times as a function of incoming rate.

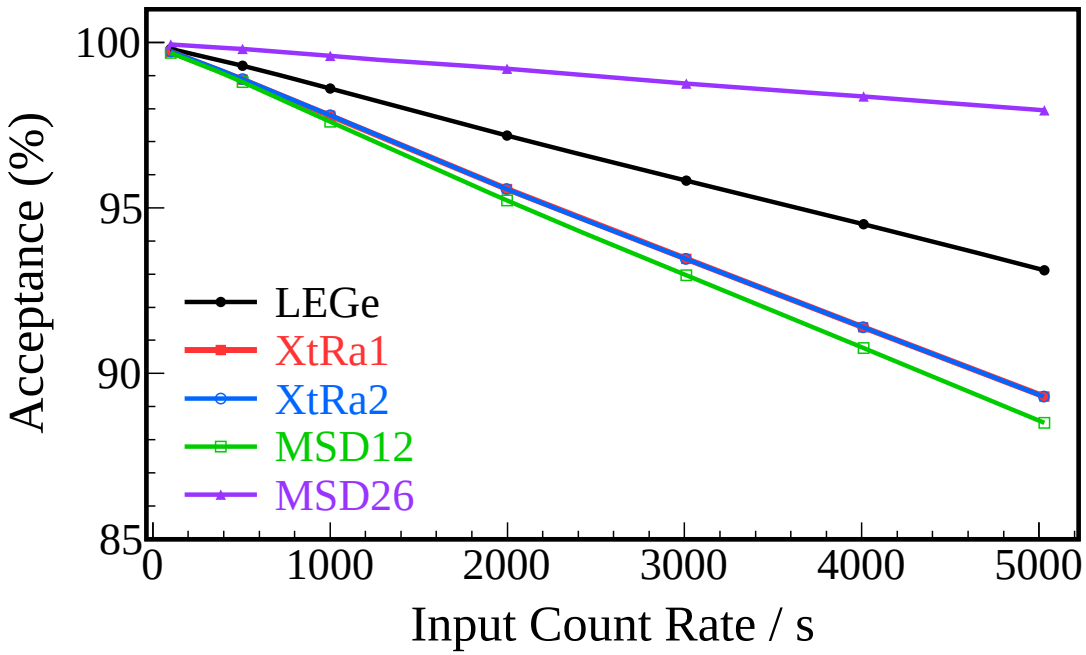

Figure 2.10 Live time of each detector in LIBRA as a function of incoming event rate [5]. [10]

nium is via photo absorption. Notice in Figure 2.12, the abrupt decrease in efficiency which lines up with the K-edge of Germanium, signaling the increase in likelihood for the photon to interact with the Germanium. This is a result of the increased likelihood for a photon, whose energy is greater than ~11 keV, to interact with these K-shell electrons, producing a characteristic Ge X-ray and that X-ray subsequently escaping. This effect will increase with an increasing dead layer in the Ge crystal from Lithium drift over time. Additionally, effects such as source encapsulation (Mylar attenuation for ^{152}Eu), and count rates affecting DAQ live time mean that the ^{152}Eu efficiency curve is a lower limit estimate, and the ^{241}Am represents a more favorable scenario.

2.4.2 γ-ray Tests

The large volume XtRa detector tests were carried out in a similar way to the LEGe tests. The energy spectra were taken in two spatial configurations. In the upper half of Figure 2.13, the detectors were placed 28 cm from each other, with the source placed in the middle. In the lower panel, the sources were placed in the center of the LIBRA chamber, and the detectors were positioned as close to the source as possible from outside the chamber, as shown in Figure 2.5. The efficiencies of the XtRa detectors were determined in this chamber configuration, and compared to simula-

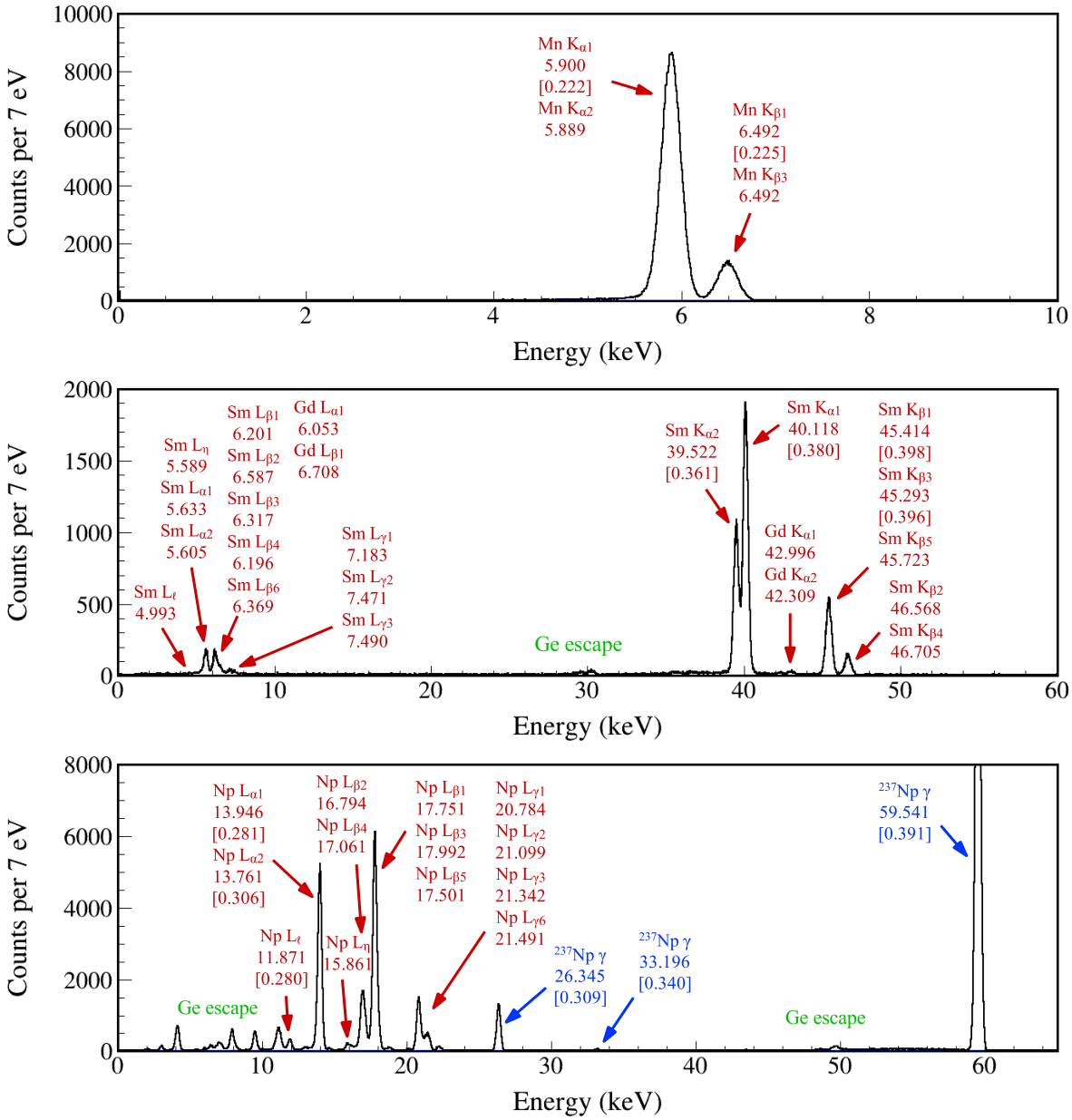

Figure 2.11 X-ray and γ-ray spectra measured by the LEGe detector using the ^{55}Fe (top), ^{152}Eu (middle), and ^{241}Am (bottom) sources. Taken from Sun, et al. [5].

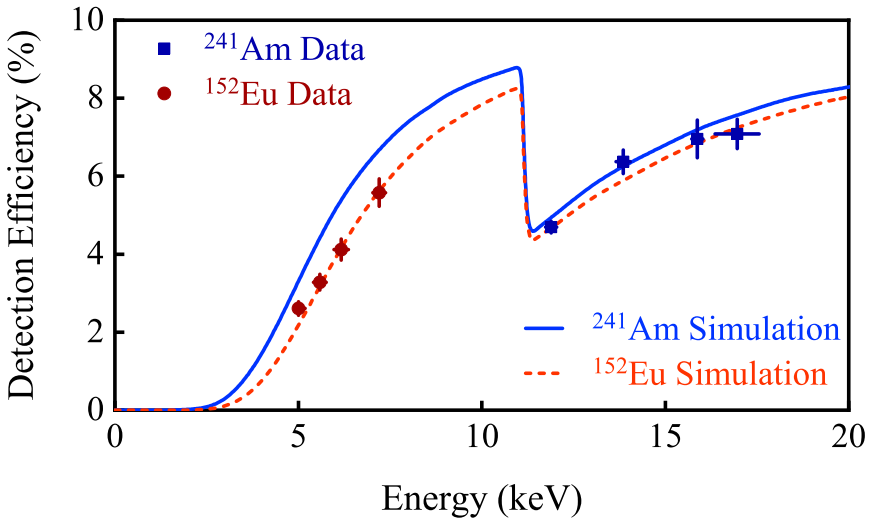

Figure 2.12 Photopeak efficiency of the LEGe X-ray detector using the characteristic X-rays of Samarium and Neptunium from ^{152}Eu and ^{241}Am, respectively. X-ray tests were taken with the LEGe attached to the LIBRA chamber, with the sources placed in the center of the chamber at a 45° angle to mimic the position of the target during an experiment. Dashed and solid lines represent simulated data from GEANT4. Taken from Sun, et al. [5].

tion. In this arrangement, both detectors were equidistant from the center of the chamber, 158.5 mm, but because of the differences in crystal shape[11], the XtRa1 detector subtends a solid angle of 1.70%, while XtRa2 covers 1.51%. The X-ray peaks in the chamber configuration are blocked by the flanges, meaning that during a beam experiment we fully rely on the LEGe detector for low energy X-ray information. Efficiency runs using the ^{152}Eu, ^{137}Cs, and ^{60}Co were taken to get the broadest energy coverage. These experimental data were compared with scaled simulation data, shown in Figure 2.14.

2.4.3 Charged Particle Tests

The Silicon MSD detectors were benchmarked with an ^{241}Am alpha source. Shown in the inset of Figure 2.5, the source and MSDs are placed in chamber, with the source occupying the space that the collection foil does during a real experiment. The source has a 2 mm aperture installed to focus the alpha particles to enter the Silicon detectors orthogonally. In an experimental measurement, the charged particle data would be affected by events that enter the MSDs at varying angles, but for characterizing the detectors the aperture is ideal. Since the MSD012 is so thin, it does not fully stop

[11] see the appendix for Germanium crystal shape dimensions, as well as the manufacturer's performance data

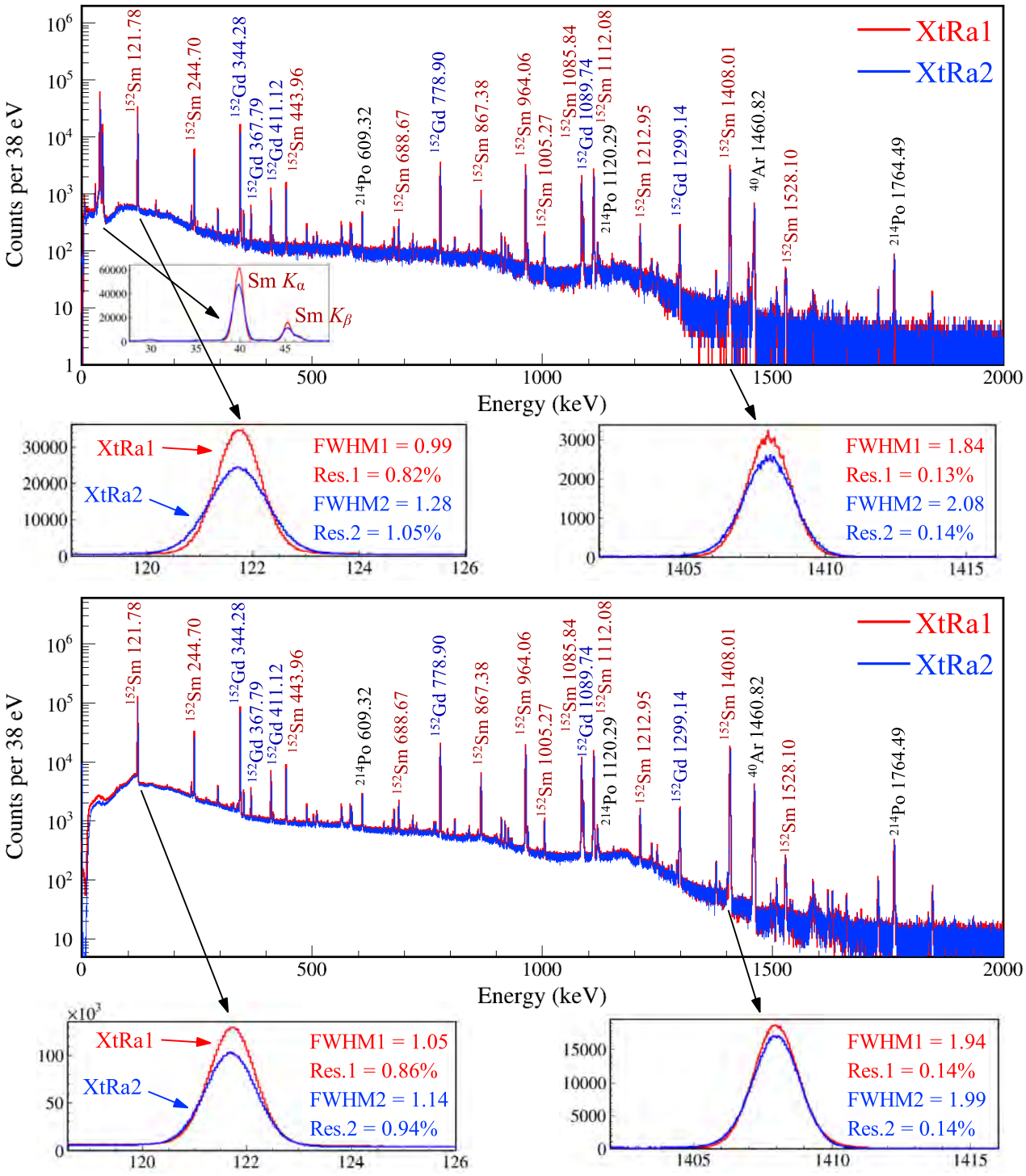

Figure 2.13 γ-ray spectra measured with XtRa1 (red) and XtRa2 (blue) using a ^{152}Eu source. Top panel: the ^{152}Eu source is placed midway between the two XtRa detectors facing each other. Bottom panel: the ^{152}Eu source is placed at the center of the vacuum chamber, with the two XtRa detectors positioned as shown in Figure 2.5. All γ-ray energies are adopted from Ref. [117] and rounded to the nearest 0.01 keV. The insets demonstrate the detector responses at 122 and 1408 keV. Taken from Sun et al. [5].

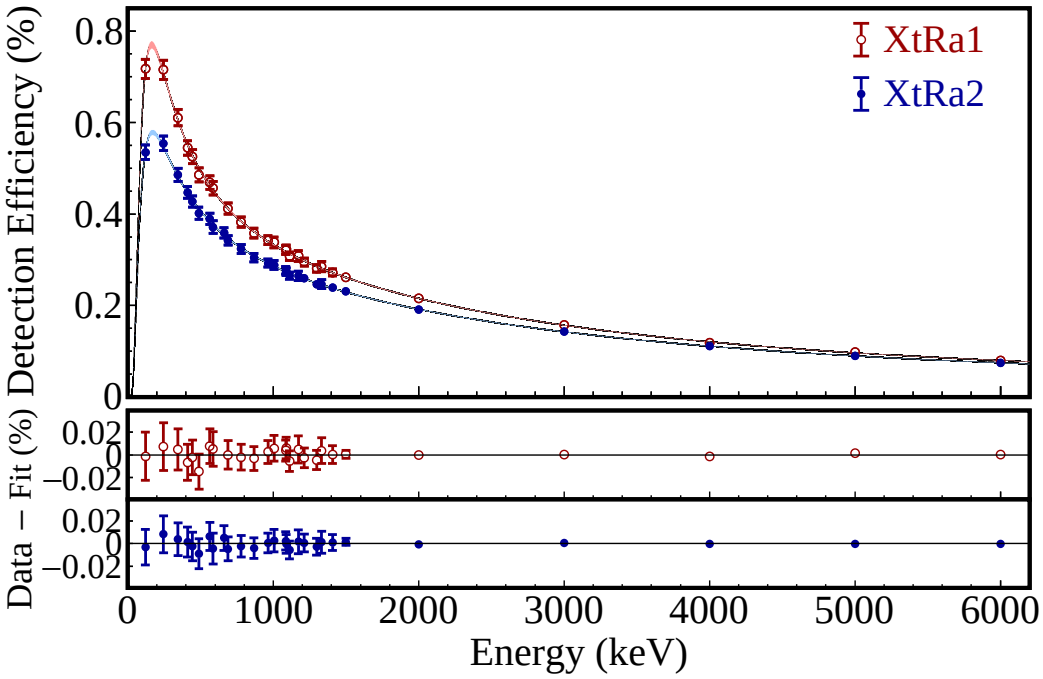

Figure 2.14 Absolute γ-ray photopeak detection efficiency of the two XtRa detectors were determined using the ^{152}Eu, ^{137}Cs, and ^{60}Co sources placed at the center of the chamber. For energies above 1500 keV, efficiency values were obtained from GEANT4 simulations and scaled to align with the experimentally measured low-energy data. The efficiency curves along with the 1σ uncertainty bands are generated by fitting all data points. Taken from Sun et al. [5].

alpha particles above 3 MeV (based on SRIM calculations). Notice in the top panel of Figure 2.23, the simulated alpha band stops at 3,000 keV. Therefore, we only show a 1D histogram of the energy spectrum of ^{241}Am taken with the MSD026, Figure 2.15.

To benchmark the MSD012, we use the Silicons in the telescope configuration and show the results of the ^{241}Am run in Figure 2.16. This type of plot allows us to distinguish protons from alphas during an experiment. We find that the sum peak in the upper panel of Figure 2.15 has a FWHM of 0.95%. We can also use this data to determine the thickness of the MSD012 detector. This is useful because its thickness determines the lowest energy alpha it is possible to identify in the telescope set up. We find that the effective thickness of the MSD012 is 11.65(8) μm. The manufacturer quotes the thickness of the MSD012 detector as 12 ± 10%.

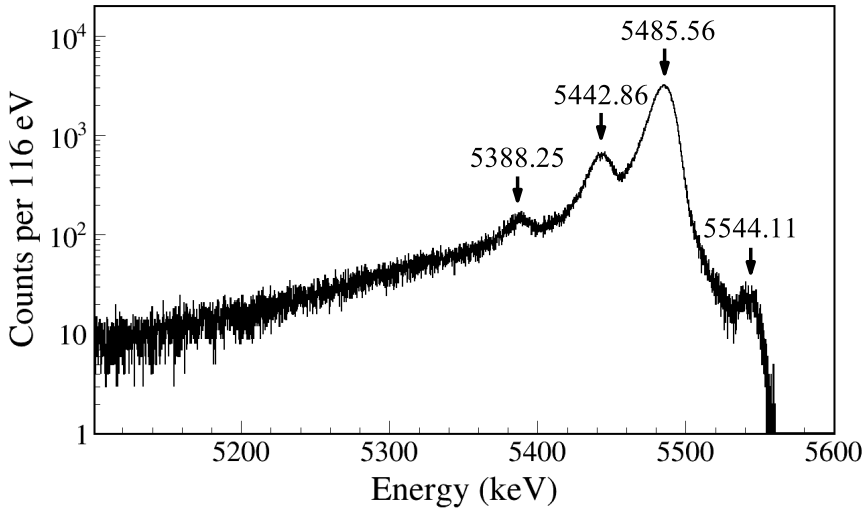

Figure 2.15 α spectrum measured by MSD26 using the ^{241}Am source. The energy resolution of the MSD026 at 5485 keV is 031% (FWHM is 17.0 keV). Taken from Sun et al. [5].

2.4.4 Timing Tests

We use the ^{60}Co source to measure $\gamma - \gamma$ coincidences in the XtRa detectors. We use the 40-46 keV X-ray and 1408 keV γ-ray in ^{152}Eu to do the X$-\gamma$ coincidence measurements between the XtRa detectors and the LEGe detectors. And the ^{241}Am source provides $\alpha - \gamma$ coincidences via an alpha decay to an excited state (59.54 keV) in Neptunium. The results of these tests are shown in Figure 2.17. Keep in mind that this timing resolution is more than sufficient for a lifetime measurement via PXCT, the point is that we use well-known X-ray lifetimes to measure sub-femtosecond half-lives of nuclear states. We use the coincidence timing to narrow our event window to a few hundred nanoseconds in the DDAS software.

To investigate coincidence capabilities and background suppression, $\alpha - \gamma$ and electron$-\gamma$ coincidence measurements were performed using ^{241}Am and ^{152}Eu sources, respectively.

With the ^{241}Am source placed at the center of the chamber facing the MSD telescope, the $\alpha - \gamma$ coincidence spectrum (Figure 2.18) shows the 59.5-keV ^{237}Np γ-ray and its associated escape peaks in the LEGe detector in coincidence with the alpha emitted by the ^{241}Am.

In a demonstration of the background suppression via coincidence gates, we took a measurement using the ^{152}Eu source at the chamber center, and γ-ray spectra from the XtRa1 detector were analyzed in coincidence with either Sm K X-rays detected by LEGe or electrons detected by MSD026,

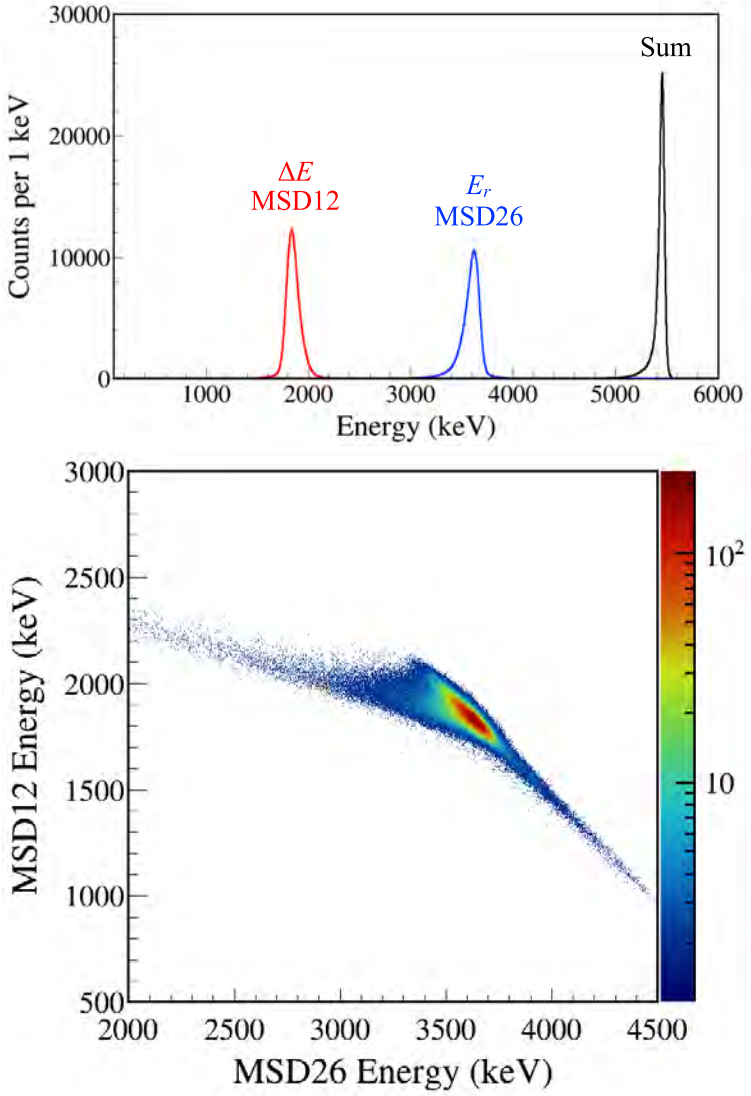

Figure 2.16 Upper: α-energy spectra measured by MSD12 (red), MSD26 (blue), and MSD12+MSD26 (black) using the ^{241}Am source. Lower: ΔE-E 2D plot of the same data. Taken from Sun et al. [5].

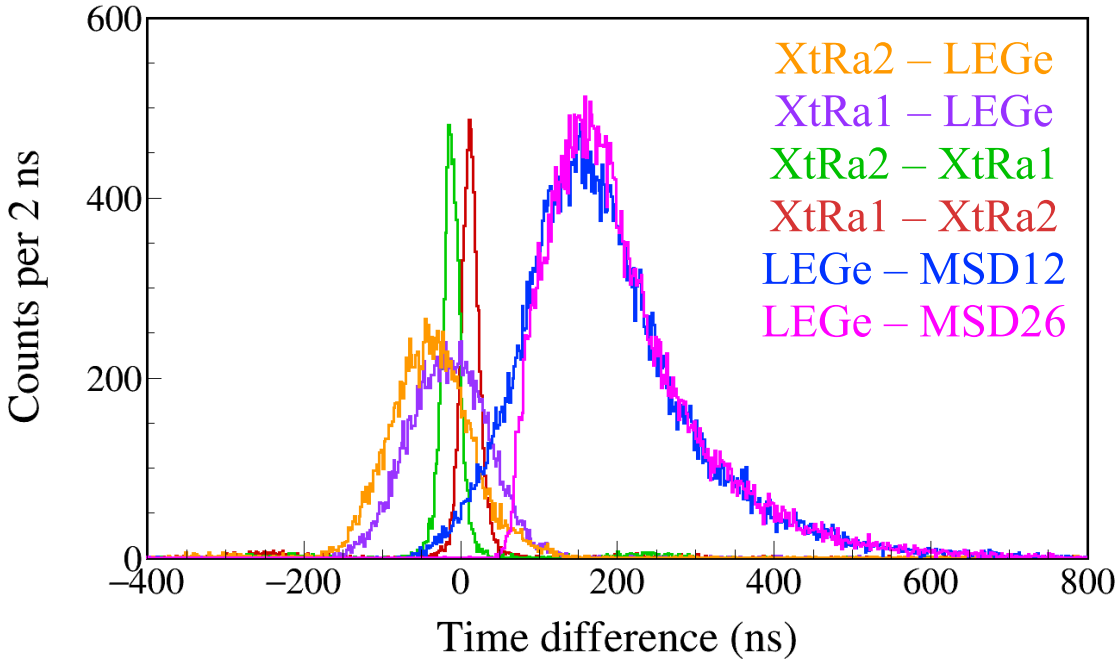

Figure 2.17 Coincidence timing between detectors in LIBRA. Taken from Sun et al. [5].

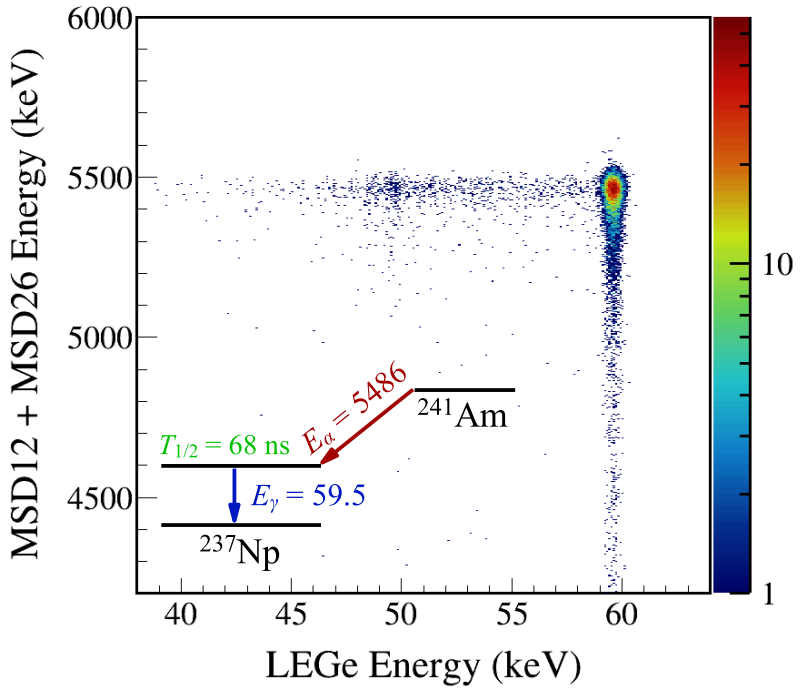

Figure 2.18 Coincidence spectrum between the MSD detector telescope and LEGe obtained using an ^{241}Am source placed at the center of the chamber. A simplified ^{241}Am decay scheme illustrating the dominant α-γ sequence is also shown as an inset. Taken from Sun et al. [5].

shown in Figure 2.19. Coincidence gating with characteristic X rays effectively suppressed room background and ^{152}Gd γ-rays, while electron gating suppressed both room background and ^{152}Sm γ-rays. These results demonstrate that the detection of a wide range of decay products significantly enhances interpretation of the data, which is especially advantageous for radioactive beam experiments aiming to unambiguously identify radiation origins.

2.5 Lifetime Measurement

As part of the characterization of our detectors, calibration data was taken with the ^{241}Am source, whose activity was 3.44 $\times 10^3$ Bq. We found that, using the MSD telescope and LEGe detectors, we could cleanly measure the half-life of the 59.54 keV state in ^{237}Np. The source was again placed in the center of the chamber, facing the MSD telescope with a 2 mm Al aperture. We took three runs of source data in the LIBRA chamber totaling nearly 2200 hours of data collection. Runs 1 and 3 use the ΔE-E telescope and run 2 only uses the MSD026. The resulting data are shown in Figures 2.20 and 2.21.

In Figure 2.21, the timing spectrum comes from the difference in time between the 5486 keV α-particle entering the MSD and the 59.5 keV γ-ray entering the LEGe detector (see Figure 2.18). By fitting the spectra with the function:

$$f_{\text{direct}}(t; N_{59}, T_{59}, B) = \frac{N_{59} \ln 2}{T_{59}} \exp\left[-\frac{t \ln 2}{T_{59}}\right] + B \tag{2.4}$$

where N_{59} is the total number of decays, T_{59} is the decay half-life of the 59.5 keV state, and B is the background, we can extract the lifetimes of the excited state in Neptunium.

However, there are also alpha decays to excited states above the 59.5 keV state of interest. The 103 keV state in ^{237}Np is close enough in energy that the associated alpha particle (5443 keV) is also caught in the gate we use for coincidence with the 5486 keV alpha in runs 1 and 3. The 103 keV state then populates the 59.5 keV state by interal conversion. We take into account these direct and indirect feedings of the 59.5 keV state with equation 2.5.

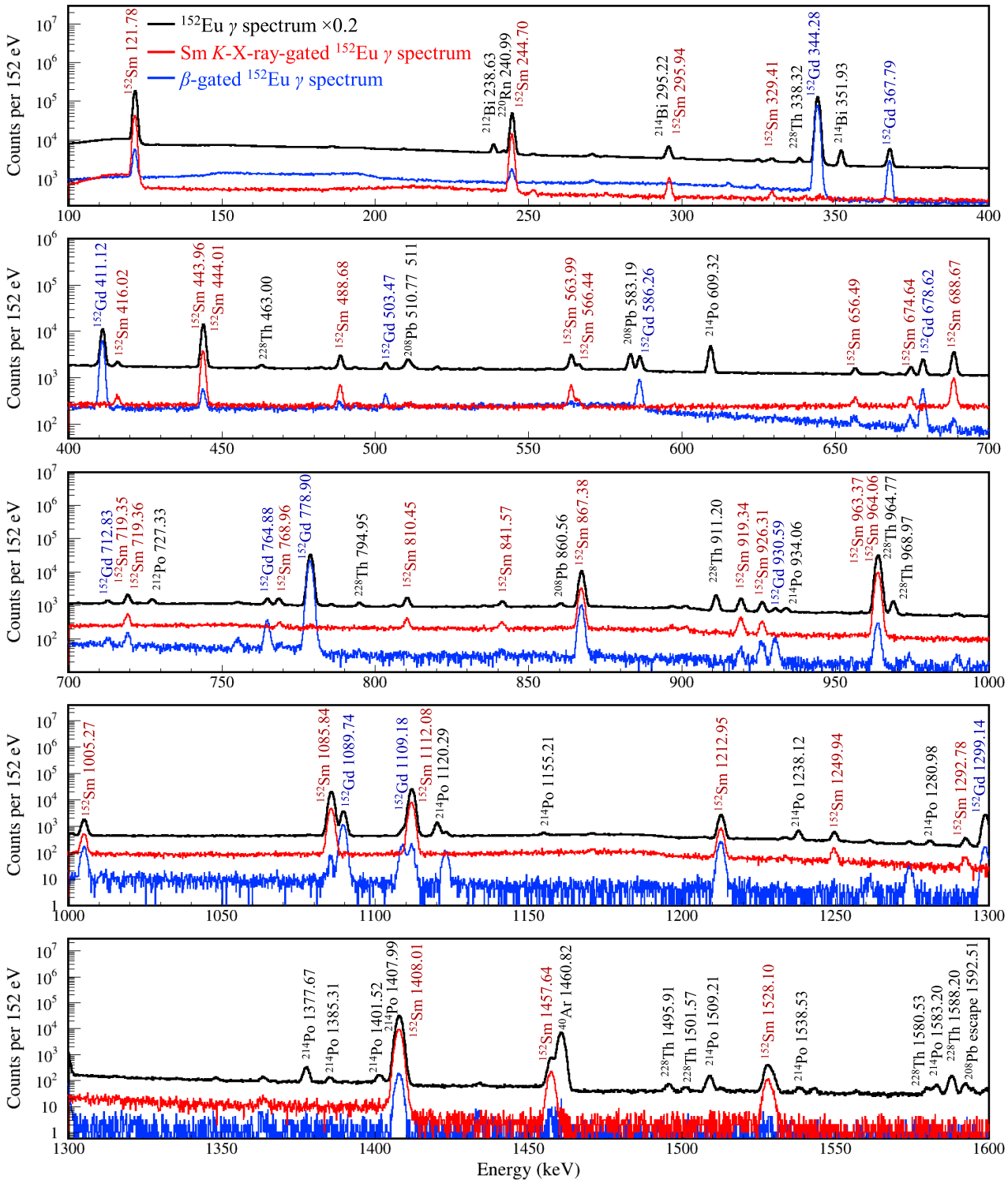

Figure 2.19 Black line represents the ungated γ spectrum of ^{152}Eu measured by the XtRa 1 detector. This spectrum has been scaled down by a factor of 5. The red spectrum is the same data as the black, but gated on coincident, characteristic X-rays from Samarium measured by the LEGe detector. The blue spectrum represents the data from the black spectrum, gated on β-particles measured by MSD026. Taken from Sun et al. [5].

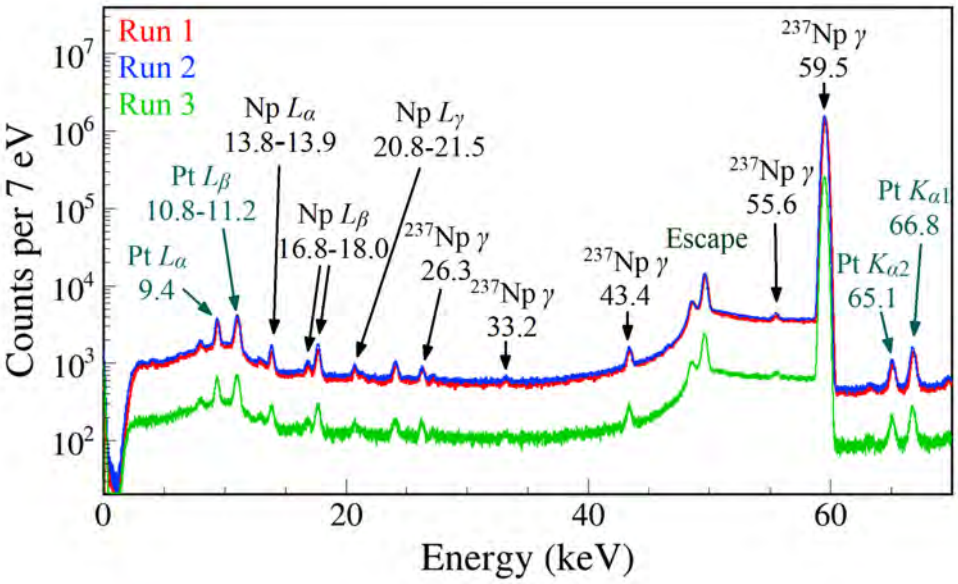

Figure 2.20 ^{241}Am X-ray and γ-ray energy spectra measured by LEGe. X-ray energy values are adopted from Ref. [118] rounded to the nearest 0.01 keV. γ-ray energy values are adopted from Ref. [119] rounded to the nearest 0.01 keV.

$$f_{\text{cascade}}(t; N_{59}, T_{59}, T_{103}, k, B) = \frac{N_{59}\ln 2}{T_{59}} \exp\left[-\frac{t\ln 2}{T_{59}}\right] + k \cdot N_{59} \cdot \frac{\ln 2}{T_{103}} \cdot \frac{\ln 2}{T_{59}} \cdot \frac{\exp\left[-\frac{t\ln 2}{T_{103}}\right] - \exp\left[-\frac{t\ln 2}{T_{59}}\right]}{\frac{\ln 2}{T_{59}} - \frac{\ln 2}{T_{103}}} + B. \tag{2.5}$$

Figure 2.22 shows the $\alpha - \gamma$ time difference distribution, plotted using timestamps from the 5486 keV α measured in the MSDs subtracted from the timestamps of the 59.5 keV γ-rays detected by LEGe. Our preliminary results for the half-life of the 59.5 keV excited state in ^{237}Np is 68.08(9) ns (MSD012) and 68.01(7) ns (MSD026). The fit was conducted using the Bayesian method with the affine invariant ensemble sampler for Markov chain Monte Carlo (MCMC) in the emcee package [120]. The MCMC was run with 100 walkers taking 10,000 steps, giving a total of 106 samples. The half-life value and its 1σ uncertainties are determined by extracting the 16th, 50th, and 84th percentile values from the marginalized posterior distribution. These results are consistent with the precision measurements of Takács et al. [121] at 67.86(9) ns and Dutsov et al. [122] at 67.60(25) ns.

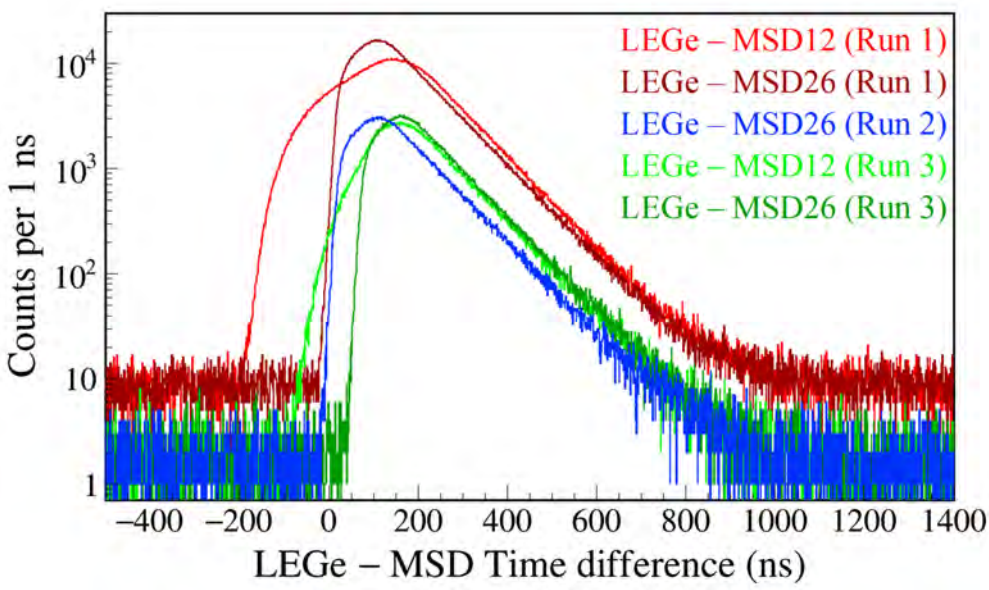

Figure 2.21 Time differences between the 59.5 keV γ-ray signals in LEGe and the 5486-keV α signals in MSD. For Run 1 and Run 3, an α gate of 5417 ± 60 keV is set on the MSD sum energy. For Run 2, an α gate of 5479 ± 20 keV is set on the energy measured by MSD026 alone.

2.6 ^{60}Ga Decay Measurement

Using PXCT with our LIBRA set up, we can measure the relevant nuclear data (lifetimes and branching ratios of excited states in ^{60}Zn, the compound nucleus of ^{59}Cu + p) to provide insight on the entrance and exit channels and constrain the reaction rates. As discussed in Section 1.2.4, the study of this compound nucleus has implications to the rp-process and light curves of XRBs.

This experiment is planned to be carried out at the Facility for Rare Isotope Beams (FRIB). Recalling Figure 2.6, FRIB will accelerate a primary beam of ^{70}Ge to 249 MeV/nucleon, and will impinge on a rotating carbon target to produce a cocktail beam. This secondary beam will be separated with the Advanced Rare Isotope Separator (ARIS), where ^{60}Ga will be selected and slowed with metal degraders and a helium gas stopper, and finally delivered to the LIBRA setup.

At FRIB's maximum primary beam power of 400 kW and under ideal conditions, we expect a ^{60}Ga beam rate of 3 $\times 10^5$ pps. Before this beam is delivered, the beam is tuned with a stable beam and delivered to our LIBRA set up in the Faraday cup configuration to minimize transmission losses (see the insets of Figure 2.5). The Faraday configuration is then swapped for the collection foil configuration, and the experiment is carried out. The collection foil must be thick enough to

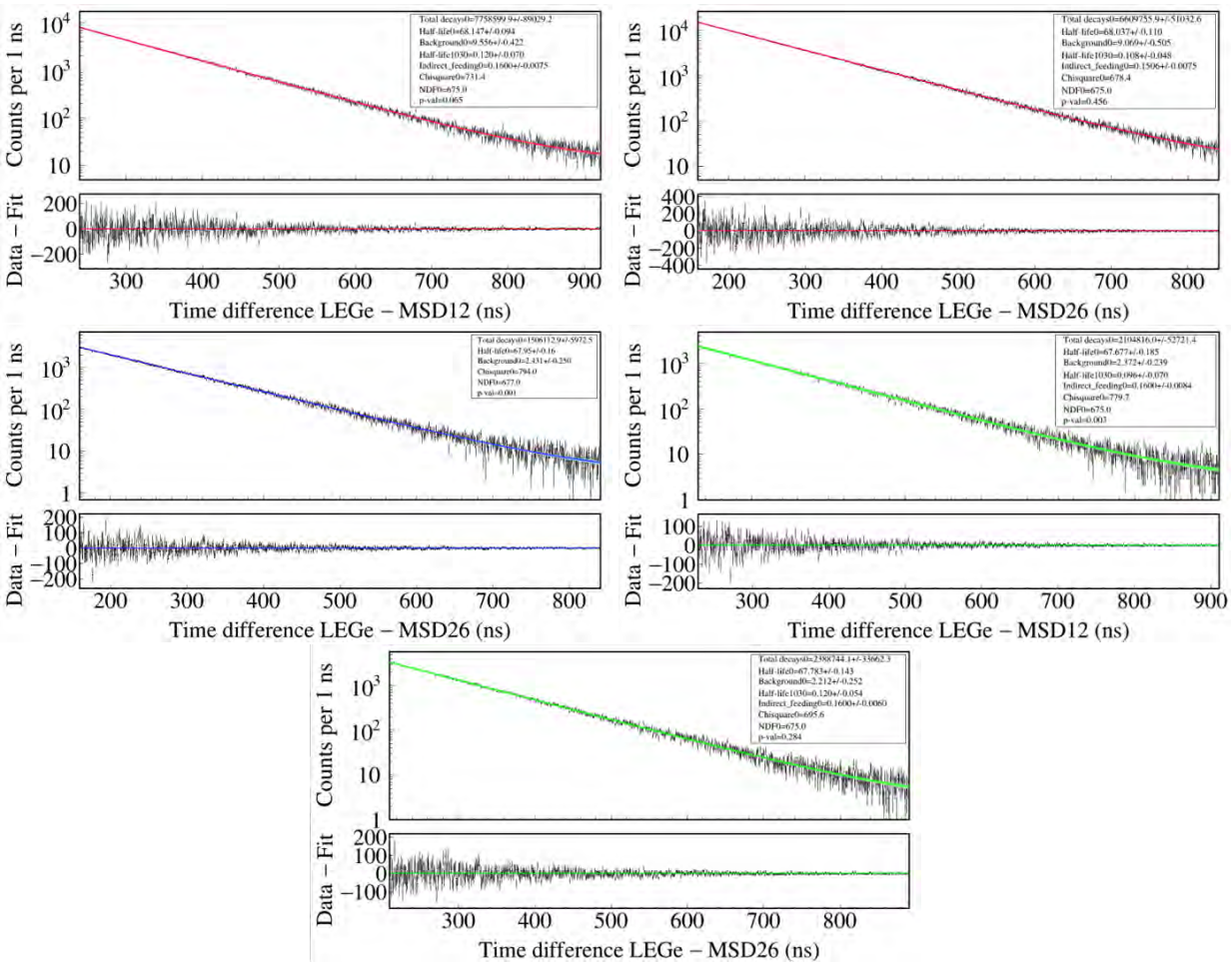

Figure 2.22 Time differences between the 59.5 keV γ-ray signals in LEGe and the 5486 keV α signals in MSD. The fit curves in red, blue, and green represent Run1, Run2, and Run3, respectively.

stop the ^{60}Ga beam, while also remaining thin enough to allow both the X-rays and charged particles from the decays to pass through the foil to our detectors. Because of this, the in-flight fragmented beam is slowed and re-accelerated with a smaller momentum spread and lower energy (10's of keV) prior to entering LIBRA. We have reached a vacuum within the LIBRA chamber of 1.47×10^{-7} torr, which is low enough to allow us to couple to the FRIB beam line.

2.6.1 Simulations

The simulations used to find the efficiency curves shown in Figure 2.12 were also used to assess the feasibility of various experiments. We have developed capabilities in GEANT4 to simulate the decay of ^{60}Ga with the associated X-rays depending on the branching path the decay takes. The result of this simulation is shown in Figure 2.23. The particle identification plot shows good sep-

aration of alpha particles and protons, and demonstrates our ability to gate on specific resonances in ^{60}Zn. Using this information, we can find the branching ratios of the proton and alpha decays to measure resonance strengths of individual resonances. Next, we can gate on the protons and look at the resulting X-ray spectrum shown in the middle panel of Figure 2.23 to employ the PXCT method. Using the ratio of these two peak amplitudes, we can find the other half of the puzzle, the lifetimes of the excited states.

$$\tau_{\text{p-emit}} = \frac{\tau_{\text{K shell(Zn)}}}{R_{\text{Cu/Zn}}} \tag{2.6}$$

where $\tau_{\text{p-emit}}$ is the lifetime of the nuclear state, $\tau_{\text{K shell(Zn)}}$ is the lifetime of the K-shell vacancy in the atom, and $R_{\text{Cu/Zn}}$ is

$$R_{\text{Cu/Zn}} = \frac{I_{K_{\alpha(\text{Cu})}} \times F \times E}{I_{K_{\alpha(\text{Zn})}}} \tag{2.7}$$

which includes the ratio of the X-ray peak intensities as well as correction factors for efficiency (E) and for the fluorescence yield of the X-rays (F). $I_{K_{\alpha(\text{Cu})}}$ and $I_{K_{\alpha(\text{Zn})}}$ are the X-ray peak intensities of the copper and zinc Kα lines, respectively. Even if the individual resonances cannot be measured, Hauser-Feshbach calculations could still be done, using a statistical average of the lifetimes and branching ratios over a range of excitation energies.

To demonstrate the general sensitivity of the setup to PXCT lifetime measurements, the bottom panel shows the Cu/Zn K$_\alpha$ X-ray count ratios as a function of proton energies, along with the corresponding lifetimes of the proton emitting states in ^{60}Zn. The integrated X-ray ratio of $R_{\text{Cu/Zn}} = 3.2(3)$ corresponds to the average lifetime for all proton emitting states in ^{60}Zn, $\tau_{\text{p-emit}} = 0.126(11)$ fs. The main source of systematic uncertainty comes from the input value of the Zn K-shell lifetime, which is taken from Campbell et al. [74]: $\Gamma_{K\text{shell}(Zn)} = 1.62$ eV with an estimated uncertainty of $5 - 25\%$. With this kind of measurement, we are able to measure lifetimes around the K-shell vacancy lifetime (for Zn this is ~0.4 fs). If the lifetime of the proton emitting state is much higher or lower than this, we would require greater statistics to measure finite value for the

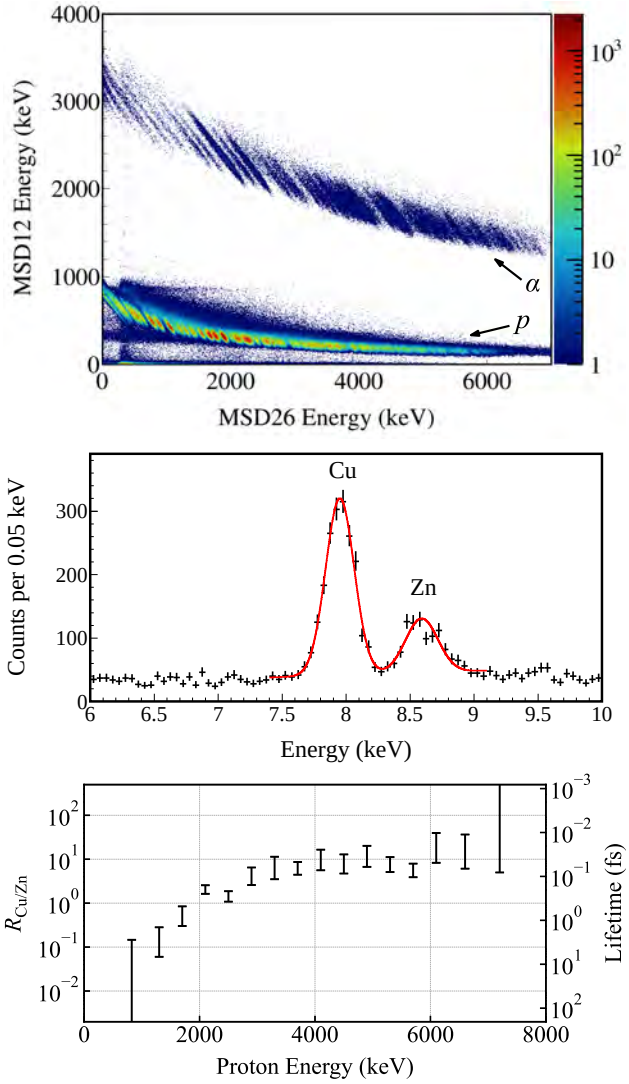

Figure 2.23 Top panel: Charged-particle ΔE–E spectrum simulated using the theoretical decay properties of ^{60}Ga together with the measured detectors' responses. Middle panel: X-ray spectrum gated on all protons in the ΔE–E spectrum, yielding a total X-ray ratio of $R_{\mathrm{Cu/Zn}} = 3.2(3)$. A double-Gaussian function with a linear background is fit on the Cu and Zn K_α peaks. Bottom panel: Cu/Zn K_α X-ray count ratio and the inferred lifetime as a function of the coincident proton energy. The error bars show statistical uncertainties, with the leftmost and rightmost points representing upper and lower limits, respectively. Taken from Sun et al. [5].

amplitudes of both of the X-ray peaks. In these cases, the lifetime can be constrained by an upper or lower limit.

CHAPTER 3

MOTIVATION FOR DOUBLE ALPHA DECAY SEARCH

This chapter discusses the history of simultaneous double decays, and the recent interest in searching for the missing $\alpha\alpha-$decay experimentally, prompted by theory papers published in the last five years that predict lower than previously thought half-lives of $\alpha\alpha-$decay in a variety of nuclei. The theories' methods of calculation were outlined in Chapter 1, Section 1.3.2.

3.1 Double Decays

After radiation was first observed by Becquerel, Rutherford quickly began working to uncover their mysteries, eventually categorizing the emanations into two different groups: $\alpha-$ and $\beta-$particles [66]. It turned out Becquerel covering the Uranium ore in paper blocked all of the $\alpha-$particles from exposing the film, ultimately revealing the radiation he observed was β particles from the decay of thorium 234. Similar work was being done by Paul Villard in 1900, when he "observed with the use of photographic methods that radium was the source of 'radiations très pénétrantes.'" Over the next decade or two, the nuclear physics community solidified their understanding of $\alpha-$, $\beta-$, and $\gamma-$rays.

In the 1980's nuclear decay channels via a double decay were being discovered. In 1980, Moe and Lowekthal observed double beta decay for the first time in ^{82}Se, which is forbidden energetically from decaying via single $\beta-$decay, but $2\beta-$decay is energetically allowed, with a Q-value of 3.0 MeV [123]. Additionally, nuclear decays with the simultaneous emission of two protons (2p) and two neutrons (2n) have been found in multiple nuclei over the past three decades, see Ref. [124]. Components of the LIBRA set up were even involved in an experiment measuring the angular correlations of 2p decay of ^{22}Al and ^{26}P to excited states in 2024 [109].

In 1987, Kramp et al. observed a two-photon nuclear decay ($\gamma\gamma-$decay) from a 0^+ to a 0^+ state in ^{16}O for the first time [125]. In 1985, as mentioned in Section 1.3.2.1 of Chapter 1, Sandulescu et al. published work discussing theoretically the possibility of nuclear decay via emission of two $\alpha-$particles. $\alpha\alpha-$decay has yet to be observed.

3.2 Previous Work on Double Alpha Decays

3.2.1 Theoretical

In recent years, there has been a large increase in the interest of theoretically quantifying predictions of this $\alpha\alpha-$decay. The techniques by which these predictions are being made are based off of models used to understand phenomena from $\alpha-$decay to fission. Observing $\alpha\alpha-$decay would constrain these models and provide information to better understand nuclear structure and dynamics at heavy masses.

In 1985, Poenaru and Ivascu used superasymmetric fission models to estimate the half-lives of spontaneous emission of two $\alpha-$particles, as well as single- and multiple-heavy ion emission [57].

3.2.1.1 First Experimental Limit and Future Experimental Prospects

In 2021, Tretyak revived an interest in the search for the $\alpha\alpha-$decay mode. Tretyak states that the energy release for $\alpha\alpha-$decay can be very large, and that if we 'suppose an exponential dependence of half-life $T_{1/2}$ on $Q_{2\alpha}$ similar to single alpha decay, this increases probability of success.' He sets an experimental limit on ^{209}Bi $\alpha\alpha-$decay of $T_{1/2} > 2.9 \times 10^{20}$ y at 90% C.L. using recent experimental data on the single alpha decay of de Marcillac et al. [126]. Tretyak also includes previous work from 2002 calculating half-lives of $\alpha\alpha-$decay using Poenaru's supersymmetric fission model [55]. He concludes by stating that 'the calculated $T_{1/2}$ values are very big, 10^{33} y or more, making prospects for future observation of such processes very pessimistic [127].'

3.2.1.2 The Microscopic Description

Despite the pessimistic outlook of these earlier estimates, Tretyak includes in a *note added in proofs* that there has recently been published a description of $\alpha\alpha-$decay in a microscopic framework based on energy density functionals, and that the results of this newly published work give 'more hopes for experimental investigation of this process.'

Indeed, Mercier et al. [128] state that instead of analyzing this decay mode through a semimicroscopic approach that treats $\alpha\alpha-$decay as a ^{8}Be-like decay mode, a fully self-consistent microscopic approach, using energy density functional theory, may be more accurate, given its successes in

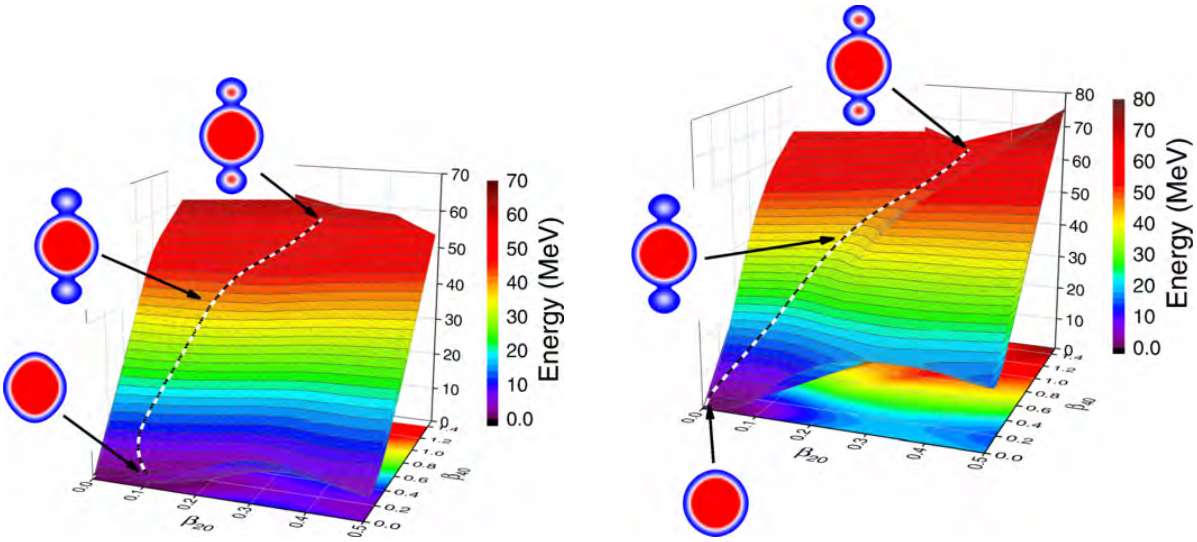

(a) ^{224}Ra (b) ^{212}Po

Figure 3.1 Deformation energy surface of ^{224}Ra calculated with the relativistic Hartree-Bogoliubov model based on the DD-PC1 functional and separable pairing interaction. The β_{20} and β_{40} axes represent the quadrupole and hexadecapole deformations, respectively. The black and white line follows the least-action path of $\alpha\alpha-$decay from equilibrium deformation to the scission point. Figures taken from Mericer et al. [128].

computing nuclear structure phenomena [129], cluster states [130, 131], spontaneous and induced fission [132–136], and single $\alpha-$decay [137–139].

This approach, as described in Section 1.3.2, minimizes the action of a deformed nucleus to calculate the path of decay the nucleus takes along a potential energy surface. They select on the emerging fragment mass equal to the mass of 2 α particles, and the results for these calculations are shown in Figure 3.1. The results for ^{224}Rn using this technique find the $\log T_{\alpha\alpha}[\mathrm{s}] = 14.24$, which is much shorter than the half-life calculated by Poenaru using the semiempirical model for cluster decay: $\log T_{\alpha\alpha}[\mathrm{s}] = 27.87$ [55]. Mercier et al. state, 'it could, therefore, be interesting to reconsider the cluster detection experiment for this nucleus, aiming to detect two α clusters in coincidence at 180°.'

Additionally, Mercier et al. include in this publication a map of the $\alpha\alpha-$decay landscape based on the Q-values of single alpha decays in the sequence and the total double alpha decay energies, which serves as an overview of nuclei worth examining theoretically and experimentally, shown in Figure 3.2. The red and blue nuclei are interesting, representing candidates where one of the alpha

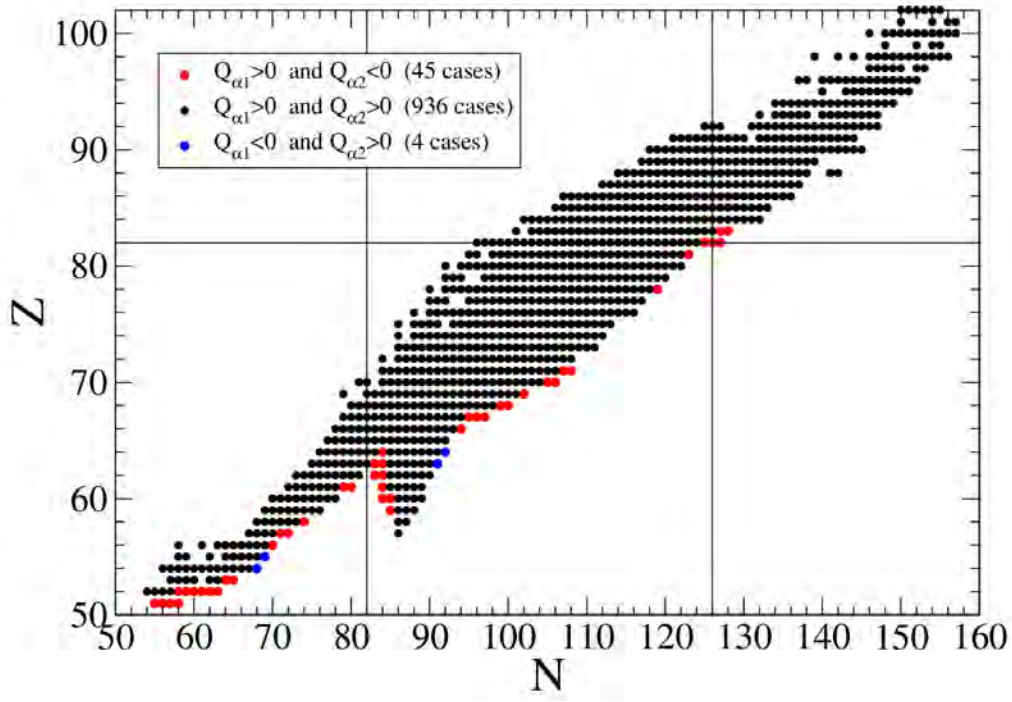

Figure 3.2 Nuclei with Z and N greater than 50, whose $Q_{\alpha\alpha} > 0$, computed from experimentally measured masses in AME 2003 [140]. The red dots represent nuclei whose second alpha decay in the sequential decay is energetically forbidden, and the blue dots represent nuclei whose first alpha decay is energetically forbidden. Figure from Mercier et al. [128].

decays in the sequence is energetically forbidden, drastically lowering one of the likely problematic backgrounds to a signal for experimental observation of double alpha decay. Of these red and blue candidates, 7 are naturally abundant, and 80 nuclei potentially unstable to $\alpha\alpha-$decay are naturally abundant (found in Tretyak [127]).

3.2.1.3 Modified Generalized Liquid Drop Model

In the same month Mercier et al. published their paper, Santhosh and Jose [62] submitted their results for calculations of the $\alpha\alpha-$decay half-lives of various isotopes. This was the first paper where the half-life of ^{220}Rn was predicted, and the results for Radon and Francium are shown in Figure 3.3. They also note that calculations assuming spherical nuclei in the parent and daughters have predicted half-lives larger than when a deformation is assumed.

Additionally, in 2023, Chandran and Santhosh [61] published another paper using the same MGLDM technique to explore $\alpha\alpha-$decay of various isotopes. They find that the half-life for $\alpha\alpha-$decay is minimum for nuclei whose daughter nucleus has a magic number of neutrons, namely

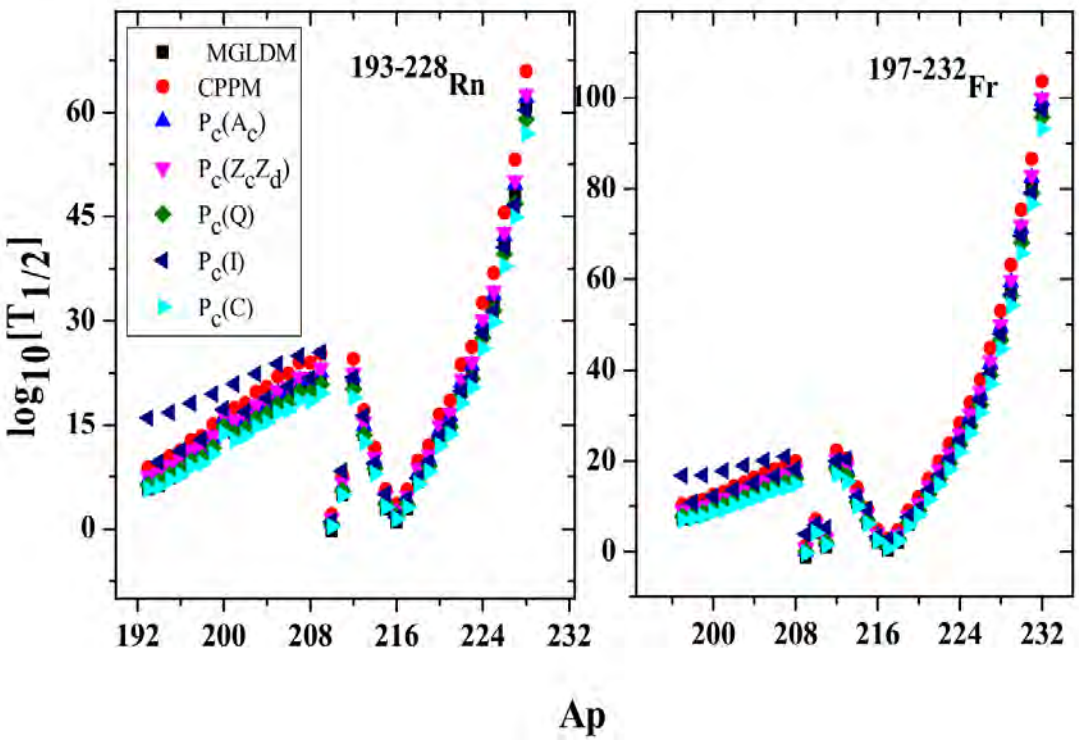

Figure 3.3 Santhosh and Jose's calculations showing the half-life vs the mass number of the parent nuclei for Radon and Francium [62].

126 and 162, and a maximum when the parent nucleus has 126 or 162 neutrons. This makes sense from the lens of nuclear structure, we assume that nuclei are most stable in configurations where the number of protons and neutrons are magic, meaning that our parent either wants to stay in this configuration, creating a long half-life, or readily emits two alphas to create a daughter nucleus whose neutrons number 126 or 162.

3.2.1.4 The Lower Limit of $\alpha\alpha-$decay Half-Life in ^{220}Rn

In 2022, Denisov extended the unified model for $\alpha-$decay and $\alpha-$capture (UMADAC) to calculate the half-lives of 32 even-even nuclei. In this case, the $\alpha\alpha$ half-life is found to be reduced greatly compared to the ^{8}Be decay channel half-life. These results are the most optimistic, predicting the half-life for $\alpha\alpha-$decay in ^{220}Rn to be 2.57×10^{4} s, and a ground-state to ground-state branching ratio of 8.51×10^{-3}. With a branching ratio of that magnitude, we expect one in every 117 ^{220}Rn decays to be a $\alpha\alpha-$decay. The calculation of the half-life here is dependent on the choice of preformation factors. Denisov also considers the shape of the parent nuclei prolate, and the shape of the

daughter nucleus spherical in this model, which means that the model expects the alpha clusters to form on opposite ends of the nucleus and travel 180° from each other.

3.2.1.5 Microscopic Calculations for ^{220}Rn

Later in 2022, Zhao et al. [141] submit a paper to Physical Review C that is the first to calculate results for the $\alpha\alpha-$decay half-life ^{220}Rn using a microscopic approach. Similar to Mericer et al., the relativistic Hartree-Bogoliubov framework is used to calculate the potential energy surface of the nucleus over various deformation parameters. They show in previous works that it is important to include at least three deformation parameters to accurately describe $\alpha-$decay. The quadrupole degree of freedom (β_{20}) describes the elongation of the nucleus, while the octupole (β_{30}) and hexadecapole (β_{40}) are higher order deformations that are responsible for forming the alpha cluster on the surface of the nucleus and forming a neck which leads to scission of the $\alpha-$particles, respectively. For double alpha decay, because of the reflection symmetry about the equatorial plane, only β_{20} and β_{40} are used, as shown for ^{220}**Ra** in Figure 3.4. [1]

Once the deformation energy surface and least-action path have been calculated, the barrier penetration probability can be found using the WKB approximation:

$$P = \frac{1}{1 + \exp[2S(L)]}. \tag{3.1}$$

This, along with the number of assaults on the potential barrier per unit time (n), calculated based on the vibrational frequency of the ground-state, gives us the half-life of $\alpha\alpha-$decay:

$$T_{1/2} = \frac{\ln 2}{nP} \tag{3.2}$$

Zhao et al. use this same approach for calculating the competing decays' (single α, ^{14}C) half-lives in this paper as well. The results of all of these calculations can be found in Figure 3.5, and a half-life for $\alpha\alpha-$decay in ^{220}Rn is reported: $\log_{10}(T_{2\alpha}[s]) = 8.04$, with a corresponding branching ratio calculated to be 4.0×10^{-7}.

[1] Gaffney et al. [142] conclude that ^{220}Rn has weaker octupole collectivity than ^{224}Ra, see Figure 4 in their paper.

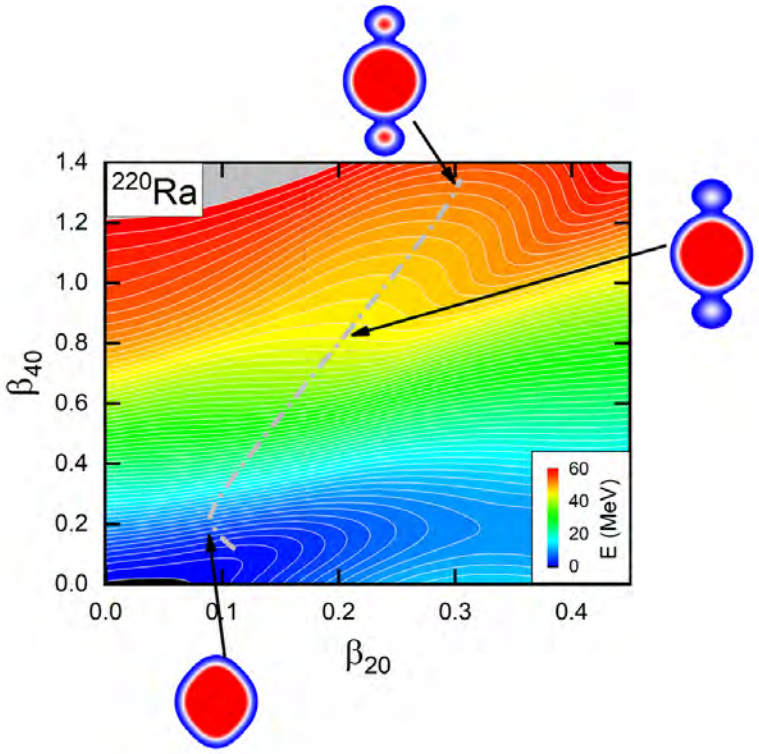

Figure 3.4 The reflection-symmetric deformation energy surface is plotted in the quadrupole-hexadecapole plane, calculated with RHB with a DD-PC1 functional. The gray curve shows the least-action path, with insets displaying the nuclear densities from equilibrium deformation to scission [141]. Figure from Zhao et al. [141].

Zhao et al. finds that the least-action paths for each of the four nuclei shown are very similar, beginning with a decrease in β_{20}, followed by a linear increase in both β_{20} and β_{40}. They also find that the least-action integrals up to the scission point are very similar, meaning the $\alpha\alpha$ decay rates are mostly determined by the $Q_{\alpha\alpha}-$value. The calculated $\alpha\alpha$ branching ratio is also calculated for each of the nuclei, ruling out only ^{212}Po, which has an unfavorably small branching ratio because of the ^{208}Pb + α configuration of the nucleus. They conclude by stating that optimal candidates for the experimental search for $\alpha\alpha-$decay would be $^{216-220}$Rn and $^{220-224}$Ra, and that additional deformation degrees of freedom, such as triaxiality, if incorporated, would decrease the predicted half-lives, so the results they obtain should be taken as an upper limit.

There has been continued theoretical exploration of this topic [143], where models are being adjusted and unified to make more accurate predictions of this two alpha decay channel. Experimental data is crucial for progress in this topic.

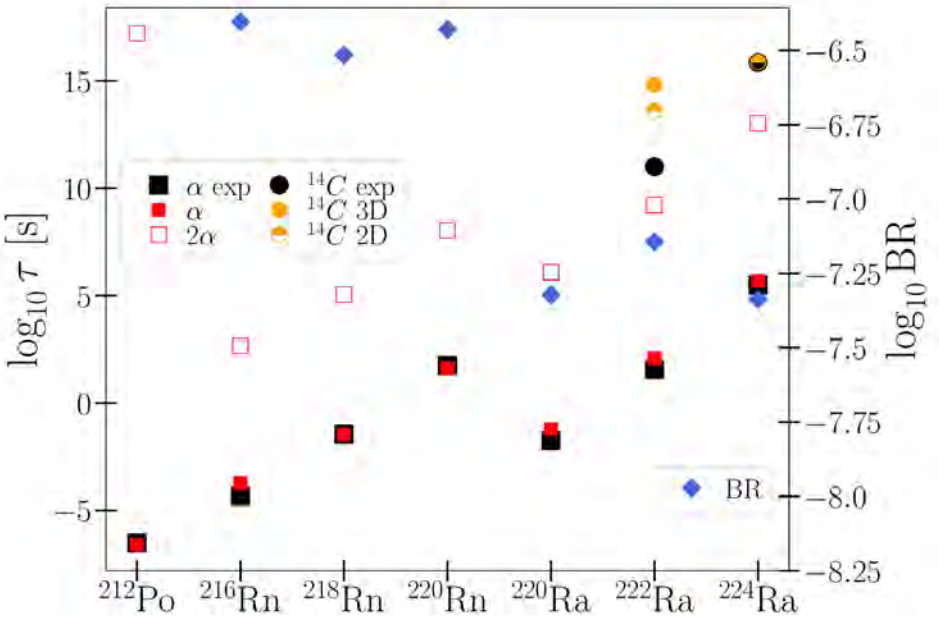

Figure 3.5 Results from Zhao et al.'s calculations of the different decay mode half-lives (and equivalent branching ratios in blue diamonds, labeled on the right y-axis) for ^{212}Po, $^{216-220}$Rn, and $^{220-224}$Ra, compared to available experimental values in black. Figure from Zhao et al. [141]

Theory	Branching Ratio	Half-Life
UMADAC [144]	8.51×10^{-3}	2.57×10^{4} s
Microscopic [141]	3.98×10^{-7}	1.1×10^{8} s
MGLDM [62]	$\sim 10^{-20}$	$\sim 5.6 \times 10^{21}$ s

Table 3.1 All published predictions of $\alpha\alpha-$decay half-life and branching ratios for ^{220}Rn.

3.2.2 Experimental

There is no published data on experimental searches for $\alpha\alpha-$decay. In Table 3.1, the theoretical predictions on the half-life and branching ratio of $\alpha\alpha-$decay for all published results on ^{220}Rn are shown. It is the goal of this thesis work to probe down to the sensitivity of the Microscopic description results, testing two of the three theory predictions' validity.

Proposals were submitted in 2021 and 2022 by Christophe Theisen and Elias Khan et al. to measure $\alpha\alpha-$decay in ^{224}Ra [145, 146]. Based on the EDF work described in the previous sections of this chapter, they propose measuring the half-life of ^{224}Ra; the predicted $\alpha\alpha$ partial half-life is 10^{14} s, using a covariant energy density functional. ISOLDE has proven able to deliver ^{224}Ra with sufficient intensity for their experiment, as that nucleus has been used to study octupole deformation

in the past [142]. They run at a reduced intensity to minimize random coincidences, and propose running for a week to collect on the order of 10^{10} decays, hoping to observe 10 double alpha decays; a rate of 5×10^4 pps is requested. The ^{224}Ra would be implanted on a thin carbon or silicon nitride foil. They will detect these alpha decays using 4 highly segmented DSSD Si semiconductor detectors from the MUSETT and MUST II collaborations. Each Si detector has 128 segments, an area of 10×10 cm^2, and a thickness of 300μm, giving a total efficiency of $\alpha\alpha$ detection of 45%. Because they are measuring a nucleus higher up the decay chain from our parent nuclei (^{220}Rn), they will receive more single alpha events as rate background (total activity is 6× the implantation rate).

This first proposal was not accepted due to concerns about contamination from single alpha events in the E_{sum} region drowning the real signal. It was reproposed in 2022, this time with a ^{222}Ra beam, after GEANT4 simulations showed that the concerns were well founded [146]. The collaboration made new calculations for ^{220}Ra and ^{222}Ra, with the same formalism used in Mercier et al. [128], and predicted branching ratios of 1.1×10^{-8} and 1.6×10^{-8}. They choose to run with ^{222}Ra because of its longer half-life and cleaner decay chain (only 3 single $\alpha-$decays in the chain until it reaches ^{210}Pb, with a half-life of 22.2 y). With a beam rate request of 2×10^4 pps, they expect to see ~85 $\alpha\alpha-$decays. They also assume perfectly equal energy sharing of the $\alpha-$particles. If this assumption holds true, they avoid being overwhelmed by single $\alpha-$decays in the chain, see Figures 2 and 4 of Ref. [146].

Members of this CERN experiment collaboration also work at GSI, using a ^{228}Th source in the FRS ion catcher. This can be used for calibration of the gas catcher, but they are also extracting any science they can out of it, similarly to the GADGET collaboration's goals. It may be possible that there are signatures of $\alpha\alpha-$decay in data they have already taken.

Additionally, the PandaX collaboration uses a ^{228}Th source to flow ^{220}Rn into the active region of their TPC, and have used this method to measure the half-life of ^{216}Po [147]. The GADGET detection system also uses this ^{220}Rn flow method to calibrate the detector prior to experiments [148].

CHAPTER 4

PREPARING TO SEARCH FOR RARE EVENTS

4.1 LIBRA Germanium Setup

The HPGe detectors from LIBRA were set up and coupled with the GADGET system in order to detect $\gamma-$rays in coincidence with $\alpha-$decays. The relative location of the "north" and "south" germanium detectors can be seen in Figure 4.1 This would allow observation of ^{220}Rn $\alpha-$decays to excited states in ^{216}Po, and decays to excited states in subsequent nuclei further down the chain.

The decay of ^{228}Th has nine known alpha decay energies [149], the decay of ^{224}Ra has five known alpha decay energies [150], and the two subsequent nuclei in the ^{228}Th decay chain (^{220}Rn and ^{216}Po) have only two known alpha decay energies, the ground state to ground state decays, and decays to the first excited states [151, 152].[1] Our detection method is suited to measure the decays of ^{220}Rn and ^{216}Po, because the parent nuclei (^{224}Ra and above) are not carried to the detector, reducing the background in the measurement.

4.1.1 Coupling to GADGET Triggers

Since the GET system is specialized for high data throughput for use with TPCs [153], an additional DAQ system was run alongside the GET DAQ for collecting $\alpha - \gamma$ coincidence data, with optimized energy resolution for $\gamma-$rays. The DAQ of choice is the XIA Pixie-16L, with a bit

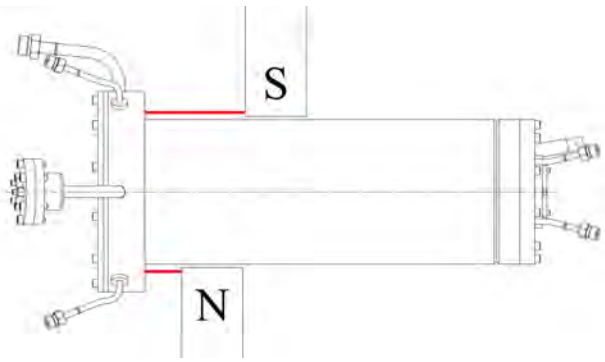

Figure 4.1 Schematic of the top-down view of the TPC, with the LIBRA germanium detectors flanking the chamber. The red lines indicate the distance from the lip of the chamber to the edge of the germaniums, which was 11.4 cm for the south detector and 4.2 cm for the north.

[1]For the previous four Nuclear Data Sheet references, also see the references within to find the papers whose data was used in the compilation of these mass chain evaluations.

Parameter	GADGET Mesh	GADGET Trigger	North Ge	South Ge
Trigger T_{Rise} (μs)	0.040	0.504	0.064	0.064
Trigger T_{Gap} (μs)	0.976	0.504	0.952	0.952
Threshold (ADC units)	6553	520	300	700
Energy T_{Rise} (μs)	7.040	0.256	10.240	10.752
Energy T_{Gap} (μs)	2.048	0.348	1.792	1.280
CFD Delay (μs)	0.0304	N/A	0.304	0.304
CFD Scale	7	N/A	7	7
CFD Threshold (ADC units)	6000	N/A	300	700
Tau (μs)	50	0.05	50	50

Table 4.1 DDAS trapezoidal filter and timing parameter settings for each input in the double alpha search experiment. Note that the GADGET trigger is a TTL logic signal, and thus uses leading edge timing rather than CFD timing.

resolution of 16 and a digitization frequency of 250 MHz. This is plugged into the XIA Pixie-16 crate for power and data routing, along with a NI PXI-8336, which allows one to interface with the data via an optical fiber connection to a PC. This PC runs DDAS and FRIBDAQ to configure the DAQ and write the data to disk, see Ref. [154]

4.1.2 Digital Data Acquisition Settings

The Pixie-16 modules are configured via the file, 'cfgPixie16.txt'. This provides information on the type of physical DAQ system being used, i.e. one crate, one module, and the slot number that the module is plugged into. From here, the qtscope program can be run to determine the optimal parameters of the energy and timing filters for each channel's signal, see Table 4.1.

Once these values are dialed in for both the energy and timing, they can be loaded in to the readout shell to be used during data acquisition.

The two most important pieces of information to recover from the waveform data are the energy (maximum amplitude) and arrival time of the pulse. To consistently find the energy of the pulse, a trapezoidal filter is applied to the waveform as it is read from the ring buffer. This allows for a longer max point of the pulse, and an easier way to read off the highest ADC amplitude, thus more consistently measuring the energy of the trace. For timing, typically constant fraction discrimination (CFD) is used. In this method, the waveform is split into two, where one is attenuated to a fraction of the original. The other is delayed and inverted, so that when they are added together, the

zero-crossing point is used as the calculated time stamp of the trace. This is intended to prevent a time walk that occurs due to a dependence on a signal's amplitude that would have occurred simply using a leading edge trigger.

4.2 TPC

Time projection chambers are radiation detectors whose operating principle is based on radiation's interaction with gaseous, or liquid, matter. A TPC is composed of a few core components, the drift region, the amplification region, and the readout. As charged-particle radiation passes through the gas within the drift region of the chamber, it ionizes the gas. The drift region has an electric field applied to it, in order to drift the free electrons to one end of the detector. Once these electrons reach the end of the detector, the amplification region multiplies the free electrons through an avalanche process in a proportional way, using an even larger electric field. This amplified signal ends up at the cap of the TPC, where the readout collects the charge pad-by-pad and sends that full trace data to be stored. Because the end cap contains many pads, the event's x- and y-position information is stored in the data. Additionally, the z-position can be recovered via the timing information from the traces, allowing for full three dimensional reconstruction of each radiation event's track of energy deposition.

Time projection chambers require careful design and precise manufacturing techniques to create a uniform electric field in both the drift and amplification region. High density electronics are also required for charge collection on these millimeter-scale pads. Additionally, since each trace of each pad is saved for every event, the amount of data collected by a TPC can be staggeringly large. For example, without complicated trigger logic, ALICE at CERN would produce $\sim$ 3.5 TB **per second** of raw data [155], which is not only difficult to store, but even to move and process in real time. Because of these difficulties, TPCs are a more recent detector technology in low energy nuclear physics, and can be utilized in interesting ways to do novel research. See Refs. [153, 156–159] and references therein.

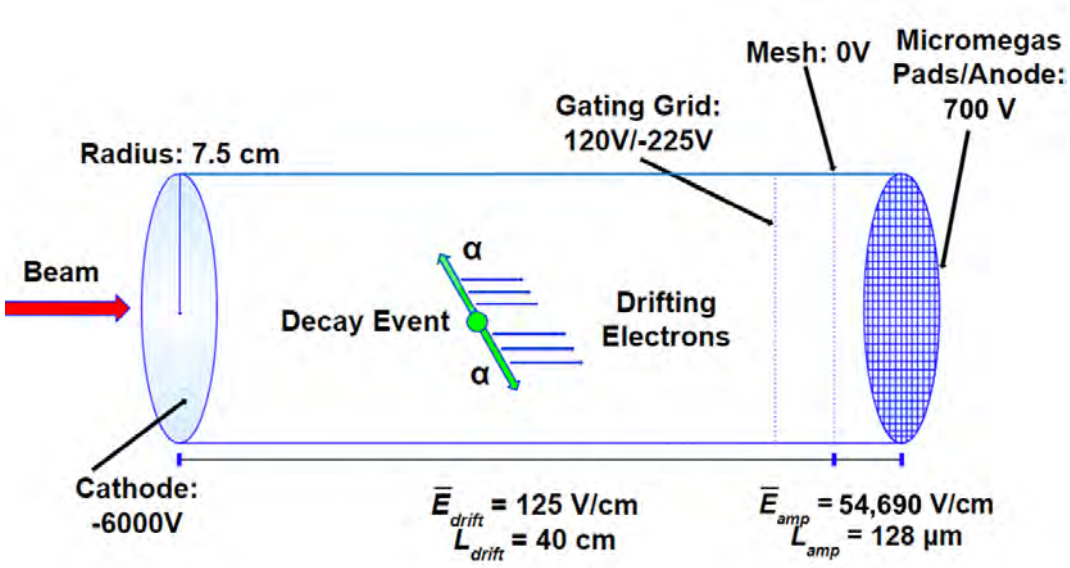

Figure 4.2 Cartoon schematic of the GADGET II TPC with a $\alpha\alpha-$decay event.

4.2.1 GADGET II TPC

In the GADGET II TPC, resistive micromegas are employed for the amplification region of the TPC, and the GET electronics are utilized for the front end readout and data processing.

Resistive micromegas are designed to act as a two dimensional RC network, spreading out the charge deposited and inducing signals on adjacent pads. The idea of the resistive micromegas is twofold: one, it suppresses sparks from the detector and prevents damage of the readout plane, and two, the spread of the charge is intended to increase the resolution of the track with respect to the pitch; GADGET II's micromegas are designed to not spread out the tracks. Additionally with resistive micromegas, the mesh is set to ground while the anode is at a high positive voltage. The insulation of the pads and electronics, provided by the resistive anode, allows for the removal of the previous generation readouts' anti-spark protection circuitry. [160]

GADGET also employs the General Electronics for TPCs (GET) for data acquisition of the 1020 channels and traces processed for every event. It is described in more detail in Section 4.3.1, along with its configuration for the $\alpha\alpha-$decay search.

The gas handling system (GHS) for GADGET regulates the gas pressure and flow rate through the chamber and is shown in Appendix A.4.2. A bottle of P10 (or another gas of choice) is connected

to valve 1a or 1b via a regulator, and opened to flow no more than 40 psi of gas to the MKS mass flow controller. This controller monitors the gas pressure downstream, and adjusts the pressure to meet a desired flow rate through the detector. The detector requires consistent replenishment of the operating gas due to build up of impurities over time during radiation detection experiments. The pressure of the system is also monitored by three independent gauges to ensure the operating pressure of the GHS and detector are as one expects.

The method by which ^{220}Rn is delivered to the chamber is highly reminiscent of Rutherford's set up discussed in Section 2.1. Shown in Figure 4.3, the ^{228}Th source is placed on the end of a rod and inserted into the gas handling system (GHS) of GADGET II. Because radon is a noble gas, once ^{228}Th and its daughter ^{224}Ra have both alpha decayed, the radon will occasionally leave the source and mix into the gas, which is subsequently pumped into the chamber, where the radon undergoes decay [148]. Valve 3 was closed and valves 6 and 7 were opened, allowing for the gas to carry radon into the chamber for measurement. Once the ^{220}Rn reaches the chamber, it decays via a chain shown in Figure 4.4

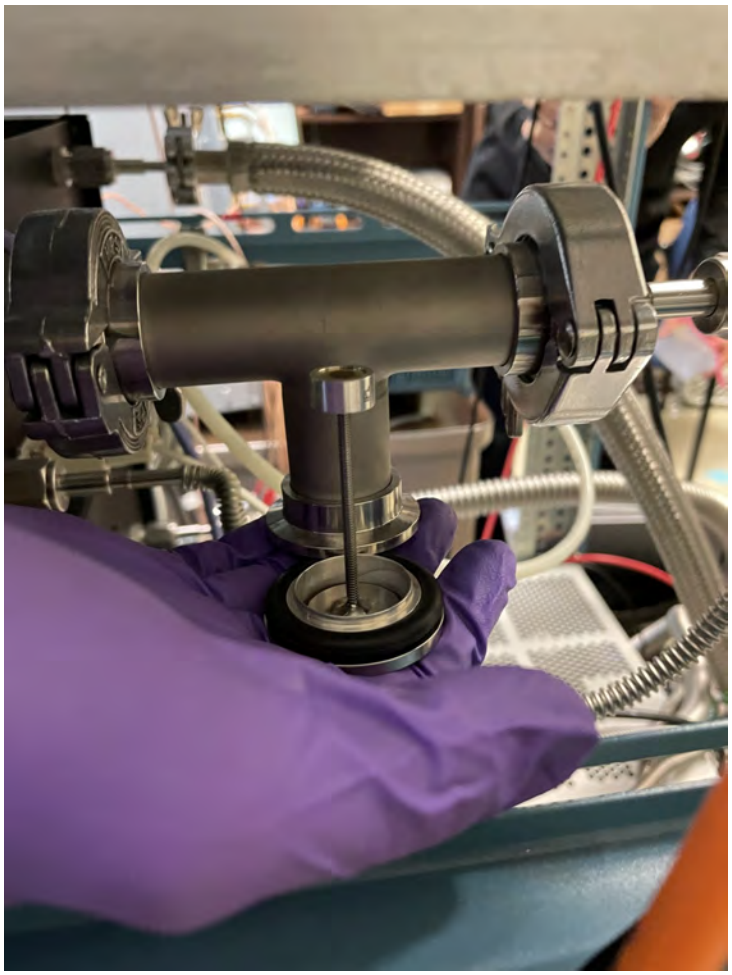

Figure 4.3 ^{228}Th Source location in the GADGET II gas handling system.

4.2.2 Modifying the Detector to Work at Higher Pressures

GADGET was originally designed to operate near atmospheric pressures and, as such, operators did not have to worry substantially about high differential pressures on the chamber.[2] However, due to the nature of the double-alpha search, increasing the gas pressure substantially increases the detection efficiency because the higher pressure shortens the particle tracks, making them less likely to escape the detection region. This is especially true if they occur back-to-back, as some theories predict. From Figure 4.5, one can see a simulation of how the alpha tracks shorten at a higher pressure.

In order to achieve this increase in efficiency, modifications were made to ensure safe operation

[2] See Section 5.1.3 for more information on where this assumption brings trouble.

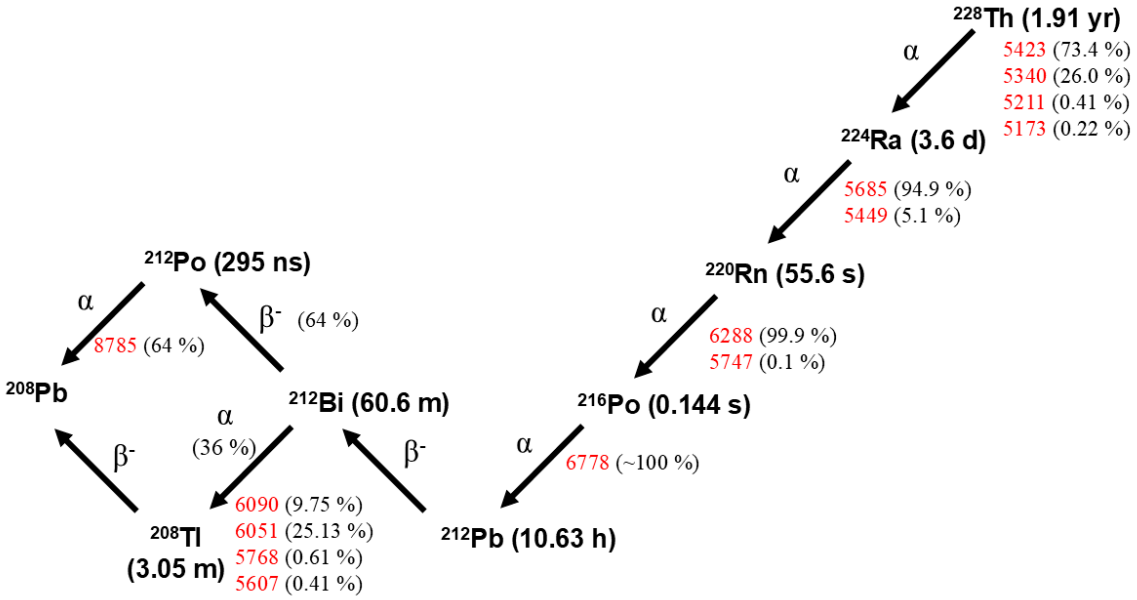

Figure 4.4 ^{228}Th decay chain to the stable isotope ^{208}Pb. Numbers in red are the alpha particle energies in keV. Only ^{220}Rn can make it into the chamber in theory, so the TPC only observes decays below radon.

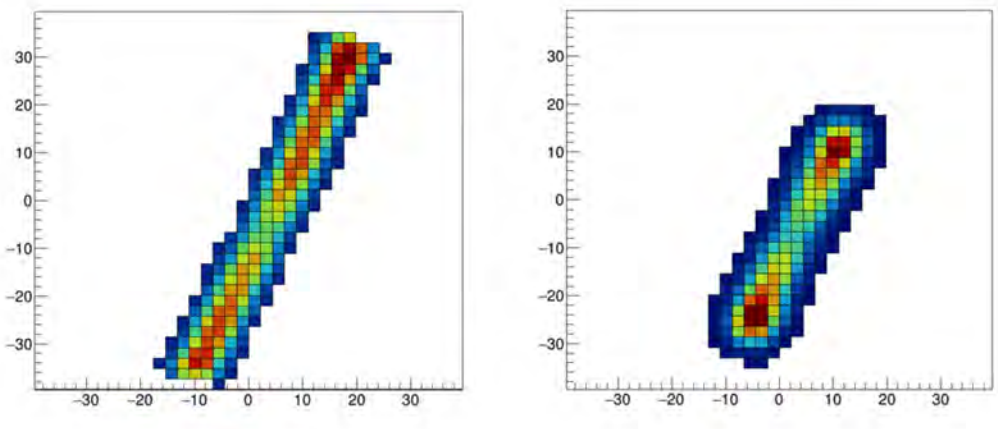

Figure 4.5 ATTPCROOT simulation of a double alpha track in gas at 800 torr and 2000 torr, respectively.

GADGET II TPC Properties	
No. of Pads	1020
No. of Veto Pads	8
Measurement Pad Size	2.2×2.2 mm^2
Pad Plane Area	50.24 cm^2
Total Veto Pad Area	28.26 cm^2
Length of Drift Region	400 mm
Gating Grid Parameters	
No. of Gold-Plated Copper Wires	60
Wire Diameter	20 μ m
Wire Separation	2 mm
GET Parameters	
Sampling Rate	50 MHz
Signal Shaping Time	117 ns
GET Gain	1 pC
Gas Amplifier Parameters	
Gas Composition	P10 (90% Ar + 10% CH_4)
Gas Pressure	2000 torr
Gas Gain	40 for ^{220}Rn $\alpha-$particles
Drift Field	150 V/cm
Amplification Field	54.7 kV/cm
Drift Velocity	3.9 cm/μs
Temperature	20 $^\circ$ C
MICROMEGAS Parameters	
Resistance	10 MΩ/square
Capacitance (calculated)	287 nF
Mesh - Anode Separation	128 μm

Table 4.2 Operating Parameters for the GADGET II TPC during the double alpha search [110]. Note the gating grid was always set to a transparent voltage.

at higher pressures. First, the chamber itself was reinforced via a metal plate over the micromegas board to prevent the readout plane from bowing at high pressure. Additionally, the kapton window at the cathode end of the chamber (opposite the readout plane) was replaced with an aluminum cover to prevent flexing or breakage of the window while the TPC operated at differential pressures near 2 atm. See Figures 4.6 and 4.7 for the results of these upgrades.

In addition to these chamber upgrades, a high accuracy, 60 psi pressure transducer was added to the diagnostic box of the GHS to ensure proper pressure readings at pressures above 1,500 torr. Finally, a fine adjustment valve (valve 11 in Figure A.2) was added to the system to allow for small changes in gas flow, especially at higher pressures, allowing gas flow to be set easily, and also to

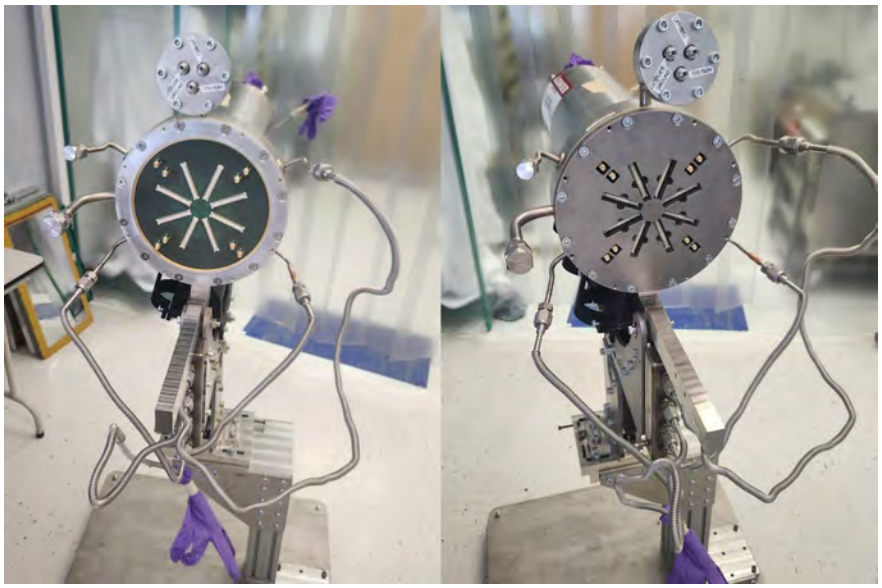

Figure 4.6 Metal plate reinforcement of the micromegas board for safe operation at higher pressures.

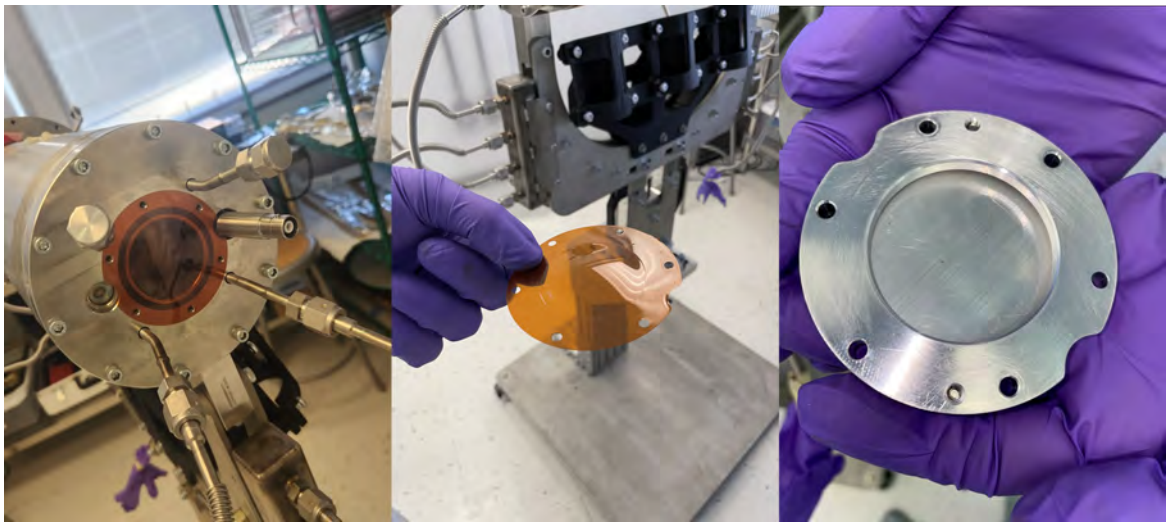

Figure 4.7 Replacing the kapton window with an aluminum window to be used during the $\alpha\alpha-$decay search. This entrance window is where a beam would enter the detector during a beamline decay experiment. For future experiments, the new metal window can be left on, or replaced with kapton again, depending on the experiment's needs. Notice that the kapton shows signs of minor wear and flexing due to pumping the detector to vacuum and back to atmosphere many times over years. That being said, it remains durable and may be reused if necessary.

giving the ability to close gas flow and restart gas flow at the same rate without having to carefully open the rough adjust valve 5.

Optimizing settings for the TPC operating at 2000 torr requires a few pieces of detailed background on TPCs which will now be discussed. The drift voltage remains at 6 kV for the double alpha experiment. The amplification region must be set at a different voltage for the electric field to produce adequate multiplication of electrons [161]. The gain in an amplification region for a TPC can be found from the following equation

$$G = \frac{n}{n_0} = e^{\alpha x}, \tag{4.1}$$

where x is the distance traveled in the amplification region, n_0 and n are the number of electrons before and after amplification, and α is called the 'Townsend coefficient'. This Townsend coefficient is a function of many parameters, such as gas composition, pressure, and the nature of the electric field. Sharma and Sauli measured this coefficient for many different configurations of a parallel plate chamber, where α was derived from the Townsend relation:

$$\alpha/p = A \exp(-Bp/E) \tag{4.2}$$

in which the parameters A and B are derived from a fit to data.

Using data from table 1 in their paper [161], a configuration of Argon-Methane (83.4%-16.6%) is chosen, which gives $A = 2.7$ cm^{-1} torr^{-1}, $B = 81.7$ cm^{-1} torr^{-1}, and for this case let's assume E/p of $\frac{700\ V}{128\ \mu m}$/2000 torr = 27.3 V/cm/torr. Plugging all of this in results in a gain of 32.6. This is extrapolating to lower E/p, and in reality the experiment uses a mixture of gas that includes a higher percentage of Argon. In the case that Argon is 90% the fraction of the active gas, the A and B parameters would be higher and lower, respectively.

4.3 Calibration

Once the hardware changes were made to the TPC, the system still required testing and calibration to properly operate at a higher gas pressure. The operating pressure was slowly raised from ~800 torr to 2,000 torr, while the micromegas voltage was adjusted, as well as the calibration file parameters for the CoBos, described in the following subsection.

Pressure on MKS (torr)	Micromegas Voltage Range
866	300 - 400
1157	400 - 515
1255	526 - 580
1351	580
1447	580
1544	580 - 600
1623	600 - 630
1721	630 - 640
1854	640 - 760

Table 4.3 The range of volatges tested on the Micromegas as the pressure of the gas was increased in the TPC. The flow rate was adjusted throughout the tests, as well as values in the GET software. The gas pressure shown here is what was read out by the MKS flow controller, but the DATAQ pressure transducer, which is believed to be more accurate in this range of pressures, read about 150 torr grater than the MKS throughout the experiment and test runs.

The voltage was slowly increased at each 100 torr increment so that the signal amplitude remained the same throughout the tests, and the runs taken during this time ensured there was no sparking occurring in the detector and that the alpha particle traces were clearly being recorded by the GET DAQ. Table 4.3 shows the voltage ranges tested as the pressure was increased.

4.3.1 GET Data Acquisition and its Configuration for the Double Alpha Search

The GET DAQ consists of four ASIC and ADC (AsAd[3]) boards connected via T-ZAP boards to the micromegas readout plane. The T-ZAP boards are merely four layer PCBs custom designed to route the data from each pad to the AsAd front end. Each AsAd board contains four AGET chips which contains a charge sensitive preamplifier, an analog shaper, and a switched capacitor array structure that allows for storage to a circular buffer of 512 samples[4]. The AGET chips also have the ability to set threshold and trigger logic, and this can be done in a limited capacity channel-by-channel, for each of the 64+4 channels[5] a single AGET chip is responsible for. The signal stored on the AGET chip and the sample rate is determined by the write clock frequency, up to 200 MHz. Once it meets the trigger logic requirements, it is extracted at the read clock frequency of 25 MHz.

[3]Where ASIC and ADC stand for Application Specific Integrated Circuit and Analog to Digital Converter

[4]The SCA modes can be adjusted to have 256 or 128 cells as well, and doing so can improve dead time in experiments with a high data rate and improve the overall throughput in the electronics.

[5]64 readout channels and 4 fixed-pattern noise (FPN) channels. These FPN channels are placed on each edge of the chip and are intended help with background subtraction of the trace.

For the $\alpha\alpha-$decay search experiment, the write clock was set to 50 MHz so that each of the 512 time bins were 20 ns apart for a total trace window of 10.24 μs. The signal is extracted with a 4-channel 12-bit ADC onboard the AsAd, and the AsAd FPGA is used to synchronize the sampling of the ADCs with the readout of the SCA [153]. The information is then sent to modules installed in a MicroTCA where event information can be used to decide if the trigger requirements are met.

The concentration board (CoBo) is a module developed for the GET DAQ. It can be connected via VHDCI to up to four AsAd boards, meaning that GADGET can run in a single CoBo configuration. It is the CoBo's function to take the data given to it via the AsAds and send it to the MuTanT module where the trigger decision is made. It also sends the data via the MicroTCA backplane to the computers which store the accepted events in the form of .graw files. In addition to this 'data path' the CoBos are also responsible for the 'control path', which accepts the configuration files sent to it via ethernet and configures the CoBos, as well as transmitting the parameters to the AsAds. The live time of the detector is typically bottle-necked at the CoBos [110, 153], and therefore 4 CoBos are typically employed for high-rate experiments. In the case of the $\alpha\alpha-$decay search, the experiment was run at rates no greater than 70 events per second, so 2 CoBos is more than enough to maintain effectively 100% live time. Finally, the Multiplicity, Trigger and Time (MuTanT) is a module that generates and distributes the master clock signal to the rest of the GET DAQ (CoBos and AsAds). It can also, in principle, provide a three-level trigger system. Along with the internal trigger logic configured via files sent to the CoBos, the MuTanT module also offers 7 external LEMO connector, NIM logic signals. Three serve as external trigger request, optional trigger inhibit, and optional multi-purpose input. Two are outputs and send a fast trigger accept signal and the system dead time. And the last two are programmable logical inspections. The trigger logic for GADGET is configured to only accept triggers whose mesh signal is above a certain threshold, and utilizes the system dead time output to ensure the system is not busy processing a previous event before it accepts the signal and begins piping the event through the GET DAQ.

4.3.2 Calibration Runs Before, During, and After the Experiment

For all calibration runs, the same procedure for flowing ^{220}Rn into the chamber was used, although the flow rates were typically around $\sim$ 100 sccm. This alpha data was used to test GADGET II at higher pressures, where the gain was adjusted, via both the micromegas voltage as well as the gain parameter in GET. Additional parameters that were varied during calibration for higher pressure operation include and were ultimately set at:[6]

- Gain - 1 pC
- Gate Delay - 2.5 μs
- Write Clock Frequency - 50 MHz
- Peaking Time - 117 ns
- LSB Threshold - 12
- GSB Threshold (called Global Threshold in the config file) - 0
- isAllChannelRead - False

Once the GET DAQ was set properly for the $\alpha\alpha-$decay search, the two HPGe detectors from LIBRA were placed on either side of the GADGET TPC for measurement of the $\gamma-$rays.

In order to correlate the $\gamma-$rays to an $\alpha-$decay event, the voltage induced on the mesh of the Micromegas is sent from the GADGET TPC micromegas to one XIA channel, along with a logic signal that tells whether or not the GET DAQ accepted the event. This way, the correlation data is entirely contained in the .evt files produced by the XIA DAQ. The parameters of the XIA DAQ were tuned using ^{220}Rn calibration runs taken before the experiment for the GADGET Mesh and GADGET Trigger Logic channels, and the HPGe channels were calibrated with a ^{152}Eu source. The ^{152}Eu source was placed at 5 different locations along the outside of the GADGET chamber. The resulting parameters of these calibration runs are shown in Table 4.1.

[6]Calibration file is available upon request. It cannot be read by default by a standard word processor. VS Code seems to work well enough to view the ranges and selections of all parameters, but it is better to view and edit it with the executable found on the GADGET mac mini called cconfiged (in ~/Documents/GET-software/bin/cconfiged).

Background runs were taken prior to the experiment, with no gas flow and the ^{228}Th source installed in the GHS, as well as a run where the ^{228}Th source was moved to the room next door and placed in the source locker there. They were also taken partially through the experiment after a significant amount of grow in of the daughter nuclei had occurred (runs 0070-0072, 0109-0125). At the end of the experiment, the ^{152}Eu source calibration runs were performed in the same manner as at the start of the experiment, together with the background runs for the GADGET TPC. Lead bricks were added to block $\gamma-$rays from the ^{228}Th source from run 0344 on, although this did not seem to make a clear improvement on the background of the $\gamma-$spectra, likely because the vast majority of the background comes from decay of radioactive nuclei inherent to the materials in the room, such as uranium and thorium and their decay chains and ^{40}K.

CHAPTER 5

EXPERIMENTAL DATA AND ANALYSIS

5.1 Data Processing

This section describes the process of converting the data written to disk by the DAQs to formats that are used in analysis.

5.1.1 Gamma Data

The gamma data is stored directly after being written to disk as .evt binary files. The ddasdumper provided by FRIB converts these .evt files to .root files that can be analyzed using CERN's ROOT software package[1]. The .evt files have a size limit of 2 GB, so once the .root files are created, the sub-runs are merged to create a single .root file for each run[2]. Finally, an optional script can be run to format the tree within the .root files and run an energy calibration based on ^{152}Eu test runs. These calibrated .root files are sorted in a way to quickly access energy histograms of each channel recorded in the run, and the tree contains event-by-event branches for each channel recorded by the XIA DAQ. Without this last step, the .root files produced by the ddasdumper are not intuitive to navigate and can complicate further analysis.

5.1.2 TPC Data

Once the GET data is collected, written to disk, and the run is ended, the .graw files from each mac mini are merged into one HDF5 (.h5) file. Much like the .evt files for XIA, the .graw files are limited to 2 GB per file. The merger stitches these sub-runs together along with combining data from each AsAd via the channel mapping provided to the merger. The .graw and .h5 files are then transferred via a .tcl script to fishtank, FRIB's general analysis and data storage computer.[3] The resulting .h5 files are formatted in the following way:

[1]The .evt files and .root files can be found on fishtank, in the directories `/mnt/daqtesting/protondetector/stagearea/experiment/` and `/mnt/daqtesting/protondetector/stagearea/`, respectively

[2]This uses the 'merge.sh' script found in the directory `/user/protondetector/readout/rootfile/`

[3]They can be found in the directory '/mnt/daqtesting/protondet2024'. Only some of the .graw files have been uploaded to fishtank due to storage contraints. All of the .graw files have been offloaded to external hard drives and are available upon request from Chris Wrede.

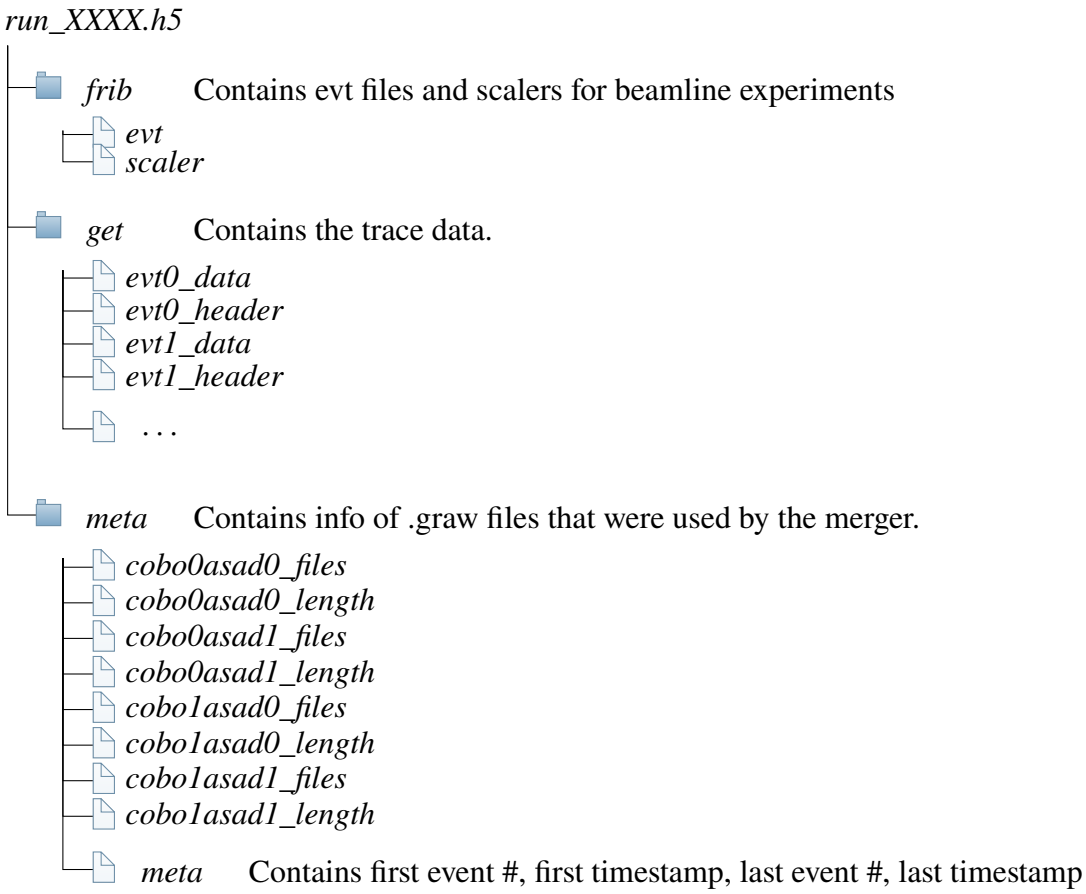

The event data are arrays with shape (n,517), where the first 5 bins are the CoBo, AsAd, AGET, channel, and pad numbers. n is the number of pads that fired. The header files in the get directory contain the event number, the MuTanT timestamp, and an external timestamp for data synchronization. An example trace is plotted in Figure 5.1, where the Bragg peak is clearly visible, and the remaining charge deposited outside of the readout plane is captured by the 764 veto pad.

Notice in this raw trace all channels 'float' above zero. This is normal, but to extract accurate energy from the integrated charge on the pads, a baseline correction must be applied to each trace before calculating the energy. For processing the runs in the $\alpha\alpha-$decay search, a fixed window baseline subtraction was used, averaging the last 100 bins in the trace and subtracting that value from every time bin, pad-by-pad. To further remove noisy parts of the trace that are not part of the actual event, the trace is zeroed outside of a window 100 time bins wide, centered on the maximum value in each pad's trace, see Figure 5.2. Additionally, outlier removal was applied, where the

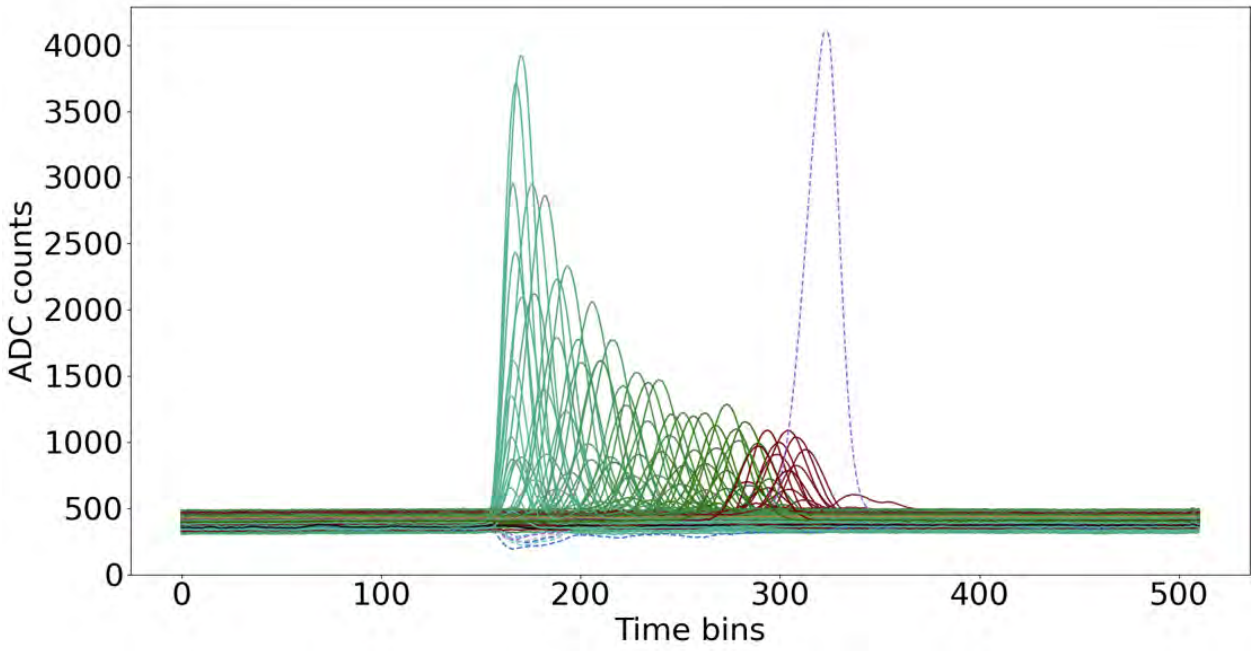

Figure 5.1 Trace data from an event in GADGET, operating at 2,000 torr. Dashed lines represent veto pad data. The ADC in the AsAds is 12-bit.

largest grouping of pixels was kept, and all pixels that fired and were not 2-connected to that group were removed from further data processing. Further analysis is done to extract the total integrated charge in ADC counts, a rough length of the track, the timestamps, the angle of the track with respect to the center z-axis (beam line axis), the maximum charge deposited on a veto pad, and the number of pads whose value reached or exceeded the maximum ADC value.

In order to calculate the length of the track, the Δt of the track must be converted to a distance. The z-scale parameter converts the time dimension along the beam axis into a spatial dimension, so the 3D tracks can be accurately recreated and information like the length of each event can be extracted. The number chosen depends on the drift velocity of the electrons, see Figure 5.3. The relationship between E/p and v is non-monotonic. When operating at a pressure of 800 torr for experiment 21072, a z-scale of 1.45 seemed to be the most accurate. In order to find which z-scale is best for each detector set up, the calculated ranges for a given z-scale are plotted against the angle from the z-axis. If the z-scale is wrong, event lengths near 90°, which do not heavily rely on a correct z-scale to find ranges, will be different from the events near 0°. So, the same run

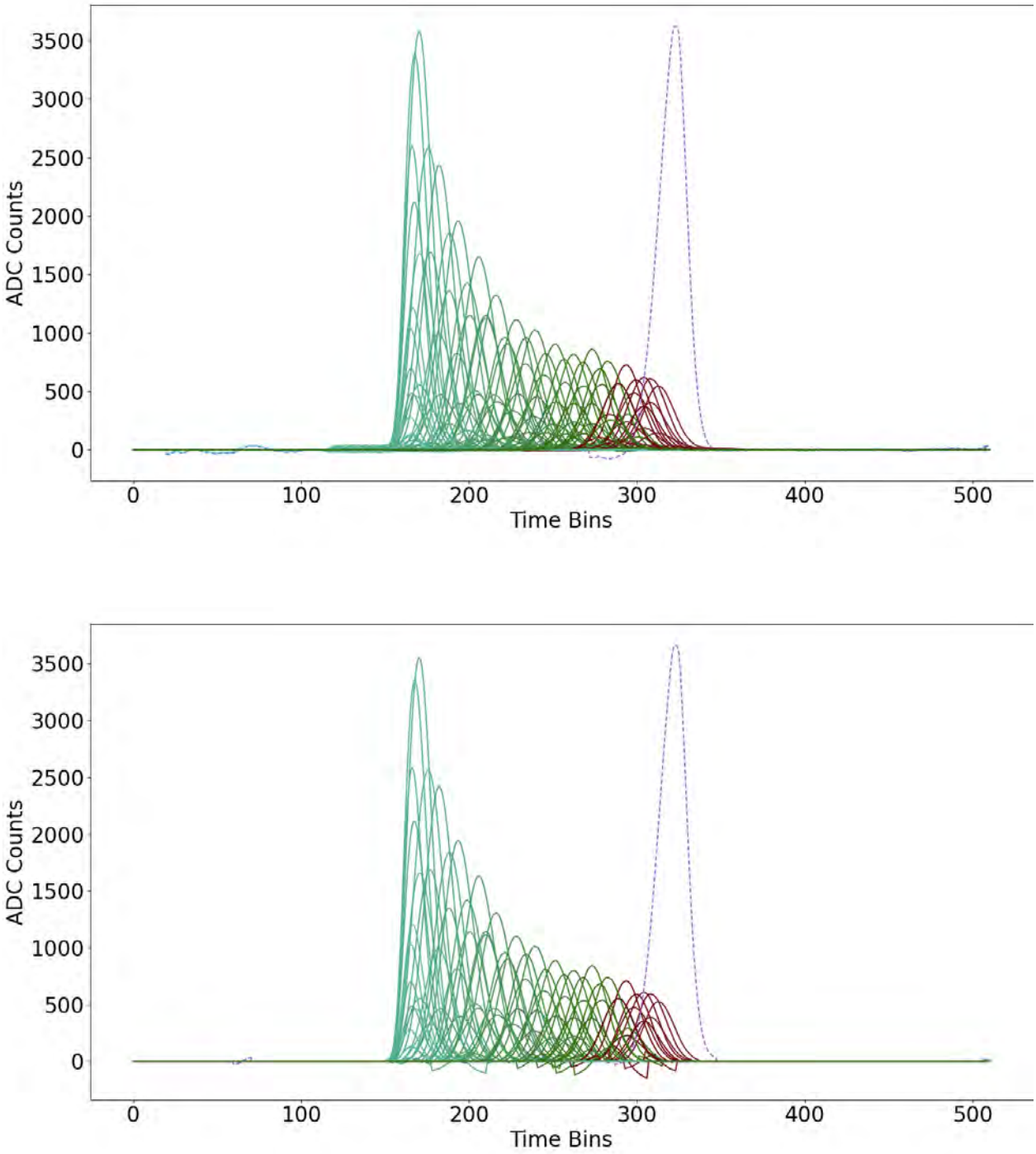

Figure 5.2 Processed trace data of the same event shown in Figure 5.1. The top image shows the background subtraction used in the double alpha search. The bottom image shows the example of a different approach to finding the peaks to keep in the background subtraction, rather than using a fixed window around the time bins nearest to the maximum value in each pad trace.

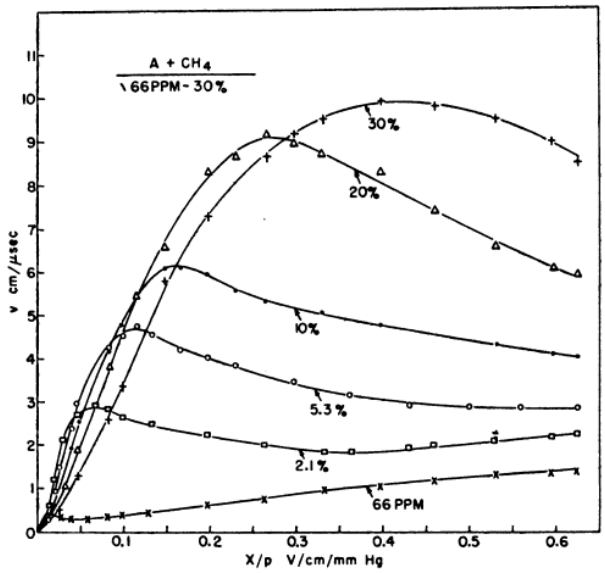

Figure 5.3 Drift Velocity of Electrons in P10 gas. Data from English and Hanna 1953 [162]

is processed with different z-scales, and a value is chosen at which the ranges of each event are independent of their angle emitted. Of course, there are a few other things that affect the length calculation, such as difference in diffusion in the x-y plane versus the diffusion along the z-axis, but this ensures the z-scale setting is not so far off as to be unphysical. This value is compared to literature drift velocities to make sure it is consistent. Once the pertinent data is extracted from the traces via the process described in Section 5.1.2, cuts can be made on the total data set to begin an in-depth search for the $\alpha\alpha-$decay candidates. From this processed information, plots can also be produced that provide information on the total number of ^{220}Rn nuclei that decayed in the detector over the course of the experiment, providing the denominator for the branching ratio calculation.

5.1.3 Pad Gain Matching

There are cases when a researcher with a TPC will pulse the MM to look for deviations in gain pad-by-pad. The pad gain one finds with this method is not the same gain a pad has due to an electron avalanche during a real event (see Giovinazzo et al. [163]). Previous attempts by the GADGET group to measure the gain on a pad-by-pad basis via pulsing the mesh resulted in a map of the routing of the pads to the AGETs, reflecting the difference in pad-mesh capacitance between pads.

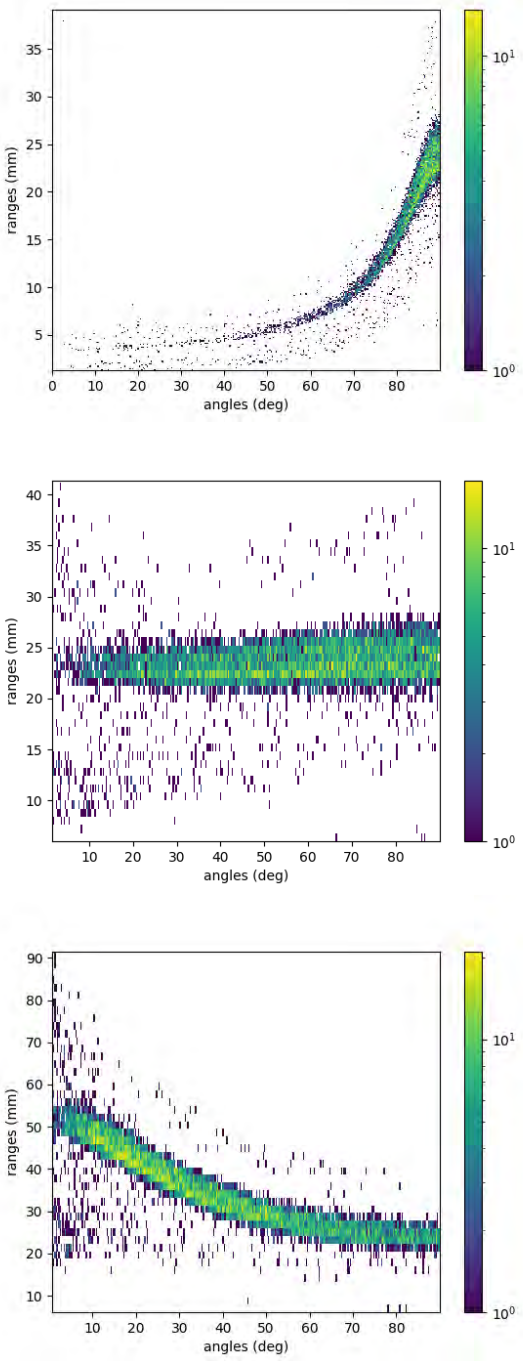

Figure 5.4 Plots of calculated ranges versus angles for three different z-scale parameter inputs. First the z-scale is set to a too low 0.1, then it is set to 0.65, and finally set to 1.45. Since this data comes from run 342 during the double alpha search, the chamber was operating at 2000 torr, and a z-scale of 0.65 looks to be about right, where the range of the event is not dependent on the angle of the track.

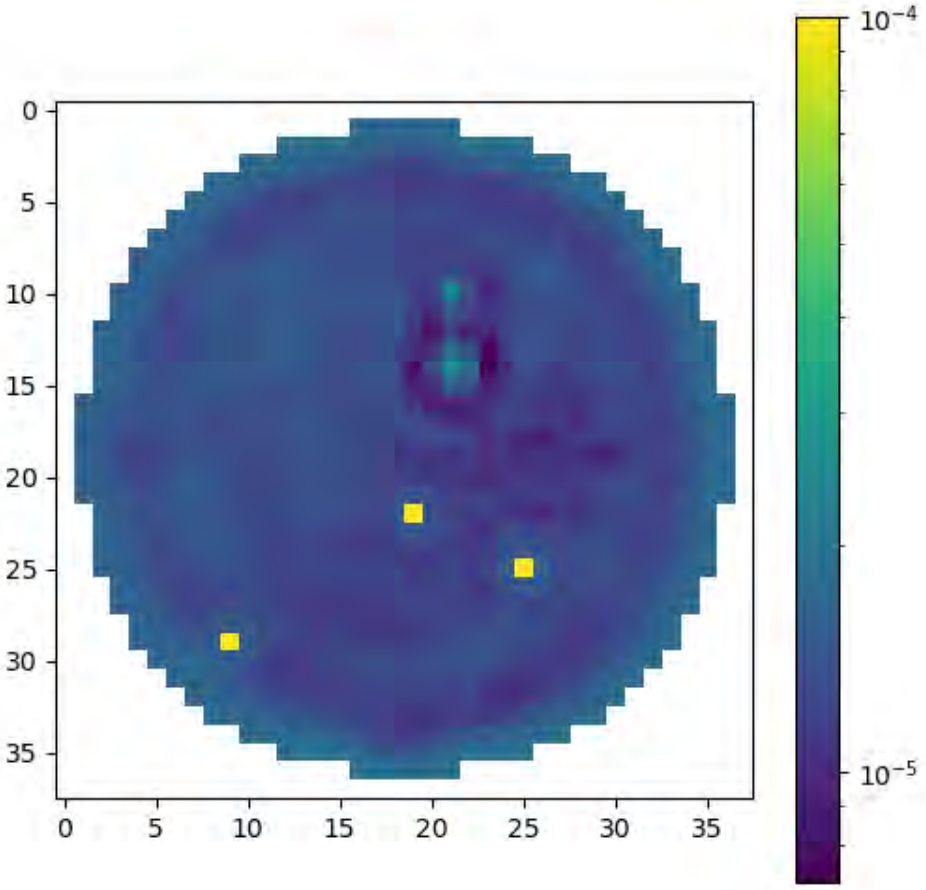

Figure 5.5 Result of measuring gain via minimization method described in the text. Each pixel represents a pad in the pad plane. The color indicates the conversion from ADC counts to energy in MeV. This uses 100,000 events from the ^{212}Po peak.

For this thesis experiment, the author developed a new method of gain matching GADGET II TPC data using the data collected, fit on alpha particles of known energies and origins. The procedure begins with a cut on a 2D histogram of events whose energies are known. This data is read in and converted to a format that allows for GPU-accelerated analysis. The goal is to find the gain factors of each individual pad such that the total measured energy in the event is as close to the true, known energy over all of the selected events. In this case, 100,000 events are used, but less data can be used to achieve similar improvements in energy resolution. The objective function of the minimizer computes the sum of squared differences between the total reconstructed energy per event and the true energy. Given that each event covers roughly 50 pads, and GADGET has a total of 1000 measurement pads, the large number of events used in the analysis allow the code to constrain the per pad gains well. The result of pad gain matching for the double alpha experiment is shown in Figure 5.5. The three outlier pads are either very noisy/dead pads or swapped positions in the pad mapping. They do not affect the overall energy resolution by more than a half a percent, so they were left as is.

The results of this pad gain matching seems to attempt to correct for two features in the data simultaneously, the deviations in the pad gains as well as energy lost from thresholding effects in each event. The optimizer is able to encode corrections to both of these effects in the PGM map, allowing for a lower FWHM for all events,from about 18% energy resolution down to $\sim$ 4%. For example, if this procedure is run on the 1.6 MeV protons in the data collected from e21072[4], the corrected range versus energy plot shows the other proton clusters not used in the fit have better energy resolution. Furthermore, the alpha clusters also receive a sizable reduction in energy FWHM, even though they are a different particle at different energies! This technique has been improved upon and used extensively in GADGET analysis performed for more recent experiments.

Note also the deviations in the pad gain around the rim of the pad plane. It is possible that this comes from flexing of the micromegas board prior to its reinforcement when the chamber was pumped to vacuum in order to swap gases or remove air contaminants. This would explain why,

[4]This was an approved FRIB beam experiment run in 2022, looking for β-delayed proton-alpha decays in ^{20}Mg.

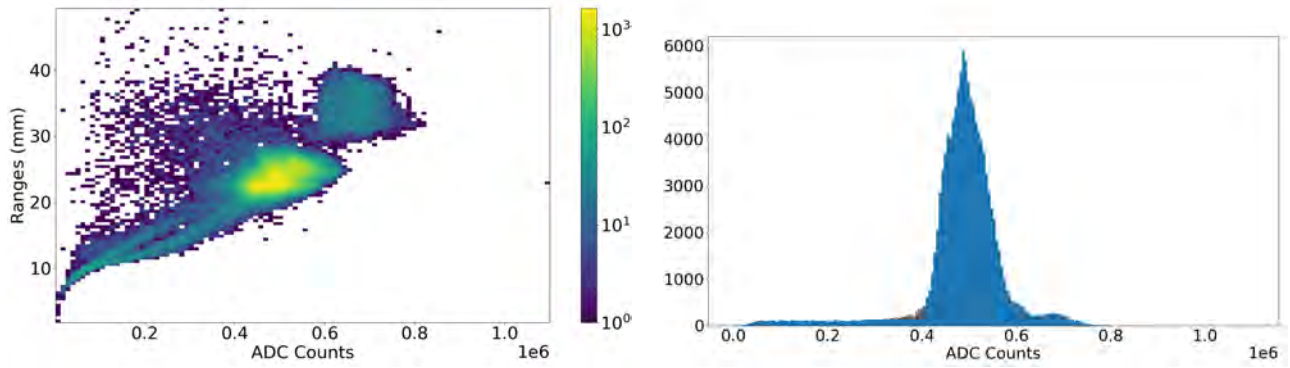

(a) Range vs. Energy

(b) Energy Histogram

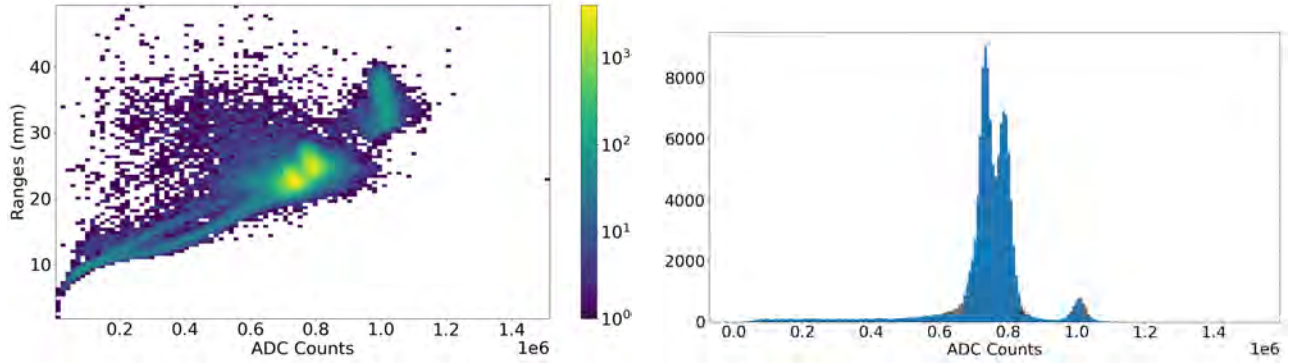

(c) Range vs. Energy Pad Gain Matched

(d) Energy Histogram Pad Gain Matched

Figure 5.6 Effect of pad gain match correction on a single run in the double alpha search data. Because of the large size of the full dataset, this pad-by-pad gain matching procedure was not applied to the entire dataset due to time and computing resource constraints.

when GADGET was first built, the energy resolution was near 5%, and after multiple cycles of pumping the detector, the pad gains deviated such that the energy resolution degraded without a pad gain match correction. Correcting for this effect restores the energy resolution to the original level, and along with other data processing advancements allows for improvement upon the 5% energy resolution cited in Ref. [110].

5.2 Energy Spectrum

As mentioned in previous sections, typically energy of particles is important to measure for nuclear physics experiments for many reasons, and as such nearly all detection set ups have the ability to record this information event-by-event. GADGET and LIBRA are no exceptions, so by the total charge liberated by the radiation (charged particles or photons), this information is derived.

One unique aspect of a TPC is that the energy information can be extracted in more than one way, using the integrated charge deposited on the readout plane, or the length of the track! Because the gas composition and pressure are closely regulated, one can accurately predict the energy of the track using stopping power data to find the projected range of the particles measured in the TPC, and convert that to an energy. For example, the ^{220}Rn alpha particles are expected to have a range of 21.8 mm in the TPC data of this experiment. Plotting this range information against the energy data the TPC collects yields range versus energy plots, shown in Figures 5.6,and 5.7. These graphs contain a few key features which correspond to the ^{220}Rn decay chain shown in Figure 4.4. The first are the two most prominent groupings of individual alpha particles. The higher range group is the 8.78 MeV $\alpha-$particle from ^{212}Po. The grouping below that contains three main energies of $\alpha-$particles, 6.05 MeV, 6.29 MeV, and 6.78 MeV from ^{212}Bi, ^{220}Rn, and ^{216}Po, respectively. The different $\alpha-$particle energies are easier to see in Figure 5.6.

The prominent tails of the α groups that end at (0,0) on the plot come from the wall effect. This occurs when there is a partial deposition of energy outside of the active volume. In other words, the start or end of an event is not captured entirely on the pad plane. The magnitude of the wall effect is reduced by implementing strict veto conditions to remove partial energy deposition events that occur laterally, however, the veto condition does not prevent events that deposit a percentage of their energy on the inactive surface of the cathode or anode of the detector from being vetoed, as can be seen in Figure 5.9. The pad-by-pad gain matching is not done for the entire dataset due to the limited time and computer resources available for the project. The initial processing of the data took months and heavily taxed the computers used during that time.

5.2.1 Alpha Energies

Because of the nature of the experiment, where data was taken over a long period of time, it is informative to examine the stability over time of the TPC. As seen from Figure 5.7, the TPC remains mostly stable in ADC gain. To examine this more closely, a cut was placed on the 8.785 MeV α from ^{212}Po for each run, and the length and energy were extracted. Figure 5.8 shows the results of this process. It is not clear what causes the increase in range over the first few dozen runs, but it

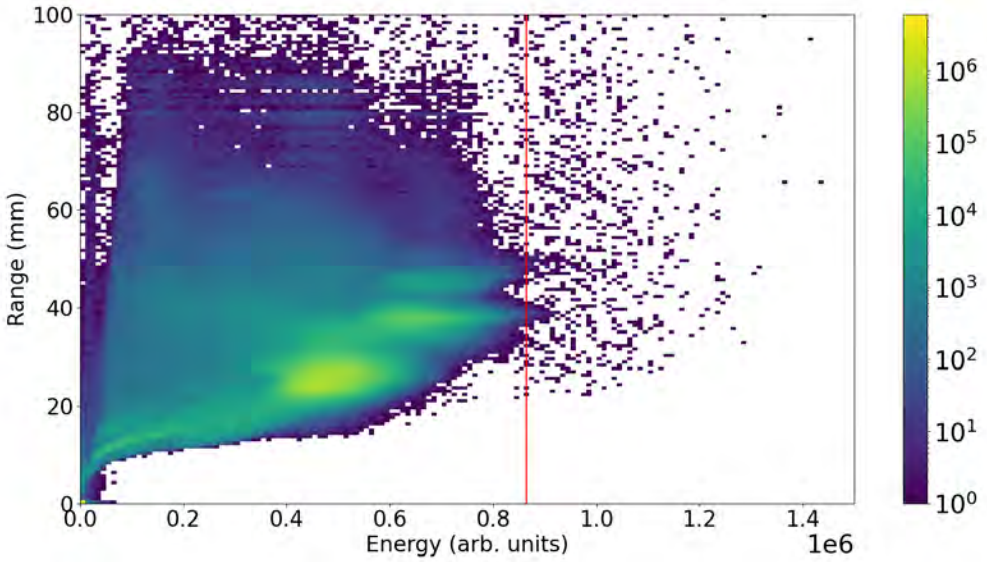

(a) With no gain matching

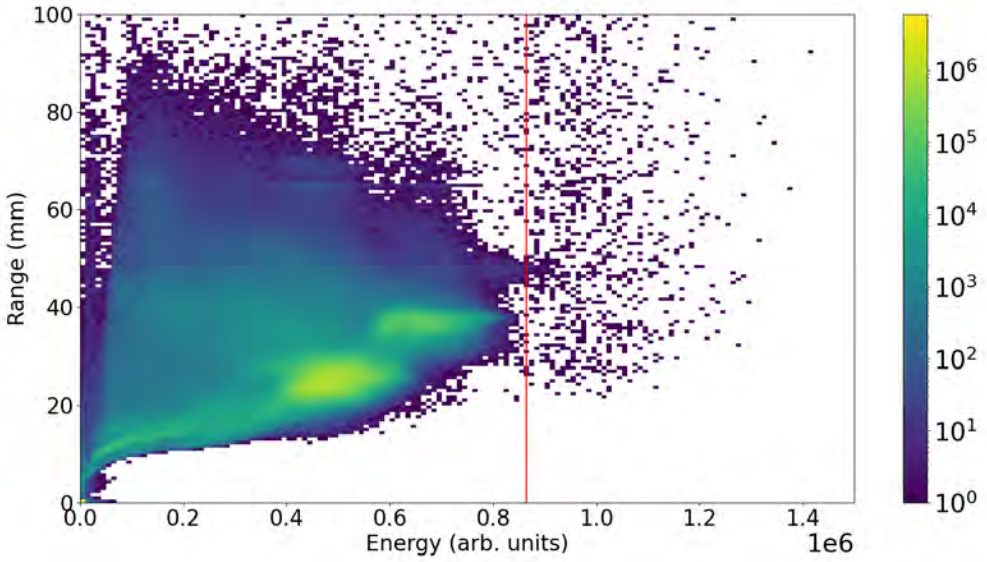

(b) Run-by-run gain matching

Figure 5.7 Range versus energy plot for all runs in the double alpha search. In panel (a) there was no attempt to center peak means run-by-run on a common value. In panel (b), the runs were aligned in range and counts by gating on and fitting the 8.78 MeV alpha peak, and adjusting the centroid to match a constant value before combining the runs. Since the gain drifts slightly on the pads throughout the experiment, the horizontal widths of the clusters in (a) are wider than in the matched version, (b).

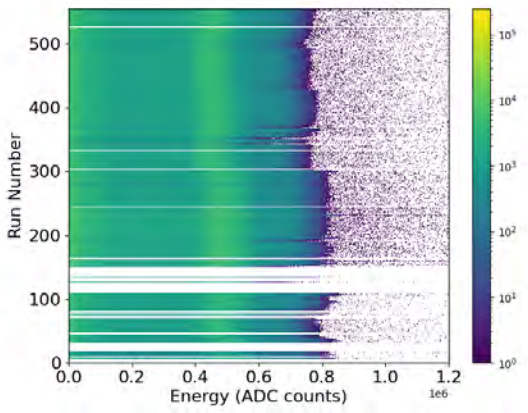

(a) Run Number versus Energy Histogram

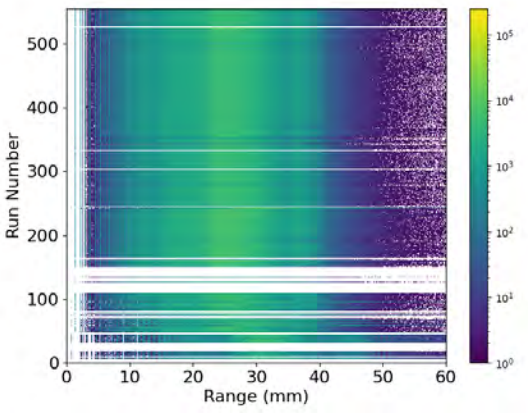

(b) Run Number versus Range Histogram

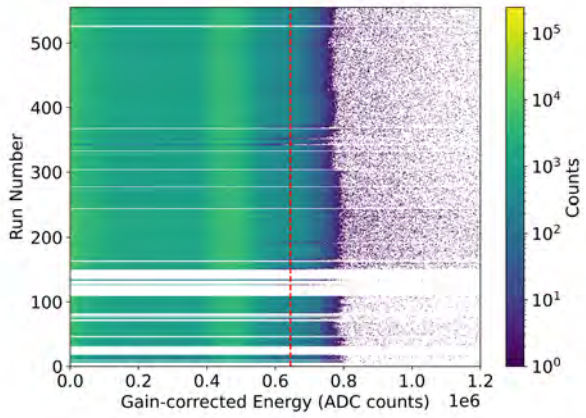

(c) Gain Matched Energy Result

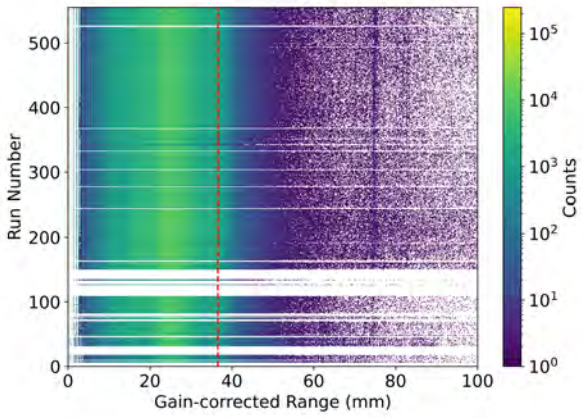

(d) Gain Matched Range Result

Figure 5.8 The top figures show the changes in the range and energy run-over-run, respectively. These runs occurred over the course of 6 months, from May to November 2024. The bottom figures correct for gain and range drift over that time. The red lines show the Po-212 reference peak used for gain matching. Panel (a) shows shifts in gain at run numbers that line up with P10 bottle changes, e.g. around run 300.

remains stable after the fact, and this can be corrected run-by-run. The only difference between the early and later runs is the flow rate of the gas through the chamber, which was increased from ~250 sccm (runs 1 to 106) to ~500 sccm (runs 126 to 555).

Similarly, the mean ADC counts of the ^{212}Po peak varies a bit throughout the runs. In this case, there seems to be a correlation between the swapping of the P10 bottles and the gain of the following runs.

However, correcting for drift in both ADC counts and range over time (run-by-run) results in a slight narrowing of the peaks, which can be seen by comparing plots in Figure 5.7.

These 2D range versus energy and 1D energy spectra for the alpha particles were used to determine how many ^{220}Rn nuclei decayed in the GADGET TPC during the experiment (denominator of the $\alpha\alpha$-decay branching ratio) and used to search for double alpha decay candidate events (numerator). The total number of ^{220}Rn decays were determined by a comparison to simulations, described in the following section. In order to narrow the search for potential $\alpha\alpha$-decays, a cut was placed at a summed ADC signal of 865,000 counts above the background which should correspond to an energy of $\sim$ 11 MeV, and events above this gate were categorized and fitted. Because of the large energy resolution of the TPC, it is likely that the single alpha events we see in this high energy cut are from the decay of ^{212}Po.

5.2.2 Simulated Alpha Data

The decay chain of ^{220}Rn was simulated using ATTPCROOTv2, and data from NNDC on the energies and branching ratios of the decays. Using this method meant that it was possible to fit the simulated data, and compare ratios of single alpha peaks to estimate the total number of ^{220}Rn nuclei decayed in our detector.

Initially a uniform distribution of all radiation sources in the detector was assumed for the simulation, which produced peaks whose relative intensities were much different than the data. However, using data from the experiment, the rough distribution of radiation can be implemented into the simulation to make it more accurate. For the x- and y-distribution, single alpha particle events were selected based on the following criteria. The event could not have been partially vetoed, the

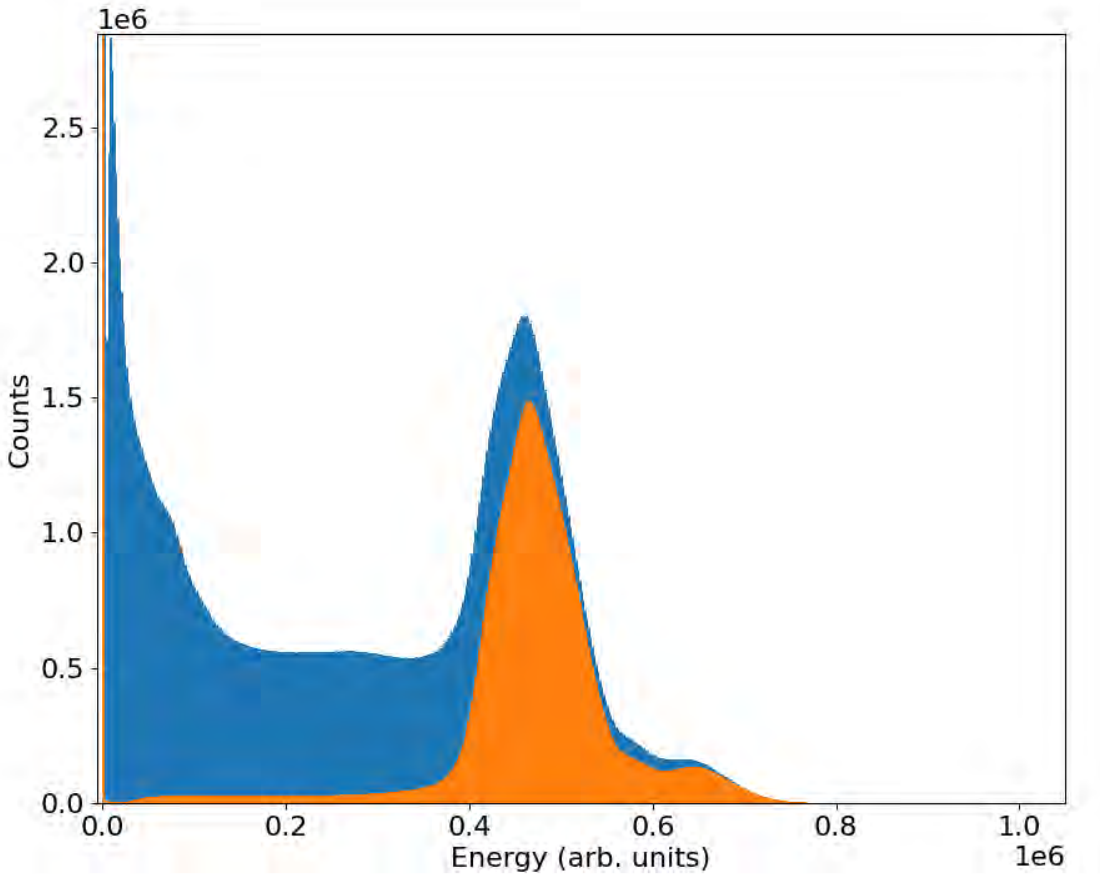

Figure 5.9 Energy histogram combined using the same procedure as was used for Figure 5.7. In blue there is no veto condition applied to the data. In orange, the data is only plotted if the hits on each veto pad do not exceed 300 ADC counts.

ADC count must have been above a certain threshold, and the measured angle off the the z-axis must be no greater than 10°. The first two conditions ensure that we are selecting real alpha particle events. The final condition makes identifying the centroid of the event on the pad plane equivalent to identifying the location of the origin of the alpha particle. From these selected events, the centroid of the pad plane image was calculated and added to a list of x- and y-distributions, shown in Figure 5.10.

These data were used as inputs to the simulations that determined the efficiency of detection of alpha particles by the TPC, and of the two HPGe detectors used to measure the alpha decays to excited states from ^{220}Rn and ^{216}Po. The results of measuring the x- and y-distributions in this

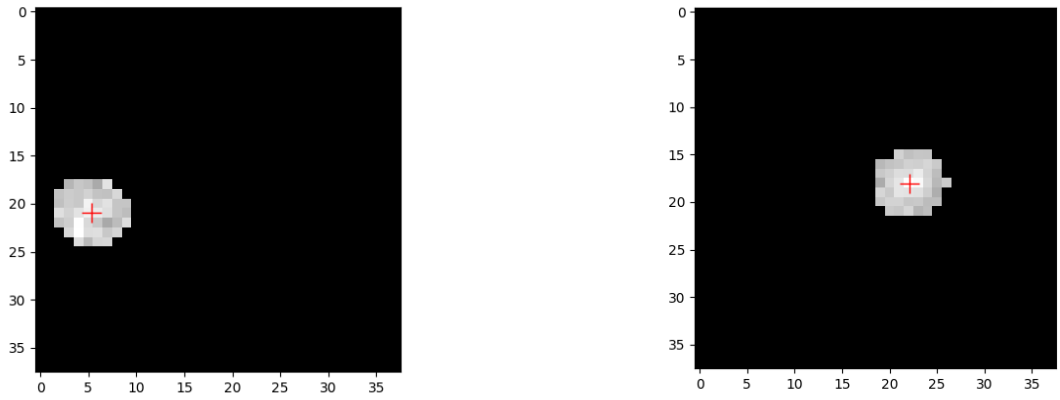

Figure 5.10 Centroid detection on events with angle no more than 10° off of the z-axis. This is done for dozens of events in each of the > 550 runs in the data, and compiled and used as our radiation distribution. Left gives a centroid of (5.4,21.0), the right gives a centroid of (22.1,18.1).

way can be seen in Figure 5.11. We suspect ^{212}Po mostly decays on the cathode, and ^{220}Rn and ^{216}Po decay near the anode, where the gas inlets to the chamber are located. Evidence for this is shown later in this chapter, based on alpha track widths. We also present some timing information that furthers this evidence in Section 5.3.3. It is not clear from either of these methods where ^{212}Bi decays, but as the $\beta-$decay parent of ^{212}Po, and with a half life of 10 hours, it stands to reason that it has already settled in the same place where the ^{212}Po decay. The gas is fed in to the detector through four inlets on the sides of the detector near the micromegas, which can be seen clearly in Figure 4.6. This is likely what causes the heterogeneity in the distribution.

To better understand what the true z-distribution of the radiation was during the experiment, a theoretical calculation was done using data from Hirst et al. [164]. It provides the diffusion coefficient for radon in argon gas, and is applied to the following equation:

$$-D\frac{\partial^2 C}{\partial z^2} = -\lambda C \tag{5.1}$$

where C is the concentration of radon, D is the diffusion coefficient of radon in argon gas [5], and λ is the decay constant of radon-220. Applying boundary conditions where the initial concentration of radon at $z = 0$ is defined as C_{in} and is the only source of radon, so we are only decaying in

[5] we scale the value given in [164] to 2,000 torr and 15°C, which comes out to 0.036 cm^2/s

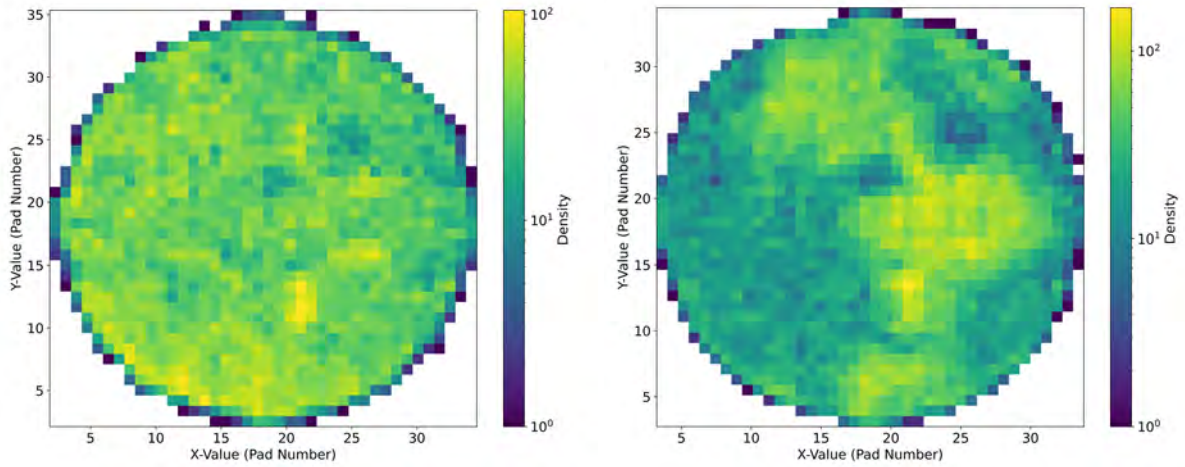

(a) $6 \times 10^5 >$ ADC Counts $> 4 \times 10^5$ (b) ADC Counts $> 6 \times 10^5$

Figure 5.11 The 2D distribution derived from real data as described in the text. The figure on the left is gated on the lower energy peak, which encompasses alphas from ^{212}Bi, ^{220}Rn, and ^{216}Po. The figure on the right is gated on the higher energy peak, alphas from the decay of ^{212}Po. This view shows the distribution of radiation on the pad plane from the view inside the chamber, in other words, from the radiation's perspective of the pad plane.

concentration to the other end of the chamber, this gives a solution to the diffusion equation of:

$$C(z) = C_{in} \exp\left(-\sqrt{\frac{\lambda}{D}}z\right) \tag{5.2}$$

where 90% of the radon-220 decays before traveling 4 cm into the chamber. Additionally, the gas flow through the inlet will push radon some distance into the detector. Using the measured flow rate by our MKS mass flow controller, and scaling for the higher pressure, we get an axial velocity in the detector of:

$$\text{Flow Rate} = 500 \text{ sccm} \times \frac{760 \text{ torr}}{2000 \text{ torr}} = 3.167 \text{ cm}^3/\text{s} \tag{5.3}$$

$$\text{Axial Velocity} = v_A = \frac{3.167 \text{ cm}^3/\text{s}}{\pi \times (6.1 \text{ cm})^2} = 0.0271 \text{ cm/s} \tag{5.4}$$

This value can be plugged into the equation:

$$\exp\left(-\frac{\lambda}{v_A}z\right), \tag{5.5}$$

which has the same shape as the diffusion distribution, but a slightly longer tail, where more than 90% of the radon-220 decays before reaching 5 cm into the chamber.

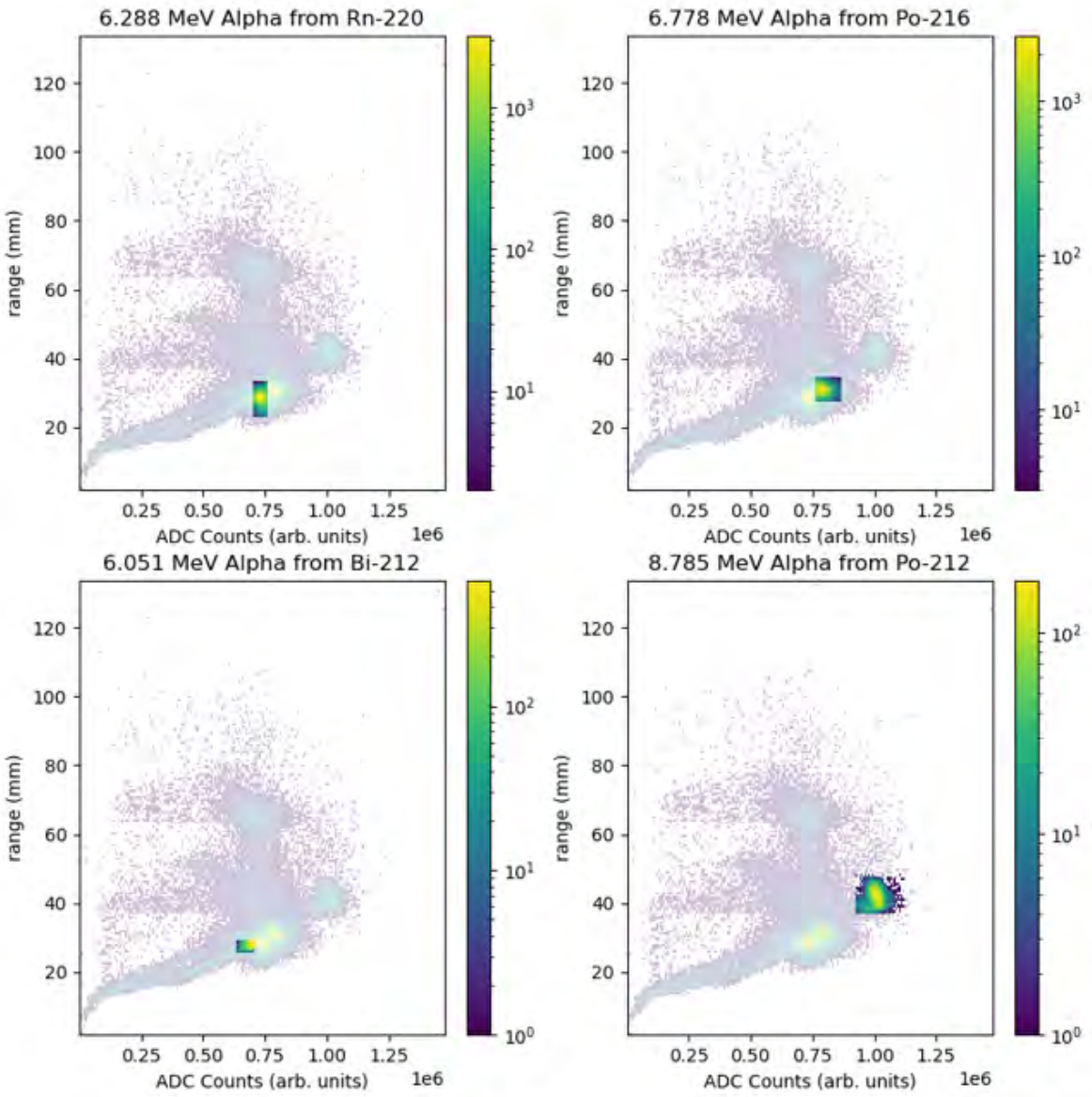

Figure 5.12 Two-dimensional cuts on the range versus energy plot, to select events whose widths were analyzed.

This theory can be compared to some experimental data to check for consistency. First, for a single run, widths of each alpha track were extracted using Principle Component Analysis (PCA). Cuts were made on the different alphas (shown in Figure 5.12) and the distribution of these widths were plotted, shown in Figure 5.13.

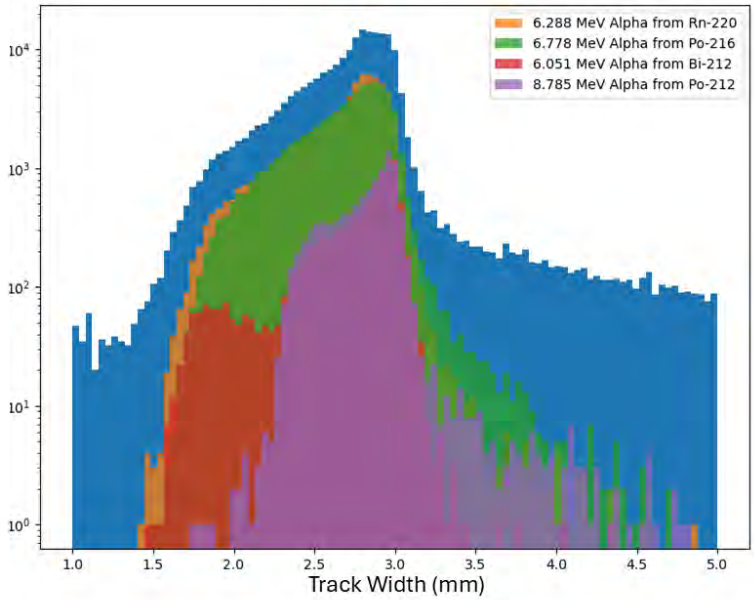

Figure 5.13 Distribution of track widths for the four cuts made. If all the decay products of ^{220}Rn decay at the cathode, one should expect their width distributions to be alike. All events' track widths are shown in blue.

The tracks of particles appear wider the further the decay occurs from the pad plane, due to space charge effects and standard diffusion of the drifting electrons [110]. The results suggest a slight preference for the daughters of ^{220}Rn to decay closer to the cathode (i.e. their widths peak at a larger value). It is also clear that there is a deficiency of ^{212}Bi and ^{212}Po events with smaller track widths, suggesting that their z-distributions peak further along in the TPC than the species in the first half of the decay chain. This will be compared to other methods of determining radiation distribution in the following sections.

All simulations carried out for this work are done by sampling from the 3D distributions obtained via the methods above, unless otherwise stated.

5.2.3 Fitting the Alpha Spectrum

First, the simulated ^{220}Rn alpha decay chain spectrum is fitted using four gaussian plus tail peaks [6] on a second degree polynomial background. The parameters from the fit of the simulation

[6] Called a Crystal Ball function

were taken and used as starting parameters to fit the data. The background was set to be near constant, the means from the simulation were allowed to be scaled together with the use of a single parameter. This accounts for the differences in gain from the real data to the simulation, while preserving the relative means of the peaks. The ratio of the heights of the Bi-212 and Po-212 peaks and the ratio of the heights of the Rn-220 and Po-216 peaks were also constrained, and allowed to be scaled based on the simulation fits. This is because it is suspected, based on track width distributions and alpha-gamma timing information, that the later half of the ^{220}Rn decay products decay on or near the cathode, whereas the first half of the decay chain decays near the anode, where the gas inlets are located. The alpha parameter of the crystal ball fit, which controls the extent of the tail of the gaussian, is forced to be the same for all 4 peaks in the simulation. It is then allowed to be scaled up or down together for all 4 peaks in the real data.

The results of the fitting are shown in Figure 5.14. The energy resolution of the simulated data comes from values set in the simulation such as shaping time and sampling rate, as physical parameters like ionization energy, fano factor, and gas properties. The electronics settings are tuned to produce simulated, summed traces that are consistent with the data. The gas properties such as density and pressure are set for the P10 at 2,000 torr used in the double alpha search. The Fano factor and other parameters were not adjusted. This means that the energy resolution of the simulated data is much better than that of the real data, allowing for easier extraction of parameters to be applied to the real data. The real data is best fit with an energy resolution of 18.5% FWHM, since the pad gain matching routine described in Section 5.1.3 was not applied. Because many shape parameters and peak ratios are constrained, the formal fit uncertainties underestimate the true yield uncertainty. We therefore assign a conservative uncertainty based on the absolute value of the fit residuals within $\pm 3\sigma$ of each peak. The residuals of the total fit to the data are shown in Figure 5.15 The total number of ^{220}Rn alphas in the peak is then found to be $(5.09 \pm 0.28) \times 10^7$, with the rest of the values displayed in Table 5.1.

Parent Nucleus	Alphas Observed
^{212}Bi	$8.74 \times 10^6 \pm 2.95 \times 10^6$
^{220}Rn	$5.09 \times 10^7 \pm 0.28 \times 10^7$
^{216}Po	$4.72 \times 10^7 \pm 0.30 \times 10^7$
^{212}Po	$1.19 \times 10^7 \pm 0.19 \times 10^7$

Table 5.1 Total Number of Alpha Particles in each Peak

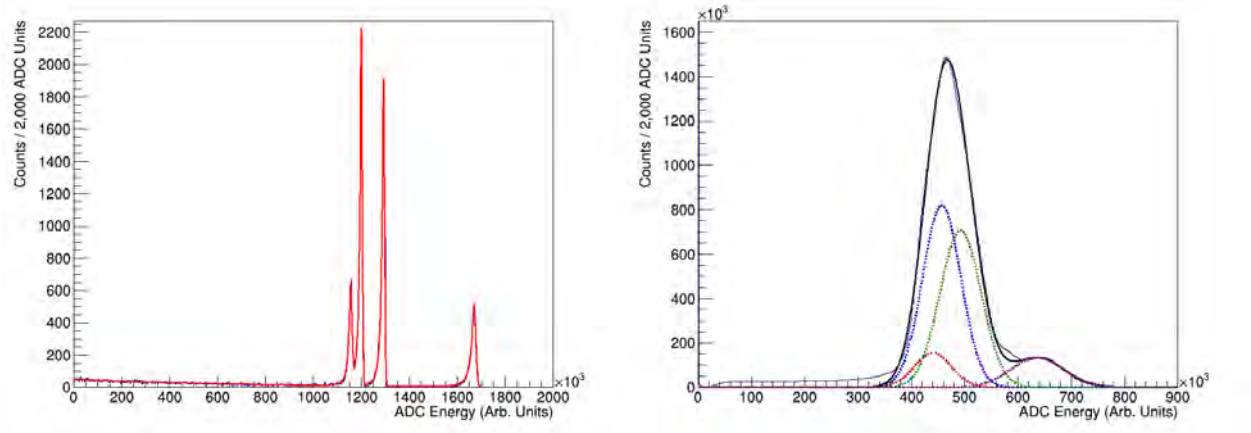

Figure 5.14 Fitted simulated (left) and real (right) alpha energy spectra. The data is gain matched run-by-run. The dashed magenta peak is ^{212}Po, green is ^{216}Po, blue is ^{220}Rn, red is ^{212}Bi. The solid black line is the sum.

5.2.4 Double Alpha Efficiency

From the previous simulations of the ^{220}Rn decay chain, it is straightforward to extract the efficiency of GADGET to detect the ^{220}Rn alpha, given our characterization of the distribution of the radiation as it flows into our detector. In the simulation, 19,892 ^{220}Rn alpha particles were emitted, and we detect 15,625 of those in the peak (taken from the integral of the fit). For the double alpha detection efficiency, we assume each alpha particle takes away half of the energy from the Q-value of the decay (^{220}Rn $\rightarrow^{212}$ Pb + 2α + 13.311 MeV). We then simulate these events at different opening angles between the particles, whose origins are alike and distributed in the same manner of the ^{220}Rn decay chain simulations. Then the energies are extracted from the sum of the individual traces from the simulated event, and it is plotted in a histogram. The full capture peak is fitted with a gaussian plus tail (Crystal Ball function). This is the same procedure as was done for the single particle fits. As a double check to ensure this is approach is reasonable, another purely geometric simulation was done using a faster simulation which does not take in to account the

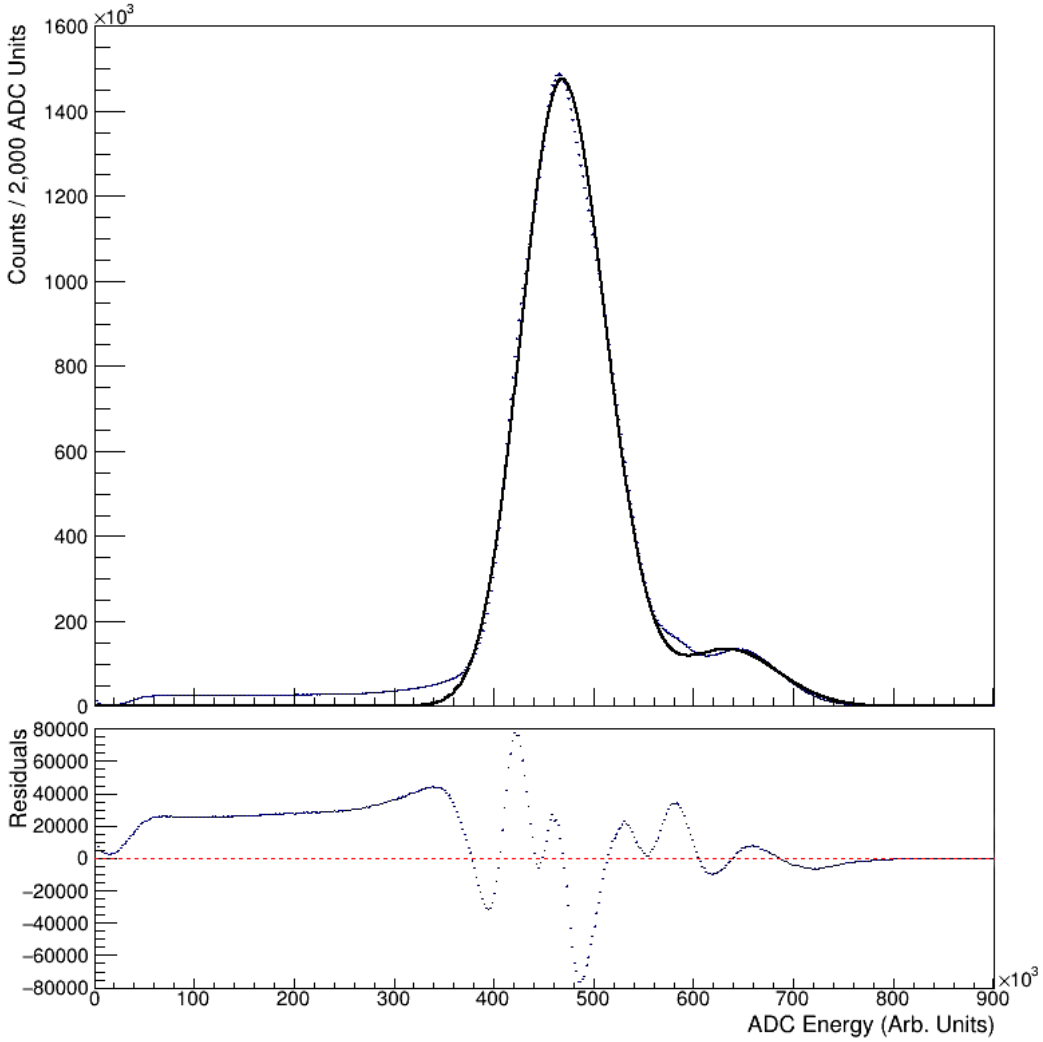

Figure 5.15 Alpha energy spectrum with the total fit, including all four peaks. In the lower half of the plot are the residuals from the fit, which are used as errors in the estimates of the total number of observed alpha particles from each nucleus, as described in the text.

detector response or charge spreading, and only ensures the entire length of the track remains in the active volume. This simulation, predictably, has a very similar shape to the more involved efficiency vs opening angle simulation, but systematically has a higher absolute efficiency. To ensure this analysis is comparing appropriately the double alpha efficiency to the single alpha efficiency, we shift both simulations to recover the correct efficiency at an opening angle of 0°. The results are shown in Figure 5.16. Because the radiation distribution is not known with good certainty, it is appropriate to apply a 20% uncertainty to the values in the plot. However, the shift of the efficiency has a limited effect on the branching ratios for double alpha decay reported, given that it must factor in the double alpha detection efficiency (weighted by opening angle distribution) and the single alpha detection efficiency. The ratio of these two quantities is what is used in the branching ratio calculation, and as long as the shape of the double alpha efficiency versus opening angle plot retains its shape regardless of detector response and charge dispersion (red data in Figure 5.16), and that the single alpha efficiency is recovered at an opening angle of 0°, there is minimal change to this quantity.

Using the shifted simulation data that takes into account detector response and charge spreading, we calculate the isotropic opening angle distributed efficiency to be 0.628 ± 0.003 (stat.) ± 0.126 (sys.). The efficiency to detect double alpha events at 180° is 0.537 ± 0.010 (stat.) ± 0.107 (sys.).

5.3 Gamma Data

5.3.1 Gamma Efficiency

The $\gamma-$ray detection efficiency of the set up was determined via GEANT4 simulations in which the geometry of the two germanium detectors and the TPC were included. The locations of the HPGe detectors relative to the TPC were measured before and after the beginning of the experiment. The geometry of the active regions of each detector was taken from data sheets provided by the manufacturer, and confirmed via calibration data and simulations done for the development of LIBRA. One set of simulations were run to determine the relative efficiency of observing a 550 keV $\gamma-$ray along the center line of the TPC, the results of which can be seen in Figure 5.17.

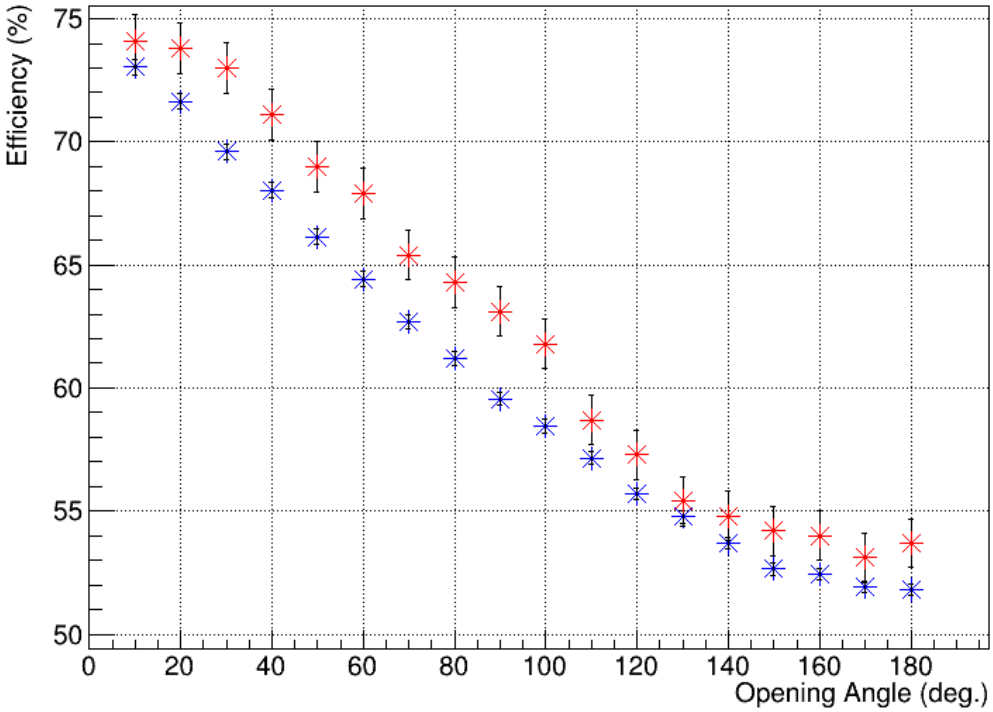

Figure 5.16 Efficiencies from both ATTPCROOT simulations (red) and geometric efficiency (blue) simulationsas a function of opening angle for two-alpha events. Both datasets are shifted to recover the efficiency to detect a ^{216}Po single alpha at an opening angle of 0°. The error shown in the plot is statistical.

Finally, a simulation was done using the same 3D distribution derived for the ^{220}Rn, based on data taken during the experiment for the xy-distribution, and theoretical estimates of the z-distribution based on flow rates and steady-state diffusion. At multiple different energies, gamma rays were simulated and the corresponding photopeak efficiency was recorded for each of the two detectors. The chosen energies simulated were based on levels in the nuclei in the decay chain of ^{220}Rn most likely to be populated after alpha decay.

As a verification of our efficiency simulation, the 550 keV excited state in ^{216}Po, populated after ^{220}Rn α-decay, was fit and the counts were integrated for the north and the south germanium detectors. The results of this fit are shown in Figure 5.19. The ratio of these counts was then compared to the values at 550 keV in Figure 5.17. There is a discrepancy in the ratio, which we expect is due to the z-distribution used in the simulations. The z-distribution comes entirely from

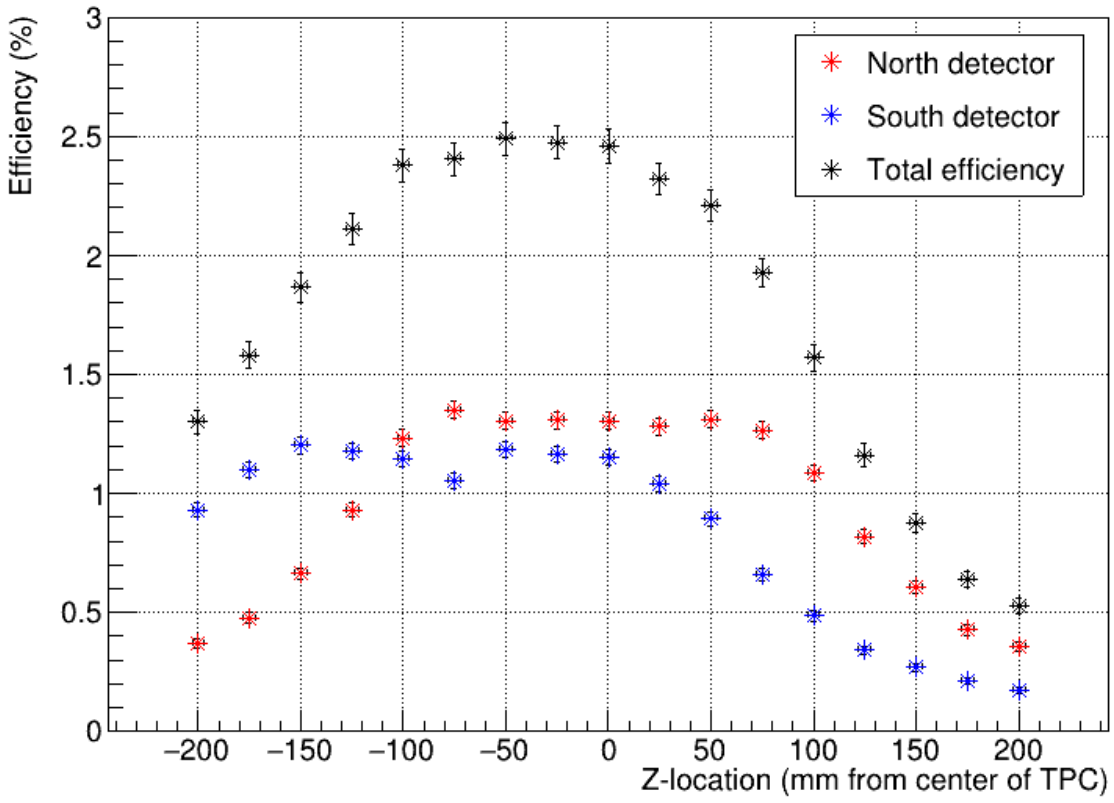

Figure 5.17 Simulated gamma efficiency of the two detectors used in the double alpha experiment. Red points are the north detector, blue points are the south detector, and black points are the combined efficiency of the two. Gammas were emitted isotropically at 550 keV. Uncertainty of ±3 mm are placed on the data based on limitations in the measurements of the absolute positions of the detectors relative to the chamber.

the theoretical model described earlier in this Chapter. This validation method suggests that the radon is moving further into the detector (more positive z-value in Figure 5.17) than we expect. A correction to efficiencies made by adjusting the values in Figure 5.18 by a scale factor that moves the simulated ratio ($\sim$ 2.12 south efficiency over north efficiency) to be in line with the actual ratio (1.11). What this means is that the radon, instead of the mean of the z-distribution being 40 mm into the detector, it is adjusted to be 90 mm into the detector. This correction is carried throughout the gamma data analysis. Because our measurement for the $\alpha-$decay to the 550 keV excited state in ^{216}Po matches previous measurements to within uncertainty, this correction is supported by the data.

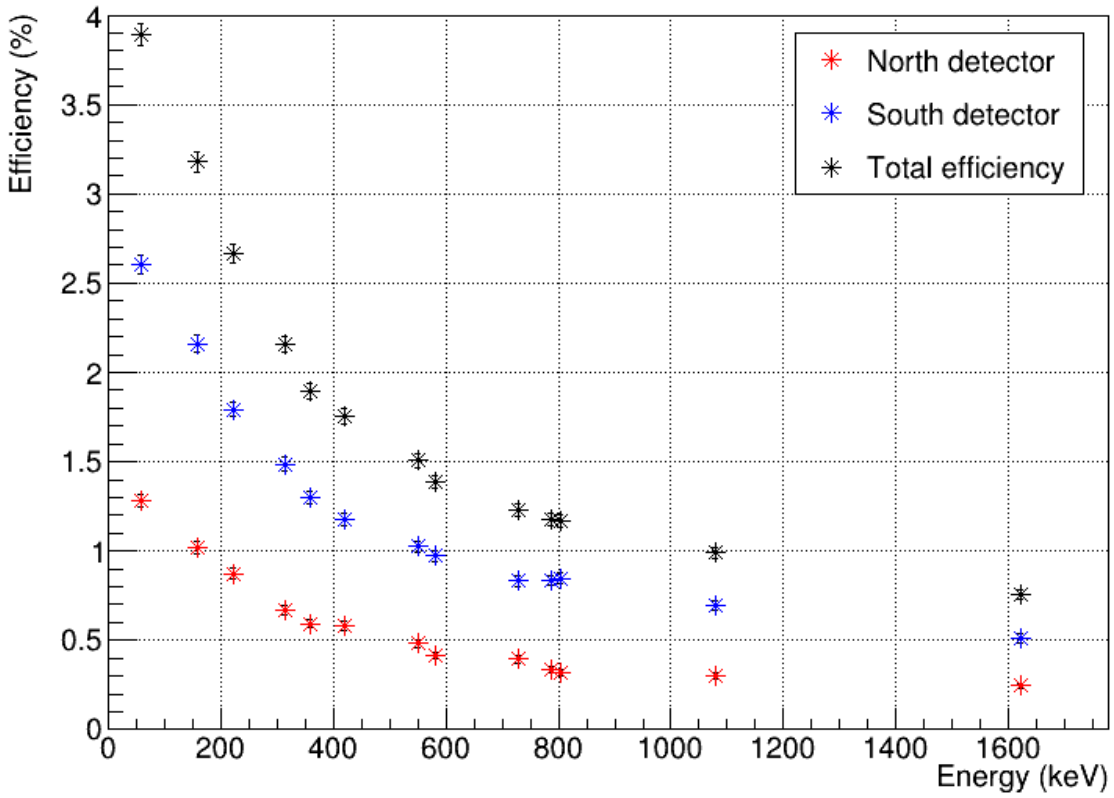

Figure 5.18 Simulated efficiency of the south (blue), north (red), and combined (black) gamma detectors versus energy of the emitted gamma ray. The distribution of the radiation in this simulation comes from the method described in Section 5.2.2.

5.3.2 Gamma Energy Spectra

The goal of adding the HPGe detectors from LIBRA to the double alpha experiment was to search for new alpha decays to excited states in the decay chain of ^{220}Rn. To that end, the gamma data was analyzed with a gate on the mesh energy spectrum provided to the XIA DAQ, shown in Figure 5.20. If an event, which had a coincidence window set to 10 μs, created a signal on the mesh of the TPC above the set threshold, and at least one of the two HPGe detectors saw an event, that was considered an alpha-gamma event. No veto from the GET DAQ was applied to this data. The alpha-gated gamma data is shown, in black, in Figure 5.21. The blue spectrum is data from the background run taken in the same location before the experiment began. The background spectrum was scaled to the alpha-gamma data using the 1460 keV ^{40}K gamma peak for normalization. From

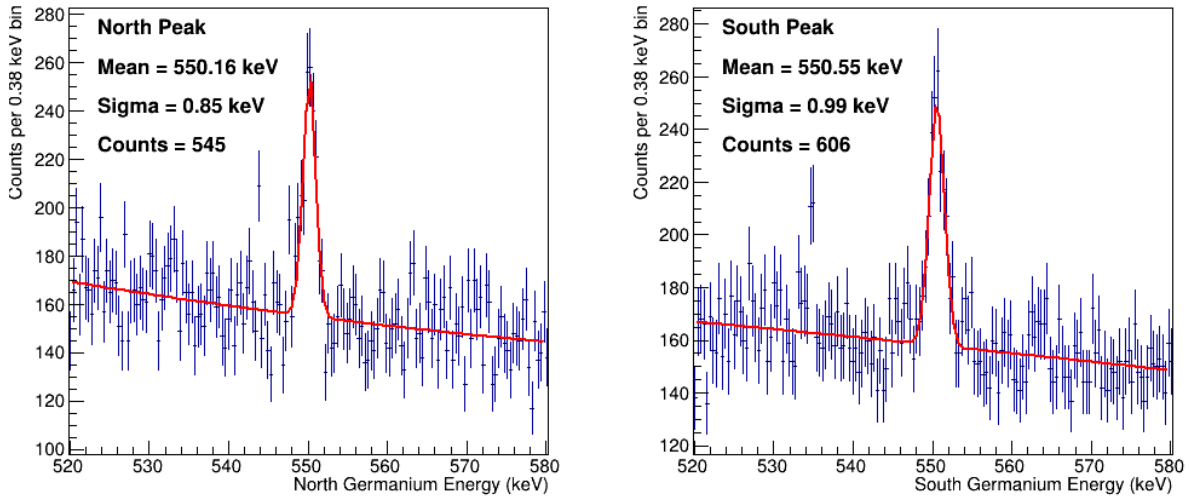

Figure 5.19 Comparing the counts found in the 550 keV peak in the north germanium detector (left) to the south germanium detector (right). Notice that the south peak is wider due to gain drift that the north detector does not experience.

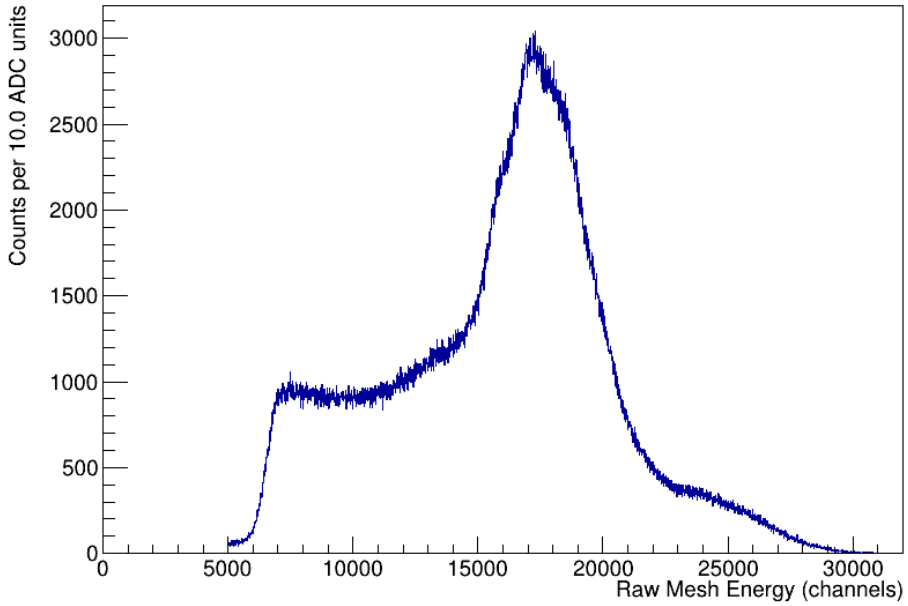

Figure 5.20 Mesh data recorded by the XIA DAQ. Events below 5,000 ADC counts are removed.

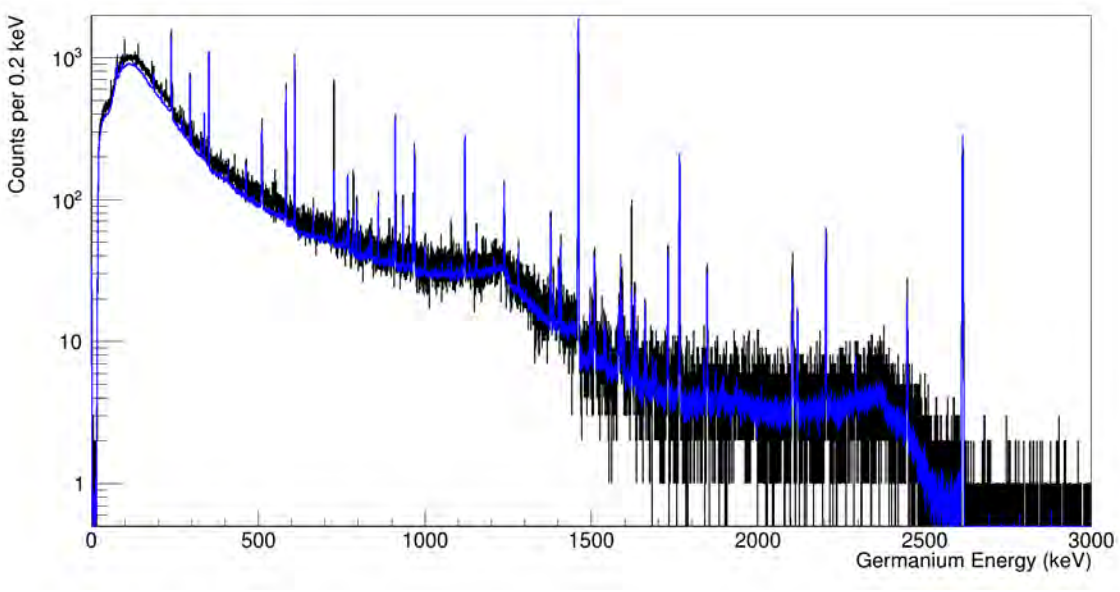

Figure 5.21 Gamma spectrum in coincidence with alphas (black). Background gamma data taken before the experiment was run, scaled to the ^{40}K gamma ray peak (blue).

this, each peak can be compared to the background to see if there is an excess of counts, indicating the presence of an alpha branch to an excited state in the daughter nuclei, which then decays to the ground state via gamma ray emission. Both the background spectrum and the data were fit with a second degree polynomial background and a gaussian peak. The routine required the gaussian peak to be within 2 keV of the expected energy, and the height of the peak to be positive. The routine also required the widths of the peaks in both the background and data histograms to be within 5% of one another. The integral of the gaussian of both fits was extracted, with uncertainties, and the results are shown in Table 5.2. There are 5 locations where this is observed: at 550, 728, 786, 1080, and 1621 keV. The 550 keV comes from the previously observed ^{220}Rn alpha decay to the first excited state of ^{216}Po [165, 166]. This can be used as an estimate of the number of ^{220}Rn decays we see in the TPC during the experiment, and can be compared to the number obtained from the alpha energy spectrum. Because our mesh signal does not account for the trigger accepted, this also needs to be factored in to the number, along with the photopeak efficiency of our Germaniums and the branching ratio:

$$N_{^{220}\text{Rn decays}} = \frac{N_{\text{peak}}}{B \times \epsilon_\gamma \times \epsilon_{\text{trigger}}} = 5.2 \times 10^7 \pm 0.6 \times 10^7, \tag{5.6}$$

Nucleus	Energy (keV)	Integral of Run Data	Integral of Background	Excess Counts
^{216}Po	550.3 ± 0.3	1120 ± 118	16.4 ± 13.6	1101 ± 118
^{212}Po	728	8750 ± 180	1540 ± 15	7210 ± 180
^{212}Po	786	1630 ± 110	512 ± 12	1120 ± 110
^{212}Po	1080	585 ± 73	96.4 ± 8.1	488 ± 74
^{212}Po	1621	1370 ± 70	315 ± 6	1060 ± 70
^{216}Po	419	51.4 ± 73.3	24.5 ± 11.0	26.9 ± 74.1
^{216}Po	359	234 ± 148	81.8 ± 22.9	152 ± 149
^{216}Po	223	156 ± 175	30.9 ± 33.6	125 ± 178
^{212}Pb	805	316 ± 167	378 ± 12	-62 ± 168
^{212}Pb	315	0 ± 79	0 ± 13	0 ± 80
^{212}Pb	157	288 ± 198	256 ± 52	32 ± 205
^{212}Pb	58.1	181 ± 90	31 ± 25	149 ± 94

Table 5.2 Alpha gated gammas compared to background. Alpha gate uses mesh spectrum above 5,000 ADC counts. Resolution of the peaks must be within 5% of each other and mean must be within 2 keV of the previously measured value.

where the gamma efficiency comes from GEANT4 simulations (including the z-distribution correction), and the trigger efficiency comes from comparing the total number of events recorded by the GET electronics (3.0356×10^8) compared to the number of mesh signal events in XIA in the energy cut (2.4830×10^8). In this case, we've included a wide gate on the mesh energy spectrum. So while the numbers from both methods are within uncertainty, the fit to the energy spectrum made from the TPC data is a more reliable number: $5.086\times10^7 \pm 0.281\times10^7$.

The other excesses originate from ^{212}Bi, due to the grow-in of this radioactive nucleus within the ^{220}Rn decay chain, causing a higher incidence of coincident events.

A measure of the excess counts in peaks of energies near excited states after alpha decay is shown in Table 5.2. The branching ratios are recorded in Table 5.3. The values are calculated using the 90% confidence level for each input variable to determine an overall upper limit on the branching ratio. For the 550 keV state, we report a finite value, confirming previous measurements with a similar uncertainty, and supporting the limits placed on the unobserved decays to excited states.

Decay	Gamma Energy (keV)	Excitation Energy	J^π	Branching Ratio (%)
^{220}Rn $\rightarrow^{216}$ Po*	550.3 ± 0.3	549.76	2^+	0.117 ± 0.014
^{220}Rn $\rightarrow^{216}$ Po*	419.2	968.94	(4^+)	<0.012
^{220}Rn $\rightarrow^{216}$ Po*	359.5	1328.4	(6^+)	<0.032
^{220}Rn $\rightarrow^{216}$ Po*	223.4	1551.8	(8^+)	<0.023
^{216}Po $\rightarrow^{212}$ Pb*	804.9	804.9	(2^+)	<0.023
^{216}Po $\rightarrow^{212}$ Pb*	315.0	1119.9	(4^+)	<0.0084
^{216}Po $\rightarrow^{212}$ Pb*	157.0	1276.9	(6^+)	<0.016
^{216}Po $\rightarrow^{212}$ Pb*	58.1	1335	(8^+)	<0.012

Table 5.3 Branching ratios for α decays of ^{220}Rn and ^{216}Po populating excited states in the daughter nuclei, inferred from the observation of α–γ coincidence peaks at the listed γ-ray energies. Energies without an uncertainty were not measured in this experiment and taken from literature. Quantities with a < symbol represent 90% confidence interval upper limits, because there is no statistically significant excess in counts in the alpha-gated gamma spectrum above background. The excitation energy and J^π of the state comes from NNDC data.

5.3.3 Timing Distribution

To check the theoretical and experimental results in the previous section, Figure 5.22 was created by plotting the time difference of events that contained both a valid trigger in GET, as well as a valid trigger in either Germanium detector. The gamma signal is used as an absolute start time of some given decay, and the GET timestamp is used as the stop time, providing the drift time of the electrons and thus, a proxy for the absolute z-position of the decay. These signals were all recorded in the XIA DAQ, and the germanium signals were delayed by 4 μs because at the time, the drift velocity of the electrons at this high a pressure was unknown. Therefore, the peak at -3.5 μs should be considered decays that occurred on the pad plane, and the peak at 5 μs, giving a rough drift velocity of 4.97 cm/μs.

Because the distribution in this plot is dependent on gamma rays being in coincidence with alpha particles, it is rather difficult to disentangle for individual gamma ray or alpha energies. Merely two distinct alpha peaks can be resolved in the mesh spectrum, and these time difference plots assume that there is an alpha particle in coincidence with a gamma ray, which we only have evidence for from ^{220}Rn and ^{212}Bi. However, gating on the highest energy alpha peak of ^{212}Po, and looking at the resultant alpha-gamma time difference plot, Figure 5.23, shows a clear increase in the number of alpha events on the cathode. This is consistent with the results found in the track width analysis

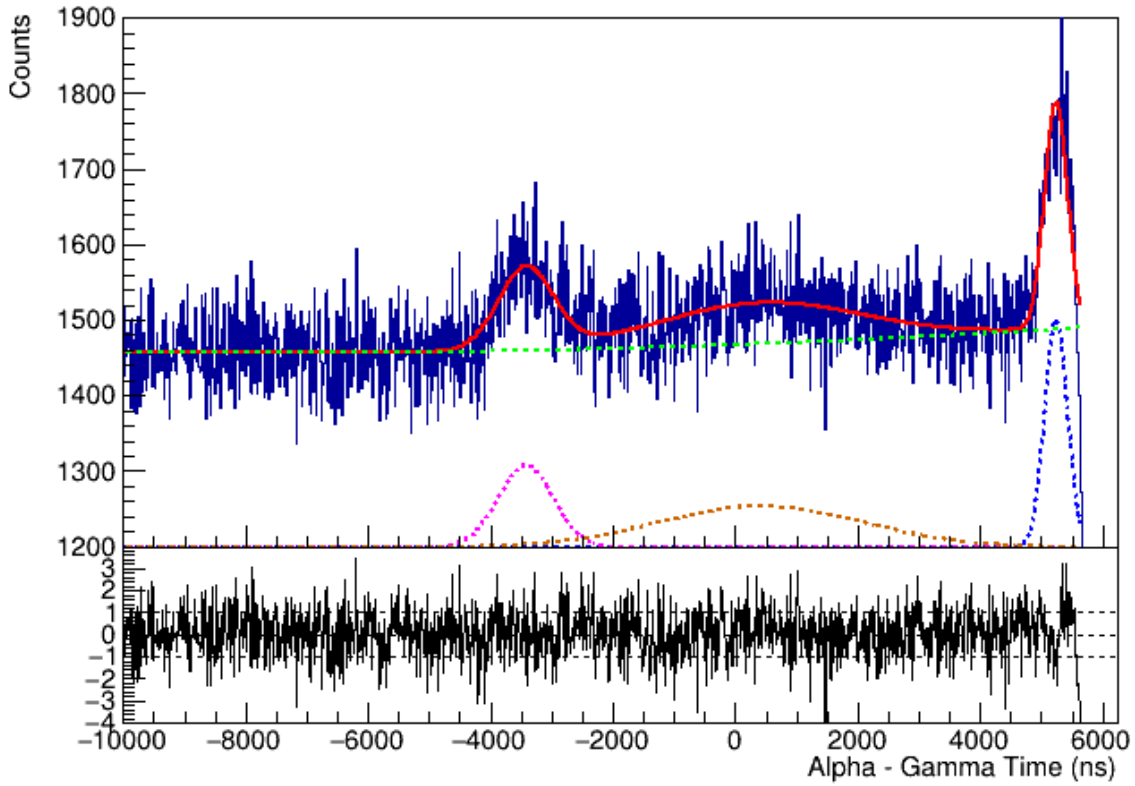

Figure 5.22 Time difference histogram between the north Germanium detector and the mesh signal from the GADGET TPC. The solid red line shows the entire summed fit with residuals. The dashed lines show each component of the fit, three gaussians and a second order polynomial. The gaussian components are shifted up by 1200 counts so they can be seen in the plot. This plot can act as an indicator of the steady-state distribution of radiation in the detector. A 4 μs delay was added to the Germanium signal in the DAQ to ensure that the alpha signals on the mesh would fall within the coincidence window.

in Figure 5.13.

There is previous work showing that ^{216}Po is usually neutrally charged after ^{220}Rn alpha decay, suggesting that the distribution of ^{216}Po alphas should be nearly the same as ^{220}Rn alphas [167].

5.4 Fitting GADGET II Data

To fit the events which include two alpha particles, a model to simulate the TPC data was created for the GADGET system. It works by combining SRIM input data for the stopping power of the particle with the TPC response, to create data that is directly comparable to the real data. As described in Section 2.3.1, the charged particles in the TPC will lose energy through inelastic interactions with the atoms of gas in the chamber. The ionized electrons produced then drift through

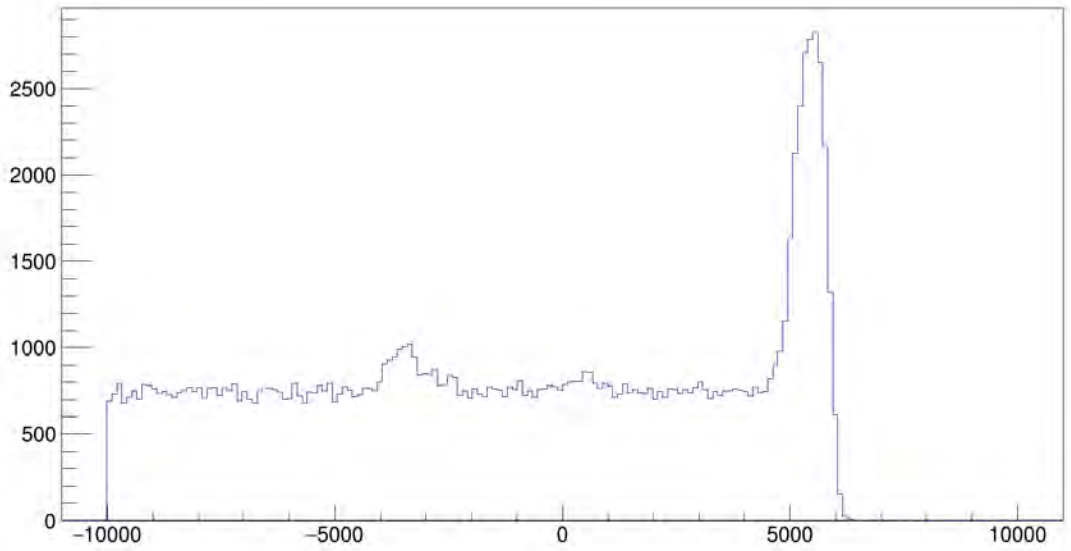

Figure 5.23 Gating on mesh spectrum events in the ^{212}Po peak and plotting those events' timestamp difference with the gammas in the same event window.

the volume of the detector and are read out via a wall of pads on the anode end of the chamber.

The simulation first calculates the energy loss per unit length through the gas via lookup tables that take information such as the type of gas and its pressure, the type of charged particle creating the ionization, and that charged particle's initial kinetic energy. Then, the total length of the track is calculated and divided up into small segments. Energy is deposited along that line at each point based on an integral of the differential stopping power provided by SRIM. This data forms the characteristic Bragg curve of the track, and is the input for simulating the detector's signals.

Once the Bragg curve is known, the simulation computes how this charge drifts in the electric field and is read out by the pad plane electronics. Space charge effects and diffusion will effect the width of the track, and the shaping time of the amplifiers in the AsAds affect the widths of the traces. These processes are modelled as a Gaussian in the (x, y) and (z) directions, characterized by standard deviations σ_{xy} and σ_z. The code then takes this track data, now modified with the detector response effects, and assigns each readout pad a waveform based on the amount of charge its finite area in x-y receives, as well as the time bin width in z. To compare simulated events with experimental data, the real pad traces are preprocessed and trimmed. After this, one can simply take

the residuals of the simulated and real traces in a direct comparison. This is used in the following sections to extract information like the origins of the particles in multi-alpha events.

5.4.1 Multiple Approaches to Fitting

Two approaches are used and compared here: cost function optimization and Bayesian inference using a Markov Chain Monte Carlo (MCMC) sampling algorithm.

In the first method, an objective function is created to quantify the agreement between the model and data. Then, a solving method is chosen to explore the space in search of minimizing the objective function, or finding the minimum parameters such that the simulation is as similar as possible to the data. This approach is computationally efficient given the wide application of general computational optimization problems that exist. However, we have seen in practice that optimization algorithms used in minimization routines are prone to convergence failures if the likelihood space they explore has strong parameter correlations, multiple maxima, and/or sharp features. For this work, ~4,500 two-particle events were fit in this way, and a subset of the results were used as starting values for the Bayesian method.

Parameter estimation using Bayesian inference requires three components, a model that produces simulated TPC pad traces from a proposed set of physical parameters (discussed in the previous section), a well-motivated likelihood function that quantifies agreement between simulated and observed data, and a sampling algorithm (MCMC) that efficiently explores the parameter space.

The MCMC algorithm is used to compare against a cost function optimization fitting method as before, and also attempts to extract uncertainties in fit parameters using their posterior distributions. The MCMC algorithm allows walkers, whose parameters are initialized with a gaussian distribution about the results from the minimization fitter, to step through the parameter space and calculate a new likelihood at that step. It then accepts or rejects this step, which can be done by a variety of algorithms, such as the affine-invariant ensemble sampler described in Ref. [120] and implemented in this work. After many of these steps, the walkers converge, and the distribution of the projection of these samples can be used for parameter estimation and uncertainty quantification. The work of determining the appropriate number of steps to take can be difficult, but the autocorrelation

values (τ), which describes the number of steps needed to get to an independent sampling of the parameters space, typically sits around 4-5, and it is suggested by Foreman-Mackey that 50τ is sufficient for convergence. Given this, the walkers are run for 600 steps for the subset of events fit here to ensure appropriate convergence. The resulting posterior samples are used for estimation of parameter uncertainty by comparing the difference between the results obtained via MCMC and non-MCMC methods.

The objective function used in this work is a gaussian likelihood function:

$$\ln \mathcal{L} = \frac{1}{2} \sum_{p} [\ln |\Sigma_p| + r_p^T \Sigma_p^{-1} r_p] \tag{5.7}$$

where $r_p = s - o$ is the residual vector between simulated and observed traces for pad p, and Σ_p is the covariance matrix incorporating both multiplicative and additive uncertainties.

The covariance matrix is defined as follows:

$$\sum = \sigma_m^2 s s^T + \sigma_c^2 I \tag{5.8}$$

where ss^T is the outer product of the simulated pad traces and I is the identity matrix. σ_m is extracted by fitting single alpha events from different decays in the ^{220}Rn decay chain, and extracting the uncertainty in pad gain for tens of these single particle events. σ_c is determined by measuring the root mean square (RMS) baseline noise in the traces of those same single alpha events. When the event is simulated, the code ensures that the pads that fired in the data are also simulated.

Pads that end up simulated but do not have a corresponding real data trace to compare to are handled in the following way. We set a pad firing threshold based on the real data, seen in Figure 5.24. Assuming gaussian fluctuations with standard deviation:

$$\sigma_i = \sqrt{\sigma_c^2 + \sigma_m^2 s_i^2}\,, \tag{5.9}$$

the probability for that single bin not firing in the data is given by the cumulative distribution function. The total log likelihood for a pad who did not fire but was simulated is then:

$$\ln \mathcal{L}_p = \sum_i \ln \left[\frac{1}{2} \mathrm{erfc} \left(- \frac{\text{threshold} - s_i}{\sqrt{2}\,\sigma_i} \right) \right], \tag{5.10}$$

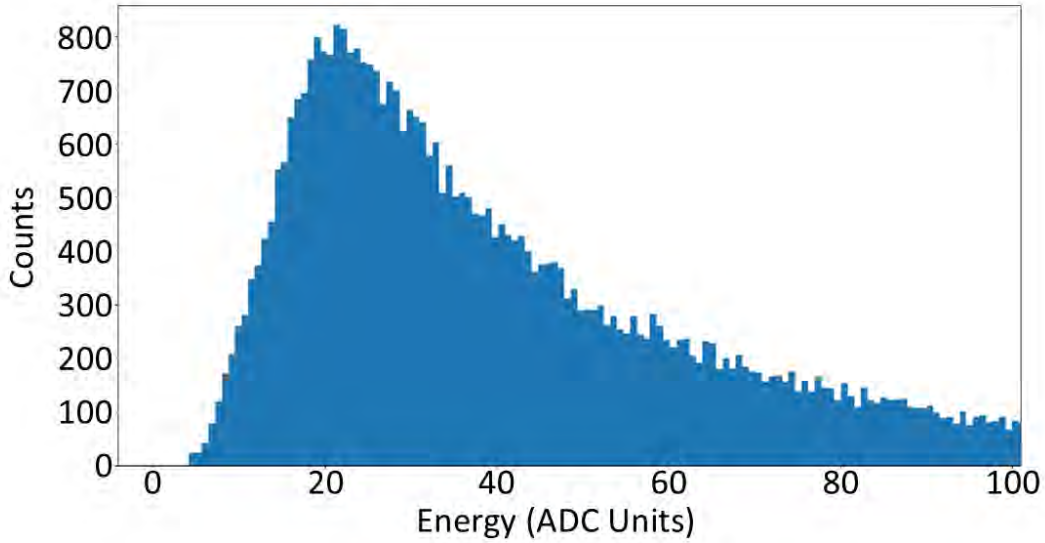

Figure 5.24 Histogram of the background-subtracted peak height of each pad that fired in random events across all runs taken for the $\alpha\alpha$-decay search.

which can then be added to the total log likelihood for use in the fitters.

In order to provide the fitter with good starting values, a k-means clustering algorithm was developed to separate the event into two distinct clusters. An example of this is shown in Figure 5.25. The lines of best fit for each cluster are used to extract reasonable starting values for some of the physical parameters in the fitter. These clusters were then fitted in all four direction combinations and the best result (lowest cost function) was chosen as the final fit results.

In order to get an understanding of the uncertainty on each parameter of the fit, 24 events were selected at random from the fit results. The only condition placed on these events is that the fitter must have exited with a successful exit message, and for 12 of the events, the origins must be within 12 mm of each other, and for the remaining 12 events, the origins must be greater than 30 mm apart. The best fit parameters in the cost function minimization approach were used as starting values for the MCMC fitter. The results of both fit methods for these two dozen events were compared for each parameter, and the standard deviation of the difference in each parameter was extracted and will be used as a rough estimate of the uncertainty of that parameter. This comparison approach, although

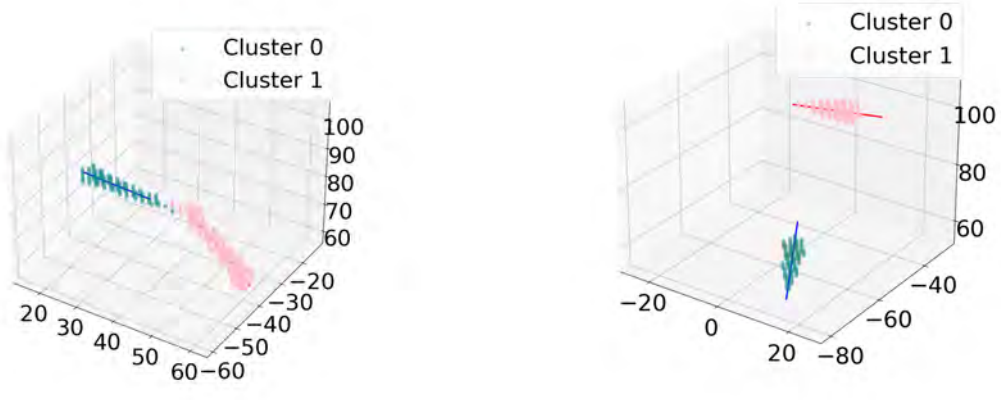

Figure 5.25 Output of the clustering algorithm written for the purpose of distinguishing between two alpha particle tracks, and using the values pulled from the algorithm as starting values for the fitter. Note that the ADC threshold used for this algorithm was set to 1300 in order to remove as much noise as possible.

using two different methods, reuses the likelihood function. So, while it gives us an estimate of the fitter's limitations, it does not take in to account issues inherent to the construction of the liklihood function, which could cause the result of both fitter to deviate from reality in some cases. One issue that came up during this analysis was the uncertainties used in the likelihood function. We assume that there is some uncorrelated noise in the traces, as well as some uncertainty in the pad-by-pad gain. However, it is almost guaranteed that the noise in the pads is highly correlated, and this is borne out in the residuals, which can have large fluctuations due to this effect, and possibly also from range straggling and uncertainties in the stopping power, neither of which are adequately handled in the fitting routine.

Nevertheless, each fit result examined has been very close by eye, and is the best method we have at extracting the relevant values for this analysis. The takeaway from this discussion is that parameter error estimation is something that should be improved upon in the future, and the values given in Table 5.4 should not be considered an upper limit, it is possible that, in reality, the uncertainties are higher.

Parameter	Uncertainty (std)
Energy 0	0.67 (MeV)
Energy 1	0.46 (MeV)
Theta 0	0.037 (rad)
Phi 0	0.057 (rad)
Theta 1	0.025 (rad)
Phi 1	0.094 (rad)
X 0	0.86 (mm)
Y 0	0.88 (mm)
Z 0	0.47 (mm)
X 1	1.2 (mm)
Y 1	1.6 (mm)
Z 1	0.91 (mm)
Sigma XY 0	0.23
Sigma Z 0	0.080
Sigma XY 1	0.37
Sigma Z 1	0.23

Table 5.4 Standard deviations (uncertainties) for reconstructed parameters.

5.4.2 Flagging Noise

After gating on events with total integrated charge above 8.65e5, which was chosen to cut out as much of the highest energy single alpha peak from ^{212}Po (8.78 MeV) as possible without reducing efficiency in the double-alpha search region, a check is done to flag certain high energy events as noise, prior to fitting the remainder of the good events. The way the trigger is set up forces the first peak in a trace to occur around time bin 150. Digital noise from the switch capacitors can trigger the GET DAQ, but these events have a high ADC count in the time bin region prior to time bin 150, which real events should not have. Therefore, an event is flagged as likely noise if the summed trace goes above an ADC count of 10,000 in the time bin range 20-80. An example of a noisy event is shown in Figure 5.26. Figure 5.27 shows the traces for a noisy event that is much less common than the other two, and is removed by hand after flagging the more common noise. For the first ~11,000 events above the energy cut, every event was checked by hand, including the ones flagged as noise. For the remaining ~25,000 events, the flagged events were assumed to be correctly identified as noise, and the rest were checked by hand, and labeled as RnPo Chain, Accidental Coincidence, or some other anomalous event.

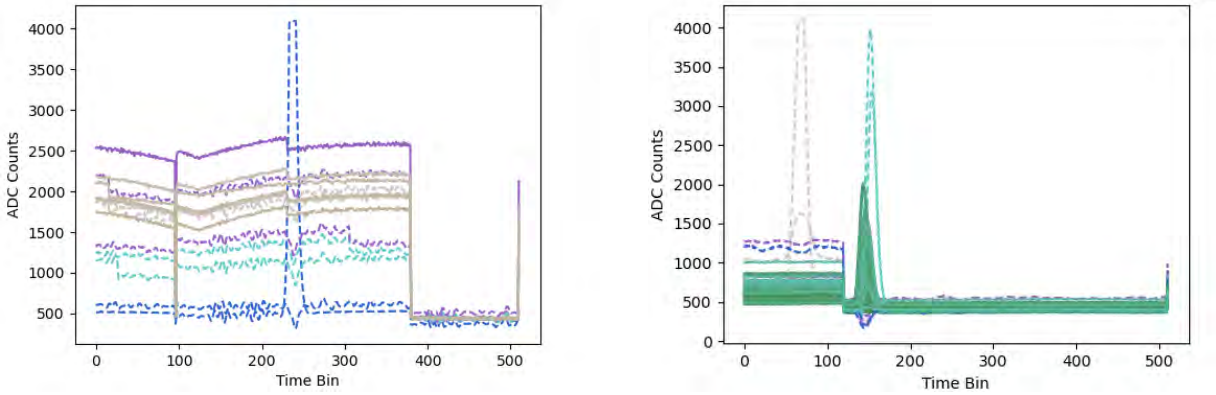

(a) (b)

Figure 5.26 Example of Noisy Events that show up above the energy cut. On the left is an event where the trace is entirely noise. On the right is an event where there was likely a real alpha particle, but the noise at the beginning of the trace comes from the electronics.

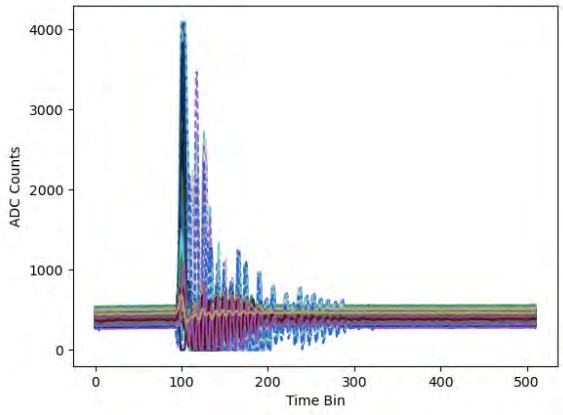

Figure 5.27 A noisy event that lights up the entire pad plane and is not caught by the flagging algorithm.

5.4.3 Disintegration Events

In the energy cut of interest, we see a few dozen (47) events I have labeled 'disintegration events.' In order to see many of these events, the veto condition is not applied. These are events which do not resemble noisy events, and appear to have more than two tracks. It is possible some of these events are actually α scattering at large angles. A few high track multiplicity examples are shown in Figure 5.28. These types of events have energies that correspond to roughly 14 MeV (for the partially captures event 393) up to 29 MeV (for event 936).

We believe these events originate from cosmic ray interactions with nuclei inside the TPC creating a nucleus in a highly excited that decays through these exotic channels that would otherwise be inaccessible. The appearance of these events raises the question of whether the same mechanism that produces these exotic events could cause background in the double-alpha decay search region. Because most of these events are anomalous, and it is unclear what they are let alone the mechanism that caused them, it is difficult to categorize them in any way, especially because many of the tracks are long enough to be vetoed in normal circumstances, so we cannot even accurately extract energies or ranges like we can with normal events. However, without applying the veto condition, and using pad gain match mapping, shown in Figure 5.5, and results shown in Figure 5.6, we see 9 disintegration events in the energy range 12-14 MeV. This is not a complete energy integral, as in most of these events, a substantial amount of the charge is deposited outside of the active volume.

We also see events in the double alpha energy region that could come from the high energy tail of the ^{212}Po peak, either due to the energy resolution, the single alpha event sitting on some noise that is not removed by the event processor, or these large energy single particle events could also be generated from cosmic ray-induced interactions. When we apply the pad gain match in the same way and look at large energy single events in the 12-14 MeV region, we see 26 large energy single particle events.

I have also included total energy and energy sharing from the fits of the two alpha events with different gates in Figures 5.29 and 5.30. From the events in the two alpha fit data, we estimate the number of anomalous two alpha events that may fall in between the dashed lines of Figure 5.31.

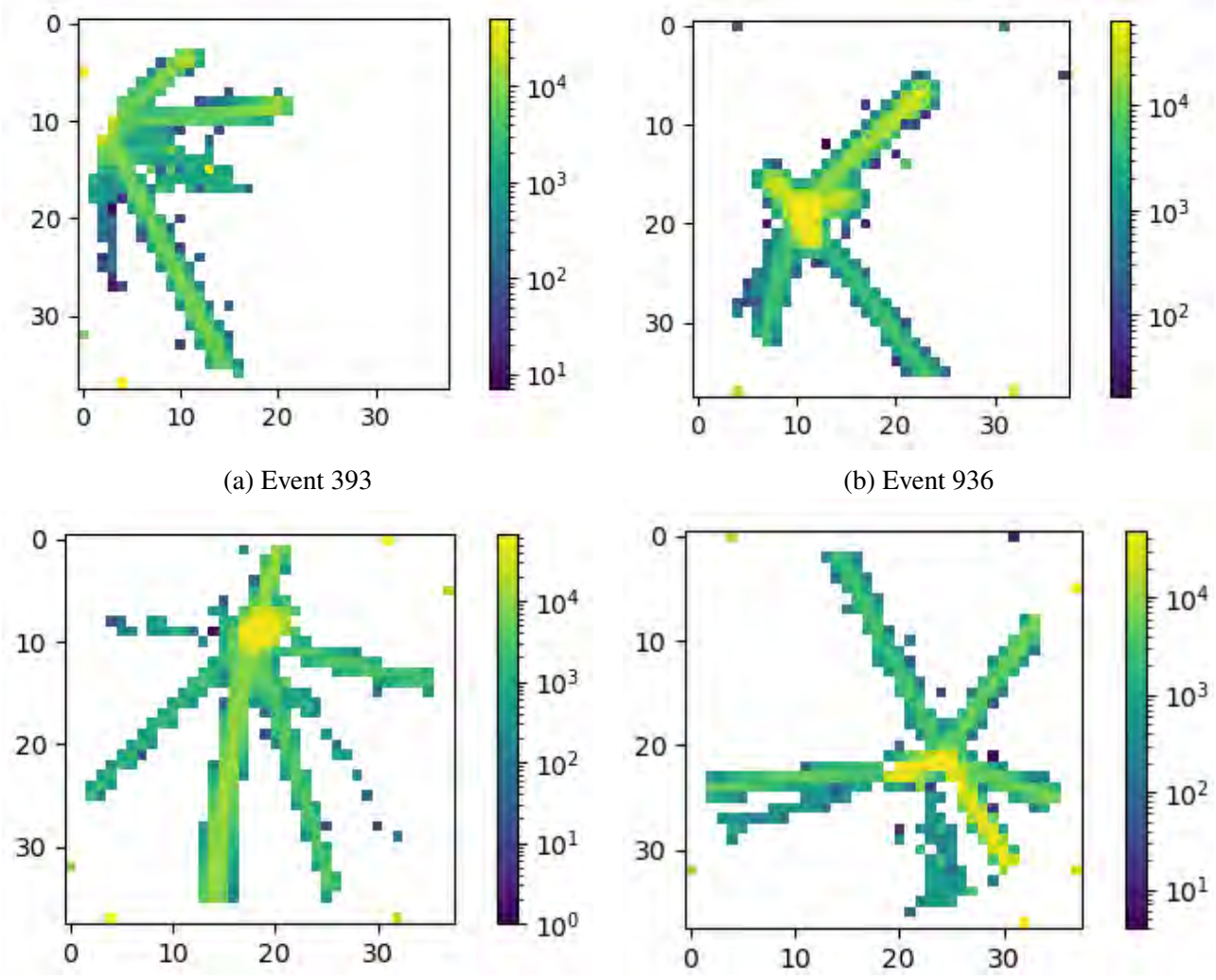

(a) Event 393

(b) Event 936

(c) Event 10477

(d) Event 15068

Figure 5.28 Four examples of events classified as disintegration events.

This region corresponds to the kinematic area expected for the two alpha decay. We see 62 two alpha events in the dashed line region, and 10 events lie outside. The events outside the dashed lines are interpreted as anomalous background events, likely originating from cosmic-ray–induced nuclear reactions or some other non-signal process. Because of this, we assume that they have a roughly uniform distribution in the energy-energy scatter plot, and use scaling phase space arguments to estimate their background within the region of interest. Based on the ratio of the phase space inside the dashed lines ($\sim 23\%$) to outside ($\sim 77\%$), we estimate the number of anomalous events to be:

$$N_{\text{anom,in}} \approx 10 \times \frac{0.23}{0.77} = 3 \text{ events.} \tag{5.11}$$

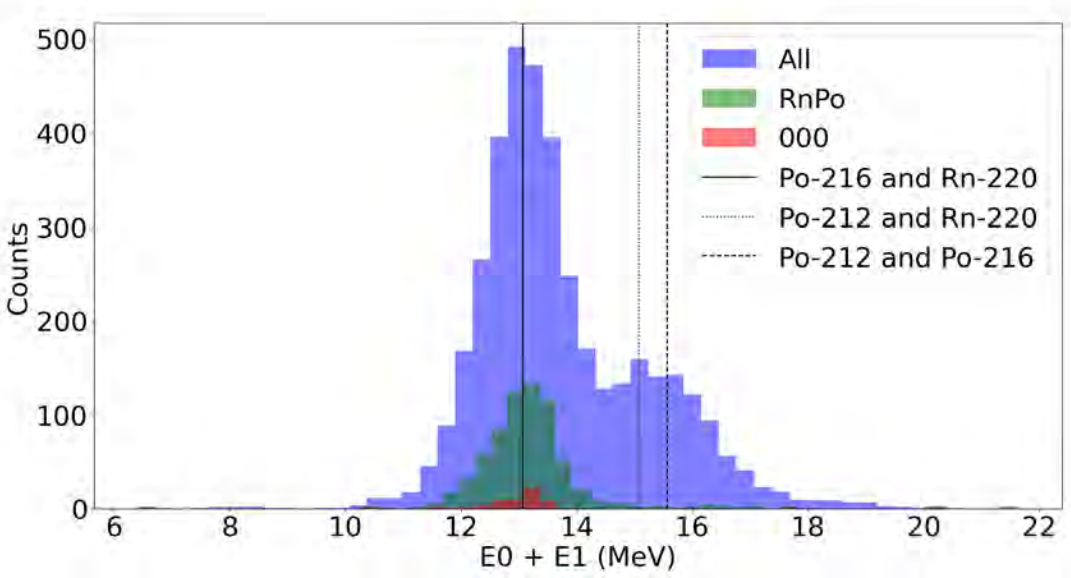

Figure 5.29 Total energy of the two alpha events from fits. The fit requires a ADC counts to MeV parameter which was set using single alpha data, and ended up systematically underestimating the energy of the particles. The data in this plot is corrected for that effect.

This lowers our estimate on the number of counts in the excess region.

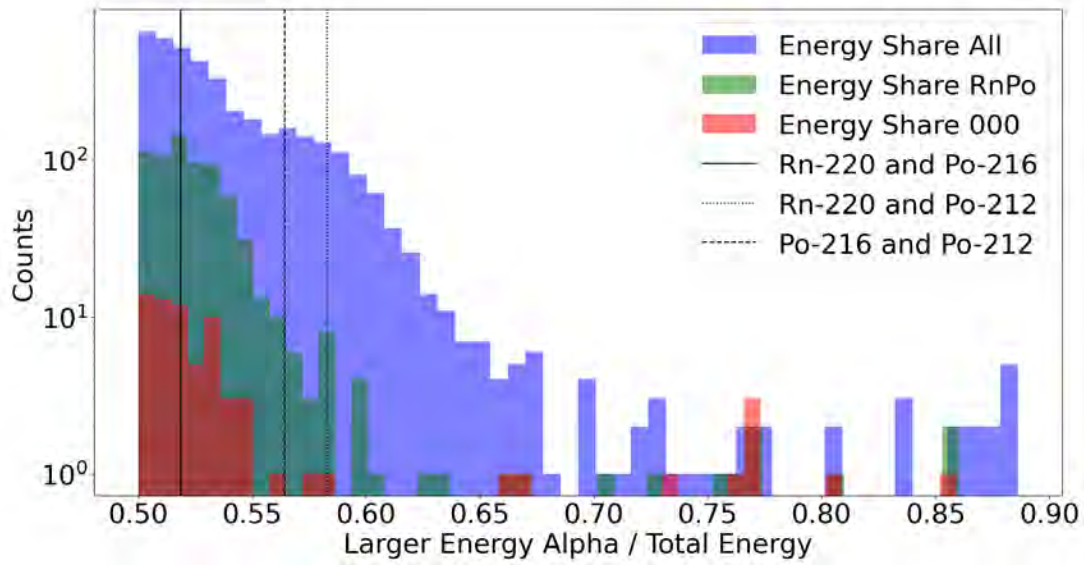

Figure 5.30 Energy sharing between the two alphas in the fitted data.

5.4.4 Results of Fitting Two Alpha Events

Of the 4,500 two alpha events in the data, an additional three constraints were applied before results were used in further analysis. A constraint that the residuals be no greater than a certain amount ($\sim 4\times$ the mean of the residuals), and that the x-, or y-values of either of the events can be no closer than 0.01 mm to the bounds set in the fitter. This is applied to ensure only good fits are used, such that events whose starting values were not chosen well, or whose particle origins fell outside the active volume of the detector (but not enough charge was placed on the veto pads for the event to be vetoed) are not included in the final results. The final constraint was that the total energy of both particles could not be outside of $\pm 15\%$ of the kinetic energy the Q-value of the decay allows, 13.3 MeV. This corresponds to the events within the diagonal lines in Figure 5.31. From these remaining fit results, the dxy (distance between origins in the xy-plane) and dz (distance between origins in time bin dimension) values were calculated, along with the opening angle between the alphas. The residual and containment condition removes 500 events, and the energy condition removes an additional 1,100 events, leaving 2,852 events that go into the two alpha analysis. Most of the events whose residuals are too high are from the fitter failing, either starting from or moving to a parameter space in which the variation of each parameter does not improve the fit, leading the optimizer to exit and return parameter values that do not match the data well.

To extract the excess counts in the search region for double alpha events, a model is needed to estimate the background. The main background comes from two distinct sources. First, alpha particles from two independent nuclei are emitted in locations and times similar enough to one another to show up in the same event. Because these events occur entirely at random, they cover a wide parameter space in the 2D histogram. Their contribution to the background was reduced during the experiment by lowering the gas flow into the detector, at the cost of decreasing the overall event rate of ^{220}Rn decays. The second background comes from the sequential alpha decay of $^{220}\text{Rn} \rightarrow {}^{216}\text{Po} \rightarrow {}^{212}\text{Pb}$. In this case, the magnitude of the background is determined by the half-life of ^{216}Po (144 ms); the longer the half-life relative to the event time window, the less likely the ^{216}Po decay is to occur within the same event as the ^{220}Rn alpha. Because the event window is

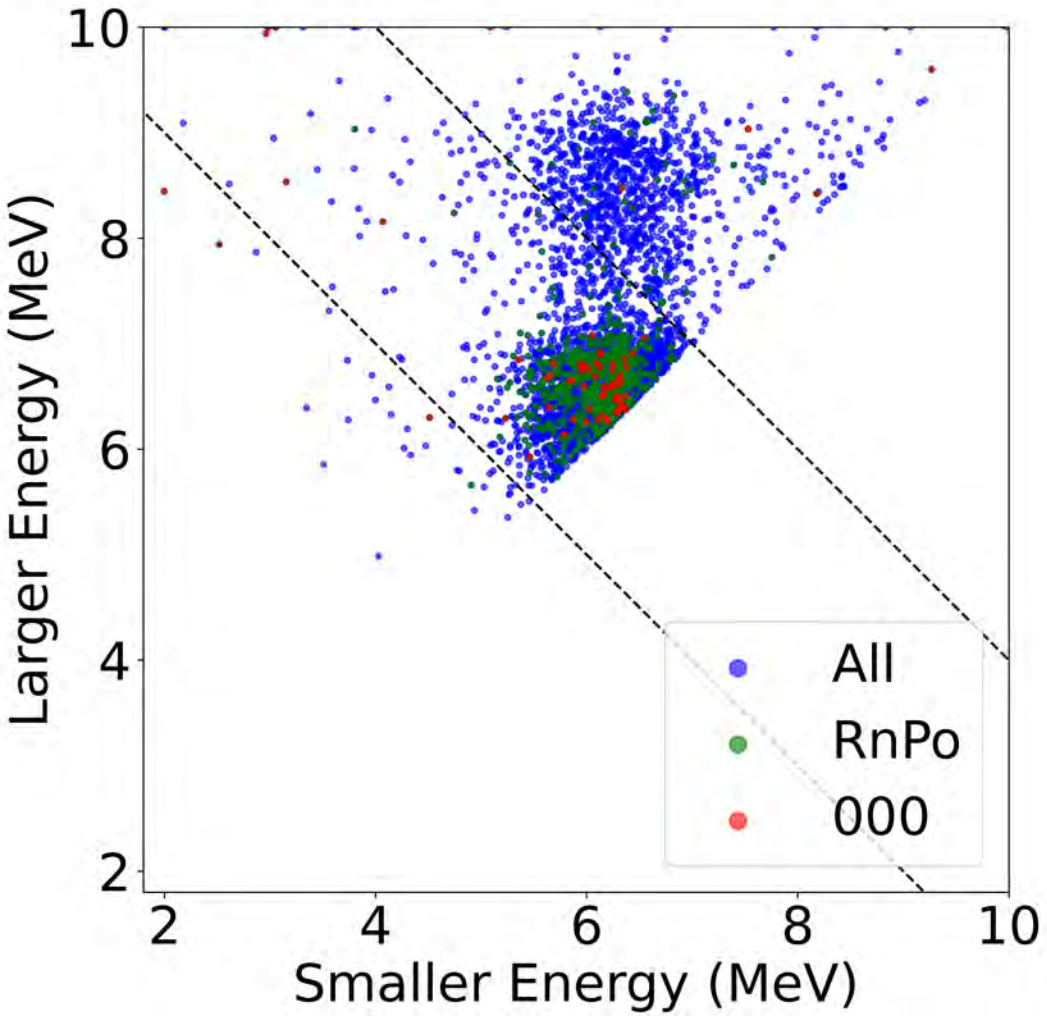

Figure 5.31 Two alpha events' energies. The larger energy is plotted on the y-axis, and the smaller energy is plotted on the x-axis. This plot incorporates the residual and location constraints described in the text. The diagonal dashed lines represent the energy cut used when extracting fit data for further double alpha analysis described later on in this chapter.

$\sim 10\ \mu$s, if the ^{216}Po decays within that window, it will not have moved far enough to be noticeable on the scale of our position resolution. The only methods it will move are via a momentum kick from the initial $^{220}\text{Rn} \rightarrow^{216}$ Po + α decay, drifting in the electric field, or Brownian motion. All three of these methods' ability to push the ^{216}Po nucleus are suppressed by the mass of the daughter nucleus, and the operating pressure of the gas. This means the origin of the alpha particle will always be at the same x-y coordinate.

One approach to model the background is entirely physics oriented from the above background discussion. Based on the xy-dist extracted from the data (Figure 5.11), and the z-distribution from theory, alpha particles were simulated in the TPC for both the accidental coincidence (AC) and sequential decay (RnPo) backgrounds. Then the particles are simulated and a veto condition is applied to the simulated data to ensure the events are confined to the active area of the TPC in the same way the veto condition is applied to the real data.

However, because the resulting background (particularly in the AC case) is highly sensitive to edge effects and radial suppression, a few approaches were taken to account for this. First, a geometrical efficiency map of the detector was created using a uniform distribution of alpha particles decaying in different regions of the detector, shown in Figure 5.32. This approach of correcting for geometric efficiency didn't work optimally for two reasons. The first is that the data it attempts to correct comes from a subset of single alpha data where the angles are nearly perpendicular to the pad plane. And second, the simulation does not take into account the charge spreading (or width) of the alpha track in the TPC. This limits the ability of the simulation to match the way the xy-distribution was created in the real data, as the nonzero width of the track accounts for the shape and degree of edge effects in the resulting distribution. A second attempt to fit the data with both these backgrounds assumes that the xy-distribution is entirely uniform, while the z-distribution still comes from theory. In this case, the 'geometric efficiency' is applied during the condition that both alpha particles must remain entirely within the active region of the detector, and no correction to the distribution is done beforehand. This results in a worse fit, given that we have evidence that the distribution is not uniform in x and y, and confirms the idea that the AC background is very

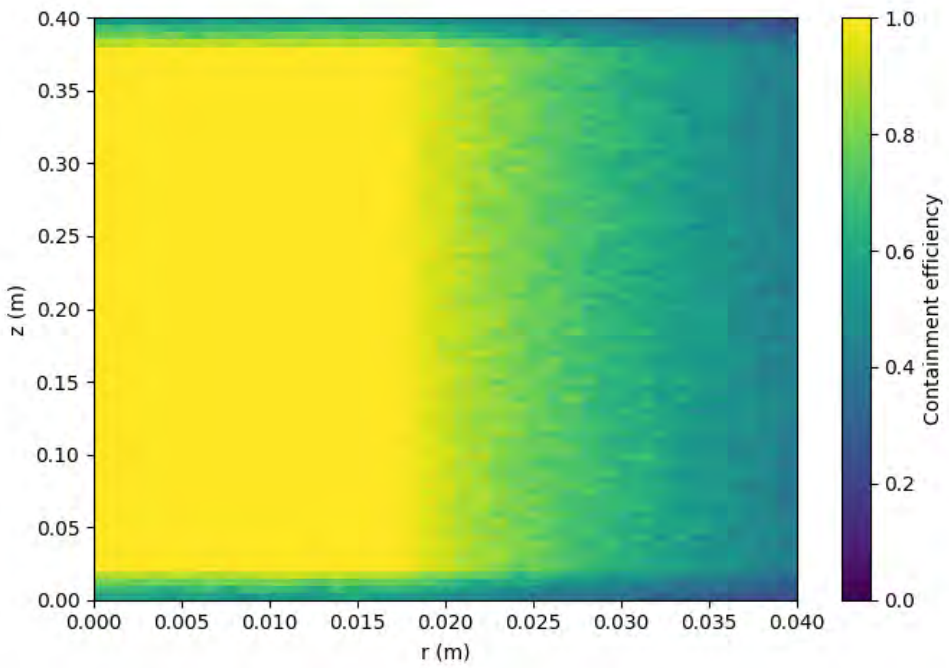

Figure 5.32 GADGET TPC alpha geometric efficiency map created from simulation.

sensitive to the xy-distribution.

Finally, in the attempt that provides the closest fit, the xy-dist. data is not corrected for efficiency, and is scaled after-the-fact in an attempt to account for the fact that the xy-dist data does not span the entire pad plane, but is missing information from the outer three pads in a ring around the pad plane. This can be seen in Figure 5.33. The TPC is 36 pads wide, so the distribution exhibits a drop off in counts prior to where one would expect, due to the finite width of the events used in extracting the distributions.

This model is simulated for 50,000 events for both the AC and RnPo background contributions, and then scaled to best fit the data from the results of the two alpha fits. The results are shown in the 2D-histogram in Figure 5.34. The dxy residuals in the AC background region are still not perfect, but the overall shape is more or less correct. Next, a gate is applied to the data and model to view the projection into dz, the results of which are shown in Figure 5.35. The right panel contains contributions from both the AC and RnPo backgrounds as well as our $\alpha\alpha$-decay signal, if it exists. The left panel only contains contributions from the accidental coincidence background, because it is assumed that the sequential decay intermediate nuclei remains virtually fixed in space during the

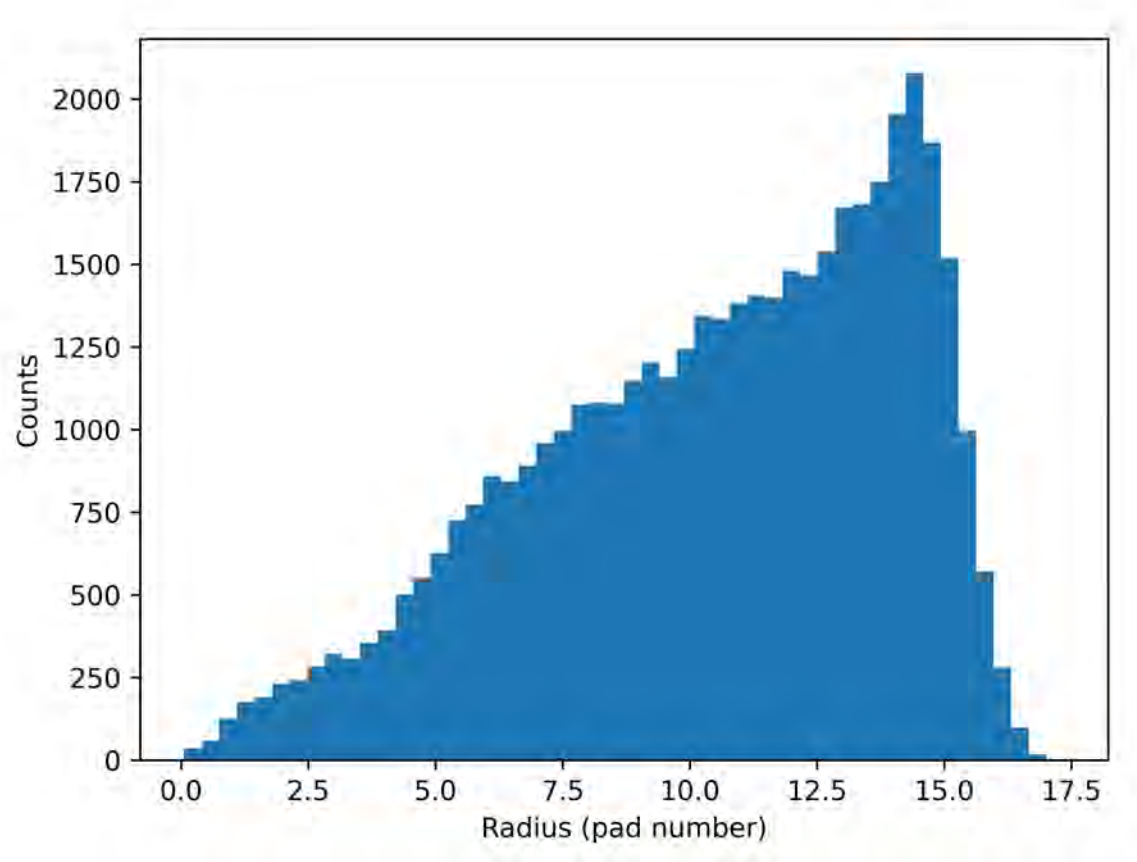

Figure 5.33 Radial distribution of radiation in the detector, generated from the centroid method shown in Figure 5.10.

$\sim$ 10 μs event window. The residuals are systematically high in the dz projection for dxy > 5.0 mm. This is due to the limitations of the two dimensional fit.

Additionally, there is slight evidence for a slope, favoring two alpha events closer in time to one another, creating a negative slope in both dz projections. We do not know the exact source of this, only that it does not appear in the simulation of the background under any conditions used for this analysis. The dz projection should be flat for the sequential RnPo events because it should be the half-life curve for ^{216}Po in the first few microseconds of its 144 millisecond half-life. To investigate and account for a potential slope, four additional models were fit to the dz projection in the AC region, using functions not driven by physics. The four models used were a zeroth, first, and second degree polynomial, as well as an exponential function. Once these fit parameters were

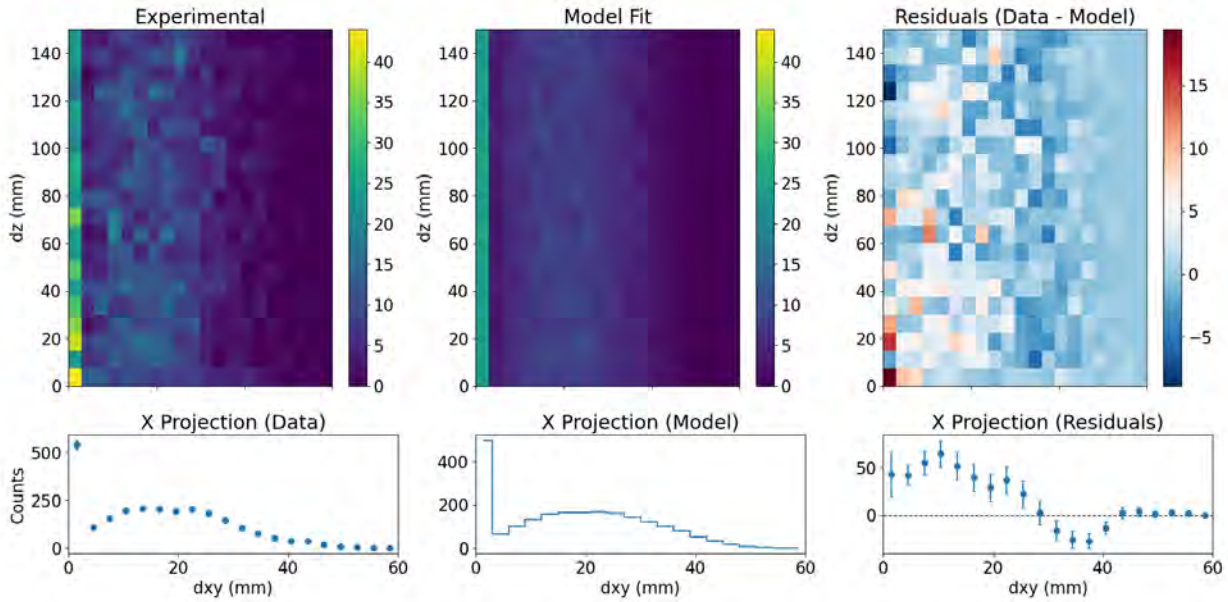

Figure 5.34 Best model fit of the dxy-dz distribution. Left panel shows the data from the fit values. Middle panel shows the scaled simulation with both the AC and RnPo background. Right panel show the residuals.

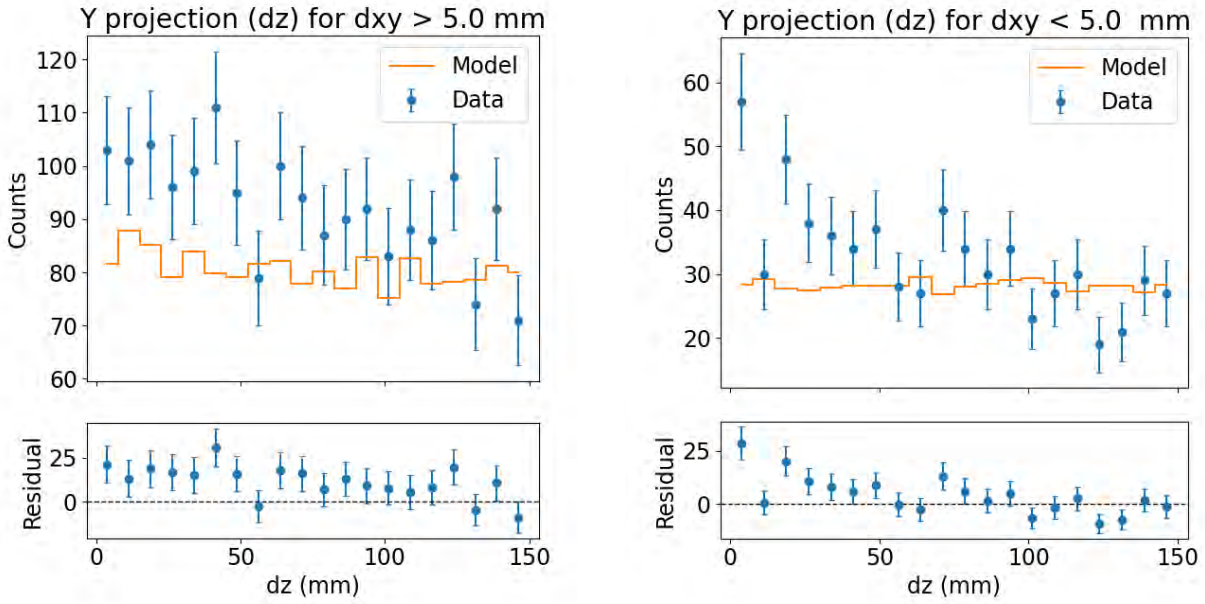

(a) $d_{xy} > 5.0$ mm

(b) $d_{xy} < 5.0$ mm

Figure 5.35 Left: Y-projection (dz) of the data and model for dxy > 5.0 mm. Right: Y-projection (dz) of the data and model for dxy < 5.0 mm.

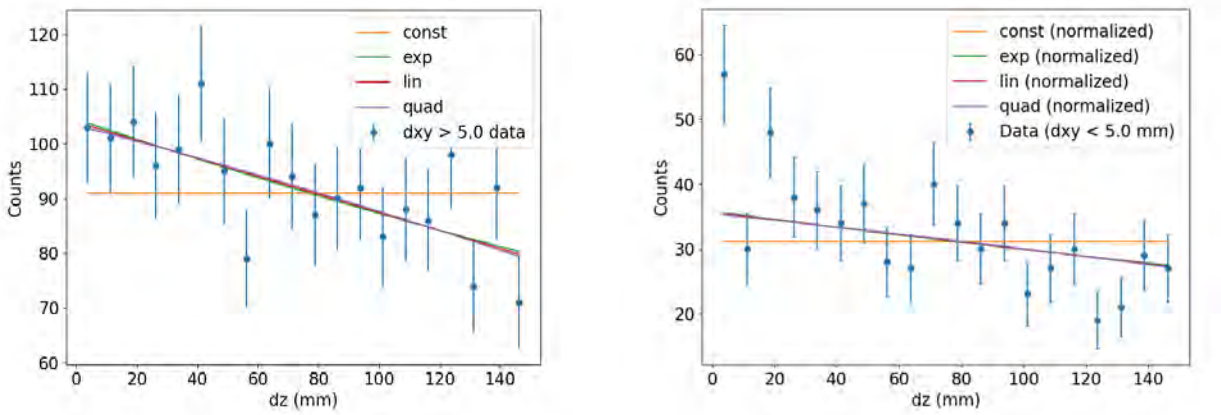

(a) $d_{xy} > 5.0$ mm (b) $d_{xy} < 5.0$ mm

Figure 5.36 Left: Projection of data and models for dxy > 5.0 mm. Right: Projection of the data and normalized models for dxy < 5.0 mm.

determined for the dxy > 5.0 mm region, the fits were normalized to the statistics in the dxy < 5.0 mm region (excluding the signal region, which is defined as dxy < 5.0 mm and dz < 7.5 mm), and used as a background to extract the excess counts in the simultaneous double alpha region near bin (dxdy,dz)=(0,0). The results of this fit process can be seen in Figure 5.35

Next, the uncertainties in the models and data were found. For the data and simulated background, the uncertainties were statistical. For the function-based models, the uncertainty in the backgrounds was calculated from the covariance matrices given by the least-squares fitting algorithm, and an estimate of the gradients of the parameters calculated from the difference in the background model based on small changes to the optimal parameters. From these uncertainties, the Feldman-Cousins 90% confidence level intervals were computed.

With the exception of the constant background function fit, all of the models predict a similar number of counts in the signal regions within their uncertainties.

However, it is also useful to consider if the shape of the dz distribution for the RnPo background is different than for the AC background. To account for this, the RnPo background was fit directly (excluding the signal bin), and compared with the data and the scaled models based on the AC background. The results are shown in Figure 5.37. It is clear that the direct fit to the background in the RnPo region results in a systematically higher estimate of the background in the signal bin

of the data. Therefore, this is factored in to the systematic error of the estimate of the background when computing the excess counts in the signal region. This is a conservative estimate, as the p-value for the constant fit does not clearly exclude this model. Additionally, there is no physical reason to model the dz projection data with a slope, except for the fact that there seems to be some unexplained detector effect causing a negative slope.

For each model, the goodness-of-fit metrics are given in Table 5.5. For the AC scaled models, the metrics are calculated from the fit to the AC data, because in these models it is assumed that the shape of the background is the same in both regions.

The full results are shown in Table 5.6. The events in the $\alpha\alpha-$decay region is higher than the background prediction, but this deviation is not greater than two standard deviations.

The direct RnPo region fit with a line was chosen as the nominal model, as it captures the slope of the background in the simplest way. This gives us a value of $N_{\text{excess}} = 18.6 \pm 8.0\ (\text{stat.})^{+10.1}_{-0.8}\ (\text{model})$, where the model uncertainty reflects the maximum deviation observed when varying the background model used. Accounting for the expected number of anomalous events in the Q-value cut region from Section 5.4.3 (3 events), the excess is reduced to a deviation below 2σ. The statistical significance of this deviation is below the level required to claim evidence for a signal. The 90% Feldman-Cousins confidence interval, obtained from the envelope of all acceptable models, is $N_{\text{excess}} \in [6.1, 42.1]$. This is the most conservative estimate of the excess in the double alpha signal region, and is used to set limits on the $\alpha\alpha-$decay branching ratio.

The next step in the analysis was to examine the opening angles of all of the two alpha events to see if it is markedly different from an isotropic distribution. The plots of the opening angle distribution are shown in Figure 5.38. In black is what the isotropic distribution should look like, weighted by the efficiency to detect a double alpha event at different opening angles. The data in blue are all two alpha events fitted, whose residuals did not exceed $\sim 4\times$ the mean of the residual distribution, and whose x- and y-values of the origins of either event did not end up near the boundaries of the fitter (±40 mm). A subset of this data is shown in red. These are candidate simultaneous double alpha events whose origins lie within 5 mm of each other in dxy and dz. If the branching ratio

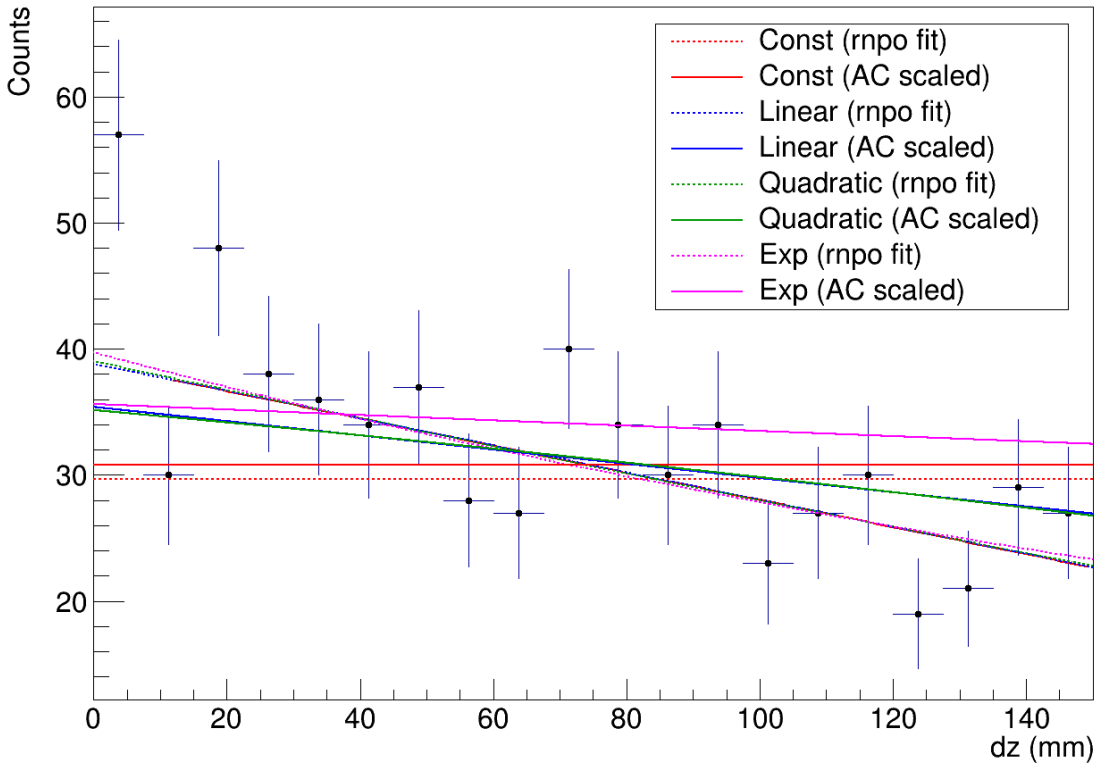

Figure 5.37 All of the models applied to the $d_{xy} < 5.0$ mm data. The solid lines represent the fits to the AC background region, which is then scaled to the statistics in the RnPo region. The dashed lines represent direct fits to the RnPo region.

Model	χ^2/dof	p-value
Constant (fit on Accidental Coin. Band)	1.20	0.244
Constant (direct)	1.56	0.060
Exponential (fit on Accidental Coin. Band)	0.65	0.864
Exponential (direct)	0.93	0.539
Linear (fit on Accidental Coin. Band)	0.65	0.866
Linear (direct)	0.93	0.542
Quadratic (fit on Accidental Coin. Band)	0.68	0.823
Quadratic (direct)	0.98	0.472

Table 5.5 Quality of the fits of the backgrounds for different models. One approach fits the background in the dxy > 5.0 mm dz projection, and scales that model to the statistics of the dxy < 5.0 mm dz projection ('fit on Accidental Coin. Band'). The values in the table for this approach represent how well the model fit the accidental coincidence band, prior to being scaled and applied to the RnPo data. The second approach fits the RnPo data (sans the first dz bin) directly as background ('direct').

Table 5.6 Results from Fitting Background to Signal Peak in Two Alpha Data. The excess uncertainties combine the Poisson uncertainty from statistics with the model uncertainty from the covariance matrices of the fit.

Model	Model Bkg in Signal Cut	Excess in Signal Cut	FC 90% CLI of Excess
Simulation	28.29 ± 0.99	28.71 ± 7.61	[16.76, 42.06]
Constant (scaled)	30.78 ± 0.74	26.23 ± 7.59	[14.49, 39.54]
Exponential (scaled)	35.54 ± 1.77	21.46 ± 7.75	[9.77, 35.25]
Linear (scaled)	35.18 ± 1.59	21.82 ± 7.72	[10.08, 35.59]
Quadratic (scaled)	34.96 ± 2.58	22.04 ± 7.98	[9.80, 36.52]
Constant (direct)	29.68 ± 1.25	27.32 ± 7.65	[15.46, 41.23]
Exponential (direct)	39.18 ± 3.18	17.82 ± 8.19	[6.13, 32.09]
Linear (direct)	38.41 ± 2.78	18.59 ± 8.04	[7.02, 33.07]
Quadratic (direct)	38.60 ± 4.49	18.40 ± 8.79	[6.14, 33.92]

of simultaneous double alpha decay is boosted by clusters forming at opposite ends of the nucleus and emitting back-to-back alphas, one would expect to see an excess of counts in the final red data point. If the two alpha particles are being produced by ^{8}Be decay into two alpha particles, one should expect an excess of counts near 10°. In both of these extreme cases, the plots do not bear this out to a statistically significant degree, so more stringent upper limits to these double alpha decay mechanisms can be set using this data.

A background to the counts in the final bin near 180° was estimated using the total counts in the dz projection for events with dxy < 5 mm and opening angles greater than 167° (6 counts), divided by the number of bins (20). This gives a value of 0.7 for counts above background at 180°. The statistics are too low for this to be used as an excess, so we report a 90% confidence interval consistent with zero: $[0.0, 4.0]$.

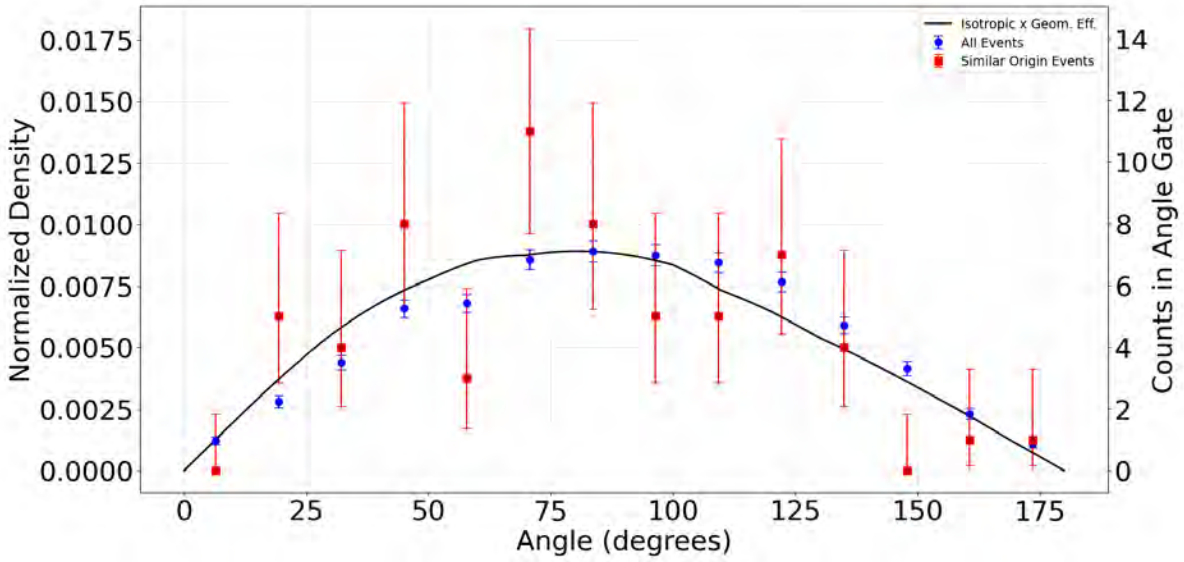

Figure 5.38 Opening angle distribution of all fitted two alpha events (blue), two alpha events with origins near (dxy < 5 mm and dz < 10 mm), and a theoretical isotropic opening angle distribution weighted by the geometric efficiency. The geometric efficiency was simulated in ten degree increments from ten degrees to 180 degrees (back-to-back). Because there is low statistics in the similar origin events data, the 68% Garwood confidence intervals were used for error bars. [168]

CHAPTER 6

SUMMARY & DISCUSSION

6.1 LIBRA and the Particle X-ray Coincidence Technique

We have demonstrated that LIBRA is a capable instrument in measuring many aspects of astrophysically relevant data. LIBRA is able to measure all charged particles, x-rays, and gamma rays emitted in EC/β^+ decay. This information combined allows us to determine the lifetimes, energies, and proton, alpha, and gamma branching ratios of resonances populated during electron capture. Coincidence measurements with LIBRA provide additional nuclear data on the proton/alpha-emitting states in the compound nucleus, and the subsequent states in the daughter nucleus. All of these data are essential inputs to statistical models for calculating reaction rates.

This comprehensive capability of LIBRA to measure all of this information in a single experiment, rather than making multiple indirect measurements, is increasingly useful as we probe harder and harder to produce nuclei. The data produced from experiments using LIBRA will constrain thermonuclear reaction rates, such as the ^{59}Cu$(p,\gamma)^{60}$Zn and ^{59}Cu$(p,\alpha)^{56}$Ni reactions.

This system can also be used in many other experiments studying similarly competing reactions, such as the ZnGa cycle, to further reduce uncertainties in p-process nucleosynthesis and X-ray burst light curve predictions.

6.2 Alpha Decay to Excited States

During this experiment, high purity germanium detectors were used in an attempt to identify new alpha decays to excited states, particularly in the alpha decays of ^{220}Rn and ^{216}Po. Only the decay of ^{220}Rn to the 550 keV excited state of ^{216}Po had been previously measured. The noble-gas nature of ^{220}Rn likely makes measurements of its α–γ decays, as well as those of its short-lived daughter ^{216}Po, more challenging using conventional methods based on solid sources. Our TPC is well suited to detect ^{220}Rn alpha particles, and when coupled with the LIBRA detectors provides a powerful system for performing this measurement.

The HPGe detector dimensions and placements relative to the TPC were implemented into

GEANT4. The ^{220}Rn radiation distribution was implemented (x- and y- dist from data, z-dist from diffusion/flow models), and simulations were run at a variety of energies to determine the detectors' efficiencies to the gamma rays of interest, see Figure 5.18. The Ge detector geometries used in the simulations were previously validated with LIBRA calibration data. Since the source of radiation distribution was unknown, their efficiencies were tuned along the total efficiency curve of Figure 5.17 to match the data via the ratios of the counts in the 550 keV peak in the north and south detectors (i.e. instead of a total efficiency of 1.46%, as predicted by the simulation of the 550 keV gammas decaying in the modeled radiation distribution, it is shifted further along the z-axis of Figure 5.17 until the ratios of the peaks are closer to one, and the total efficiency then becomes 2.27%). This method results in an $\alpha\gamma-$decay branching ratio to the 550 keV excited state in ^{216}Po that is in agreement with the previously measured data, and gives confidence that the other limits set are using reasonable efficiencies.

In the search for new alpha decays to excited states in the ^{220}Rn decay chain, alpha-gamma coincident events were extracted in the following way. A gate was placed on the mesh signal above a certain threshold, and data from events from the HPGe detectors that occurred within the coincidence window of 10 μs were plotted in an energy spectrum. The data in this histogram was compared to a pre-experiment background spectrum, normalized with the 1460 keV ^{40}K peak.

We observed a significant intensity at 550 keV, consistent and competitive with the most precise previous measurement of the known ^{220}Rn $\rightarrow^{216}$ Po* decay, as well as at 728, 786, 1080, and 1621 keV, which are all from increased activity from ^{212}Bi due to its presence in the ^{220}Rn decay chain.

We use the known 550 keV alpha-gamma ^{216}Po state as a complementary method to find the number of ^{220}Rn decays in the TPC, although this method is less precise and may be affected by uncertainties in the radiation source distribution.

In the search for evidence for new single alpha decays to ^{216}Po excited states, we examine multiple candidate states that show no statistically significant excess, allowing us to place upper limits on the branching ratios to these excited states for ^{220}Rn $\rightarrow^{216}$ Po* + α and ^{216}Po $\rightarrow^{212}$ Pb* + α decay.

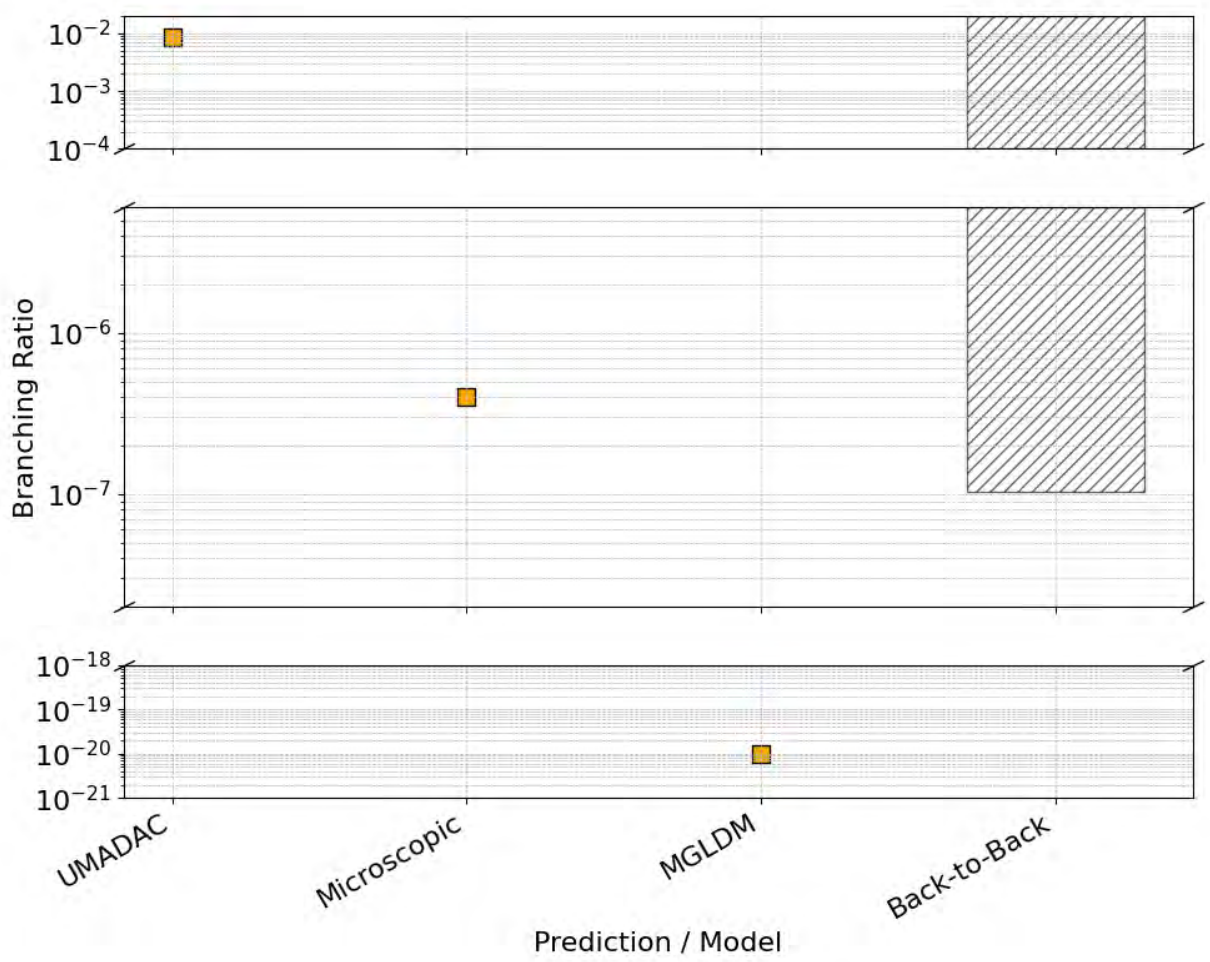

Figure 6.1 ^{220}Rn $\alpha\alpha-$decay branch. Results from different fits to the data compared to the theoretical estimates. The nominal model is the direct linear fit, and the error takes into account model and statistical uncertainties. The hatched region on the right uses the excess in counts in the last bin of Figure 5.38, and assumes back-to-back alpha particles. It shows the 90% confidence interval.

6.3 Double Alpha Decay Branching Ratio

We present the upper limit of the branching ratio for simultaneous, back-to-back $\alpha\alpha-$decay in ^{220}Rn in Figure 6.1. The shaded region represents the excluded region for the back-to-back signal, using the 90% confidence upper limit from the back-to-back opening angle bin in Figure 5.38.

For each of the background models, no angular constraint is placed on the data. The number of counts observed in the dxydz distribution is slightly larger than the background predicted by serveral models. Using the linear fit directly to the RnPo data as a nominal background model gives a difference of $N_{\text{excess}} = 18.6 \pm 8.0\ (\text{stat.})^{+10.1}_{-0.8}\ (\text{model})$. This is interpreted as being consistent with

background fluctuations, especially when lowered by the estimated 3 anomalous events calculated from Section 5.4.3.

The opening angle distribution provides an important test of the decay kinematics predicted by the models. They assume a back-to-back emission of the two $\alpha-$particles, and no excess is observed in the 180° bin of Figure 5.38. The data is consistent with the isotropic expectation. Therefore, a 90% confidence limit is set on the 180° opening-angle bin data. Consequently, the data does not support the specific back-to-back decay mechanism predicted by two of the three the theoretical models. The limit shown in Figure 6.1 can be directly compared with the microscopic model prediction.

Possible sources of coincident, alpha-like events induced via reactions rather than decays were briefly examined. No clear mechanism capable of producing significant numbers of events within the signal region was identified. Given the statistical limitations of the dataset, the results are conservatively interpreted as limits rather than evidence for a new decay.

Searches for simultaneous $\alpha\alpha-$decay requires more experimental work with larger statistics and improved background constraints.

CHAPTER 7

OUTLOOK

Although no statistically significant evidence for $\alpha\alpha-$decay was observed in thsi work, the analysis demonstrates that the technique is sensitive to branching ratios approaching the range predicted by recent theoretical models.

7.1 Future Improvements to Data Analysis

For this analysis, the biggest improvements that could be made right now, given enough computing resources to parse the terabytes of data, would be improvements to the background subtraction of the traces for energy calculation purposes, as well as pad-by-pad gain-matching to improve the energy resolution of the alpha spectra. This would allow for tighter gates on the alphas of interest, and smaller uncertainties in the final results. However, because the pad gain matching data takes into account a variety of information, such as thresholding and edge effects as well as the differences in pad gain, it would still not be used for fitting individual events.

In the fitting of events, there are a few improvements to discuss. Firstly, a free parameter that controls the uncertainty in noise and pad gain could be added along with the physical parameters in an effort to account for correlated and unaccounted for uncertainties not included in the likelihood function, see Ref. [169] for more information. Emulators could also be implemented to reduce the computation time of the likelihood function, allowing for faster iteration and more improvements being made due to the ease of experimentation with fitting the data. As of now, iterating on TPC data fits can be difficult given the slow time to converge and amount of compute necessary to process even one event, or tens of events in a highly parallelized way.

Additionally, it would be ideal to run a more comprehensive analysis of the errors associated with each fit parameter by profiling the likelihood function for each fit. However, as discussed, this is highly computationally expensive and would take a very long time with the tools currently available.

7.2 Future Tests of Double Alpha Decay

In future offline experiments measuring double alpha decay, it would be most useful to get a better validation of the source distribution of the radiation in the detector.

Replacing the current mass flow controller used in GADGET's gas handling system with a component that can handle even higher outgoing pressure to the chamber would ensure we contain a higher percentage of the two alpha events that decay in the active volume, because it would shorten the tracks. One disadvantage of this is that we have a finite range resolution, which would cause different alpha energy clusters to overlap more and more the higher the pressure is set. A larger volume TPC, particularly a TPC with increased radius, would also be marginally beneficial, as it would lessen the impact of the edge effects discussed in Section 5.4.4. It would also allow the TPC to be run at lower pressure with longer tracks. However, this would have to be coupled with the improvement in radiation distribution. The smaller the volume of gas between the original ^{228}Th source and the active volume of the detector, the more ^{220}Rn nuclei can reach the chamber before decaying.

7.2.1 Beamline Experiments

A beamline experiment has the advantage that the beam distribution is well-modeled, and it produces the nucleus of interest at rates much higher than the work presented here. However, larger rates can prove difficult given the additional background from accidental coincidences. Provided that the accidental coincidence rate can be controlled, an ideal candidate would be one whose sequential, intermediate α-decay is either extremely long-lived, or entirely energetically forbidden. ^{108}Xe would be a particularly interesting candidate to study with GADGET II, given that FRIB is one of (if not the only) places on earth that will be able to produce it in sufficient quantities, but also the $\alpha\alpha$-decay channel creates ^{100}Sn, a doubly magic nucleus, which possibly enhances the branching ratio of this channel. Unfortunately, there is not enough known about the intermediate ^{104}Te nucleus' structure, and thus it would be difficult to disentangle the $\alpha\alpha$-decay channel from a sequential $\alpha-$decay channel, which would require on our part very narrow energy resolution. Thus, it would be better to stick to cases where one of the two $\alpha-$decay Q-values are energetically

forbidden, of which there are ~50 cases to choose from [128].

BIBLIOGRAPHY

[1] Christian Iliadis. *Nuclear Physics of Stars*. Weinheim, Germany: Wiley-VCH, 2015.

[2] Erik Aver et al. "The primordial helium abundance from updated emissivities". In: *Journal of Cosmology and Astroparticle Physics* 2013.11 (Nov. 2013), p. 017. DOI: 10.1088/1475-7516/2013/11/017. URL: https://dx.doi.org/10.1088/1475-7516/2013/11/017.

[3] Christopher Sneden and John J. Cowan. "Genesis of the Heaviest Elements in the Milky Way Galaxy". In: *Science* 299.5603 (2003), pp. 70–75. DOI: 10.1126/science.1077506. eprint: https://www.science.org/doi/pdf/10.1126/science.1077506. URL: https://www.science.org/doi/abs/10.1126/science.1077506.

[4] R. H. Cyburt et al. "DEPENDENCE OF X-RAY BURST MODELS ON NUCLEAR REACTION RATES". in: *The Astrophysical Journal* 830.2 (Oct. 2016), p. 55. DOI: 10.3847/0004-637X/830/2/55. URL: https://dx.doi.org/10.3847/0004-637X/830/2/55.

[5] L. J. Sun et al. "Extension of the particle x-ray coincidence technique: The lifetimes and branching ratios apparatus". In: *Phys. Rev. C* 111 (5 May 2025), p. 055806. DOI: 10.1103/PhysRevC.111.055806. URL: https://link.aps.org/doi/10.1103/PhysRevC.111.055806.

[6] Richard H. Cyburt et al. "The JINA REACLIB database: Its recent updates and impact on type-I X-ray bursts". In: *The Astrophysical Journal Supplement Series* 189.1 (June 2010), pp. 240–252. DOI: 10.1088/0067-0049/189/1/240.

[7] J. S. Randhawa et al. "First direct measurement of ^{59}Cu$(p,\alpha)^{56}$Ni: A step towards constraining the Ni-Cu cycle in the cosmos". In: *Phys. Rev. C* 104 (4 Oct. 2021), p. L042801. DOI: 10.1103/PhysRevC.104.L042801. URL: https://link.aps.org/doi/10.1103/PhysRevC.104.L042801.

[8] D. Soltesz et al. "Determination of the ^{60}Zn level density from neutron evaporation spectra". In: *Phys. Rev. C* 103 (1 Jan. 2021), p. 015802. DOI: 10.1103/PhysRevC.103.015802. URL: https://link.aps.org/doi/10.1103/PhysRevC.103.015802.

[9] Chanhee Kim et al. "Estimation of the NiCu Cycle Strength and Its Impact on Type I X-Ray Bursts". In: *The Astrophysical Journal* 929.1 (Apr. 2022), p. 96. DOI: 10.3847/1538-4357/ac5f09. URL: https://dx.doi.org/10.3847/1538-4357/ac5f09.

[10] Konrad Schmidt. *NSCL Experiment 18039*. Tech. rep. URL: https://publicapps.nscl.msu.edu/completedExperiments/experiments/view/1157.

[11] Melina Avila. *FRIB Experiment 21026*. Tech. rep. URL: https://userportal.frib.msu.edu/Pac/Experiments/PublicList.

[12] Claudia Lederer. *The ^{59}Cu(p,α) cross section and its implications for nucleosynthesis in core collapse supernovae*. Tech. rep. 2.1E5 59Cu ions per second at HIE-ISOLDE experimental station. Geneva: CERN, 2015. URL: https://cds.cern.ch/record/2021520.

[13] Gavin Lotay. *FRIB Experiment 21014*. Tech. rep. URL: https://userportal.frib.msu.edu/Pac/Experiments/PublicList.

[14] Takumi Okamura. "Determination of spin parity of ^{60}Zn excited states for rp process." Ph.D. Thesis. PhD thesis. Osaka, Japan: Osaka University, 2024. URL: https://jglobal.jst.go.jp/en/detail?JGLOBAL_ID=202402271203007377.

[15] Tatsuya Furuno. private communication. Experiment to measure ^{59}Cu(^{3}He,d) ^{60}Zn reaction using a ^{59}Cu beam to populate ^{60}Zn states and to measure the decay branching ratios.

[16] Zach Meisel. *NSCL Experiment 17009*. Tech. rep. URL: https://publicapps.nscl.msu.edu/completedExperiments/experiments/view/1011.

[17] Christopher Wrede. *FRIB Experiment 23035*. Tech. rep. URL: https://userportal.frib.msu.edu/Pac/Experiments/PublicList.

[18] N. Bhathi et al. "Direct Measurement of 59Cu(p,α)56Ni Precludes a Strong NiCu Cycle in Type-I X-Ray Bursts". In: *The Astrophysical Journal* 999.1 (Feb. 2026), p. 8. DOI: 10.3847/1538-4357/ae3de6. URL: https://doi.org/10.3847/1538-4357/ae3de6.

[19] S. E. A. Orrigo et al. "β decay of the very neutron-deficient ^{60}Ge and ^{62}Ge nuclei". In: *Phys. Rev. C* 103 (1 Jan. 2021), p. 014324. DOI: 10.1103/PhysRevC.103.014324. URL: https://link.aps.org/doi/10.1103/PhysRevC.103.014324.

[20] S. F. Paul et al. "Mass measurements of $^{60–63}$Ga reduce x-ray burst model uncertainties and extend the evaluated $T = 1$ isobaric multiplet mass equation". In: *Phys. Rev. C* 104 (6 Dec. 2021), p. 065803. DOI: 10.1103/PhysRevC.104.065803. URL: https://link.aps.org/doi/10.1103/PhysRevC.104.065803.

[21] M. Wang et al. "Mass Measurement of Upper fp-Shell $N = Z - 2$ and $N = Z - 1$ Nuclei and the Importance of Three-Nucleon Force along the $N = Z$ Line". In: *Phys. Rev. Lett.* 130 (19 May 2023), p. 192501. DOI: 10.1103/PhysRevLett.130.192501. URL: https://link.aps.org/doi/10.1103/PhysRevLett.130.192501.

[22] Meng Wang et al. "The AME 2020 atomic mass evaluation (II). Tables, graphs and references*". In: *Chinese Physics C* 45.3 (Mar. 2021), p. 030003. DOI: 10.1088/1674-1137/abddaf. URL: https://dx.doi.org/10.1088/1674-1137/abddaf.

[23] C. Mazzocchi et al. "First measurement of β-decay properties of the proton drip-line nucleus 60Ga". In: *The European Physical Journal A - Hadrons and Nuclei* 12 (3 Nov. 2001), pp. 269–277. DOI: https://doi.org/10.1007/s100500170004.

[24] Alexandre Obertelli and Hiroyuki Sagawa. *Modern Nuclear Physics: From Fundamentals to Frontiers*. 1st ed. Springer, 2021.

[25] Kenneth Krane. *Introductory Nuclear Physics*. John Willow and Sons Inc., 1998.

[26] *Basic Properties of the Atomic Nucleus. Handbook of Nuclear Chemistry: Basics of Nuclear Science; Elements and Isotopes: Formation, Transformation, Distribution; Chemical Applications of Nuclear Reactions and Radiations; Radiochemistry and Radiopharmaceutical Chemistry in Life Sciences; Instrumentation, Separation Techniques, Environmental Issues*. Boston, MA: Springer US, 2004, pp. 44–136. ISBN: 978-0-387-30682-7. DOI: 10.1007/0-387-30682-X_2. URL: https://doi.org/10.1007/0-387-30682-X_2.

[27] Daniel Lay. "Novel Computational Approaches for Nuclear Fission Theory". Available at https://doi.org/doi:10.25335/ydvq-8985. PhD thesis. East Lansing, MI: Michigan State University, Mar. 2025.

[28] P. Hohenberg and W. Kohn. "Inhomogeneous Electron Gas". In: *Phys. Rev.* 136 (3B Nov. 1964), B864–B871. DOI: 10.1103/PhysRev.136.B864. URL: https://link.aps.org/doi/10.1103/PhysRev.136.B864.

[29] W. Kohn and L. J. Sham. "Self-Consistent Equations Including Exchange and Correlation Effects". In: *Phys. Rev.* 140 (4A Nov. 1965), A1133–A1138. DOI: 10.1103/PhysRev.140.A1133. URL: https://link.aps.org/doi/10.1103/PhysRev.140.A1133.

[30] N Schunck and L M Robledo. "Microscopic theory of nuclear fission: a review". In: *Reports on Progress in Physics* 79.11 (Oct. 2016), p. 116301. DOI: 10.1088/0034-4885/79/11/116301. URL: https://dx.doi.org/10.1088/0034-4885/79/11/116301.

[31] Nicolas Schunck, ed. *Energy Density Functional Methods for Atomic Nuclei*. 2053-2563. IOP Publishing, 2019. ISBN: 978-0-7503-1422-0. DOI: 10.1088/2053-2563/aae0ed. URL: https://dx.doi.org/10.1088/2053-2563/aae0ed.

[32] A Sandulescu, D N Poenaru, and W Greiner. "New type of decay of heavy nuclei intermediate between fission and. cap alpha. decay". In: *Sov. J. Particles Nucl. (Engl. Transl.); (United States)* 11:6 (Nov. 1980). URL: https://www.osti.gov/biblio/6189038.

[33] H. J. Rose and G. A. Jones. "A new kind of natural radioactivity". In: *Nature* 307 (5948 Jan. 1984). URL: https://doi.org/10.1038/307245a0.

[34] P. B. Price et al. "Discovery of Radioactive Decay of ^{222}Ra and ^{224}Ra by ^{14}C Emission". In: *Phys. Rev. Lett.* 54 (4 Jan. 1985), pp. 297–299. DOI: 10.1103/PhysRevLett.54.297. URL: https://link.aps.org/doi/10.1103/PhysRevLett.54.297.

[35] D. Weselka, P. Hille, and A. Chalupka. "Decay of ^{226}Ra by ^{14}C emission". In: *Phys. Rev. C* 41 (2 Feb. 1990), pp. 778–781. DOI: 10.1103/PhysRevC.41.778. URL: https:

//link.aps.org/doi/10.1103/PhysRevC.41.778.

[36] R. Bonetti et al. "Revising the chart of the nuclides by exotic decay". In: *Physics Letters B* 241.2 (1990), pp. 179–183. ISSN: 0370-2693. DOI: https://doi.org/10.1016/0370-2693(90)91274-F. URL: https://www.sciencedirect.com/science/article/pii/037026939091274F.

[37] M. Hussonnois et al. "Search for a fine structure in the ^{14}C decay of ^{222}Ra". In: *Phys. Rev. C* 43 (6 June 1991), pp. 2599–2604. DOI: 10.1103/PhysRevC.43.2599. URL: https://link.aps.org/doi/10.1103/PhysRevC.43.2599.

[38] R. Bonetti et al. "Neon radioactivity of uranium isotopes". In: *Phys. Rev. C* 44 (2 Aug. 1991), pp. 888–890. DOI: 10.1103/PhysRevC.44.888. URL: https://link.aps.org/doi/10.1103/PhysRevC.44.888.

[39] E. Hourani et al. "Fine structure in ^{14}C emission from ^{223}Ra and ^{224}Ra". In: *Phys. Rev. C* 44 (4 Oct. 1991), pp. 1424–1434. DOI: 10.1103/PhysRevC.44.1424. URL: https://link.aps.org/doi/10.1103/PhysRevC.44.1424.

[40] R. Bonetti et al. "Discovery of oxygen radioactivity of atomic nuclei". In: *Nuclear Physics A* 556.1 (1993), pp. 115–122. ISSN: 0375-9474. DOI: https://doi.org/10.1016/0375-9474(93)90241-O. URL: https://www.sciencedirect.com/science/article/pii/037594749390241O.

[41] S. P. Tret'yakova et al. "Cluster decay of ^{236}U". In: 59 (6 1994), p. 368. URL: http://jetpletters.ru/ps/0/article_19753.shtml.

[42] M. Hussonnois et al. "Cluster decay of ^{236}Pu and correlations of the probabilities of a decay, cluster decay, and spontaneous fission of heavy nuclei". In: 62 (9 1995), p. 685. URL: http://jetpletters.ru/ps/0/article_18439.shtml.

[43] R. Bonetti et al. "First observation of spontaneous fission and search for cluster decay of ^{232}Th". In: *Phys. Rev. C* 51 (5 May 1995), pp. 2530–2533. DOI: 10.1103/PhysRevC.51.2530. URL: https://link.aps.org/doi/10.1103/PhysRevC.51.2530.

[44] A. A. Ogloblin et al. "Observation of cluster decay of ^{242}Cm". In: *Phys. Rev. C* 61 (3 Feb. 2000), p. 034301. DOI: 10.1103/PhysRevC.61.034301. URL: https://link.aps.org/doi/10.1103/PhysRevC.61.034301.

[45] S. W. Barwick, P. B. Price, and J. D. Stevenson. "Radioactive decay of ^{232}U by ^{24}Ne emission". In: *Phys. Rev. C* 31 (5 May 1985), pp. 1984–1986. DOI: 10.1103/PhysRevC.31.1984. URL: https://link.aps.org/doi/10.1103/PhysRevC.31.1984.

[46] R. Bonetti et al. "Cluster decay of 230U via Ne emission". In: *Nuclear Physics A* 686.1 (2001), pp. 64–70. ISSN: 0375-9474. DOI: https://doi.org/10.1016/S0375-9474(00)00508-X. URL: https://www.sciencedirect.com/science/article/pii/S037594740000508X.

[47] E. Hourani et al. “Evidence for the radioactive decay of 226Ra by 14C emission”. In: *Physics Letters B* 160.6 (1985), pp. 375–379. ISSN: 0370-2693. DOI: https://doi.org/10.1016/0370-2693(85)90004-8. URL: https://www.sciencedirect.com/science/article/pii/0370269385900048.

[48] S. W. Barwick et al. “Systematics of spontaneous emission of intermediate mass fragments from heavy nuclei”. In: *Phys. Rev. C* 34 (1 July 1986), pp. 362–365. DOI: 10.1103/PhysRevC.34.362. URL: https://link.aps.org/doi/10.1103/PhysRevC.34.362.

[49] C. E. Price and G. E. Walker. “Self-consistent Hartree description of deformed nuclei in a relativistic quantum field theory”. In: *Phys. Rev. C* 36 (1 July 1987), pp. 354–364. DOI: 10.1103/PhysRevC.36.354. URL: https://link.aps.org/doi/10.1103/PhysRevC.36.354.

[50] Shicheng Wang et al. “Heavy fragment radioactivity of ^{238}Pu: Si and Mg emission”. In: *Phys. Rev. C* 39 (4 Apr. 1989), pp. 1647–1650. DOI: 10.1103/PhysRevC.39.1647. URL: https://link.aps.org/doi/10.1103/PhysRevC.39.1647.

[51] K. J. Moody et al. “Heavy-fragment radioactivity of ^{234}U”. In: *Phys. Rev. C* 39 (6 June 1989), pp. 2445–2447. DOI: 10.1103/PhysRevC.39.2445. URL: https://link.aps.org/doi/10.1103/PhysRevC.39.2445.

[52] S. P. Tretyakova et al. “Observation of nucleon clusters in the spontaneous decay of234U”. in: *Zeitschrift für Physik A Atomic Nuclei* 333.4 (Dec. 1989), pp. 349–353. ISSN: 0939-7922. DOI: 10.1007/BF01299687. URL: https://doi.org/10.1007/BF01299687.

[53] A.A. Ogloblin et al. “Detection of radioactive 236Pu decay with emission of 28Mg nuclei”. In: *Physics Letters B* 235.1 (1990), pp. 35–39. ISSN: 0370-2693. DOI: https://doi.org/10.1016/0370-2693(90)90092-K. URL: https://www.sciencedirect.com/science/article/pii/037026939090092K.

[54] Walter Greiner and Raj K. Gupta. *Heavy elements and related new phenomena*. Vol. 1. World Scientific, 1999. DOI: https://doi.org/10.1142/3664.

[55] D. N. Poenaru et al. “Systematics of cluster decay modes”. In: *Phys. Rev. C* 65 (5 Apr. 2002), p. 054308. DOI: 10.1103/PhysRevC.65.054308. URL: https://link.aps.org/doi/10.1103/PhysRevC.65.054308. Erratum. Poenaru et al. [170].

[56] D. N. Poenaru and M. Ivaşcu. “Heavy ion radioactivities, cold fission and alpha decay in a unified approach”. In: *Symmetries and Semiclassical Features of Nuclear Dynamics*. Ed. by A. A. Raduta. Berlin, Heidelberg: Springer Berlin Heidelberg, 1987, pp. 364–382. ISBN: 978-3-540-47112-7.

[57] D.N. Poenaru and M. Ivascu. In: *J. Physique Lett.* 46.13 (July 1985), pp. 591–594. DOI: 10.1051/jphyslet:019850046013059100.

[58] G Royer and B Remaud. "Fission processes through compact and creviced shapes". In: *Journal of Physics G: Nuclear Physics* 10.8 (Aug. 1984), p. 1057. DOI: 10.1088/0305-4616/10/8/011. URL: https://dx.doi.org/10.1088/0305-4616/10/8/011.

[59] G. Royer and B. Remaud. "Static and dynamic fusion barriers in heavy-ion reactions". In: *Nuclear Physics A* 444.3 (1985), pp. 477–497. ISSN: 0375-9474. DOI: https://doi.org/10.1016/0375-9474(85)90464-6. URL: https://www.sciencedirect.com/science/article/pii/0375947485904646.

[60] Stanley Cohen and Wladyslaw J Swiatecki. "The deformation energy of a charged drop: Part V: Results of electronic computer studies". In: *Annals of Physics* 22.3 (1963), pp. 406–437. ISSN: 0003-4916. DOI: https://doi.org/10.1016/0003-4916(63)90385-3. URL: https://www.sciencedirect.com/science/article/pii/0003491663903853.

[61] Megha Chandran and K. P. Santhosh. "α and 2α decay of nuclei in the region $94 \leq Z \leq 101$ using the modified generalized liquid drop model". In: *Phys. Rev. C* 107 (2 Feb. 2023), p. 024614. DOI: 10.1103/PhysRevC.107.024614. URL: https://link.aps.org/doi/10.1103/PhysRevC.107.024614.

[62] K. P. Santhosh and Tinu Ann Jose. "Theoretical investigation on double-α decay from radioactive nuclei". In: *Phys. Rev. C* 104 (6 Dec. 2021), p. 064604. DOI: 10.1103/PhysRevC.104.064604. URL: https://link.aps.org/doi/10.1103/PhysRevC.104.064604.

[63] E. Rutherford. "I. A radio-active substance emitted from thorium compounds". In: *The London, Edinburgh, and Dublin Philosophical Magazine and Journal of Science* 49.296 (1900), pp. 1–14. DOI: 10.1080/14786440009463821.

[64] Milorad Mladjenović. *The History of Early Nuclear Physics (1896-1931)*. 128 Farrer Road, Singapore 9128: World Scientific Publishing Co. Pte. Ltd., 1992.

[65] W. Kurcewicz et al. "Collective states fed by weak α-transltions in the 232U chain". In: *Nuclear Physics A* 289.1 (1977), pp. 1–14. ISSN: 0375-9474. DOI: https://doi.org/10.1016/0375-9474(77)90516-4. URL: https://www.sciencedirect.com/science/article/pii/0375947477905164.

[66] Abraham Pais. *Inward Bound: Of Matter and Forces in the Physical World*. New York: Oxford University Press, 1986.

[67] E. Rutherford H. T. Brooks. "The New Gas from Radium". In: vol. ser. 2, v. 7 (1901). https://www.biodiversitylibrary.org/bibliography/10076. Ottawa [etc.], Société royale du Canada, 1901, p. 21. URL: https://www.biodiversitylibrary.org/page/10745147.

[68] E. Rutherford and H.T. Brooks. "I. Comparison of the radiations from radioactive substances". In: *The London, Edinburgh, and Dublin Philosophical Magazine and Journal of*

Science 4.19 (1902), pp. 1–23. DOI: 10.1080/14786440209462814. eprint: https://doi.org/10.1080/14786440209462814. URL: https://doi.org/10.1080/14786440209462814.

[69] HARRIET BROOKS. "A Volatile Product from Radium". In: *Nature* 70.1812 (July 1904), pp. 270–270. ISSN: 1476-4687. DOI: 10.1038/070270b0. URL: https://doi.org/10.1038/070270b0.

[70] E. RUTHERFORD. "Emanations from Radio-active Substances". In: *Nature* 64.1650 (June 1901), pp. 157–158. ISSN: 1476-4687. DOI: 10.1038/064157a0. URL: https://doi.org/10.1038/064157a0.

[71] Marelene F. Rayner-Canham and Geoffrey Rayner-Canham. *Harriet Brooks Pioneer Nuclear Scientist*. McGill University Press, 2009.

[72] P J Nolan and J F Sharpey-Schafer. "The measurement of the lifetimes of excited nuclear states". In: *Reports on Progress in Physics* 42.1 (Jan. 1979), p. 1. DOI: 10.1088/0034-4885/42/1/001. URL: https://dx.doi.org/10.1088/0034-4885/42/1/001.

[73] J. C. Hardy et al. "Nuclear Lifetimes in the Region of 10^{-16} sec Measured by a New Technique". In: *Phys. Rev. Lett.* 37 (3 July 1976), pp. 133–136. DOI: 10.1103/PhysRevLett.37.133. URL: https://link.aps.org/doi/10.1103/PhysRevLett.37.133.

[74] J.L. Campbell and Tibor Papp. "WIDTHS OF THE ATOMIC K–N7 LEVELS". in: *Atomic Data and Nuclear Data Tables* 77.1 (2001), pp. 1–56. ISSN: 0092-640X. DOI: https://doi.org/10.1006/adnd.2000.0848. URL: https://www.sciencedirect.com/science/article/pii/S0092640X00908489.

[75] S. T. Perkins et al. *Tables and graphs of atomic subshell and relaxation data derived from the LLNL Evaluated Atomic Data Library (EADL), Z = 1–100*. Tech. rep. Lawrence Livermore National Lab. (LLNL), Livermore, CA (United States), Oct. 1991. DOI: 10.2172/10121422. URL: https://www.osti.gov/biblio/10121422.

[76] Walter Bambynek et al. "X-Ray Fluorescence Yields, Auger, and Coster-Kronig Transition Probabilities". In: *Rev. Mod. Phys.* 44 (4 Oct. 1972), pp. 716–813. DOI: 10.1103/RevModPhys.44.716. URL: https://link.aps.org/doi/10.1103/RevModPhys.44.716.

[77] J.H. Scofield. "6 - Radiative Transitions". In: *Atomic Inner-Shell Processes*. Ed. by Bernd Crasemann. Academic Press, 1975, pp. 265–292. ISBN: 978-0-12-196901-1. DOI: https://doi.org/10.1016/B978-0-12-196901-1.50012-1. URL: https://www.sciencedirect.com/science/article/pii/B9780121969011500121.

[78] Karol Kozioł. "Relativistically calculated K-shell level widths and fluorescence yields for atoms with $20 \leq Z \leq 30$". In: *Phys. Rev. A* 89 (2 Feb. 2014), p. 022515. DOI: 10.1103/PhysRevA.89.022515. URL: https://link.aps.org/doi/10.1103/PhysRevA.89.

022515.

[79] P. Asboe-Hansen et al. “Average excited state lifetimes in 73Br”. In: *Nuclear Physics A* 361.1 (1981), pp. 23–34. ISSN: 0375-9474. DOI: https://doi.org/10.1016/0375-9474(81)90469-3. URL: https://www.sciencedirect.com/science/article/pii/0375947481904693.

[80] J. Giovinazzo, Ph. Dessagne, and Ch. Miehé. “The delayed proton emission in the A 65–77 mass region, statistical aspects and structure effects”. In: *Nuclear Physics A* 674.3 (2000), pp. 394–410. ISSN: 0375-9474. DOI: https://doi.org/10.1016/S0375-9474(00)00142-1. URL: https://www.sciencedirect.com/science/article/pii/S0375947400001421.

[81] J.C. Hardy et al. “Tz = case12 β-delayed proton precursors: (II). The decays of 65Ge and 73Kr”. In: *Nuclear Physics A* 371.3 (1981), pp. 349–363. ISSN: 0375-9474. DOI: https://doi.org/10.1016/0375-9474(81)90051-8. URL: https://www.sciencedirect.com/science/article/pii/0375947481900518.

[82] J.A. Macdonald et al. “Tz = 12β-delayed proton precursors: (I). The decay of 69Se”. In: *Nuclear Physics A* 288.1 (1977), pp. 1–22. ISSN: 0375-9474. DOI: https://doi.org/10.1016/0375-9474(77)90078-1. URL: https://www.sciencedirect.com/science/article/pii/0375947477900781.

[83] C. H. Johnson. “Statistical model radiation widths for $75 < A < 130$ and the enhancement of P-wave neutron capture for $A \approx 90$”. In: *Phys. Rev. C* 16 (6 Dec. 1977), pp. 2238–2248. DOI: 10.1103/PhysRevC.16.2238. URL: https://link.aps.org/doi/10.1103/PhysRevC.16.2238.

[84] W. Dilg et al. “Level density parameters for the back-shifted fermi gas model in the mass range 40 < A < 250”. In: *Nuclear Physics A* 217.2 (1973), pp. 269–298. ISSN: 0375-9474. DOI: https://doi.org/10.1016/0375-9474(73)90196-6. URL: https://www.sciencedirect.com/science/article/pii/0375947473901966.

[85] Matt Newville et al. *xraypy/XrayDB: 4.5.1*. Version 4.5.1. Aug. 2023. DOI: 10.5281/zenodo.8212749. URL: https://doi.org/10.5281/zenodo.8212749.

[86] E. Browne and J.K. Tuli. “Nuclear Data Sheets for A = 65”. In: *Nuclear Data Sheets* 111.9 (2010), pp. 2425–2553. ISSN: 0090-3752. DOI: https://doi.org/10.1016/j.nds.2010.09.002. URL: https://www.sciencedirect.com/science/article/pii/S0090375210000866

[87] J.C. Hardy et al. “A new series of beta-delayed proton precursors”. In: *Physics Letters B* 63.1 (1976), pp. 27–30. ISSN: 0370-2693. DOI: https://doi.org/10.1016/0370-2693(76)90460-3. URL: https://www.sciencedirect.com/science/article/pii/0370269376904603.

[88] K. Vierinen. “High resolution Gamow-teller strength measurement via β-decay of 65Ge”. In: *Nuclear Physics A* 463.3 (1987), pp. 605–619. ISSN: 0375-9474. DOI: https://doi.org/10.1016/0375-9474(87)90633-6. URL: https://www.sciencedirect.com/science/

article/pii/0375947487906336.

[89] C.D. Nesaraja. "Nuclear Data Sheets for A=69". In: *Nuclear Data Sheets* 115 (2014), pp. 1–134. ISSN: 0090-3752. DOI: https://doi.org/10.1016/j.nds.2013.12.001. URL: https://www.sciencedirect.com/science/article/pii/S0090375213000938.

[90] Ph. Dessagne et al. "β^+–electron-capture decay of ^{69}Se". In: *Phys. Rev. C* 37 (6 June 1988), pp. 2687–2693. DOI: 10.1103/PhysRevC.37.2687. URL: https://link.aps.org/doi/10.1103/PhysRevC.37.2687.

[91] Balraj Singh and Jun Chen. "Nuclear Data Sheets for A=73". In: *Nuclear Data Sheets* 158 (2019), pp. 1–257. ISSN: 0090-3752. DOI: https://doi.org/10.1016/j.nds.2019.02.006. URL: https://www.sciencedirect.com/science/article/pii/S0090375219300195.

[92] P. HornshøJ et al. "Beta-delayed proton emitter 73kr". In: *Nuclear Physics A* 187.3 (1972), pp. 637–640. ISSN: 0375-9474. DOI: https://doi.org/10.1016/0375-9474(72)90687-2. URL: https://www.sciencedirect.com/science/article/pii/0375947472906872.

[93] Ch. Miehé et al. "The β+-electron capture decay of 73Kr". In: *The European Physical Journal A - Hadrons and Nuclei* 5 (2 June 1999), pp. 143–150. DOI: https://doi.org/10.1007/s100500050270.

[94] P. Asboe-Hansen et al. "Excited state lifetimes in 73Br measured by the particle X-ray coincidence technique". In: *Physics Letters B* 77.4 (1978), pp. 363–366. ISSN: 0370-2693. DOI: https://doi.org/10.1016/0370-2693(78)90578-6. URL: https://www.sciencedirect.com/science/article/pii/0370269378905786.

[95] Balraj Singh and Ninel Nica. "Nuclear Data Sheets for A = 77". In: *Nuclear Data Sheets* 113.5 (2012), pp. 1115–1314. ISSN: 0090-3752. DOI: https://doi.org/10.1016/j.nds.2012.05.001. URL: https://www.sciencedirect.com/science/article/pii/S0090375212000403.

[96] Jean Blachot. "Nuclear Data Sheets for A = 113". In: *Nuclear Data Sheets* 111.6 (2010), pp. 1471–1618. ISSN: 0090-3752. DOI: https://doi.org/10.1016/j.nds.2010.05.001. URL: https://www.sciencedirect.com/science/article/pii/S0090375210000529.

[97] Z. Janas et al. "Lifetimes of proton unstable states in 113I measured by the particle-X-ray coincidence technique". In: *The European Physical Journal A - Hadrons and Nuclei* 24 (2 2005), pp. 205–209. DOI: https://doi.org/10.1140/epja/i2004-10137-2.

[98] Z. Janas et al. "Total absorption spectroscopy of the β-delayed proton emitter 117Ba". In: *The European Physical Journal A - Hadrons and Nuclei* 23 (3 2005), pp. 401–408. DOI: https://doi.org/10.1140/epja/i2004-10103-0.

[99] JEAN BLACHOT. "Nuclear Data Sheets for A = 117". In: *Nuclear Data Sheets* 95.3 (2002), pp. 679–836. ISSN: 0090-3752. DOI: https://doi.org/10.1006/ndsh.2002.0007. URL: https://www.sciencedirect.com/science/article/pii/S0090375202900074.

[100] Balraj Singh and Jun Chen. "Nuclear Data Sheets for A=64". In: *Nuclear Data Sheets* 178 (2021), pp. 41–537. ISSN: 0090-3752. DOI: https://doi.org/10.1016/j.nds.2021.11.002. URL: https://www.sciencedirect.com/science/article/pii/S0090375221000624.

[101] X. Zhou et al. "Mass measurements show slowdown of rapid proton capture process at waiting-point nucleus 64Ge". In: *Nature Physics* 19.8 (Aug. 2023), pp. 1091–1097. ISSN: 1745-2481. DOI: 10.1038/s41567-023-02034-2. URL: https://doi.org/10.1038/s41567-023-02034-2.

[102] B. Rubio et al. "Beta decay of the Tz=-2 nucleus 64Se and its descendants". In: *Journal of Physics: Conference Series* 1308.1 (Aug. 2019), p. 012018. DOI: 10.1088/1742-6596/1308/1/012018. URL: https://dx.doi.org/10.1088/1742-6596/1308/1/012018.

[103] A.C.C. Villari et al. "Gas stopping and reacceleration techniques at the Facility for Rare Isotope Beams (FRIB)". in: *Nuclear Instruments and Methods in Physics Research Section B: Beam Interactions with Materials and Atoms* 541 (2023), pp. 350–354. ISSN: 0168-583X. DOI: https://doi.org/10.1016/j.nimb.2023.05.037. URL: https://www.sciencedirect.com/science/article/pii/S0168583X23002422.

[104] T. Xu et al. "Completion of FRIB Superconducting Linac and Phased Beam Commissioning". In: *Proc. SRF'21* (East Lansing, MI, USA). International Conference on RF Superconductivity 20. JACoW Publishing, Geneva, Switzerland, Oct. 2022, MOOFAV10, pp. 197–202. ISBN: 978-3-95450-233-2. DOI: 10.18429/JACoW-SRF2021-MOOFAV10. URL: https://jacow.org/srf2021/papers/moofav10.pdf.

[105] P. B. PRICE and R. M. WALKER. "Observation of Fossil Particle Tracks in Natural Micas". In: *Nature* 196.4856 (Nov. 1962), pp. 732–734. ISSN: 1476-4687. DOI: 10.1038/196732a0. URL: https://doi.org/10.1038/196732a0.

[106] Andrzej K. Drukier et al. "Paleo-detectors: Searching for dark matter with ancient minerals". In: *Phys. Rev. D* 99 (4 Feb. 2019), p. 043014. DOI: 10.1103/PhysRevD.99.043014. URL: https://link.aps.org/doi/10.1103/PhysRevD.99.043014.

[107] Glenn F. Knoll. *Radiation detection and measurement*. 3rd ed. Wiley, 2000.

[108] *MIRION LEGe™ Low Energy Germanium Detector*. URL: https://www.mirion.com/products/lege-low-energy-germanium-detector (visited on 05/14/2025).

[109] Erik Jensen. "Decays At The Edge: Probing Light Proton-Rich Nuclei at State-Of-The-Art Rare Ion Beam Facilities". Ph.D. Thesis. PhD thesis. Aarhus, Denmark: Aarhus University, 2024. URL: https://pure.au.dk/portal/en/publications/decays-at-the-edge-probing-

[110] Ruchi Mahajan et al. “Time projection chamber for GADGET II”. in: *Phys. Rev. C* 110 (3 Sept. 2024), p. 035807. DOI: 10.1103/PhysRevC.110.035807. URL: https://link.aps.org/doi/10.1103/PhysRevC.110.035807.

[111] Mitch Allmond et al. *FRIB Decay Station White Paper*. Accessed: 2025-06-21. 2020. URL: https://fds.ornl.gov/wp-content/uploads/2020/09/FDS-WP.pdf.

[112] *mesytec MPR-1*. URL: https://www.mesytec.com/products/nuclear-physics/MPR-1.

[113] Paul Horowitz and Winfield Hill. *The Art of Electronics*. Cambridge University Press, 2015.

[114] K. Starosta et al. “Digital Data Acquisition System for experiments with segmented detectors at National Superconducting Cyclotron Laboratory”. In: *Nuclear Instruments and Methods in Physics Research Section A: Accelerators, Spectrometers, Detectors and Associated Equipment* 610.3 (2009), pp. 700–709. ISSN: 0168-9002. DOI: https://doi.org/10.1016/j.nima.2009.09.016. URL: https://www.sciencedirect.com/science/article/pii/S0168900209017392.

[115] C.J. Prokop et al. “Digital data acquisition system implementation at the National Superconducting Cyclotron Laboratory”. In: *Nuclear Instruments and Methods in Physics Research Section A: Accelerators, Spectrometers, Detectors and Associated Equipment* 741 (2014), pp. 163–168. ISSN: 0168-9002. DOI: https://doi.org/10.1016/j.nima.2013.12.044. URL: https://www.sciencedirect.com/science/article/pii/S0168900213017488.

[116] Valentin T. Jordanov and Glenn F. Knoll. “Digital synthesis of pulse shapes in real time for high resolution radiation spectroscopy”. In: *Nuclear Instruments and Methods in Physics Research Section A: Accelerators, Spectrometers, Detectors and Associated Equipment* 345.2 (1994), pp. 337–345. ISSN: 0168-9002. DOI: https://doi.org/10.1016/0168-9002(94)91011-1. URL: https://www.sciencedirect.com/science/article/pii/0168900294910111.

[117] M.J. Martin. “Nuclear Data Sheets for A = 152”. In: *Nuclear Data Sheets* 114.11 (2013), pp. 1497–1847. ISSN: 0090-3752. DOI: https://doi.org/10.1016/j.nds.2013.11.001. URL: https://www.sciencedirect.com/science/article/pii/S0090375213000744.

[118] Matt Newville et al. *xraypy/XrayDB: 4.5.1*. Version 4.5.1. 2023. DOI: 10.5281/zenodo.8212749. URL: https://doi.org/10.5281/zenodo.8212749.

[119] M.S. Basunia. “Nuclear Data Sheets for A = 237”. In: *Nuclear Data Sheets* 107.8 (2006), pp. 2323–2422. ISSN: 0090-3752. DOI: https://doi.org/10.1016/j.nds.2006.07.001. URL: https://www.sciencedirect.com/science/article/pii/S0090375206000585.

[120] Daniel Foreman-Mackey et al. “emcee: The MCMC Hammer”. In: *Publications of the Astronomical Society of the Pacific* 125.925 (Feb. 2013), p. 306. DOI: 10.1086/670067. URL: https://dx.doi.org/10.1086/670067.

[121] Marcell P. Takács and Karsten Kossert. "Half-life determination of short-lived nuclear levels in 237Np (59.54 keV), 233Pa (86.47 keV) and 227Ac (27.37 keV)". in: *Applied Radiation and Isotopes* 176 (2021), p. 109858. ISSN: 0969-8043. DOI: https://doi.org/10.1016/j.apradiso.2021.109858. URL: https://www.sciencedirect.com/science/article/pii/S0969804321002591.

[122] Chavdar Dutsov et al. "Measurement of the half-life of excited nuclear states using liquid scintillation counting". In: *Applied Radiation and Isotopes* 176 (2021), p. 109845. ISSN: 0969-8043. DOI: https://doi.org/10.1016/j.apradiso.2021.109845. URL: https://www.sciencedirect.com/science/article/pii/S0969804321002463.

[123] M. K. Moe and D. D. Lowenthal. "Double beta decay of ^{82}Se". In: *Phys. Rev. C* 22 (5 Nov. 1980), pp. 2186–2203. DOI: 10.1103/PhysRevC.22.2186. URL: https://link.aps.org/doi/10.1103/PhysRevC.22.2186.

[124] M. Pfützner et al. "Radioactive decays at limits of nuclear stability". In: *Rev. Mod. Phys.* 84 (2 Apr. 2012), pp. 567–619. DOI: 10.1103/RevModPhys.84.567. URL: https://link.aps.org/doi/10.1103/RevModPhys.84.567.

[125] J KRAMP et al. "Nuclear two-photon decay in 0+→0+ transitions". English. In: *Nuclear Physics A* 474.2 (Nov. 1987), pp. 412–450. ISSN: 0375-9474. DOI: 10.1016/0375-9474(87)90625-7.

[126] Pierre de Marcillac et al. "Experimental detection of α-particles from the radioactive decay of natural bismuth". In: *Nature* 422.6934 (Apr. 2003), pp. 876–878. ISSN: 1476-4687. DOI: 10.1038/nature01541. URL: https://doi.org/10.1038/nature01541.

[127] V.I. Tretyak. "Spontaneous double alpha decay: First experimental limit and prospects of investigation". In: *Nucl. Phys. At. Energy* 22 (2021), pp. 121–126.

[128] F. Mercier et al. "Microscopic Description of 2α Decay in ^{212}Po and ^{224}Ra Isotopes". In: *Phys. Rev. Lett.* 127 (1 July 2021), p. 012501. DOI: 10.1103/PhysRevLett.127.012501. URL: https://link.aps.org/doi/10.1103/PhysRevLett.127.012501.

[129] D. Vretenar et al. "Relativistic Hartree–Bogoliubov theory: static and dynamic aspects of exotic nuclear structure". In: *Physics Reports* 409.3 (2005), pp. 101–259. ISSN: 0370-1573. DOI: https://doi.org/10.1016/j.physrep.2004.10.001. URL: https://www.sciencedirect.com/science/article/pii/S0370157304004545.

[130] P. Marevi ć et al. "Quadrupole and octupole collectivity and cluster structures in neon isotopes". In: *Phys. Rev. C* 97 (2 Feb. 2018), p. 024334. DOI: 10.1103/PhysRevC.97.024334. URL: https://link.aps.org/doi/10.1103/PhysRevC.97.024334.

[131] P. Marevi ć et al. "Cluster structures in ^{12}C from global energy density functionals". In: *Phys. Rev. C* 99 (3 Mar. 2019), p. 034317. DOI: 10.1103/PhysRevC.99.034317. URL:

https://link.aps.org/doi/10.1103/PhysRevC.99.034317.

[132] Jie Zhao et al. "Multidimensionally constrained relativistic Hartree-Bogoliubov study of spontaneous nuclear fission". In: *Phys. Rev. C* 92 (6 Dec. 2015), p. 064315. DOI: 10.1103/PhysRevC.92.064315. URL: https://link.aps.org/doi/10.1103/PhysRevC.92.064315.

[133] Jie Zhao et al. "Multidimensionally-constrained relativistic mean-field study of spontaneous fission: Coupling between shape and pairing degrees of freedom". In: *Phys. Rev. C* 93 (4 Apr. 2016), p. 044315. DOI: 10.1103/PhysRevC.93.044315. URL: https://link.aps.org/doi/10.1103/PhysRevC.93.044315.

[134] H. Tao et al. "Microscopic study of induced fission dynamics of ^{226}Th with covariant energy density functionals". In: *Phys. Rev. C* 96 (2 Aug. 2017), p. 024319. DOI: 10.1103/PhysRevC.96.024319. URL: https://link.aps.org/doi/10.1103/PhysRevC.96.024319.

[135] Jie Zhao et al. "Microscopic self-consistent description of induced fission dynamics: Finite-temperature effects". In: *Phys. Rev. C* 99 (1 Jan. 2019), p. 014618. DOI: 10.1103/PhysRevC.99.014618. URL: https://link.aps.org/doi/10.1103/PhysRevC.99.014618.

[136] Jie Zhao et al. "Time-dependent generator-coordinate-method study of mass-asymmetric fission of actinides". In: *Phys. Rev. C* 99 (5 May 2019), p. 054613. DOI: 10.1103/PhysRevC.99.054613. URL: https://link.aps.org/doi/10.1103/PhysRevC.99.054613.

[137] F. Mercier et al. "Microscopic description of the self-conjugate ^{108}Xe and ^{104}Teα-decay chain". In: *Phys. Rev. C* 102 (1 July 2020), p. 011301. DOI: 10.1103/PhysRevC.102.011301. URL: https://link.aps.org/doi/10.1103/PhysRevC.102.011301.

[138] J.-P. Ebran et al. "Single-particle spatial dispersion and clusters in nuclei". In: *Phys. Rev. C* 97 (6 June 2018), p. 061301. DOI: 10.1103/PhysRevC.97.061301. URL: https://link.aps.org/doi/10.1103/PhysRevC.97.061301.

[139] J-P Ebran, E Khan, and R-D Lasseri. "Nucleonic localisation and alpha radioactivity". In: *Journal of Physics G: Nuclear and Particle Physics* 48.2 (Dec. 2020), p. 025106. DOI: 10.1088/1361-6471/abcf25.

[140] A.H. Wapstra, G. Audi, and C. Thibault. "The Ame2003 atomic mass evaluation: (I). Evaluation of input data, adjustment procedures". In: *Nuclear Physics A* 729.1 (2003). The 2003 NUBASE and Atomic Mass Evaluations, pp. 129–336. ISSN: 0375-9474. DOI: https://doi.org/10.1016/j.nuclphysa.2003.11.002. URL: https://www.sciencedirect.com/science/article/pii/S0375947403018086.

[141] J. Zhao et al. "Microscopic description of α, 2α, and cluster decays of $^{216-220}$Rn and $^{220-224}$Ra". In: *Phys. Rev. C* 107 (3 Mar. 2023), p. 034311. DOI: 10.1103/PhysRevC.107.034311. URL: https://link.aps.org/doi/10.1103/PhysRevC.107.034311.

[142] L. P. Gaffney et al. "Studies of pear-shaped nuclei using accelerated radioactive beams". In: *Nature* 497.7448 (May 2013), pp. 199–204. ISSN: 1476-4687. DOI: 10.1038/nature12073. URL: https://doi.org/10.1038/nature12073.

[143] Gudveen Sawhney, Chahat Jindal, and Manoj K. Sharma. "From α to 2α and cluster emission: A unified study of actinium and thorium isotopes". In: *Phys. Rev. C* 112 (5 Nov. 2025), p. 054301. DOI: 10.1103/tbxv-tlbf. URL: https://link.aps.org/doi/10.1103/tbxv-tlbf.

[144] V.Yu. Denisov. "Estimation of the double alpha-decay half-life". In: *Physics Letters B* 835 (2022), p. 137569. ISSN: 0370-2693. DOI: https://doi.org/10.1016/j.physletb.2022.137569. URL: https://www.sciencedirect.com/science/article/pii/S037026932200703

[145] Christophe Theisen and Elias Khan. *Probing two-alpha radioactivity with 224Ra*. Tech. rep. Geneva: CERN, 2021. URL: https://cds.cern.ch/record/2782408.

[146] Christophe THEISEN and Elias KHAN. *Probing two-alpha radioactivity with 224Ra*. Tech. rep. Geneva: CERN, 2022. URL: https://cds.cern.ch/record/2809125.

[147] PandaX Collaboration et al. *Precise Measurement of ^{216}Po Half-life with Exact Parent-daughter Pairing in PandaX-4T*. 2025. arXiv: 2507.13241 [nucl-ex]. URL: https://arxiv.org/abs/2507.13241.

[148] M. Friedman et al. "GADGET: a Gaseous Detector with Germanium Tagging". In: *Nuclear Instruments and Methods in Physics Research Section A: Accelerators, Spectrometers, Detectors and Associated Equipment* 940 (2019), pp. 93–102. ISSN: 0168-9002. DOI: https://doi.org/10.1016/j.nima.2019.05.100. URL: https://www.sciencedirect.com/science/article/pii/S0168900219308162.

[149] Sukhjeet Singh and Balraj Singh. "Nuclear Data Sheets for A = 224". In: *Nuclear Data Sheets* 130 (2015), pp. 127–182. ISSN: 0090-3752. DOI: https://doi.org/10.1016/j.nds.2015.11.003. URL: https://www.sciencedirect.com/science/article/pii/S0090375215000575.

[150] E. Browne and J.K. Tuli. "Nuclear Data Sheets for A = 220". In: *Nuclear Data Sheets* 112.4 (2011), pp. 1115–1161. ISSN: 0090-3752. DOI: https://doi.org/10.1016/j.nds.2011.03.002. URL: https://www.sciencedirect.com/science/article/pii/S009037521100021

[151] S.-C. Wu. "Nuclear Data Sheets for A = 216". In: *Nuclear Data Sheets* 108.5 (2007), pp. 1057–1092. ISSN: 0090-3752. DOI: https://doi.org/10.1016/j.nds.2007.04.001. URL: https://www.sciencedirect.com/science/article/pii/S0090375207000415.

[152] K. Auranen and E.A. McCutchan. "Nuclear Data Sheets for A=212". In: *Nuclear Data Sheets* 168 (2020), pp. 117–267. ISSN: 0090-3752. DOI: https://doi.org/10.1016/j.nds.2020.09.002. URL: https://www.sciencedirect.com/science/article/pii/S0090375220300351.

[153] E.C. Pollacco et al. "GET: A generic electronics system for TPCs and nuclear physics instrumentation". In: *Nuclear Instruments and Methods in Physics Research Section A: Accelerators, Spectrometers, Detectors and Associated Equipment* 887 (2018), pp. 81–93. ISSN: 0168-9002. DOI: https://doi.org/10.1016/j.nima.2018.01.020. URL: https://www.sciencedirect.com/science/article/pii/S0168900218300342.

[154] URL: https://docs.frib.msu.edu/daq/newsite/home.php.

[155] Chiara Zampolli. *ALICE data processing for Run 3 and Run 4 at the LHC*. 2020. arXiv: 2012.04391 [physics.ins-det]. URL: https://arxiv.org/abs/2012.04391.

[156] S. Beceiro-Novo et al. "Active targets for the study of nuclei far from stability". In: *Progress in Particle and Nuclear Physics* 84 (2015), pp. 124–165. ISSN: 0146-6410. DOI: https://doi.org/10.1016/j.ppnp.2015.06.003. URL: https://www.sciencedirect.com/science/article/pii/S0146641015000459.

[157] J. Bradt et al. "Commissioning of the Active-Target Time Projection Chamber". In: *Nuclear Instruments and Methods in Physics Research Section A: Accelerators, Spectrometers, Detectors and Associated Equipment* 875 (2017), pp. 65–79. ISSN: 0168-9002. DOI: https://doi.org/10.1016/j.nima.2017.09.013. URL: https://www.sciencedirect.com/science/article/pii/S0168900217309683.

[158] Y. Ayyad et al. "Next-generation experiments with the Active Target Time Projection Chamber (AT-TPC)". in: *Nuclear Instruments and Methods in Physics Research Section A: Accelerators, Spectrometers, Detectors and Associated Equipment* 954 (2020). Symposium on Radiation Measurements and Applications XVII, p. 161341. ISSN: 0168-9002. DOI: https://doi.org/10.1016/j.nima.2018.10.019. URL: https://www.sciencedirect.com/science/article/pii/S0168900218313342.

[159] T. Roger et al. "Demonstrator Detection System for the Active Target and Time Projection Chamber (ACTAR TPC) project". In: *Nuclear Instruments and Methods in Physics Research Section A: Accelerators, Spectrometers, Detectors and Associated Equipment* 895 (2018), pp. 126–134. ISSN: 0168-9002. DOI: https://doi.org/10.1016/j.nima.2018.04.003. URL: https://www.sciencedirect.com/science/article/pii/S016890021830477

[160] D. Attié et al. "Characterization of resistive Micromegas detectors for the upgrade of the T2K Near Detector Time Projection Chambers". In: *Nuclear Instruments and Methods in Physics Research Section A: Accelerators, Spectrometers, Detectors and Associated Equipment* 1025 (Feb. 2022), p. 166109. ISSN: 0168-9002. DOI: 10.1016/j.nima.2021.166109. URL: http://dx.doi.org/10.1016/j.nima.2021.166109.

[161] A. Sharma and F. Sauli. "First Townsend coefficient measured in argon based mixtures at high fields". In: *Nuclear Instruments and Methods in Physics Research Section A: Accelerators, Spectrometers, Detectors and Associated Equipment* 334.2 (1993), pp. 420–424. ISSN: 0168-9002. DOI: https://doi.org/10.1016/0168-9002(93)90802-O. URL: https://www.sciencedirect.com/science/article/pii/0168900293908020.

[162] W. N. English and G. C. Hanna. "GRID IONIZATION CHAMBER MEASUREMENTS OF ELECTRON DRIFT VELOCITIES IN GAS MIXTURES". in: *Canadian Journal of Physics* 31.5 (1953), pp. 768–797. DOI: 10.1139/p53-070. eprint: https://doi.org/10.1139/p53-070. URL: https://doi.org/10.1139/p53-070.

[163] J. Giovinazzo et al. "Metal-core pad-plane development for ACTAR TPC". in: *Nuclear Instruments and Methods in Physics Research Section A: Accelerators, Spectrometers, Detectors and Associated Equipment* 892 (2018), pp. 114–121. ISSN: 0168-9002. DOI: https://doi.org/10.1016/j.nima.2018.03.007. URL: https://www.sciencedirect.com/science/article/pii/S0168900218303243.

[164] W. Hirst and G. E. Harrison. "The Diffusion of Radon Gas Mixtures". In: *Proceedings of the Royal Society of London. Series A, Mathematical and Physical Sciences* 169.939 (1939), pp. 573–586. ISSN: 00804630. URL: http://www.jstor.org/stable/97163 (visited on 12/04/2025).

[165] RJ Walen. "PHYSIQUE NUCLEAIRE-SPECTROGRAPHIE ALPHA DU RADIUM 224 ET DE SES DERIVES". in: *COMPTES RENDUS HEBDOMADAIRES DES SEANCES DE L ACADEMIE DES SCIENCES* 255.14 (1962), p. 1604.

[166] R J Poynter et al. "Studies of octupole structures in the isotopes 220,222Rn populated via α decay." In: *Journal of Physics G: Nuclear and Particle Physics* 15.4 (Apr. 1989), p. 449. DOI: 10.1088/0954-3899/15/4/008. URL: https://doi.org/10.1088/0954-3899/15/4/008.

[167] N Wandkowsky et al. "Modeling of electron emission processes accompanying radon-α-decays within electrostatic spectrometers". In: *New Journal of Physics* 15.8 (Aug. 2013), p. 083040. DOI: 10.1088/1367-2630/15/8/083040. URL: https://doi.org/10.1088/1367-2630/15/8/083040.

[168] F. Garwood. "Fiducial Limits for the Poisson Distribution". In: *Biometrika* 28.3/4 (1936), pp. 437–442. ISSN: 00063444. URL: http://www.jstor.org/stable/2333958 (visited on 02/10/2026).

[169] C. D. Pruitt, J. E. Escher, and R. Rahman. "Uncertainty-quantified phenomenological optical potentials for single-nucleon scattering". In: *Phys. Rev. C* 107 (1 Jan. 2023), p. 014602. DOI: 10.1103/PhysRevC.107.014602. URL: https://link.aps.org/doi/10.1103/PhysRevC.107.014602.

[170] D. N. Poenaru et al. “Erratum: Systematics of cluster decay modes [Phys. Rev. C 65, 054308 (2002)]”. In: *Phys. Rev. C* 66 (4 Oct. 2002), p. 049902. DOI: 10.1103/PhysRevC.66.049902. URL: https://link.aps.org/doi/10.1103/PhysRevC.66.049902.

[171] L Fonda, G C Ghirardi, and A Rimini. “Decay theory of unstable quantum systems”. In: *Reports on Progress in Physics* 41.4 (Apr. 1978), p. 587. DOI: 10.1088/0034-4885/41/4/003. URL: https://dx.doi.org/10.1088/0034-4885/41/4/003.

APPENDIX

A.1 Brief Aside about Half-lives

Since the discovery of the nature of half-lives of radioactive nuclei in 1900 by Rutherford, there are two observed properties that allow us to derive the exponential decay law. First, each radioactive nucleus has some probability of decay, and second, this probability 'does not depend on the past history of the individual decaying nuclei.' From this, we get a phenomenological description of exponential decay: 'the variation of the number $N(t)$ of radioactive nuclei which are present at time t during the infinitesimal interval of time dt must be proportional to $N(t)$ and dt:

$$dN(t) = -\lambda N(t)dt \tag{1}$$

from which we get the exponential decay law

$$N(t) = N(0)\exp(-\lambda t) \tag{2}$$

where λ is the decay constant of the radioactive nucleus' [171]. While Equation 2 describes experimental observations extremely well, it does not *theoretically* describe why this is the case. Semi-classically, this was first tackled by R W Gurney and E U Condon, and by G Gamow in 1928. The argument was based on an alpha particle in the nuclear potential well with some non-zero probability to tunnel through and create a decay event, leading to this aleatory property of nuclear decay.

In the case where a nucleus has more than one way it can decay, these 'decay channels' (a and b) can end up producing 2 different nuclei after the decay. 'The rate of decay into mode a $(dN/dt)_a$ is determined by the *partial decay constant* λ_a, and the rate of decay into mode b $(dN/dt)_b$ by λ_b':

$$\lambda_a = \frac{-(dN/dt)_a}{N} \tag{3}$$

$$\lambda_b = \frac{-(dN/dt)_b}{N} \tag{4}$$

The *total decay rate* $(dN/dt)_t$ is

$$-\left(\frac{dN}{dt}\right)_t = -\left(\frac{dN}{dt}\right)_a - \left(\frac{dN}{dt}\right)_b = N(\lambda_a + \lambda_b) = N\lambda_t \tag{5}$$

where $\lambda_t = \lambda_a + \lambda_b$ is the total decay constant. It is useful to keep in mind that whether you are detecting decays from modes a or b, the thing you are ultimately observing is always the total decay constant, λ_t. In order to measure the partial decay constants, we must accurately measure the amount of initial particles we have (N), and have a really good idea of the efficiency of our detection set up to get an accurate number for total decays coming from specifically mode a, for example. Alternatively, we need an accurate measurement of the ratios between all of the decay modes to measure the partial decay constants and branching ratios.

At our current place in time as physicists, the randomness of the decay process does not bother us. However, at the time these discoveries were being made, it was harder to accept that it is impossible to know what an individual system will do at a given time, as quantum mechanics was not a well-established field of study. Keep in mind that this randomness is markedly different than say a roll of dice. In the case of a dice roll, a physicist, given precise enough starting conditions (shape and position of dice, force applied during the roll), could reliably predict the outcome every time. In quantum mechanics, this is not the case. The level of precision we would need to accurately predict when a given nucleus would decay is impossible to measure; forbidden by the underlying formalism of quantum mechanics. This inherent uncertainty is born out as randomness, which allows us to model nuclear decay as exponential.

A.2 LIBRA Detector Information

Physical copies of LIBRA's detector and hardware manuals can be found in room 1035. The following pages are scans of the datasheets sent to us by the manufacturers of the detectors used in the LIBRA setup. For more general information on these semiconductor detectors, see Knoll [107], and this link to Mirion's System Considerations with High Resolution Detectors and this link to Mirion's Germanium Detector User's Manual. FRIB's online copy of Mirion's Cryo-Pulse 5 plus Electrically Refrigerated Cryostat user's manual.

A.3 Why ^{220}Rn?

Santhosh, Zhao, Chandran, and Denisov agree we should expect minimum half-lives for double alpha decays where the daughter is most stable. In the case of looking for double alpha decays then,

we should be using nuclei with proton/neutron numbers of 6, 12, 24, 32, 54, 86, or 130. Indeed, Denisov states that ^{108}Xe is a very promising experimental probe of $\alpha\alpha-$decay. Enthusiastic readers might inquire, 'well if that is the case, ^{220}Rn satisfies this for proton number (86), but not for neutron number (134), why not use ^{216}Rn!?' And while it is true that using ^{216}Rn might mean that, theoretically, the half life of double alpha decay might be lower, and thus easier to measure against the competing and dominant single alpha decay, there are a few issues experimentally with this. One, we have an extremely convenient set up whereby we can, with the use of a common test source, pump ^{220}Rn into our detector to be measured offline. If we were to use ^{216}Rn, this would require us to produce it in some other, much more expensive way, which is likely unfeasible for the long duration we ran the experiment; this is also why an 'ideal' nucleus like ^{108}Xe is not among the first candidates being measured. Extremely enthusiastic readers might have noticed the second issue, which is that the single alpha decay channel goes through ^{212}Po, which has a half-life of <300 ns, meaning that there is a high probability that we see the sequential decay occurring simultaneously (in view of our detector), reducing our ability to probe for the double alpha decay mode we are interested in. Other $\alpha\alpha$ candidate nuclei in this region may be produced by a full-powered FRIB in the future at rates that make it possible to conduct the search for $\alpha\alpha-$decay, but such beam time is not guaranteed, and may be a decade or more away.

In any case, Zhao et al. show that the predicted half-lives for $\alpha\alpha-$decay are highly dependent on the Q-value of that decay, and our choice of ^{220}Rn lies in the 'golden region' shown in Figure A.1 [141].

A.4 GADGET II Operation Guides

Procedure	0	1	3	4	5	6	7	8	9	10
Pump GHS	X	V	V	X	X	V	V	V	V	X
Pump Detector	X	V	V	V	V	V	V	V	V	V
Flow Gas	V	V	V	V	V	X	X	X	X	X
Introduce Rn	V	V	X	V	V	V	V	X	X	X

Table .1 Valve Status Summary (V – open, X - closed)

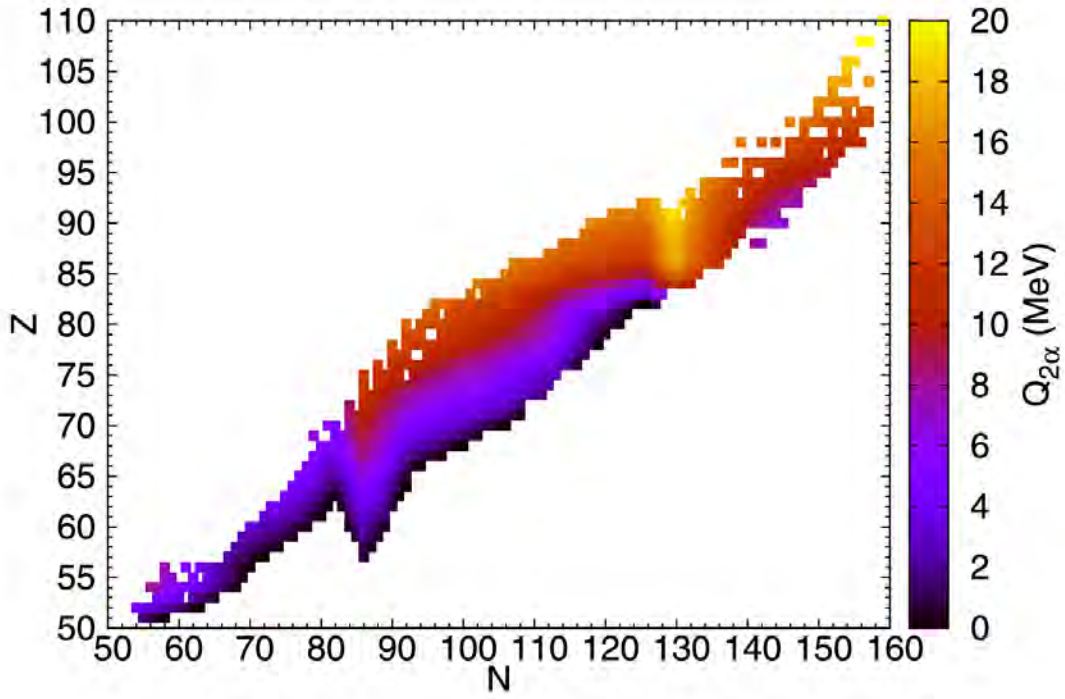

Figure A.1 Zhao et al.'s version of Figure 3.2. The chart shows nuclei whose Z and N are > 50, and whose $Q_{2\alpha}$ values are > 0. Zhao et al. states the higher the Q-value, the more favorable that nuclei is as a candidate [141].

A.4.1 Gas Handling System Operating Procedure

The following are instructions to operate GADGET under different circumstances.

Pump Gas Handling System (GHS):

1. Check voltages are off (cathode, gating grid, and Micromegas). Turn off both crates to ensure this is the case.
2. Monitor detector pressure.
3. Isolate detector by closing valves 4, 5, 10.
4. Valves 0a, 0b, 4, 5, 8, 9, 10 closed. Valves 3, 6, 7 open.
5. Only open 1a or 1b if connected to bottle.
6. Open 1a/1b.

7. Open valve 9.

8. Turn on pump.

9. Turn off mass-flow controller or set pressure to zero. Open valve 8.

Pump Detector:

NOTE: always try to avoid situation of holding the detector at lower pressure than the GHS while valve 4 is open.

1. Follow procedure to pump GHS.

2. Valves 0a, 0b, 4, 5, 10 should be closed. Valves 3, 6, 7, 8, 9 open.

3. Only open 1a or 1b if connected to bottle.

4. Open 1a/1b.

5. Open valve 5 for slow pumping (about 10 torr per second at most).

6. When pressure in chamber drops below 200 torr, open valves 4, 5 (fully), and 10.

7. If swapping gas bottles, pump to about 10 millitorr before reintroducing gas to the system and detector.

Flow Gas Through Detector:

1. Follow instructions for pumping GHS and detector.

2. Close valves 0a, 0b, 1a, 1b, 4, 5, 7, 8, 9, 10. Valves 3 & 6 should be open.

3. Recheck voltages are off (cathode, gating grid, and micromegas).

4. Set mass-flow controller to the desired pressure.

5. Regulator attached to the gas bottle should NOT be set higher than 30 psig.

6. Open valve 0a or 0b, then open the corresponding valve 1a or 1b.

7. Use valve 4 to break vacuum at no more than 10 torr per second.

8. Open 4 fully when complete.

9. Adjust valve 5 to allow the desired flow rate.

Introduce 220Rn to gas:

1. Follow instructions for flowing gas through detector.

2. Open valves 6 & 7.

3. Close valve 3.

Turn HV on:

1. Inspect system to verify:

    - 20 kV SHV (red cable) is connected to the cathode, and the grounding SMA (white) is connected to the "cathode ground" electrical feedthrough. The other end of the red cable should be connected to the CAEN HV module.
    - Two SMA (black cables) are connected to the 'gg pos' and 'gg neg' electrical feedthroughs. The other ends should be connected to the gating grid switch.
    - Two or three cables connect the MHV-4 module to the switch, according to the relevant gating grid mode. Connecting "POS" input at lower absolute potential relative to "NEG" in the same port will damage the switch.
    - The preamp is connected to the Mesytec MHV-4 module.
    - A grounding cable is connecting the electronics rack to the network ground. Make sure the inner frame of the electronics rack is connected to ground, not the outer blue frame.
    - A grounding cable is connecting the rack to the detector.

- A grounding cable is connecting the preamp grounding screw to the Micromegas support ring.

2. Verify the pressure in the chamber. Note that while valve 4 is closed, the mass-flow controller does not measure the pressure in the chamber. Make sure that the HV that you are about to apply is appropriate for the pressure in the chamber. Specify Pressure.

3. Set interlocks for both HV modules. The interlocks should be no more than 20 μA for the MHV-4 module and 40 μA for the CAEN module.

4. If the chamber was exposed to air since the last time HV was applied, set ramping rate of 5 V/s in both modules. Otherwise a ramping rate of 50 V/s is normal.

5. Turn on the CAEN HV. Monitor the current as it is ramping. 3.75 μA/kV is normal. Wait until ramping is complete. The field cage should be set to 6 kV.

6. Turn on the gating grid high voltage. Monitor the current. Up to a few μA is normal

7. Turn on the Micromegas bias slowly. A transient current should go up to 20 μA, but zero current is expected at steady state.

NOTE for HV remote operation:

- As a general rule, avoid remote control of the HV if it is not necessary.
- Before switching the CAEN HV module to "remote" mode, all the steps should be made as for turning it on.
- When dealing with any of the HV cables during experiment, one must exit "remote" mode until the work is complete.

Turn HV off:

1. Make sure not to kill the HV on the CAEN module, but to turn it off (switch in the middle position) so that the module can ramp down the voltage more safely.

A.4.2 Schematic of GADGET Gas Handling System

A.5 GADGET Group Analysis Repository

GADGET Group Github

ATTPC Group uses data analysis tools that are very similar to our group's. Their code can be found here for reference: ATTPC Group Github

The coincidence analysis is done via the scripts found in directories `/user/protondetector/readout/rootfile/` and `/mnt/daqtesting/protondetector/stagearea/`.

A.6 Other Figures

The Thorium series, with names of the isotopes from the early 1900's illustrating early nuclear physicists' understanding at the time:

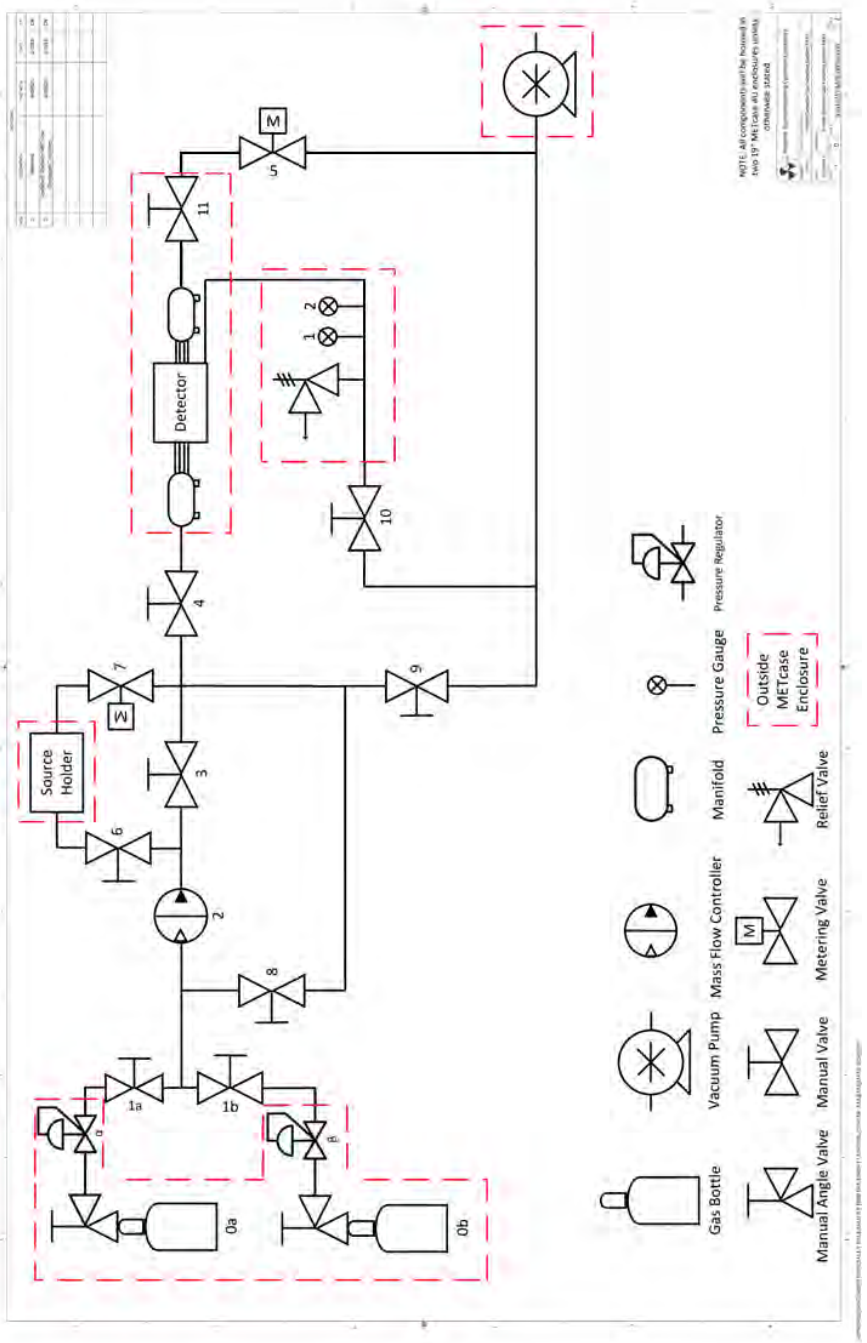

Figure A.2 Schematic of GADGET Gas Handling System (GHS). Components highlighted in a dashed red line are outside of the GHS rack-mounted enclosure.

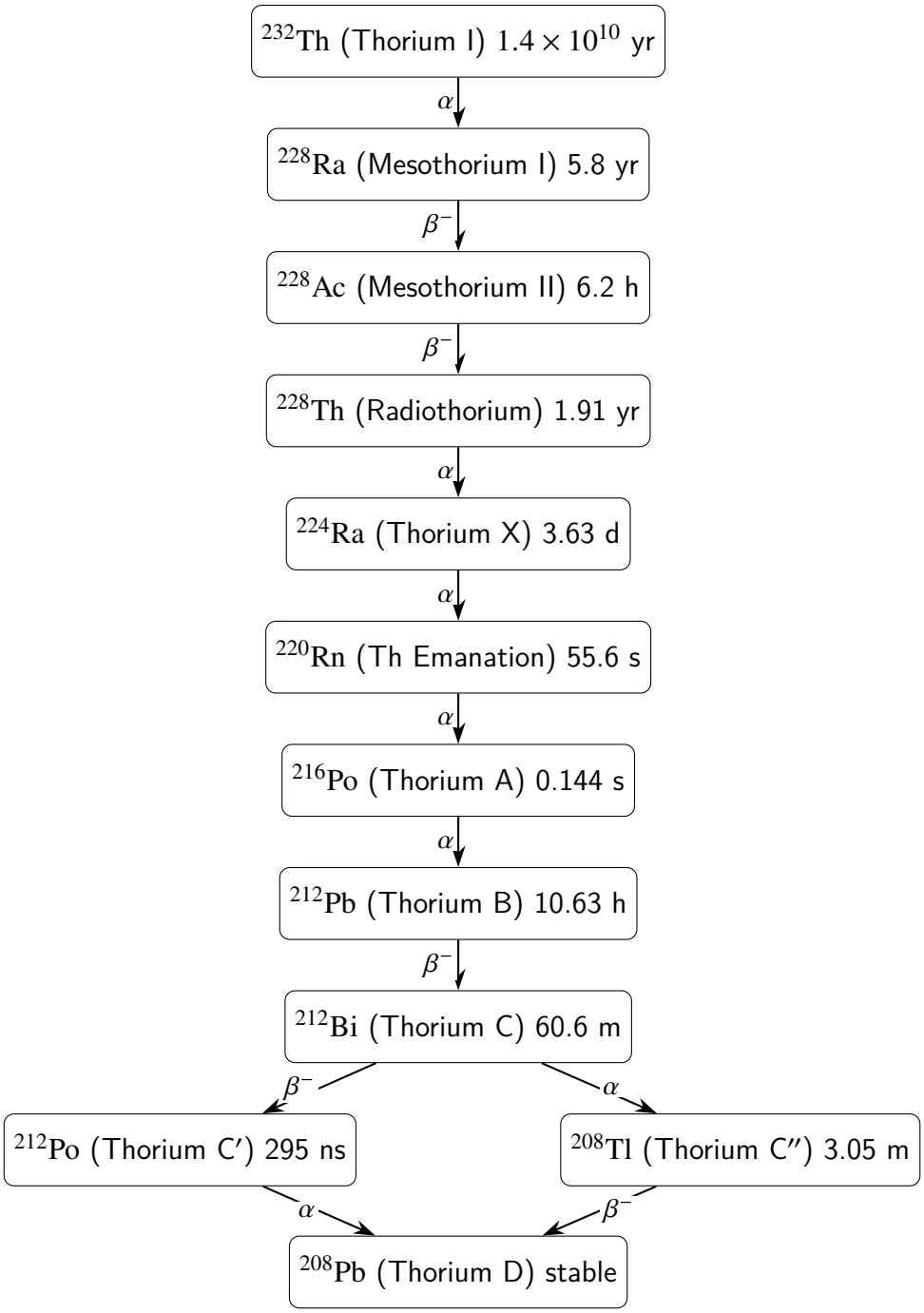

A.6.1 dxy vs dz plots

Another method was attempted using the efficiency corrected radial distribution of the radiation. The x- and y-distributions were corrected for geometric efficiency and fitted with a few functions, of which a quadratic seemed to perform the best. This function was then used to extend the radial distribution to the edge of the detector in an attempt to eliminate the edge effects caused by the

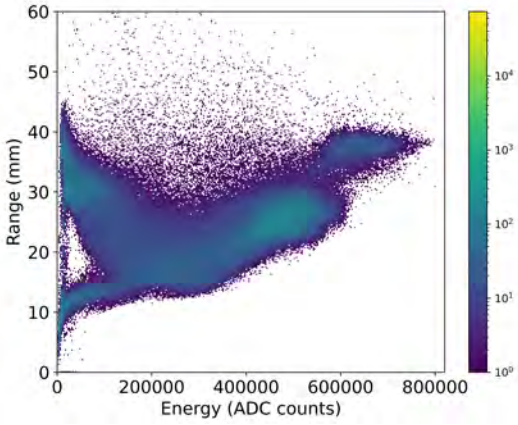

(a) Run 55

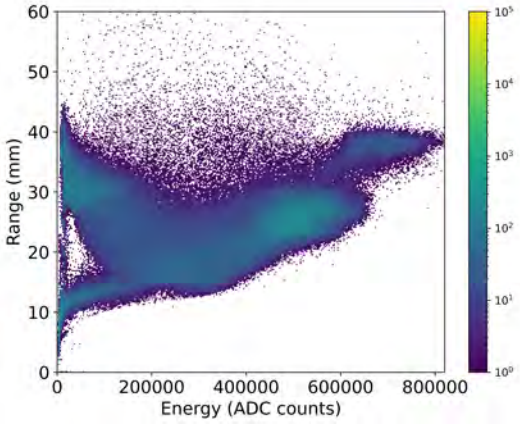

(b) Run 155

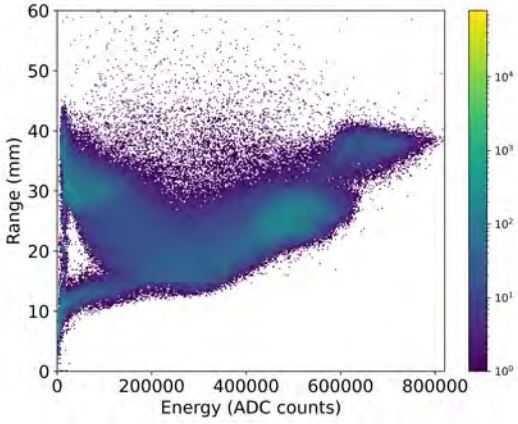

(c) Run 255

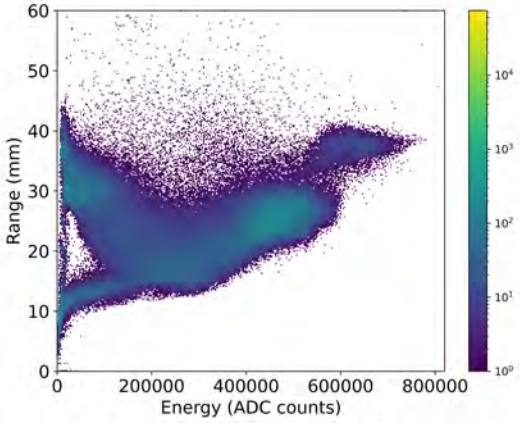

(d) Run 355

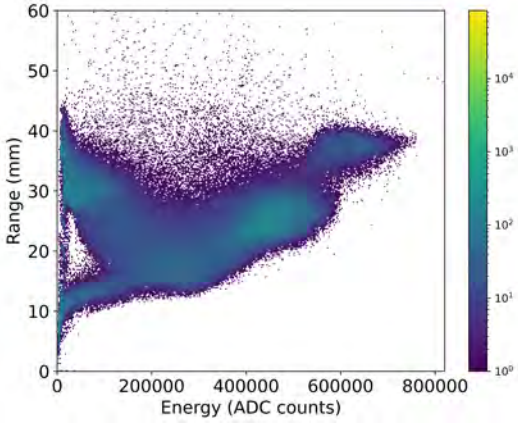

(e) Run 455

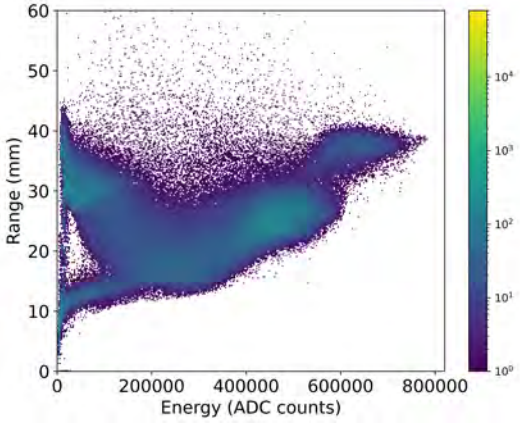

(f) Run 555

Figure A.3 Range versus Energy plots with no veto condition for runs throughout the experiment

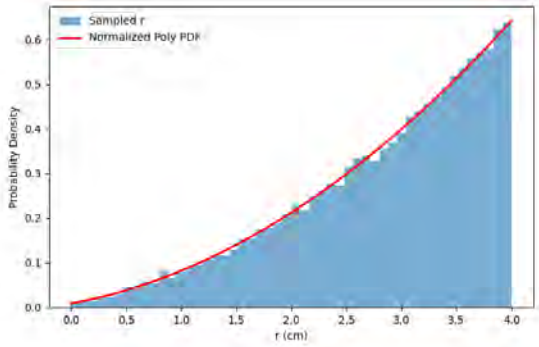

Figure A.4 Efficiency corrected radial distribution of the radiation, fit with a quadratic and extended to the edge of the radius of the active surface of the TPC.

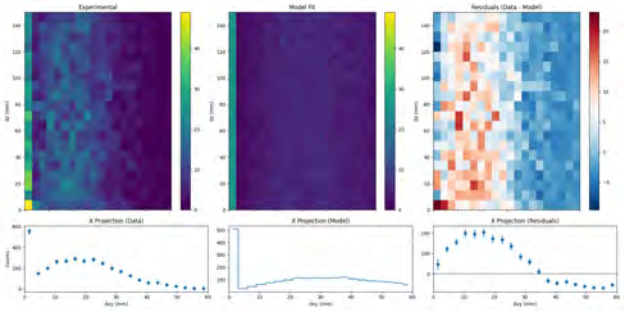

Figure A.5 Results of fitting the data with the simulation using the extended quadratic radial distribution.

centroid method shown in Figure 5.10. The subsequent radial distribution is shown in Figure A.4. However, the resulting dxy vs dz plot produced by this simulation is much too broad, reflecting much the same issue that the other models used for this simulation exhibit, shown in Figure A.5.

I believe it makes sense that the geometric efficiency corrected distribution does not work well here, because the geometry correction is using alphas emitted isotropically, whereas the x- and y-distributions come only from events emitted along the z-axis.

A.6.2 ^{220}Rn Decay Chain

There is not entirely clear evidence that ^{212}Bi decays mostly on the cathode, so it is assumed that it has an efficiency to be detected closer to ^{220}Rn and ^{216}Po than ^{212}Po, which we have more evidence for. In the case that ^{212}Bi does decay near the cathode, there would be a lowering of the efficiency to observe it in the detector, as about half of the alphas would be emitted directly into a solid, and not be observed. The plot in Figure A.6 shows this assumption by halving the number of

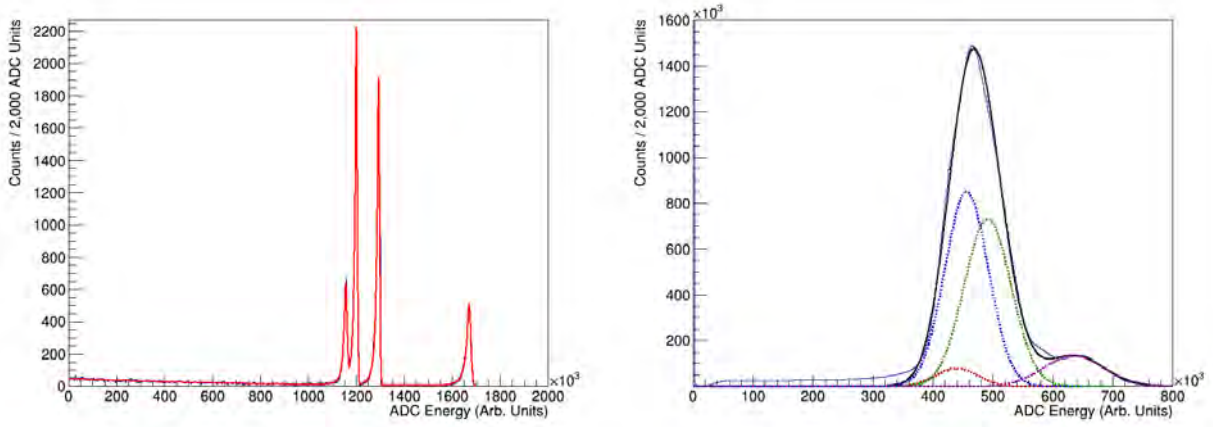

Figure A.6 The same simulated data is plotted on the left. However, when the parameters of that fit are used to fit the real data on the right, the ^{212}Bi peak (lowest energy) is assumed to have half the counts in it in an attempt to compensate for a scenario in which the Bismuth is decaying after getting stuck to the surface of the cathode.

Parent Nucleus	Alphas Observed
^{212}Bi	$(4.43 \pm 3.15) \times 10^6$
^{220}Rn	$5.31 \pm 0.30 \times 10^7$
^{216}Po	$(4.93 \pm 0.30) \times 10^7$
^{212}Po	$(1.21 \pm 0.19) \times 10^7$

Table .2 Total number of alpha particles in each peak, assuming Bismuth decays on the cathode.

alphas in the Bismuth peak after fitting the simulation.

This effect would boost the relative number of ^{220}Rn and ^{216}Po alphas in the spectrum, which Table .2 shows.

A.6.3 Disintegration Events

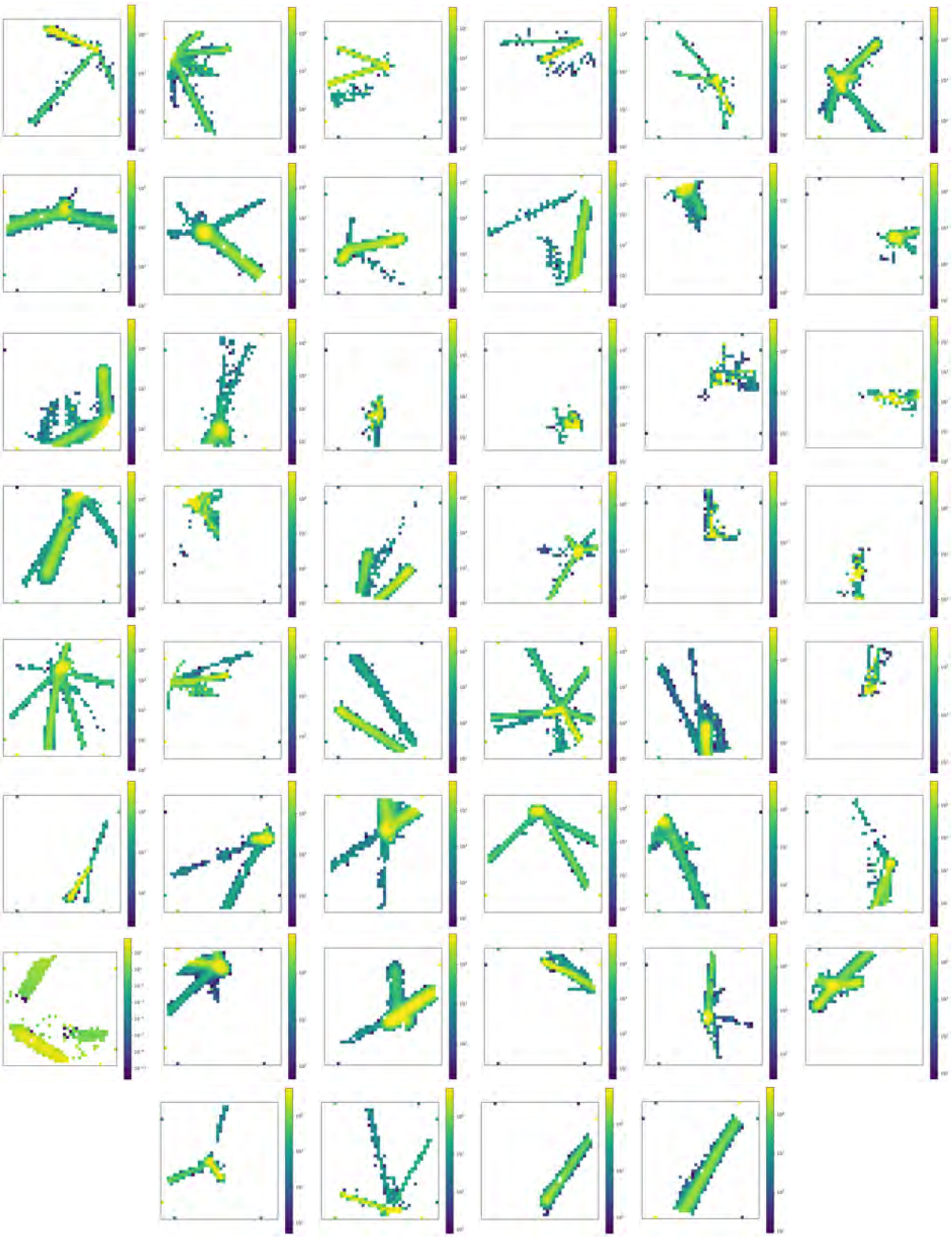

Figure A.7 Event displays for selected runs.